Orthotropic Cyclic Continuum Constitutive Model For Masonry Structures And Comparative Studies

Sousamli, M.

DOI
10.4233/uuid:34614723-9a3c-42c8-b70c-e4ac1dca5e8c

Publication date
2024

Document Version
Final published version

Citation (APA)
Sousamli, M. (2024). *Orthotropic Cyclic Continuum Constitutive Model For Masonry Structures And Comparative Studies*. [Dissertation (TU Delft), Delft University of Technology]. https://doi.org/10.4233/uuid:34614723-9a3c-42c8-b70c-e4ac1dca5e8c

Orthotropic Cyclic Continuum Constitutive Model For Masonry Structures and Comparative Studies

Orthotropic Cyclic Continuum Constitutive Model For Masonry Structures and Comparative Studies

Dissertation

for the purpose of obtaining the degree of doctor
at Delft University of Technology,
by the authority of the Rector Magnificus, Prof. dr. ir. T.H.J.J. van der Hagen,
Chair of the Board for Doctorates,
to be defended publicly on
Thursday 23 May 2024 at 12:30 o'clock

by

Marianthi SOUSAMLI

Master of Science in Civil Engineering, Delft University of Technology, The Netherlands
born in Heraklion, Greece.

This dissertation has been approved by the promotors:

Promotor: Prof. dr. ir. J.G. Rots
Co-promotor: Dr. F. Messali

Composition of the doctoral committee:

Rector Magnificus	chairperson
Prof. dr. ir. J.G. Rots	Delft University of Technology, Promotor
Dr. F. Messali	Delft University of Technology, Co-promotor
Independent members:	
Prof. dr. D. Addessi	Sapienza University of Rome, Italy
Prof. dr. G. Milani	Polytechnic University of Milan, Italy
Prof. dr. L. Pelà	Technical University of Catalonia, Spain
Prof. dr. ir. M.A.N. Hendriks	Delft University of Technology
Prof. dr. ir. L.J. Sluys	Delft University of Technology

This research was performed under the project Physical testing and modelling - Masonry structures, Groningen, and was funded by *Nederlandse Aardolie Maatschappij B.V. (NAM).*

Keywords: unreinforced masonry, orthotropic constitutive model, continuum mechanics, fracture mechanics, in-plane, cyclicity, comparative studies
Printed by: Ipskamp Printing, The Netherlands.
Cover design: Marianthi Sousamli

ISBN 978-94-6384-584-7

An electronic version of this dissertation is available at
http://repository.tudelft.nl/.

You should love responsibility. You should say: It is my duty, and mine alone, to save the earth. If it is not saved, then I alone am to blame.

Nikos Kazantzakis

Contents

Summary

There is a very popular fable, dating back to the early 1800s, about three little pigs that build their houses of different materials and a wolf that tries to catch them by blowing down their houses. From the three houses built from straws, sticks or bricks, only the house made out of bricks withstands the blow of the wolf. Although the moral of the story is unrelated to structural mechanics, the use of bricks (masonry) to symbolize strength and durability is noteworthy. However, despite its broad and impressive use over the centuries, the different material properties of its constituents, as well as their geometric arrangement, make masonry a material with a highly nonlinear and anisotropic mechanical response. Even though masonry structures have been designed to withstand gravitational loads, they are less capable to resist horizontal loads, like cyclic lateral loads from earthquakes, uneven settlements or even floods. In such cases, the structures might exhibit damage or failure in the form of tensile cracking, bed-joint shear sliding, and crushing, splitting or spalling under compression. It is, therefore, crucial to assess the response and the safety of existing structures, especially when the conditions and circumstances of loading change, for example due to climate change, or due to human-induced earthquakes in previously non earthquake-prone zones, as is the case in the area of Groningen in the Netherlands.

To assess the response of the structures, this complex mechanical behavior of masonry and all the different failure mechanisms should also be captured in the numerical models. Thanks to the advances in the field of computational mechanics, four different numerical approaches have been developed for the modelling of masonry structures: macro-element based methods, discrete element methods, finite element methods and hybrid methods. Among those, the finite element method is the most popular numerical method used to date, where masonry can be modelled based on a micro-modelling or a macro-modelling approach. Micro-modelling approaches have been shown to be more accurate but are computationally very demanding, while macro-models are regarded a good compromise between numerical accuracy and computational effort. They are, therefore, the most common computational strategy used to model large structures. Existing macro-models are formulated based on one of the following frameworks: smeared cracking, damage mechanics, plasticity, or damage-plasticity. Each framework has its own advantages and disadvantages, but a common shortcome of many macro-models is their inability to capture both the localized crack patterns and predict accurately the hysteretic behavior of structures.

The aim of this thesis is to address the abovementioned limitation firstly by developing a new macro-model and secondly, by systematically reviewing and comparing the performance of existing constitutive models (alongside the new macro-model) against experimental results and against each other.

The first part of the research was devoted to developing a cyclic, nonlinear and orthotropic continuum constitutive model that needed to satisfy the following criteria: predicting the right failure mechanism, predicting accurately the force capacity, the ductility/-softening and the dissipated energy of masonry structures, as well as capturing the brittle

localized cracks. To do so, a total-strain-rotating-crack approach was selected; an approach developed and used succesfully for brittle materials like concrete, but not as satisfactorily for masonry structures, mainly due to the adopted secant unloading/reloading and to the lack of initial orthotropy. Therefore, the inclusion of orthotropy and the description of cyclicity were of utmost importance. Orthotropic behavior is incorporated both in the elastic and in the post-peak phase. A novelty in this model is the variation of the elastic and inelastic properties with respect to the principal stress and strain direction. During the elastic phase the material properties in the two orthogonal directions are varied nonlinearly in the case of tensile strength and linearly for the remaining material parameters. After cracking, the material parameters are fixed to those corresponding to the direction of the principal stresses/strains at the onset of cracking. Even though the material properties are now fixed, a coaxial rotating stress-strain concept is still followed. For the description of the inelastic behavior an angle is defined and used as an extra material input parameter. This angle acts as a threshold and helps to distinguish between flexural and diagonal shear cracks. As a consequence, if at the onset of cracking the direction of stresses falls within the sub-horizontal or sub-vertical angles that correspond to flexural cracks the bilinear stress-strain relationship adopted in tension is associated with brittle behavior, with steep softening rate and secant unloading/reloading; otherwise, the tensile behavior has a slow softening rate and elastic-plastic unloading/reloading. The behavior in compression is described through two nonlinear curves and bilinear unloading/reloading is adopted, with the aim to resemble the elastic-plastic unloading/reloading observed during shear sliding. Finally, an internal iterative loop was implemented to regulate the Coulomb-friction based shear stress capacity alongside the bed-joint direction, in order to avoid the overestimation of the base shear force often observed in fracture mechanics models.

The constitutive model, developed for plane-stress elements, was implemented in the finite element software DIANA FEA, and was validated against experimental results obtained from four masonry walls tested cyclically in their in-plane direction. The numerical and experimental results were compared in terms of peak base shear capacity, residual base shear capacity, energy dissipation, damage localization and failure mechanism. Overall, a good agreement between numerical and experimental results was found, especially regarding the base shear capacity. The damage localization was also very representative of the experimental crack patterns. A mesh sensitivity study was performed too by varying the element size and the order of the elements. A variation of 9% was observed in the case of maximum base shear capacity and a variation of 29% in the case of residual base shear. Overall, linear elements with larger mesh size exhibited the least softening while quadratic elements exhibited more softening.

The next goal of the research was to systematically compare the accuracy of constitutive models used to model masonry, including the newly developed model. For this purpose three additional macro-models and two micro-models were selected. The three chosen macro-models comprised an orthotropic, plasticity-based model (Rankine-Hill-Anisotropy plasticity model RHAPM), and two total-strain-based models: the isotropic Total-Strain-Rotating-Crack model (TSRCM), and the orthotropic Engineering Masonry Model (EMM), whereas the micro-models comprised a plasticity-based interface model developed for masonry (Combined Cracking Crushing Shearing PCCCS) and a total-strain based interface model that adopted a sub-step incremental algorithm with elements of plasticity and damage

mechanics (SI-CCS). The six constitutive models were used to model six masonry walls, four of which were tested cyclically and two were tested monotonically. The numerical results were compared to one another and to the experimental results. From the comparisons, it was clear that there is no single model that outperforms the others consistently throughout all the analyses, but the one that provided poorer predictions was the TSRCM; an isotropic model originally developed for concrete structures but often used for modelling masonry structures as well. As expected, the two micro-models were in general better able to capture both the crack localization observed in the experiments and the hysteretic behavior. Within the macro-models, the developed model was the one able to best combine the prediction of sharp damage localization, and accurate hysteretic behaviour and energy dissipation.

In the third part of the research the sensitivity of the six constitutive models to four material parameters was investigated to identify (a) which material properties, once varied, influence the behavior of masonry walls the most, and (b) to which material variation is each of the examined constitutive models more sensitive. The four material properties examined were the tensile strength, the compressive strength, the cohesion and the friction coefficient. To make a consistent comparison between the six different constitutive models, the six masonry walls introduced above were used, and each of the material properties was varied individually and independently of the rest. In total 224 sensitivity analyses were performed and compared. Regarding aspect (a), it was found that the friction coefficient leads to higher variances of the peak base shear, residual shear and energy dissipation for the examined walls. This was followed by the compressive strength, that influenced more walls that had exhibited crushing or cracks through the bricks during the tests. Variations in the tensile strength led to small variations in the base shear capacity and hysteretic behavior of the walls, while variations in the cohesion are negligible in the case of slender walls, but not for squat walls. As for aspect (b), the variation of the friction coefficient influenced the most the behavior of the constitutive models that include it as input material parameter, and even led to a shift in the failure mechanism from shear failure to flexural failure. From the examined models, the TSRCM was the most sensitive to variations of the tensile strength, while the developed model led to slightly larger variations in the peak base shear, residual base shear and dissipated energy than the other three macro-models for the remaining three material parameters.

As for all studies, this one too had limitations, regarding both the development and performance of the constitutive model, and its comparison with other constitutive models. The main drawback of the developed constitutive model relates to the numerical difficulties caused by the inclusion of the internal iterative shear loop. Numerical convergence is not always satisfied and as a consequence the computational time may be increased, when compared to other models. Finally, the comparison between the different constitutive models could be made more complete if more finite element software were used and if constitutive models based on damage, or damage-plasticity were included.

Samenvatting

Er is een zeer populaire fabel, die dateert uit het begin van de 19e eeuw, over drie kleine biggetjes die hun huizen bouwen van verschillende materialen en een wolf die hen probeert te vangen door hun huizen omver te blazen. Van de drie huizen die gebouwd zijn van rietjes, stokken of bakstenen, is alleen het huis van bakstenen bestand tegen de klap van de wolf. Hoewel de moraal van het verhaal niets te maken heeft met constructiemechanica, is het gebruik van bakstenen (metselwerk) om kracht en duurzaamheid te symboliseren opmerkelijk. Maar ondanks het brede en indrukwekkende gebruik door de eeuwen heen, maken de verschillende materiaaleigenschappen van de bestanddelen en hun geometrische rangschikking metselwerk tot een materiaal met een zeer niet-lineaire en anisotrope mechanische respons. Hoewel metselwerkconstructies zijn ontworpen om gravitatiebelastingen te weerstaan, zijn ze minder goed bestand tegen horizontale belastingen, zoals cyclische dwarsbelastingen door aardbevingen, ongelijke zettingen of zelfs overstromingen. In dergelijke gevallen kunnen de constructies schade of bezwijken vertonen in de vorm van trekscheuren, afschuiving van de beddingverbindingen en verbrijzeling, splijten of afbrokkelen onder druk. Het is daarom van cruciaal belang om de respons en de veiligheid van bestaande constructies te beoordelen, vooral wanneer de condities en omstandigheden van belasting veranderen, bijvoorbeeld door klimaatverandering of door aardbevingen die door mensen worden veroorzaakt in gebieden die voorheen niet gevoelig waren voor aardbevingen, zoals het geval is in het gebied van Groningen in Nederland.

Om de respons van de constructies te beoordelen, moeten dit complexe mechanische gedrag van metselwerk en alle verschillende bezwijkmechanismen ook in de numerieke modellen worden vastgelegd. Dankzij de vooruitgang op het gebied van computermechanica zijn er vier verschillende numerieke benaderingen ontwikkeld voor het modelleren van metselwerkconstructies: op macro-elementen gebaseerde methoden, discrete elementmethoden, eindige-elementenmethoden en hybride methoden. Van deze methoden is de eindige-elementenmethode tot op heden de meest gebruikte numerieke methode, waarbij metselwerk kan worden gemodelleerd op basis van een micro-modellering of een macromodellering. Het is aangetoond dat micro-modelleringsbenaderingen nauwkeuriger zijn maar rekenkundig zeer veeleisend, terwijl macromodellen worden beschouwd als een goed compromis tussen numerieke nauwkeurigheid en rekenkundige inspanning. Ze zijn daarom de meest gebruikte rekenstrategie voor het modelleren van grote constructies. Bestaande macromodellen zijn gebaseerd op een van de volgende raamwerken: uitgesmeerde scheurvorming, schademechanica, plasticiteit of schade-plasticiteit. Elk raamwerk heeft zijn eigen voor- en nadelen, maar een gemeenschappelijke tekortkoming van veel macromodellen is hun onvermogen om zowel de gelokaliseerde scheurpatronen vast te leggen als het hysterische gedrag van constructies nauwkeurig te voorspellen.

Het doel van dit proefschrift is om de bovengenoemde beperking aan te pakken door ten eerste een nieuw macromodel te ontwikkelen en ten tweede de prestaties van bestaande constitutieve modellen (naast het nieuwe macromodel) systematisch te beoordelen

en te vergelijken met experimentele resultaten en met elkaar. Het eerste deel van het onderzoek was gewijd aan het ontwikkelen van een cyclisch, niet-lineair en orthotroop continuum constitutief model dat aan de volgende criteria moest voldoen: het voorspellen van het juiste bezwijkmechanisme, het nauwkeurig voorspellen van de krachtcapaciteit, de vervormbaarheid/verzachting en de gedissipeerde energie van metselwerkconstructies, evenals het vastleggen van brosse gelokaliseerde scheuren. Om dit te doen is gekozen voor een totale-rek-roterende-scheur benadering; een benadering die met succes is ontwikkeld en gebruikt voor brosse materialen zoals beton, maar die niet zo bevredigend is voor metselwerkconstructies, voornamelijk vanwege de toegepaste secante ontlading/herlading en het gebrek aan initiële orthotropie. Daarom waren het opnemen van orthotropie en de beschrijving van cycliciteit van het grootste belang. Orthotroop gedrag wordt zowel in de elastische fase als in de fase na de piekbelasting opgenomen. Nieuw in dit model is de variatie van de elastische en inelastische eigenschappen ten opzichte van de hoofdspannings- en rekrichting. Tijdens de elastische fase worden de materiaaleigenschappen in de twee orthogonale richtingen niet-lineair gevarieerd in het geval van treksterkte en lineair voor de overige materiaalparameters. Na het scheuren worden de materiaalparameters gefixeerd op de parameters die overeenkomen met de richting van de hoofdspanningen/rek bij het begin van het scheuren. Hoewel de materiaaleigenschappen nu vastliggen, wordt nog steeds een coaxiaal roterend spanning-rek concept gevolgd. Voor de beschrijving van het inelastische gedrag wordt een hoek gedefinieerd en gebruikt als een extra materiaalinvoerparameter. Deze hoek werkt als een drempel en helpt om onderscheid te maken tussen buigscheuren en diagonale schuifscheuren. Als gevolg hiervan, als bij het begin van het scheuren de richting van de spanningen binnen de sub-horizontale of sub-verticale hoeken valt die overeenkomen met buigscheuren, wordt de bilineaire spanning-rek relatie die wordt aangenomen in trek geassocieerd met bros gedrag, met steile verwekingssnelheid en secante ontlading/relading; anders heeft het trekgedrag een langzame verwekingssnelheid en elastisch-plastische ontlading/relading. Het gedrag in compressie wordt beschreven door twee niet-lineaire curven en er wordt een bilineaire ontlasting/relading aangenomen, met als doel te lijken op de elastisch-plastische ontlasting/relading die wordt waargenomen tijdens afschuiving. Tot slot werd een interne iteratieve lus geïmplementeerd om de op Coulomb-frictie gebaseerde schuifspanningscapaciteit langs de bedding-verbinding te regelen, om de overschatting van de basisschuifkracht die vaak wordt waargenomen in breukmechanicamodellen te vermijden.

Het constitutieve model, ontwikkeld voor vlakke-spanningselementen, werd geïmplementeerd in de eindige-elementen software DIANA FEA en werd gevalideerd aan de hand van experimentele resultaten van vier metselwerkmuren die cyclisch werden getest in hun inplantingsrichting. De numerieke en experimentele resultaten werden vergeleken op het gebied van piekbasisafschuifcapaciteit, residuele basisafschuifcapaciteit, energiedissipatie, lokalisatie van schade en bezwijkmechanisme. Over het algemeen werd er een goede overeenkomst gevonden tussen de numerieke en experimentele resultaten, vooral met betrekking tot de basisafschuifcapaciteit. De lokalisatie van de schade was ook zeer representatief voor de experimentele scheurpatronen. Er werd ook een netgevoeligheidsstudie uitgevoerd door de elementgrootte en de volgorde van de elementen te variëren. Er werd een variatie van 9% waargenomen in het geval van maximale afschuifcapaciteit van de basis en een variatie van 29% in het geval van residuele afschuiving van de basis. In het

algemeen vertoonden lineaire elementen met een grotere maaswijdte de minste verweking, terwijl kwadratische elementen meer verweking vertoonden.

Het volgende doel van het onderzoek was het systematisch vergelijken van de nauwkeurigheid van constitutieve modellen die worden gebruikt om metselwerk te modelleren, inclusief het nieuw ontwikkelde model. Hiervoor werden drie aanvullende macromodellen en twee micromodellen geselecteerd. De drie gekozen macromodellen bestonden uit een orthotroop, op plasticiteit gebaseerd model (Rankine-Hill-Anisotropy plasticity model RHAPM) en twee op totale rek gebaseerde modellen: Het isotrope Total-Strain-Rotating-Crack-model (TSRCM) en het orthotrope Engineering Masonry Model (EMM), terwijl de micromodellen bestonden uit een op plasticiteit gebaseerd interfacemodel ontwikkeld voor metselwerk (Combined Cracking Crushing Shearing PCCCS) en een op totale vervorming gebaseerd interfacemodel dat een stapsgewijs algoritme met elementen van plasticiteit en schademechanica (SI-CCS) toepaste. De zes constitutieve modellen werden gebruikt om zes metselwerkmuren te modelleren, waarvan er vier cyclisch en twee monotoon werden getest. De numerieke resultaten werden met elkaar en met de experimentele resultaten vergeleken. Uit de vergelijkingen bleek duidelijk dat er niet één model is dat consistent beter presteert dan de andere modellen in alle analyses, maar het model dat slechtere voorspellingen gaf was TSRCM; een isotroop model dat oorspronkelijk is ontwikkeld voor betonconstructies, maar dat vaak ook wordt gebruikt voor het modelleren van metselwerkconstructies. Binnen de macromodellen was het ontwikkelde model het beste in staat om de voorspelling van scherpe lokalisatie van schade te combineren met nauwkeurig hysteretisch gedrag en energiedissipatie.

In het derde deel van het onderzoek werd de gevoeligheid van de zes constitutieve modellen voor vier materiaalparameters onderzocht om vast te stellen (a) welke materiaaleigenschappen na variatie het gedrag van metselwerkwanden het meest beïnvloeden en (b) voor welke materiaalvariatie elk van de onderzochte constitutieve modellen gevoeliger is. De vier onderzochte materiaaleigenschappen waren de treksterkte, de druksterkte, de cohesie en de wrijvingscoëfficiënt. Om een consistente vergelijking te maken tussen de zes verschillende constitutieve modellen, werden de zes hierboven geïntroduceerde metselwerkmuren gebruikt en werd elk van de materiaaleigenschappen afzonderlijk en onafhankelijk van de rest gevarieerd. In totaal werden 224 gevoeligheidsanalyses uitgevoerd en vergeleken. Met betrekking tot aspect (a) bleek dat de wrijvingscoëfficiënt leidt tot hogere varianties van de piekbasisafschuiving, restafschuiving en energiedissipatie voor de onderzochte muren. Dit werd gevolgd door de druksterkte, die van invloed was op meer muren die tijdens de testen verbrijzeling of scheuren door de bakstenen vertoonden. Variaties in de treksterkte leidden tot kleine variaties in de basisafschuifcapaciteit en het hysteretisch gedrag van de muren, terwijl variaties in de cohesie verwaarloosbaar zijn in het geval van slanke muren, maar niet voor hurkmuren. Wat betreft aspect (b) beïnvloedde de variatie van de wrijvingscoëfficiënt het gedrag van de constitutieve modellen die deze als materiaalparameter hebben en leidde zelfs tot een verschuiving in het bezwijkmechanisme van bezwijken door afschuiving naar bezwijken door buiging. Van de onderzochte modellen was het TSRCM het meest gevoelig voor variaties in de treksterkte, terwijl het ontwikkelde model leidde tot iets grotere variaties in de piekbasisafschuiving, residuele basisafschuiving en gedissipeerde energie dan de andere drie macromodellen voor de overige drie materiaalparameters.

Zoals alle studies had ook deze studie beperkingen, zowel wat betreft de ontwikkeling en prestaties van het constitutieve model, als de vergelijking met andere constitutieve modellen. Het belangrijkste nadeel van het ontwikkelde constitutieve model heeft te maken met de numerieke problemen die worden veroorzaakt door het opnemen van de interne iteratieve schuiflus. Er wordt niet altijd voldaan aan de numerieke convergentie en als gevolg daarvan kan de rekentijd toenemen in vergelijking met andere modellen. Tenslotte zou de vergelijking tussen de verschillende constitutieve modellen vollediger kunnen zijn als er meer eindige-elementen software zou worden gebruikt en als constitutieve modellen gebaseerd op schade of schade-plasticiteit zouden worden meegenomen.

1

Introduction

1

1.1 Background

Masonry is one of the oldest building materials in the world. Due to its aesthetics, availability and ease of construction it is still found in many structures around the world, from historic monuments to residential buildings. Masonry comprises units, such as bricks, stones and blocks, and joints, dry or mortar, arranged in a geometrical pattern. The different material properties of its constituents (units and joints), as well as their geometric arrangement make masonry an inhomogeneous and orthotropic material. This means that it has different material properties and behavior along different directions; a characteristic that influences its global behavior and failure. Just like in concrete and other quasi-brittle materials, failure in masonry can occur due to tension, compression or shear. Depending on the loading directions, the loading conditions and the difference between the brick and mortar properties, this damage can occur along the joints, through the brick units or even both through the mortar and the bricks (Figure 1.1). Commonly, the (mortar) joints act as weak planes, due to their low tensile and shear strength.

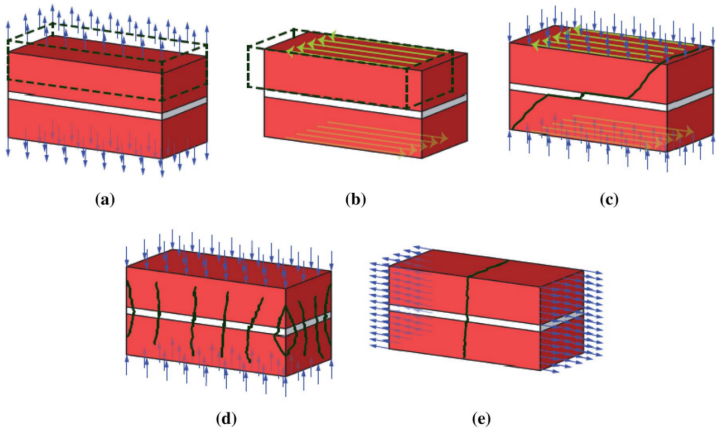

Figure 1.1: Local failure mechanisms of brick masonry: (a) tensile failure of brick-mortar bond, (b) shear sliding, (c) diagonal cracking, (d) crushing and (e) tensile cracking through the bricks and mortar. Image taken from [1].

Even though masonry structures have existed for millenniums, until recently their design was based on empirical calculations and traditional techniques. This has hindered the development of masonry as a structural material and its application on more innovative designs. During the last 50 years efforts to better understand the behavior of the material and to develop more complete design codes have significantly increased. However, equally important as designing new masonry structures is the assesment of existing ones. The majority of existing masonry structures was built to withstand gravitational loads, such as their self-weight and static loads, but was less equipped to resist horizontal loads, such as cyclic lateral loads from earthquakes, loads from uneven settlements and flooding. Given that masonry is a composite material, with complex mechanical behavior and brittle failure, such loads could cause damage to the structure and even collapse (Figure 1.2). The behavior of the structures is even more complicated when structural elements are pre-damaged due to previous loads (e.g., earthquakes in the past, settlements).

Figure 1.2: Damage in masonry structures due to earthquakes, taken from [2, 3].

Therefore, it is important to have the right tools to evaluate the response of masonry structures to external loads. Thanks to the advances in the field of numerical methods, four different approaches have been developed for the numerical modelling of masonry structures: macro-element based methods, like the lumped mass approach and the Equivalent Frame Method [4–6], Discrete Element Methods (DEM) [7–10], Finite Element Methods (FEM), and most recently hybrid methods, like the Finite-Discrete Element Methods (F-DEM) [11, 12] or the Macro-Distinct Element Methods (M-DEM) [13]. In FEM, which currently is the most commonly used approach, masonry is modelled according to two methods: the micro-modelling, detailed or simplified, and the macro-modelling approach. According to micro-modelling the brick units and the joints are modelled separately, whereas the mortar joints and their interfaces to the bricks are either represented via simplified interface elements (simplified micro-modelling) or modelled in detail (detailed micro-modelling) [14–17]. On the other hand, in the macro-modelling or continuum approach, masonry is considered to be a homogeneous material and the damage is distributed over the continuum. Macro-models can be based either on direct approaches, where the constitutive equations and material properties adopted should represent the behavior of masonry and should be obtained by tests performed on sufficiently large specimens, or on homogenization approaches (e.g. [18–20]), where the constitutive laws are derived through a homogenization process that relates the materials microscale material to the structural scale. The micro-modelling approach is more accurate and is better able to predict the hysteretic behavior and local failure mechanisms of a structure. However, it is computationally very demanding and its use, up to now, is mostly limited to simulating single structural elements, like walls. On the other hand, macro-models constitute a good compromise between accuracy and computational effort, and are often preferred for modelling large structures, in order to reduce the required computational time.

In order to increase the accuracy of direct macro-models, the orthotropy of the material needs to be included. Currently, a number of constitutive models is available for masonry, based on the frameworks of smeared cracking [21, 22], damage mechanics [23–26], and plasticity [27, 28]. However, even though these models include orthotropy in the description of the mechanical behavior, more challenges need to be overcome. Firstly, predicted crack patterns are often too diffuse: wide zones of smeared cracked Gauss points have been reported (e.g., [21, 23]), deviating from the localized discrete cracks identified in the final stages of tests. This is in part expected, since macro-models do not depict the exact

geometry of a structure; however, a realistic damage localization is an important factor to consider when the structure needs to be strengthened. Secondly, most of the existing models have been validated only against experimental results of monotonic tests, whereas the few that have been validated against cyclic tests [21, 23, 28] tend to underestimate the energy dissipation, especially in the case of shear walls. The cyclic hysteretic response may be partially missed because of the unloading/reloading characteristics of the existing models: either fully secant for damage/smeared cracking models or fully elastic for plasticity models. Damage-plasticity models tackle this issue, but even though such models have been developed for concrete (e.g., [29, 30]), and some attempts have been made for interface elements [14, 17, 31], only few are specifically developed for macro-modelling of masonry (e.g., [28]). Thirdly, existing models may not always estimate the post-peak part of the load-displacement response correctly, and in general models require the calibration of many material input parameters to obtain accurate predictions. In summary, constitutive models for masonry have progressed significantly over the years, but their accuracy still needs to be improved, particularly for macro-models.

1.2 Research objective and method

1.2.1 Research goal

The goal of this research is to develop a new orthotropic, constitutive macro-model that will focus on the *nonlinear cyclic* behavior of masonry and that will lead to a more accurate appraisal of masonry structures. The accuracy of the model and its improvement with respect to the existing ones will be evaluated in terms of hysteretic behavior (force-displacement capacity and energy dissipation) and damage localization. Subsequently, the objectives of this thesis are:

- To develop an in-plane, orthotropic continuous constitutive model based on fracture mechanics, focusing on the cyclic behavior of masonry walls
- To validate the accuracy and performance of the model against experimental results, in terms of failure mechanism, damage localization and load-displacement envelope curve, including maximum and residual base shear capacity, post-peak ductility and energy dissipation.
- To compare the accuracy and performance of the model with existing models, in terms of hysteretic behavior, damage localization and numerical performance.
- To evaluate the sensitivity of the developed model and other existing models with respect to variations of the input material parameters.

1.2.2 Research method

In order to develop a constitutive model that will address the deficiencies of the existing models, both macro-models and micro-models, these weaknesses should first be identified and approached from the right perspective, asking questions like “what assumptions were made in this model and why”, “what has not been considered”, “what needs improvement” and “how does each material property influence the final numerical results”. To this end, an extensive literature study has been carried out into the different modelling approaches and

the characteristics that the constitutive model needs to include: the orthotropy; failure criteria and stress-strain behavior under compression, tension and shear; cyclicity (unloading and reloading dependent on the type of failure).

In order to include the orthotropy in the constitutive model, first the material properties of masonry along different loading directions must be defined. For the definition of the properties, experimental data are used, where available. In the case that experimental data are limited to properties only along the two main directions (parallel to the bed and head joints), it is assumed that the material properties, namely stiffness, strength and fracture energy, vary in linear interpolation between those two.

Once the material properties are defined, the next step is to develop the constitutive equations that describe the different types of failure. The main types of failure in masonry that should be included have already been defined as: failure in tension (cracking), failure in shear (sliding friction), and failure in compression (crushing). Naturally, in macro-modelling, no distinction is made between brick or mortar joint failure, instead the behavior of the homogenized material is described. While tensile and compressive failure are always included in damage, plasticity and fracture mechanics models, the inclusion of shear failure is more challenging. It is observed that masonry structures that fail due to shear or a combination of shear and crushing or tensile cracking have a higher capacity and dissipate more energy. Ignoring the shear contribution can lead to wrong force capacity estimation and underestimation of the energy dissipation.

The next step in the methodology was the selection of a constitutive format. From the available frameworks of plasticity, damage mechanics and fracture mechanics, the last was selected. Moreover, out of the fixed or rotating concept of the standard total-strain based approach, a motivated selection was made for a total-strain based rotating crack approach. THe developed constitutive model is orthotropic and describes tensile and compressive failure in the rotating principal directions, while including indirectly shear failure, based on a Coulomb friction criterion, through an internal iterative algorithm. Two distinctions are made regarding the tensile post-peak and unloading/reloading behavior based on the crack orientation at crack initiation: a steep softening branch and secant unloading are adopted when the crack angle corresponds to in-plane flexural failure, and a gradual softening branch and bilinear unloading are adopted when the crack angle corresponds to diagonal shear failure. In compression, bilinear unloading/reloading is adopted, aiming at resembling the cyclic behavior in shear.

Having defined the constitutive model, the next step is to implement them in a FEM software. In order to validate the accuracy of the model, the numerical results are compared against experimental results that were derived from in-plane, cyclic tests on brick masonry walls. The comparison is made in terms of force-capacity, dissipated energy, stiffness degradation and crack/damage localization. In case that the numerical results did not satisfactorily describe the experimental behavior of the walls, appropriate and mechanically sound modifications were made in the constitutive equations, until the final version of the constitutive model satisfied the accuracy criteria.

Key part of the research method is also to compare the new constitutive model with other existing constitutive models implemented in commercial software packages. This comparison includes three smeared-crack macro-models, one based on plasticity and two based on a different total-strain crack approach; and two interface micro-models, one based

on plasticity and one based on a total-displacement approach, with elements of damage and plasticity. The constitutive models are compared with each other, as well as with the experimental results, in terms of hysteretic behavior (peak shear capacity, residual shear capacity, energy dissipated over time history), damage localization and computational effort (computational time, number of total iterations, converged steps). Finally, a material sensitivity study is performed on the developed constitutive model, as well as on the five existing constitutive models. The material properties considered are the compressive strength, tensile strength, cohesion and friction coefficient.

1.3 Thesis outline

Chapter 2 presents an extensive literature review regarding masonry's mechanical behavior and properties, as well as the numerical approaches used to model masonry structures. Additionally, it presents an overview of the most popular existing constitutive models, both micro-models and macro-models, and a discussion of their accuracy and performance and their limitations.

Chapter 3 introduces the constitutive model: the Orthotropic Total-Strain Rotating Model (OTSRM) developed as part of this research, with emphasis on the nonlinear, cyclic behavior of brick masonry. The material properties, constitutive laws and the failure criteria are described in detail.

In **Chapter 4**, the constitutive model (OTSRM) is used to numerically simulate six masonry walls tested under cyclic, in-plane motion, and its accuracy is validated against experimental results in terms of force-displacement capacity, dissipated energy and damage localization. Moreover, sensitivities to mesh order and size, as well as sensitivity to the threshold angle assumption for diagonal cracks are presented and discussed.

Chapter 5 concerns the comparison between the developed constitutive model (OTSRM) and other existing constitutive models: three macro-models and two micro-models. The in-plane cyclically tested walls of Chapter 4 and two additional monotonically tested walls are simulated with the six different material models and compared with each other and with the experimental results in terms of load-displacement behavior (ultimate capacity, strength degradation, energy dissipation), crack pattern/damage localization, and finally computational performance and numerical stability.

Chapter 6 presents the results of a systematic sensitivity study regarding the variations of the four material properties: tensile strength, compressive strength, cohesion and friction coefficient. It is discussed which material properties have the biggest impact on the hysteretic behavior of the in-plane walls, and which constitutive models are most sensitive to minor variations in material properties.

Finally, **Chapter 7** contains the discussion and conclusions concerning the application of the developed constitutive model and its comparison to other models, its advantages and limitations as well as some recommendations for further research.

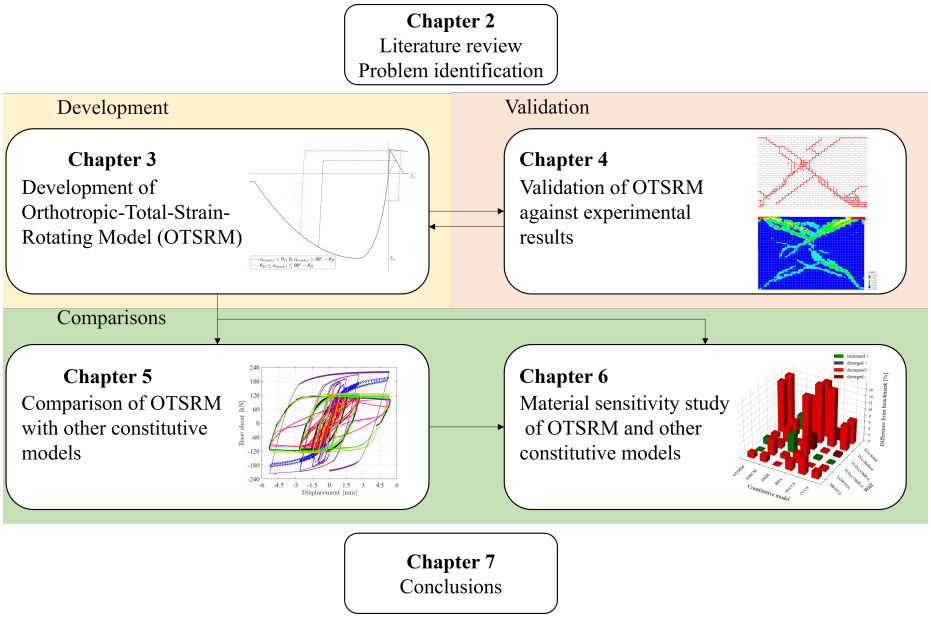

Figure 1.3: Outline of the dissertation.

2

Masonry Behavior and Modelling Techniques

Masonry is an orthotropic, nonlinear material with complex mechanical behavior and brittle failure. Even though it has been used for millenniums, significant efforts to characterize the material's behavior and to develop appropriate design codes have mostly been made in the last 50 years. The advancements in the field of computational mechanics have led to the development of numerical approaches for the modelling of masonry structures, as well as the definition of constitutive models for the description of the mechanical behavior. This chapter is devoted in bringing the reader up-to-date with the current experimental and numerical advances in the field of masonry structures. Section 2.1 presents the mechanical behavior of unreinforced masonry in tension, compression and shear based on experimental research. Subsequently, the different numerical approaches are presented in Section 2.2, accompanied by representative constitutive models for each approach. The chapter ends with a comparison of the different modelling techniques and their respective advantages and disadvantages.

2.1 Mechanical behavior of masonry

Masonry structures constitute a big percentage of the building stock around the world; the types of these structures vary: some are historic buildings, such as cathedrals or temples, others are residential buildings, where masonry components can act either as the main load-bearing elements or as non-load bearing elements (infills or claddings), and others may be different structures, such as bridges, dams or quay-walls. Masonry is a complex material, and its behavior and properties depend heavily on the properties of its constituents, the bond between them and the construction technique used. Typically, masonry blocks are brittle or quasi-brittle materials (like building stones, clay or calcium silicate bricks), connected with each other through joints (dry or mortar). The geometrical arrangement of blocks may form an organized pattern, often referred to as "bond", or it may be random. The different properties of its components and their relative arrangement constitute masonry an anisotropic and nonlinear material, with anisotropies observed both in the elastic and inelastic properties (strength, post-peak behavior). Interestingly, regular brick masonry exhibits stronger anisotropic behavior than random stone masonry [1].

Being a brittle material, damage in masonry often takes the form of cracks. The crack location depends on the strength of its constituents (bricks or blocks, mortar, or brick-mortar bond), but usually the weakest link is the bond between bricks and mortar, and the cracks often concentrate there. Local failure mechanisms are typically identified as (i) tensile failure of brick-mortar bond, (ii) tensile cracking through brick and mortar (iii) shear sliding between the brick-mortar bond, (iv) diagonal cracking, and (v) crushing, splitting and spalling under compression (Figure 2.1). In the structural level, the failure mechanisms are defined as rocking (flexural failure), diagonal cracking, shear sliding, (toe) crushing and crumbling (Figure 2.2).

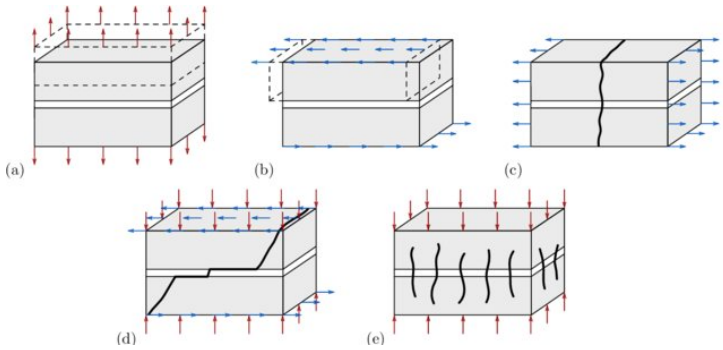

Figure 2.1: Examples of local failure mechanisms: (a) joint tensile failure, (b) joint shear failure, (c) brick and mortar tensile failure, (d) diagonal masonry failure, and (e) masonry crushing. Image taken from [32], originally adapted from [33].

In principle, to define masonry's mechanical behavior one can characterize its properties at material (constituent) level, or at structural element (component) level. The level of material characterization can influence also the selection of the modelling approach. The more material properties available, the more detailed the numerical model can be. The properties required for the definition of the mechanical behavior are the elastic properties (stiffness) and inelastic properties (strengths, fracture energies) that relate to the compressive, tensile and shear behavior.

The values of Young's modulus and Poisson's ratio are usually defined for masonry via standardized tests on either stacked masonry prisms (ASTM C1314 [39]) or on wallets (EN 1052-1:1998 [[40]]). The shear modulus is subsequently estimated to be equal to 0.4 times the value of the Young's modulus, as recommended by EN 1996-1 and confirmed by experimental findings, as reported by Salmanpour et al. [41] and Messali et al. [42]. However, in finite element modelling of large-scale structures, the values of the Young's modulus, and consequently of the shear modulus, have to be reduced for the models to better replicate the elastic behavior of experimentally tested structures, as suggested in [43].

Regarding the behavior in *compression*, the compressive strength and Young's modulus of masonry can be characterized relatively easily and a wide range of experimental data are available for different types of masonry (e.g., [44, 45]). However, the characterization of the post-peak softening behavior is more intricate [46]. Moreover, only few studies are available regarding the cyclic behavior of masonry in compression. Naraine & Sinha [47, 48]

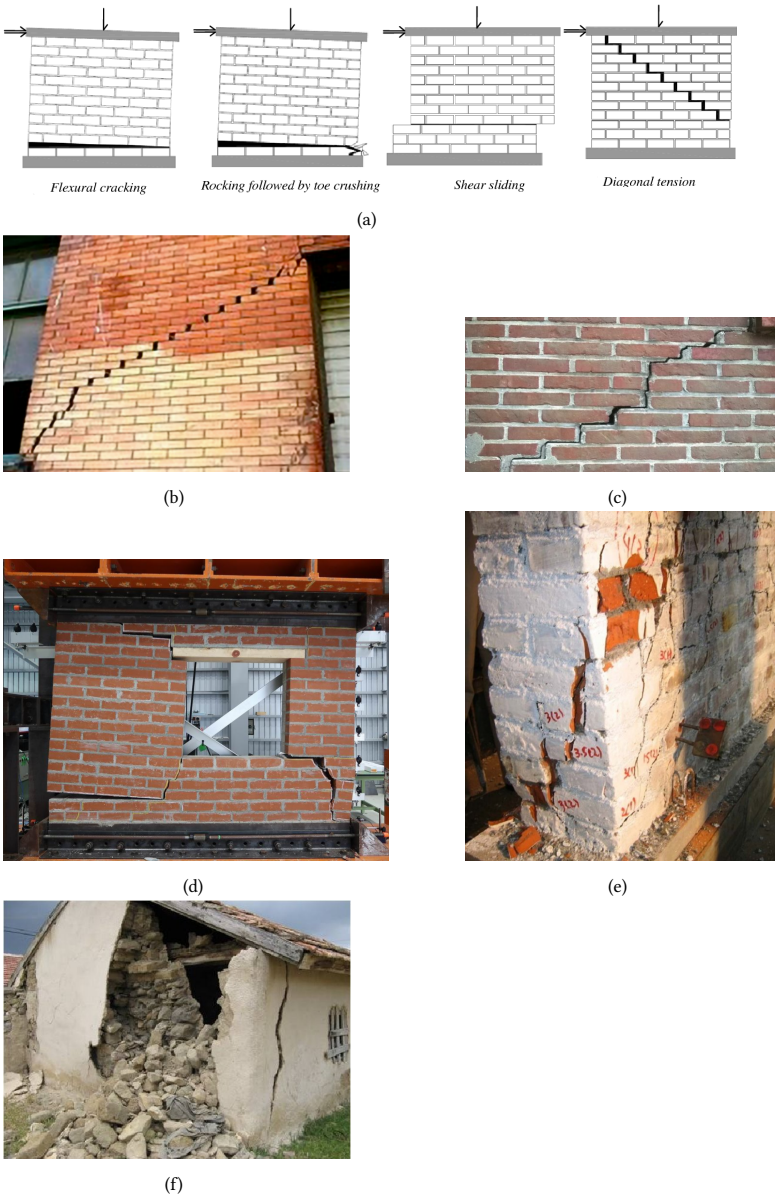

Figure 2.2: Examples of failure mechanisms in masonry structures: (a) classification [34], (b) diagonal shear sliding [35], (c) diagonal crack, (d) rocking failure with flexural cracks and toe crushing [36], (e) vertical splitting and crushing of masonry bricks [37], (f) crumbling and out-of-plane failure [38].

were the first to investigate the compressive behavior of clay and sand-blast brick masonry under semi-cyclic uniaxial or biaxial compressive loading. They defined relationships to describe the compressive stress-strain envelope curve, the common point (the uppermost

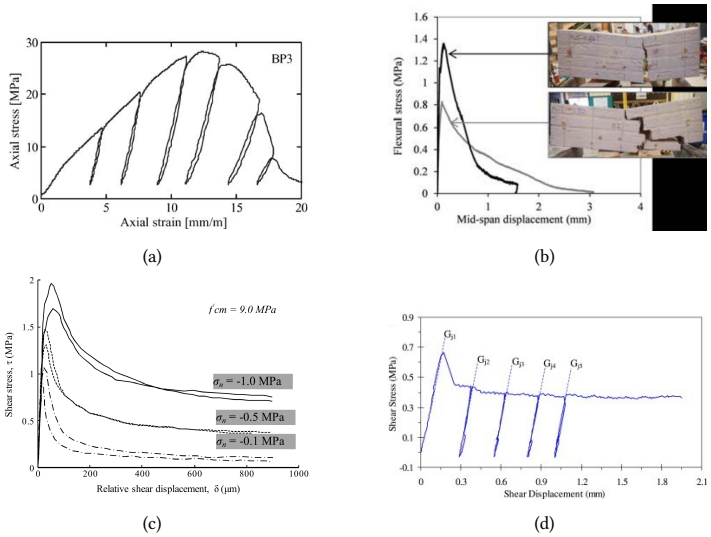

Figure 2.3: Mechanical behavior of masonry: (a) cyclic behavior of masonry under uniaxial compression [50], (b) flexural behavior from in-plane bending test [59], (c) shear-slip relationship for clay bricks under different pre-compression levels [60], (d) cyclic shear-ship relationship for clay bricks [61].

point of intersection between the unloading and reloading branch) and the stability point (the lower bound point of intersection between the unloading and reloading branches).

In recent years, more research followed regarding the cyclic behavior of masonry under compression for different types of masonry [49–53]. The main common observations between the different experiments are that the compressive strength of masonry is highly influenced by the properties of its constituents (brick and mortar) and that the stiffness of the reloading branches reduces significantly due to the developed material damage (Figure 2.3a). Based on the experimental data, analytical formulations describing the compressive envelope, plastic strains and unloading/reloading stiffness have been proposed by a number of researchers (e.g., [54–56]); a comparison between different formulations and experimental results can be found in [57]. Additional to this, the brick-mortar interaction under compression was investigated by Vermeltfoort [58], considering both the cases of concentric and eccentrically compressed specimens.

The *tensile* behavior of masonry is characterized by brittle failure. The crack pattern depends not only on the relative strength of brick units and mortar joints, but also on the orientation of the brick masonry with respect to the loading direction [62] (Figure 2.4). Measuring the uniaxial tensile strength and mode I fracture energy of masonry through direct tensile tests is challenging due to the complicated test set-up and the preparation of the samples. Moreover, the unknown effects of the boundary conditions of a direct tensile test on the post-peak response of masonry have made this testing procedure unattractive [63]. This led to other, indirect testing procedures prevailing for the characterization of the tensile behavior of masonry, such as bending tests and bond-wrench tests. The tensile strength is then assumed to be the stress corresponding to the onset of cracking when performing bending tests [64]. In literature, the ratio of tensile strength to flexural strength

can vary notably depending on the types of masonry examined and representative values can be found in relevant studies (e.g., [46, 63]).

Finally, the *shear sliding* behavior along the brick-mortar interface has been investigated extensively. Researchers have concluded that the shear strength of masonry is dependent on the level of applied pre-compression stress, irrespectively of the type of masonry (Figure 2.3c). Nevertheless, the type of masonry and the characteristics of its constituents, such as the brick type, surface roughness, mortar texture, and relative strengths of mortar and brick, influence the amplitude of the shear strength [60, 65, 66]. Apart from the initial cohesion and friction coefficient, the mode II fracture energy, relating to the cohesion strength degradation, as well as the residual friction coefficient have also been examined.

Complementary to the stress-strain (or stress-displacement) relationships for tension, compression and shear, a few failure surfaces have also been derived from biaxial tests, as seen for example in Figure 2.5

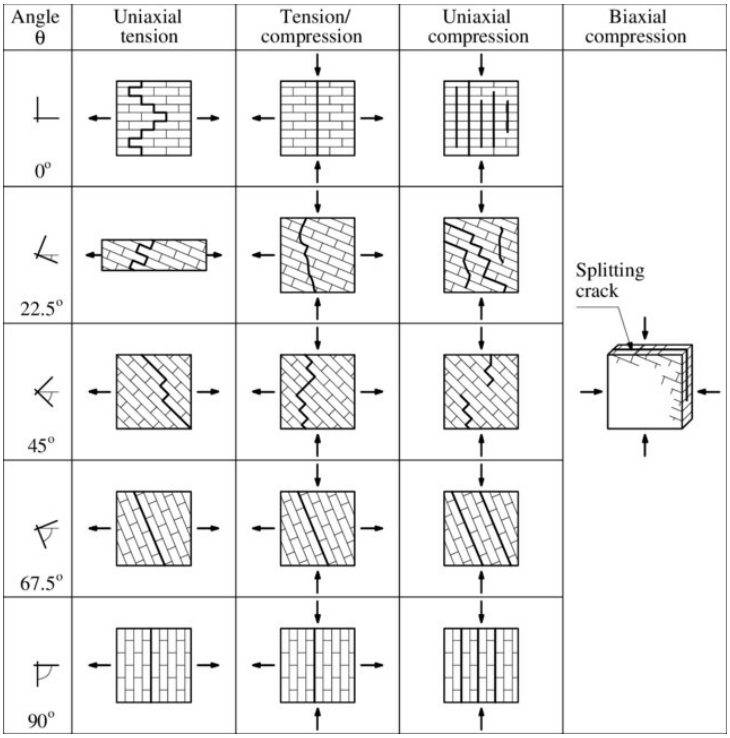

Figure 2.4: Modes of failure of masonry wallets subjected to biaxial tests, taken from [62].

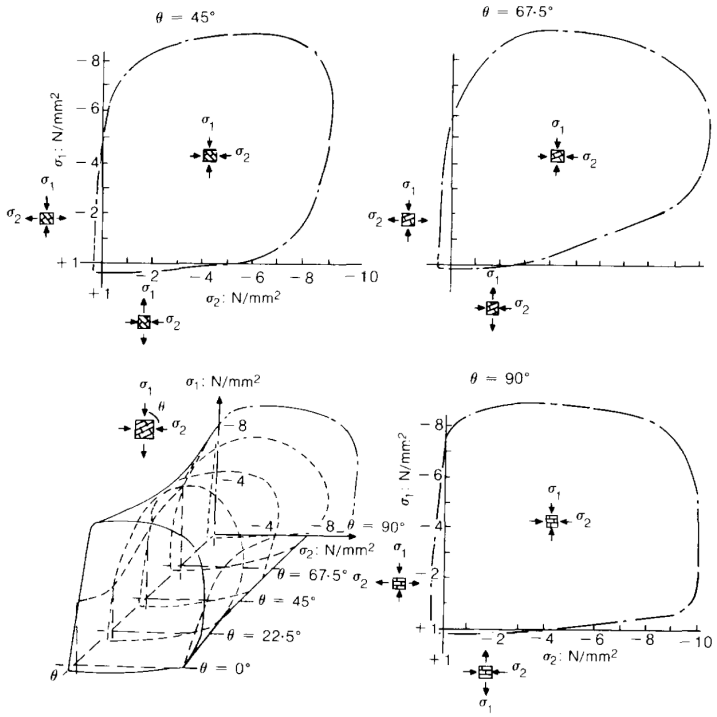

Figure 2.5: Failure surfaces, taken from [62].

2.2 Computational techniques

Modelling the behavior of masonry structures is a challenging task, given the many material variabilities and the complex mechanical behavior described above. Despite masonry being such a widely used material, over the course of history its use and design were based on rules-of-thumb, empirical formulae and knowledge passed down from master to apprentice. In the end of the 19th century, interest in the structural behavior of masonry structures (mainly arches, domes and vaults) led to the development of the theory of line of thrust, resulting in the more practical approach of graphical statics [67, 68] (Figure 2.6). In 1966, Heyman introduced the theory of limit analysis for masonry structures and defined the three principles under which it can be used: (1) the compressive strength of masonry is infinite, (2) the tensile strength of masonry is zero, and (3) sliding failure does not occur [69].

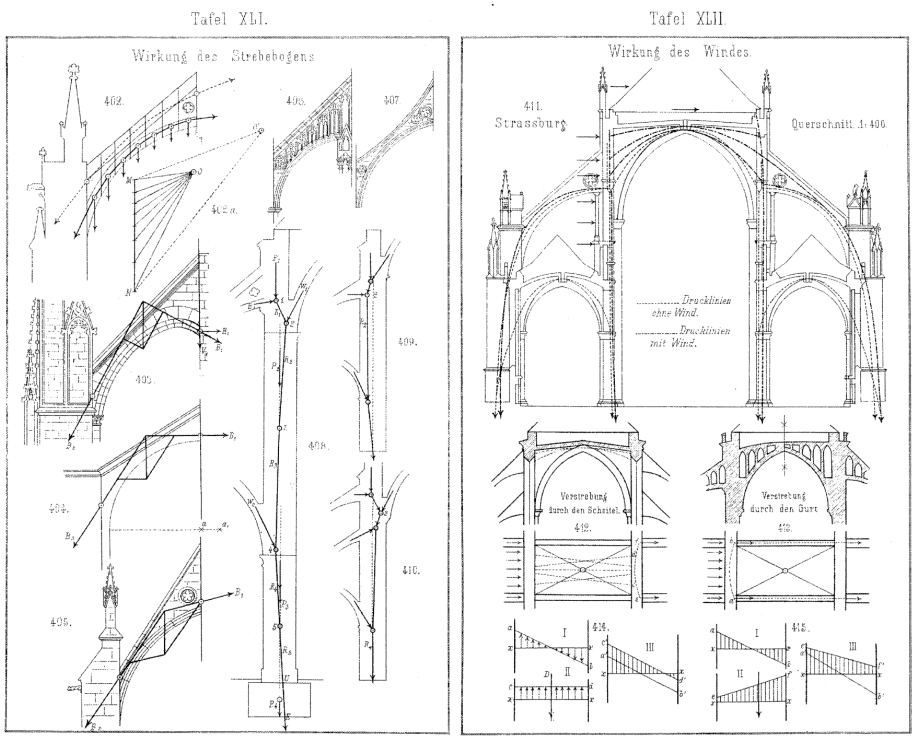

Figure 2.6: Examples of graphical analysis, taken from [70]

With the evolution of technology and computers, more elaborate methods and computational techniques were developed, An alternative to solutions based on limit analysis are solutions based on incremental-iterative analyses. Those can be classified in nonlinear static and nonlinear time history analyses. In nonlinear static analyses, the structure undergoes step-by-step actions until peak- and post-peak load, utilizing either load control, displacement control or event-by-event damage control (e.g., [71]). These analyses involve solving nonlinear differential equations, typically by linearizing them and solving them in an iterative manner. They are commonly used for simulating quasi-static experimental tests and pushover analyses, a common procedure of assessing the seismic performance of a masonry structure, by subjecting it to monotonically increasing displacements of a control node, keeping the load pattern of horizontal forces constant throughout the analysis [1]. On the other hand, nonlinear dynamic analyses involve step-by-step application of time-dependent actions, considering inertial and damping effects. Time integration methods, classified as explicit or implicit, approximate the equations of motion during each time step. Explicit methods depend solely on quantities from the previous step, while implicit methods involve values from the same step, requiring iterative refinement. Nonlinear time history analyses can simulate dynamic actions on structures, such as earthquakes or explosions, including the effects of earthquakes through accelerograms. Nowadays, engineers can choose among numerous computational techniques available for the analy-

sis of masonry structures, depending on the level of detail, accuracy and efficiency they aim for. In literature, the different modelling strategies are classified based on their level of refinement and detail. Lourenco [72], and Asteris et al. [73] classified the modelling approaches in three categories: macro-modelling, detailed micro-modelling and simplified micro-modelling. D'Altri et al. [1] broadened the classification of modelling strategies to four main categories: block-based models, which account for the simplified and detailed micro-modelling categories of the previous classification; continuum models, which represent the macro-modelling approach of the previous classification; macro-element models; and finally geometry-based models. This classification is based on the level of detail in modelling the geometry of masonry structures and the corresponding constitutive equations. In block-based models, as in micro-models, the actual geometry of the structure is considered: each brick is modelled individually and the mechanical interaction between them can be described in various ways. In continuum models (macro-models), masonry is modelled as a homogeneous material, and the constitutive equations describe the behavior of the material as a whole, not distinguishing between the interactions between the different blocks and joints. Macroelement models consider the behavior of masonry in a structural scale bigger than continuum models. Typically, the structure is split in panels, representing piers and spandrels, and the corresponding constitutive equations aim to reproduce the mechanical behavior of the panel. Finally, geometry-based models represent the structure as a rigid body, and simplified methods, mostly limit-analysis-based solutions, are used to find the equilibrium and/or collapse of the structure.

In this chapter, a different classification is given, based primarily on the numerical method used to model the material behavior, and secondarily on the level of detail that masonry's geometry is modelled. These methods are the macro-element based methods, the Discrete Element Methods (DEM), the Finite Element Methods (FEM)- which include both the macro-modelling and the micro-modelling approach- and the more recent hybrid methods. The main characteristics of these methods will be described in the following sections, alongside some of their representative constitutive models. Finally, special focus will be given on the macro-modelling approach, a subcategory of FEM models, and on its existing constitutive models, since this is currently the most commonly used modelling approach for masonry structures, and the family of constitutive models that this dissertation deals with.

2.2.1 Macro-element methods

Macro-element models, also often called component models, idealize the structure as a system of panel-scale components with a phenomenological or mechanical-based nonlinear response [1]. Generally, the panels represent two components: piers and spandrels. Piers are the vertical structural elements that carry loads both vertically and horizontally, whereas spandrels are the horizontal structural elements, typically found between openings, which connect the piers and couple their response in the case of lateral loads [4]. The choice of piers and spandrels as the representative structural elements is based on observations of the damage localization in real buildings. One of the characteristics of macroelement models, is that the geometry of spandrels and piers is defined a priori, a task that might be straight-forward for masonry facades with openings distributed regularly, but that can become complicated and uncertain when facades include openings of different sizes that are

irregularly distributed over their area. Moreover, macroelement models focus mainly on the global response of the structure, assuming that no local failure modes (such as out-of-plane failure) occur, and that the response is related to the in-plane capacity of the panels and the diaphragm action. Even though a separate analysis of the out-of-plane walls can be performed, the assumption that out-of-plane failure is prevented could lead to an inaccurate capacity estimation, since often in-plane and out-of-plane failure occur simultaneously and the failure mode of one can influence the capacity of the other [74]. Despite these disadvantages, the macroelement modelling technique is widely used by engineers for the seismic assessment of masonry structures, due to its simplicity in defining the panel geometries and to its computational efficiency. The most popular family of macroelement models are the Equivalent Frame Models (EFM), although recently spring-based approaches have been developed as well.

2.2.1.1 Equivalent Frame Models

Equivalent frame models (EFM) got their name from the idealization of masonry walls as equivalent frames. Each masonry wall is subdivided in deformable elements, where the nonlinearities are concentrated, and in rigid elements or nodes, which correspond to parts of the wall where damage is not usually expected [4].

The starting point of many macro-models was the POR method, proposed by Tomaževič [78], which considered a storey failure mechanism, based on observations of piers failing with diagonal shear mechanisms after earthquakes. The spandrels were considered rigid and fully resistant. Therefore, this approach proved sufficiently reliable only in the case of structures with weak piers and strong spandrels [1], since it did not cover all possible mechanisms that can be developed in a masonry building.

Brencich et al. [75] presented a macroelement approach for the three-dimensional simplified analysis of masonry buildings. According to their approach, each model consisted of shear walls connected to each other, as well as to a flexible floor diaphragm (Figure 2.7a). The macroelements used took into account overturning, damage and frictional sliding mechanisms by considering that each element was made up of three sub-structures: two layers at the top and bottom of the element where bending and axial actions were concentrated (and no shear deformation was allowed), and a middle layer where only shear deformations were allowed. The axial and bending response were therefore decoupled from the shear one. Additionally, compatibility conditions at the edges of the walls were imposed, ensuring that the vertical displacements of two adjacent piers would be the same.

Another macro-element model was developed by Addessi et al. [79]. The authors determined the sectional response of the beam by employing analytical integration instead of a fiber approach. This was accomplished through the formulation of a two-node force-based beam finite element, which enabled precise interpolation of the resultant stress components along the beam axis. The FE for the beam consisted of two main components: a central flexible element characterized by a no-tension constitutive relationship, and a lumped nonlinear shear hinge arranged in series. More advancements include the FE beam developed by [80], which had lumped flexural and shear hinges with elastic-plastic behavior at the two end nodes of the beam, and its further development by [81], which included a predictor-corrector method consisting of a return algorithm based on the Haar-Karman principle and the gradient projection method.

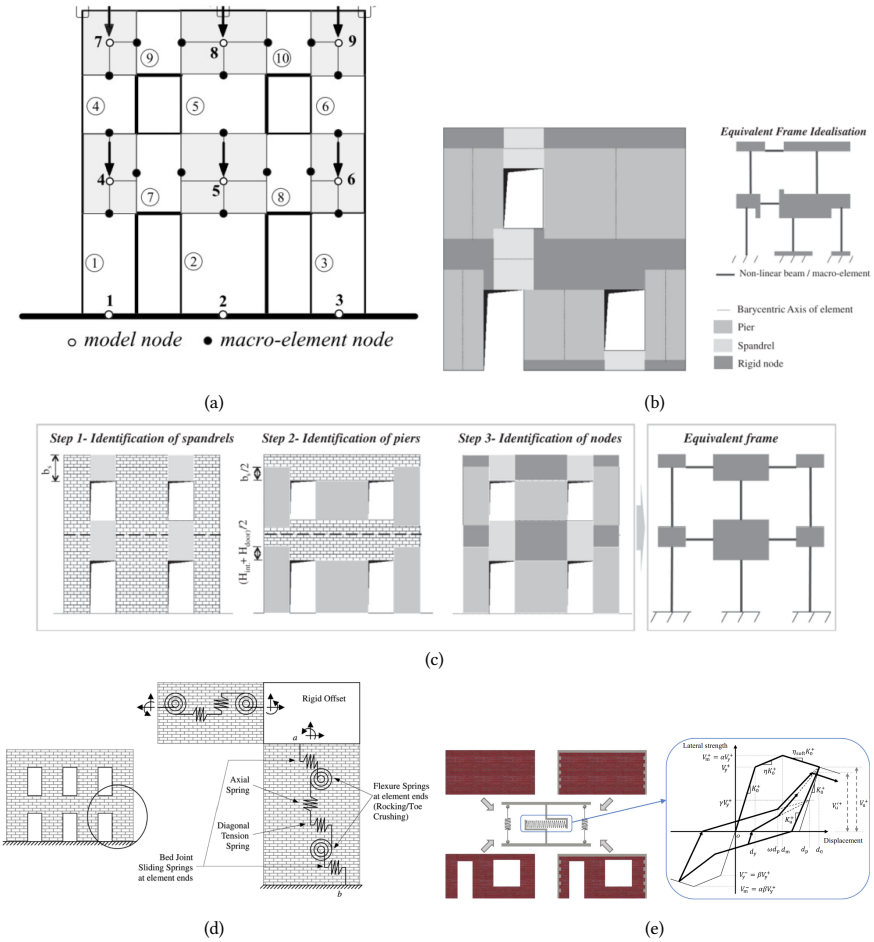

Figure 2.7: Examples of macro-element methods. Equivalent Frame Models of (a) Brencich et al. [75], and Lagomarsino et al. [4] for the identification of piers, spandrels and nodes in the case of (b) irregular and (e) regular openings; Spring-based models of (d) Chen et al. [76] and (e) Xu et al. [77].

One of the most popular EFM is the work of Lagomarsino et al. [4], which led to the development of the TreMuri software (Figure 2.7b and 2.7c). Here masonry piers and spandrels were modelled assuming bilinear relations with strength cut-off and stiffness degradation. Rocking, crushing and shear (bed-joint sliding and diagonal cracking) failure modes were included in the model, giving two different choices for the flexural strength criterion. More EF models can be found in literature and one can refer to comprehensive and extended reviews of them in [82–84], whereas a discussion about the most appropriate discretization criteria in the case of irregular openings can be found in [85].

2.2.1.2 Spring-based approaches

An alternative way of formulating macro-elements is with the use of nonlinear springs arranged in series that approximate the nonlinear in-plane response of masonry walls. Chen et al. [76] developed a new model that included rotational, shear and axial springs in series. In the case of piers, two shear springs were added at the top and bottom of the element to simulate the bed joint sliding; these springs were not needed in the case of spandrels. Penna et al. [86] based their macro-element model on the works of [87, 88], the capabilities of which they further improved. Their macro-element was subdivided in three parts: a central part where only shear deformations could occur, and two interfaces that could have relative axial displacements and rotations, and where a nonlinear degrading model for rocking damage was implemented, allowing to take into account the effect of limited compressive strength.

More recently, Xu et al. [77] proposed a macro-element model that would treat a masonry wall as a single unit (instead of dividing it in piers and spandrels). Its mechanical behavior included flexure, shear and friction and was represented by two vertical springs and a horizontal nonlinear spring for shear response (Figure 2.7e). The hysteretic behavior was derived by considering some control parameters dependent on factors like openings, confining elements, dimensions, material properties, and boundary conditions. The unified model was characterized by ten parameters, determined through analysis of over one hundred specimens.

Finally, Bracchi et al. in their two accompanying papers [89, 90] introduced an improved macro-element model that addressed some limitations of [86]. Regarding the compressive and flexural behavior, it introduced a new compressive law and a different methodology to accurately represent the flexural stiffness of the panel and to model the second-order effects. When it comes to the shear behavior, unlike [86] that required manual calibration, the new macroelement predicted the cyclic response of a shear-failing wall by considering multiple strength criteria. It automatically calculated equivalent shear parameters by using experimentally measured or code-prescribed mechanical properties. Additionally, it included a procedure to determine the deformability parameters for nonlinear shear response without the need for calibration at the beginning of the analysis.

2.2.2 Finite Element Methods

In Finite Element Methods, masonry can be modelled with a micro-modelling or a macro-modelling approach.

2.2.2.1 Micro-modelling

The micro-modelling approach represents masonry as an assembly of its individual constituents: bricks/blocks and mortar (or dry) joints. There are two levels of micro-modelling: the simplified and detailed micro-modelling. In detailed micro-modelling both the bricks/blocks and the mortar joints are modelled as distinct continuum elements, connected to and interacting with each other through the brick-mortar interfaces. On the other hand, in simplified micro-modelling, only the bricks/blocks are modelled; the properties and behavior of the mortar joints and the brick-mortar interface are integrated in the interface elements connecting the different bricks. As a result, the geometry of the bricks in this

method is extended to take into account the thickness of the mortar joints that are not explicitly modelled.

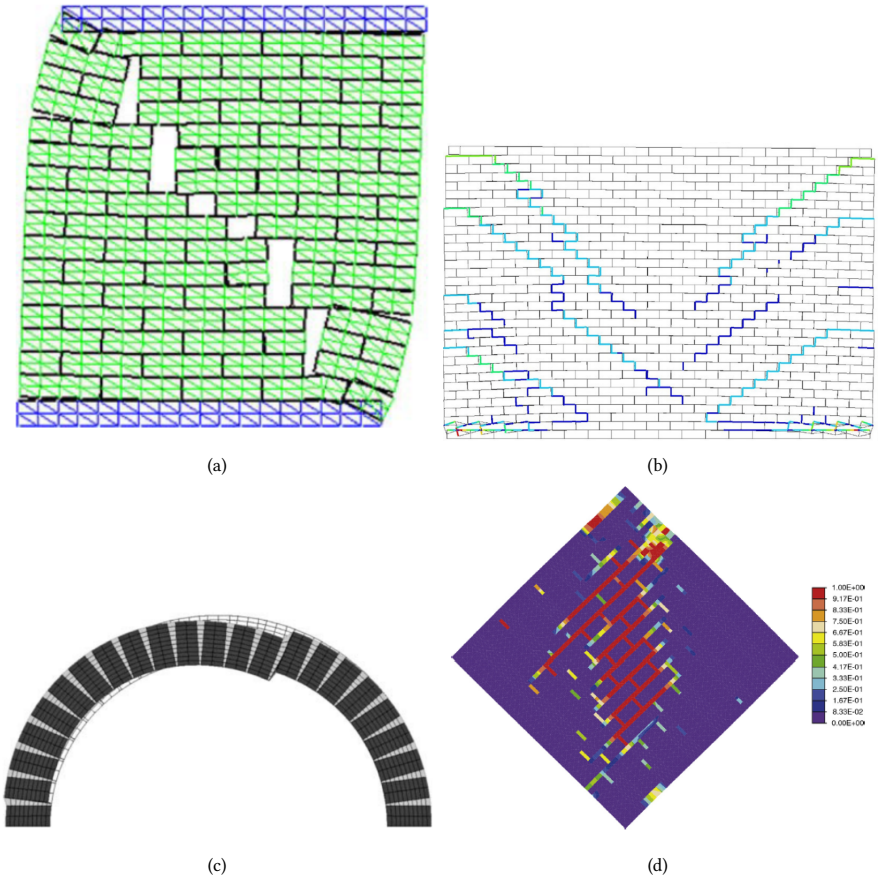

Figure 2.8: Examples of FEM micro-modelling methods, taken from (a) Chaimoon & Attard [91], (b) Xie et al. [92],(c) Sacco & Toti [93], and (d) Addessi et al. [94].

The first interface model introduced for masonry was developed by Page [95] and it considered masonry as an assemblage of elastic bricks connected to each other through linkage elements, which represented the mortar joints and had high compressive strength, low tensile strength and limited shear strength based on both strength and level of compression.

Later, Lotfi & Shing [16] proposed a one-dimensional constitutive model for dilatant interfaces, based on the theory of plasticity. The model considered a three-parameter hyperbolic yield criterion that ensured a smooth transition between the Mohr-Coulomb and the tension cut-off criteria. A nonassociated flow rule was used to avoid excessive plastic dilatancy, whereas softening was included for tension, compression and shear. In fact, tensile softening did not influence the frictional strength, whereas softening in the compressive/shear regime reduced both the tensile and frictional strength. The authors

were able to capture the mechanical behavior of masonry joints, showing the impact of the dilatancy angle on the shear response, which can vary from softening to hardening, leading to significant variations of shear stresses.

Lourenco & Rots [33] published a multisurface interface model which captured all masonry failure mechanisms: tension, compression and shear. The plasticity-based model included a Coulomb-friction envelope with tension cut-off and a compressive cap. Unlike [16], it was assumed that all nonlinearities were concentrated in the interface elements, whereas the bricks remained elastic and potential cracks through the bricks were modelled with additional interface elements. This, in combination with the return mapping algorithm, led to robust numerical models, making this one of the most commonly used interface models for masonry micro-modelling. Oliveira & Lourenco extended this model from monotonic to cyclic analyses in 2003 [31]. They introduced new yield surfaces for the unloading, assuming non-linear unloading curves for the normal stresses and elastic unloading for the shear stress. The numerical results captured the main characteristics of masonry cyclicity: stiffness degradation, energy dissipation and crack pattern.

A few years later, Giambanco et al. [96] developed an interface constitutive model based on plasticity and focused on the loss of cohesion due to shear and tensile stresses, taking into account the roughness of the mortar joint surface. They showed that the asperities play an exigent role in identifying the strength of the material, and the ductility and failure load of the structure.

The model of Lourenco & Rots [33] was further enhanced by van Zijl [97], who incorporated a variable dilatancy coefficient to capture the dilatant behavior of masonry, naming the normal uplift observed upon unconfined shearing along a masonry joint and the normal stress buildup under confined shearing. He concluded that while a constant nonzero dilatancy coefficient leads to strength overestimation, a zero dilatancy coefficient might be too conservative.

Chaimoon & Attard [91] modelled masonry using triangular units connected through interface elements. A group of triangular units would constitute a brick, and the bricks would be connected to each other through zero-thickness interfaces (Figure 2.8a); different inelastic properties were assigned to the interfaces located inside a brick and to the ones around the brick's perimeter, allowing fracture in the vertical and diagonal interfaces of a brick and the horizontal and vertical interfaces around a brick, simulating the mortar joints. The interface model, based on fracture mechanics included a Mohr-Coulomb friction failure surface, with a linear compression cap and tension cut-off. It was validated against the experimental and numerical results presented in [33] with a reasonably good match.

A year later, Minga et al. [14] developed a 3D cyclic damage-plasticity constitutive model for zero-thickness interface elements. The multi-surface yield criterion took care of the permanent plastic-strain development, while an anisotropic damage tensor coupled with the plastic work accounted for the strength and stiffness degradation. The model allowed for an algorithmic decoupling of plasticity and damage, allowing for parallel solving and reducing the number of local iterations and computational cost.

Further tackling the robustness of interface models, Kumar & Barbato [98] developed a new constitutive model for zero-thickness interface elements aiming to increase the robustness and reduce the computational time of simplified-micro-models. They achieved that by removing the singularity problem at the intersection between the Mohr-Coulomb

failure surface and the Rankine failure criterion and by using the strain hardening/softening hypothesis.

More recently, Xie et al. [92] proposed a cyclic constitutive model for masonry interfaces combining characteristics of multi-surface plasticity and damage mechanics (Figure 2.8b). It described the three main failure modes of masonry and masonry-mortar interfaces (cracking, crushing and shear sliding) through a Coulomb-friction yield surface with compression and tension cut-off; the strength and stiffness degradation were driven by two damage-factors: one coupling tension and shear and one for compression. The most innovative part of the developed constitutive model was the inclusion of a sub-stepping iterative algorithm, instead of the most commonly used return-mapping algorithms. The sub-stepping algorithm improved the robustness and numerical stability of the model, its advantages being more apparent in the case of singularity points.

Another constitutive model that utilized a sub-stepping method was the interface model of Nie et al. [99]. In their work, the authors proposed an interface model based on multi-surface plasticity, incorporating also damage, so that hardening and softening, as well as stiffness degradation would be included for tension, compression and shear or a combination of them. A huperbolic yield surface was used to describe the tension-shear failure, while an elliptic cap was used for the compression-shear failure mode. An adaptive sub-stepping scheme was implemented, where the load increment at the local level (integration point) would be automatically adjusted based on the performance of the Newton Raphson scheme in the previous sub-step. This, in combination with an effective stress-based formulation, led to enhanced robustness and improved numerical stability.

The constitutive models referred above, and most of the available micro-modelling constitutive models fall under the simplified micro-modelling approach. Research related to detailed micro-modelling has been relatively limited. This is not only due to the increased computational cost (even higher than for simplified micro-modelling), but also due to the increased number of material parameters that are required in order to define the different constituents of masonry; these additional material properties are often hard to measure through experiments. Nevertheless, in certain cases, like in the case of irregular stone masonry, zero-thickness interface elements and the subsequent modification of the block geometry could lead to subjective results [100].

Sacco & Toti [93] proposed an interface model that combined damage and friction to simulate the brick-mortar interface. The damage parameter accounted for the coupling of mode I and mode II fractures. Furthermore, the brick elements and mortar joints were modelled either with linear elastic or nonlinear (elasto-plastic) continuum elements (Figure 2.8c). Zhang et al. [100] developed a detailed micro-model using extrinsic cohesive elements in combination with a node-to-node algorithm to transmit contact and friction. Andreotti et al. [101] used detailed micro-modelling to model direct shear tests of brick masonry, focusing on the role of dilatancy. The authors modelled the brick elements with linear elastic elements and the mortar-joints interface with zero-thickness interface elements which act nonlinearly only in their normal direction. As for the mortar joints, they developed a constitutive model based on Modified Mohr-Coulomb plasticity, including a variable dilatancy angle that depends on the level of compression and shear displacement. As a last example, the detailed 3D micro-model of D'Altri et al. [17] included a *textured* unit consisting of one brick and few mortar layers (the brick and mortar joint obeying to separate

plastic-damage models), connected to the adjacent textured units through contact-based cohesive interfaces characterized by a Mohr-Coulomb failure surface with tension cut-off.

Continuous micro-models have been sporadically used as well for modelling masonry walls. In this modelling approach both the bricks/blocks and the mortar joints are modelled with continuous elements, without the presence of interfaces or contact elements to describe the brick-mortar interface (Figure 2.8d). Such an approach is presented in [102], where a continuous damage model was developed and used for the modelling of bricks and mortar joints. The model adopted a 2-parameter tension-compression framework while simultaneously incorporating phenomenologically the dilatant behavior of mortar joints. Another example of continuous micro-modelling was described in [94]. In this case, a damage-friction failure criterion was adopted for the mortar joints, whereas a damage model with two yield surfaces was adopted for the bricks, assuming that damage was governed by tensile strains.

2.2.2.2 Macro-modelling

Macro-modelling refers to the modelling of masonry structure with continuous elements, where masonry is considered as a homogeneous continuous material and the damage is smeared out over the continuum. This type of modelling strategy has the advantage of not requiring mesh discretization to describe the individual bricks and joints, allowing for finite element dimensions significantly larger than the block size. As a result, the computational effort is generally lower than for micro-model approaches. However, due to the mechanical complexities of masonry (orthotropy and discontinuous failure behavior, to name a few), defining appropriate homogeneous constitutive laws for masonry is a challenging task. This can be achieved through (a) direct approaches, such as constitutive laws calibrated based on experimental tests, or (b) homogenization procedures and multiscale approaches, where the material's constitutive laws (considered homogeneous in the structural-scale model) are derived from a homogenization process connecting the structural-scale model to a material-scale model (representing the main masonry heterogeneities). The homogenization process typically relies on refined modelling strategies, e.g., micro-models, for a representative volume element (RVE) of the structure.

Direct macro-models Direct macro-models base their constitutive equations on laws that describe the overall mechanical response of masonry. The mechanical elastic and inelastic properties can be derived or calibrated from experimental tests, without the use of homogenization procedures. A considerable number of direct macro-models have been developed so far, with their constitutive laws belonging to one of the following families: fracture mechanics (smeared crack models), damage mechanics, plasticity theory, or a combination of plasticity theory and damage mechanics.

Several constitutive models that were originally developed for concrete structures found applications in masonry modelling (e.g., [29, 30, 103]). Nevertheless, the complicated mechanical behavior of masonry due to its anisotropy and heterogeneity hinders the numerical capabilities of these models. For example, Lotfi & Shing [22] evaluated the capability of smeared crack models to capture the strength and load-resistance mechanisms of reinforced masonry wall panels. The authors adopted an elasto-plastic plane stress model combining a Von Mises yield criterion with a Rankine-type tension cut-off. The

paper considered both fixed and (coaxial and non-coaxial) rotating crack formulations. The numerical results matched well the experimental results in terms of force-displacement curve and failure pattern in the case of the flexure-dominated behavior, while they overestimated the shear resistance in the case of shear-dominated behavior during the experiment (diagonal cracking). The authors observed that the tension-softening slope influenced the global behavior more in the pre-peak phase rather than in the post-peak part of the force-displacement curve. On the other hand, the compressive strength degradation due to lateral cracking led to larger force degradation. Moreover, the authors concluded that "any shear distortion related to the opening of a diagonal crack has to be associated with a diagonal compressive strain, which results in a diagonal strut mechanism which contributed to the shear resistance after cracking.... The shear strength will remain as long as the diagonal compressive strength remains, regardless of the shear retention along the crack surface." Therefore, they suggested that a possible solution could be the development of a new smeared crack modelling technique that decouples the diagonal compressive strain from the true crack strain.

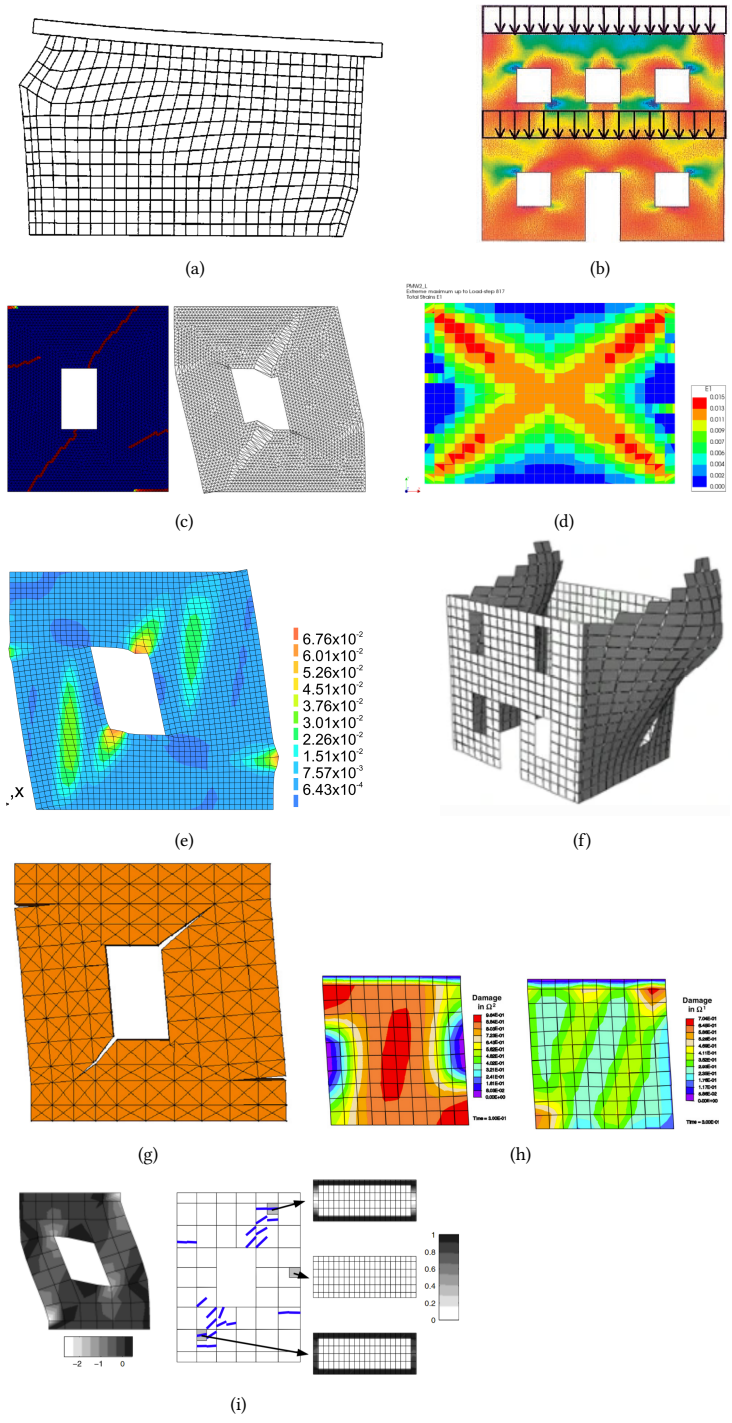

Figure 2.9: Examples of FEM macro-models, based on direct approaches, taken from (a) Lourenco et al. [27], (b) Lopez et al. [104], (c) Pela et al. [105], (d) Schreppers et al. [21],(e) Bilko and Małyszko [106]; homogenization approaches taken from (f) Bertolesi et al. [107] and (g) Milani [108]; and multi-scale approaches, taken from (h) Marfia & Sacco [109] and (i) Massart et al. [110].

Lourenco et al. [27] proposed the first direct anisotropic macro-model for quasi-brittle orthotropic masonry based on the theory of plasticity. Their plane-stress model included a composite yield criterion comprising a version of Rankine criterion for tension and a Hill criterion for compression. Regarding tension, a single scalar accounted for the amount of exponential softening in the two orthogonal directions (corresponding to the two material axes) simultaneously, despite two different fracture energies being incorporated in the model. In the case of compression, a scalar accounted for the parabolic/exponential softening, assuming isotropic hardening and anisotropic softening, making use of two different compressive fracture energies. In order to determine if one or both yield surfaces would be active (for example at a corner) a trial and error procedure was used to solve the return mapping algorithm. Either one or maximum two restarts were required to define the correct number of active yield surfaces. The model was validated against two experimental tests, predicting the correct failure mechanism for both tests (Figure 2.9a) and estimating with good accuracy the force-displacement curve of the one wall, but overestimating the capacity of the second wall, where the behavior was governed by masonry crushing. At the time of publication, the model had only been used for monotonic analyses and the authors had acknowledged that the elasto-plastic unloading/reloading would not describe correctly the unloading/reloading behavior of masonry structures, since the elastic stiffness degradation would not be captured. In the same year, Papa & Nappi [28] presented an orthotropic constitutive model based on a combination of plasticity and damage mechanics that was validated against cyclic experimental results. The yield surface consisted of two paraboloids and three ellipsoids lines and the material model accounted both for plastic strains and damage degradation. The comparison of the numerical and experimental results (for the in-plane masonry wall that was tested cyclically) showed satisfactory results with respect to the damage distribution and failure load, but the numerical model overestimated the stiffness and the dissipated energy, the latter not being discussed in the paper.

Another orthotropic constitutive model that was validated against cyclic experimental results was developed by Berto et al. [23]. The authors defined an orthotropic damage model that made use of four independent internal damage parameters, one for tension and one for compression in each of the two predefined material axes, which coincided with the bed and head joints directions. The definition of the damage surface was done in terms of the full effective stress vector and had the shape of a double pyramid with a rectangular base, the slopes of which corresponded to the friction coefficient. Overall, the model reproduced well the damage patterns of the examined walls and sufficiently the collapse load. Nevertheless, the numerical models underestimated the hysteretic energies and some differences were observed in the vertical load variation as well, due to the incapability of the secant-driven damage model to evaluate the irreversible deformations of the material. Moreover, the stiffness and strength degraded faster than in the experimental results, not including the effect of friction along an open crack.

More recently, Pela et al. [24, 105] developed an orthotropic material model based on continuum damage mechanics. By using an innovative technique, namely the mapping of the anisotropic real space in an auxiliary isotropic one, it was possible to solve the problem in the mapped isotropic space and return the results in the original space. In this way, the damage formulations could be simplified, and the computational efficiency could be increased. The model adopted different isotropic criteria for tension and compression, with

a Rankine criterion for tension and a Drucker-Prager inspired criterion for compression. Initially, the authors validated the model against experimental failure envelopes with satisfactory accuracy. Consecutively, they validated the model against experimental results obtained from testing monotonically two shear walls with a central opening. The predicted damage pattern was very representative of the experimental one (Figure 2.9c), and the numerical results agreed reasonably with the experimental ones for one of the walls, albeit with a small overestimation of the shear capacity. Despite the promising results, the model was not validated against cyclic tests, where an underestimation of the energy dissipation might be expected, due to the secant unloading/reloading that was implemented in the damage model.

Following the gas extraction-induced earthquakes in Groningen, Netherlands, and the need for seismic assessment of the masonry structures in the region, a new total-strain-based constitutive model was developed by DIANA software in collaboration with TU Delft [21, 111]. The model assumed two pre-defined axes which coincided with the direction of the head and bed joints, and the constitutive equations were described along those axes, describing tensile cracking of bed or head joints, and compressive crushing in the direction normal to the bed or head joints. It can be seen as a pre-fixed smeared crack/crush model, the total-strain-based formulation of which followed the format of isotropic concrete-oriented models in DIANA [112] that had become quite popular for masonry too, despite their isotropy. Moreover, it included frictional shear sliding and gave the option to include diagonal staircase cracking at a user-defined angle. Additionally, to address the problem of low energy dissipation of other damage and total-strain models, the unloading/reloading behavior followed a bilinear curve in compression, and an elastic unloading curve in shear, whereas secant unloading/reloading was adopted for tensile cracking. The model was validated against a number of masonry walls (Figure 2.9d) tested cyclically both in-plane and out-of-plane, providing in the vast majority of cases a good estimation of the base shear capacity of the specimens and the force degradation. However, the energy dissipation was at times overestimated (in the case of flexural based failure) or underestimated (in the case of pure shear sliding failure). In addition, the crack pattern was not captured realistically, since often the damage was diffused over a too many finite elements rather than being sufficiently localized.

This problem of damage localization in smeared crack models (macro-models) was addressed by Saloustros et al. [26], who enhanced an existing damage macro-model, developed by Cervera et al. [113], by implementing a crack-tracking algorithm. The material behavior, which was initially isotropic, would switch to damage-induced rotating orthotropic behavior upon crack-initiation. The crack-tracking algorithm aimed to ensure mesh-bias independence and realistic crack propagation, by identifying new cracks while simultaneously prohibiting the non-realistic spreading of the damage. While the numerical results demonstrated clearly the sharp damage localization of masonry structures and the mesh-independence of the model (especially when compared to classical smeared crack approaches), the model itself was not validated against experimental results.

The last direct macro-model to be discussed was developed by Bilko & Małyszko [106] and regards an orthotropic elastic-plastic constitutive model for masonry walls, extension of [27]. The authors proposed a generalization of the Hoffman criterion in the plane stress space, considering different tension and compression yield surfaces. The constitutive model

was validated against experimental yield surfaces and other constitutive models, with good accuracy between numerical and experimental results. Regarding the application of the model to masonry structures, two wall specimens were modelled and the model was able to represent correctly the failure mechanism of both of the walls (Figure 2.9e). The load capacity was overestimated for one of the walls, but predicted accurately for the other. However, like for most macro-models, the cracks were diffused.

Macro-models based on homogenization and multiscale techniques Unlike direct macro-models, macro-models based on homogenization and multiscale techniques take into account the mechanical properties and the geometrical arrangement of masonry's constituents (bricks and mortar joints) at a cell level. So, in essence, macro-modelling techniques based on homogenization provide continuum average results that include the information of the microstructure, through a mathematical process [114]. The selection of an appropriate Representative Volumne Element (RVE) is crucial for the correct definition of the constitutive relationships. It should be representative of the homogeneity of the material, and therefore many RVEs have been proposed so far to account for different bond patterns (periodic or non-periodic) of masonry.

There are three main families when it comes to homogenization and multiscale approaches: (i) a priori homogenization approaches, (ii) step-by-step multiscale approaches, and (iii) adaptive multiscale approaches.

A priori homogenization approaches consist of two steps: first deriving the mechanical properties through a homogenization process, and secondly introducing these properties to a structural scale model. The homogenized constitutive equations can be derived analytically (closed-form), quasi-analytically and by using numerical methods [1].

Pietruszczak & Niu [115] presented a mathematical formulation of the average mechanical properties of structural brick masonry, treating firstly the head joints as aligned, uniformly dispersed weak inclusions and secondly the bed joints as continuous planes of weakness, investigating also the progressive failure of masonry.

Anthoine [116] derived the in-plane elastic characteristics of masonry through a one-step homogenization procedure, and concluded that neglecting the head joints and assuming plane stress states does not change the global elastic behavior of masonry; the same cannot be concluded for the non-linear stage. More examples of homogenization models for the elastic properties of masonry can be found in [117–119], whereas in [120, 121] homogenization approaches based on Cosserat continuum were used for the derivation of the elastic behavior of masonry.

When it comes to the inelastic properties of masonry, Zucchini and Lourenco [122] derived a micro-mechanical model considering not only the actual deformations of the basic cell but also additional internal deformation modes. Both the elastic properties (Young's moduli) and the failure surfaces represented well the experimental results. They extended the constitutive equations into a continuous damage model and implemented it in a FEM software, where they validated the numerical results against experimental results in structural scale [20]. The model captured the basic global behavior of the examined walls (type of failure and type of cracks/damage), even though there were some differences in the crack location and some smaller differences in the stiffness and load estimation.

Another way of deriving homogenized failure surfaces is based on limit analysis. For example, Milani et al. [123] derived failure surfaces for the homogenized limit analysis of in-plane masonry, by assuming fully equilibrated stress fields in the basic cell and adopting a polynomial expansion for the stress field. Additionally, in [124] they applied the homogenized limit analysis model to structural examples. A few years later, Milani [108] published another lower bound limit analysis homogenization model both for the in- and the out-of-plane behavior of masonry walls (Figure 2.9g).

Additionally, a new homogenization approach was developed to be used not only exclusively with continuum finite elements, but also with rigid blocks and spring elements (e.g., [107, 125, 126]). Unlike the FEM micro-modelling and Discrete Element Method that also use rigid elements to model the bricks connected with interfaces or spring elements, in this homogenized approach the interface elements or springs do not correspond to the actual geometry of the mortar joints, but are used to localize the damage and nonlinear behavior of masonry (Figure 2.9f).

In multiscale approaches, the overall behavior of the structure is determined step-by-step by solving a boundary value problem (BVP) on the representative volume element (RVE) for each integration point in the structural-scale model. This process allows for the gradual estimation of the anticipated average response, which is then incorporated into the constitutive relations of the structural-scale model. These approaches do not directly consider the heterogeneity of masonry in the structural-scale model; instead, they explicitly address it within the material-scale RVE [1]. The variations among the models pertain to several aspects, such as the configuration of the masonry (whether it has a regular or irregular texture), the chosen constitutive model for the brick (whether it is rigid or deformable with linear or nonlinear behavior, incorporating damage and/or plasticity effects), the selected model for the mortar (whether it is represented as an interface or a continuum material with linear or nonlinear response), and the macroscopic model derived through homogenization (which may be based on Cauchy, Cosserat, or higher order continua) [127].

One of the first multiscale models is that of Gambarotta & Lagomarsino [25], who used a mortar joint (interface) model [128] to formulate the continuum damage model through a homogenization technique. Their model included both damage and friction mechanisms, as well as their coupling. One of the limitations, common in many homogenization and multiscale models, is that the element height should be chosen with care, since the Gauss points should correspond to mortar bed joints. The model was further improved by Calderini & Lagomarsino [129] by introducing more damage mechanisms for the mortar joints and including additionally damage mechanisms for the blocks.

Three years later, a new nonlinear homogenization procedure based on the Transformation Field Analysis (TFA) was developed by Sacco [130]. More specifically, in this step-by-step approach, a linear elastic behavior was considered for the blocks, whereas a nonlinear behavior, accounting also for the coupling between damage and friction phenomena, was considered for the mortar joints. Then, followed the superposition of the effects and the FE method, with the advantage of the TFA being that the micromechanical finite element analyses were necessary solely for the determination of the overall elastic moduli and localization tensors. This approach was further improved by Marfia & Sacco [109] that extended it to the case of nonuniform eigenstrain and considered nonlinear damage

behavior also for the blocks (Figure 2.9h).

Nevertheless, first-order computational homogenization schemes face two main limitations. The first arises from the assumption of uniformity imposed on structural-scale fields attributed to each RVE, which becomes less effective in regions with high deformation gradients. The second limitation stems from the cohesive behavior of masonry, leading to softening effects in stress-strain relationships. Mesh-sensitivity issues occur due to the absence of characteristic lengths in classical continuum models. Nonlocal approaches, higher-order continuum models, and regularization processes can address these limitations and ensure problem objectivity [1].

Massart et al. [110] approached this problem by proposing an enhanced multiscale model that used nonlocal isotropic damage models for both the bricks and the mortar (Figure 2.9i). To address macroscopic localization caused by damage growth in the constituents, the macroscopic description was augmented with a finite width damage band model. This enhancement enabled the consideration of localized damage growth within the material, allowing for a more accurate treatment of macroscopic effects. Alternatively, some researchers adopted Cosserat continuum models (e.g., [131–133]).

More recently, Addessi et al. [134] proposed a two-scale modeling approach for the in-plane and out-of-plane nonlinear analysis of masonry walls. In the structural macro-scale masonry was modelled as a homogenized medium, whereas in the micro-scale a representative unit cell consisting of elastic bricks and nonlinear zero-thickness interface elements was analyzed. The information transfer between macro- and micro-scale was achieved through a kinematic driven homogenization procedure, and a TFA-based procedure was used to solve the homogenization problem.

All in all, a large number of continuum macromodels have been developed, either following a direct approach or a homogenization or multiscale-based one. Most of the validated models found in literature are following a homogenization or a multiscale approach. It was also observed during the literature review, that although many direct macromodels have been used for the analysis of structures, not as many have been validated against cyclic experimental tests. On the other hand, more cyclic test validations were found for constitutive tests based on multiscale approaches. However, these models have more complex numerical implementations and generally lead to increased computational time with respect to direct macro-models. Consequently, even though they have been validated more against cyclic experiments, in engineering practice, and even in research, direct macro-models are more commonly and widely used. Finally, the need for regularization procedures to regard for mesh-sensitivity issues is a common need for all macro-modelling approaches.

2.2.3 Discrete Element Method

The Discrete Element Method is a class of numerical models that represents the mechanical behavior of systems composed by multiple blocks or particles [8]. The Discrete Element Method (DEM) was proposed by Cundall & Hart [135] for simulating the complete mechanical behavior of systems that consist of multiple discrete bodies or particles interacting with each other through their boundaries. Until then, discontinuities had been introduced in numerical models by modifying the continuum methods, for example through interfaces. The DEM was developed with the opposite focus in mind: modelling specifically the

discontinua and treating continua as a special case, if needed. To distinguish a DEM from a FEM formulation, Cundall & Hart [7] suggested that "the name Discrete Element Method should apply to a computer program only if it: (a) allows finite displacements and rotations of discrete bodies, including complete detachment, and (b) recognizes new contacts automatically as the calculation progresses". Currently, DEM have been adopted and used for the discrete modelling of masonry structures, modelling separately the blocks/brick units and the interaction between them through their contact surfaces. Since one of the characteristics of DEM is the ability to simulate complete detachment, the method is most commonly used for analyzing the structural failure, where strongly nonlinear behavior is observed.

According to [8], DEM can be classified into two categories when it comes to the modelling of masonry: block models and particle models. Block models, which are the most widely used, are composed of sets of polygonal or polyhedral bodies that represent the masonry bricks/blocks. On the other hand, particle models consist of circular or spherical particles that represent the material at a finer scale. In many DE models, the interaction between blocks is represented through contact points (point contact hypothesis); contact points are assigned a length for 2D analyses or an area for 3D analyses so that the contact forces (a function of the relative block displacements) can be transformed to stresses. This approach allows the interaction not only between faces, but also between a face and a vertex, providing a smooth transition between the two cases. Moreover, it allows large block movements and, unlike FEM, it does not require to match the mesh of the adjacent blocks to the nodal/contact points; instead, each block can be meshed independently.

Another approach is based on edge-to-edge formulations, where each block's edge is discretized in line segments that interact with the line segments of other blocks. This approach allows a linear variation of stresses on the contact surface, but may create numerical problems once the continuity of interaction forces is lost, for example in the case of large deformations [8].

Cundall & Hart [7] distinguished two methods for the mechanical representation of contacts: soft contact and hard contact. In the soft contact approach, a finite normal stiffness is adopted which represents the normal stiffness that exists at a contact, or on a joint. In numerical simulations with the soft contact approach an interpenetration of the blocks takes place for the forces to develop; physically this could be interpreted as elastic deformations of one surface when two bodies come in contact. On the other hand, in the hard contact approach no interpenetration is allowed; the two bodies can only slide on each other (shear movement) or lose contact (opening). The majority of constitutive models for masonry adopt the soft approach, since the normal stiffness can be directly related to the mortar joint thickness and properties in the case of mortared joints, and to the roughness and irregularities of the blocks' surfaces in the case of dry joints [8].

There are three main formulations of discrete element models. The first one, which is directly derived from the work of Cundall & Hart [7], is the Distinct Element Method, presented in the UDEC (Universal Distinct Element Code [141]) and 3DEC [142] software. In its current version, UDEC represents discontinuous medium in 2D as an assemblage of discrete blocks, which can be a mix of rigid or deformable blocks, while the discontinuities are treated as boundary conditions between blocks, their behavior being described by linear or nonlinear force-displacement relations in the normal and shear directions. 3DEC, on the

other hand, is the 3D version of UDEC. Both UDEC and 3DEC utilize an explicit solution scheme. Several researchers have applied this approach to model the behavior of masonry (Figure 2.10a and 2.10b), ranging from applications to columns (e.g., [143]), to towers (e.g.; [136, 144]), vaults (e.g., [145]), walls [146] and even houses [137] and monumental buildings (e.g., [147, 148]).

Another formulation of DEM is the Discontinuous Deformation Analysis (DDA), originally formulated by Shi [149, 150]. Unlike the Distinct Element Method, DDA uses an implicit solution scheme and adopts a hard-contact approach: no interpenetration of blocks is permitted. The blocks are considered deformable, but with a uniform stress and strain distribution, and rigid contacts that follow Coulomb's friction law when the blocks are in contact; sliding occurs only when the applied load exceeds the friction force. Various application examples include the modelling of stone arch bridges [151], and masonry bridges [152] and arches [153], but also to the modelling of ancient structures and monuments [154–156].

The third family of DEM is the Non-Smooth-Contact-Dynamics (NSCD) method, developed by Moreaur [157] and Jean & Mureaue [138] (Figure 2.10c). In this method, the goal is to find the contact forces transmitted between various pairs of randomly selected elements in a way that the two elements of each pair do not overlap each other throughout the analysis time step [158]. In the oldest models of NSCD the elements were rigid and the contact forces were not related to any stiffness data. The contact forces are either zero when the two elements are not in contact, or non-zero when in contact (in order to avoid overlap). This method does not provide a unique solution, since different alternative states can satisfy the equilibrium of motion, which might explain why its use in not more widespread, especially for quasi-static analyses. Some applications of the method include the analyses of stone masonry arches and bridges [159, 160], churches and other monuments [161–163]. However, despite these simulations leading to realistic results qualitatively, there is a big lack of quantitative comparisons and validations with experimental results.

More recently, additional approaches have been developed for the analyses of masonry structures, tackling mechanical issues that were not addressed and/or covered by the previous families. Sarhosis & Lemos [139] developed a detailed micro-model based on a phenomenological discontinuum approach, where masonry bricks and mortar joints were assembled together using densely packed discrete irregular particles connected with each other through zero-thickness interfaces (Figure 2.10d). They simulated small scale tests, and validated their model for all three mechanical behaviors: tension, compression and shear. Another recent addition to the discrete elements families is the Applied Element Method (AEM), originally formulated by Meguro & Tagel-Din [164]. In the AEM, the rigid blocks/units interact with each other through linear or nonlinear springs that represent the material properties. Malomo et al. [9] used the AEM to model masonry walls made out of Calcium Silicate bricks, subjected to in-plane cyclic loading. According to their approach, each brick was modelled as an assembly of units and each unit was connected to its adjacent units at their contact points through a pair of normal and shear springs. Springs with different stiffnesses and nonlinear-behavior are used to connect units belonging to the same brick, or for units connecting neighboring bricks (where a mortar joint would intervene). In that way, all five modes of masonry failure could be captured. The springs complied to a Coulomb friction criterion, with compression and tension cut-off. Later, the

constitutive model was also used to model the Out-Of-Plane response of brick masonry walls (Figure 2.10f) [140]. Finally, Sharma et al. [165] used the AEM to model rubble-stone masonry. In this approach, however, the units did not correspond to the real geometry of the rubble stones; instead a macro-modelling approach was adopted.

2.2.4 Hybrid Methods

Hybrid methods for the numerical analysis of masonry structures refer to computational approaches that combine the advantages of different modelling techniques to accurately represent the complex behavior of masonry materials and structures. These methods aim to overcome the limitations and challenges associated with traditional continuum and discontinuum models, providing more realistic and efficient solutions for the analysis and design of masonry structures. They typically integrate aspects of both continuum and discontinuum models. For example, they may employ a continuum approach to represent the overall behavior of the masonry structure, while incorporating a discontinuum representation for local regions with significant discontinuities, such as cracks or defects. Hybrid methods use various coupling strategies to integrate different modelling techniques and scales. This can include domain decomposition methods, where the masonry structure is divided into sub-domains with different modelling approaches applied to each, or hierarchical methods, where the results from one modelling technique inform the boundary conditions or material properties of another. Moreover, some hybrid methods employ adaptive mesh refinement techniques to balance computational efficiency and accuracy. By refining the mesh in regions with high stress gradients or discontinuities, these methods can provide a more accurate representation of the local behavior while reducing computational costs in other areas of the structure.

One of the examples is the combined FEM/DEM method (also often abbreviated F-DEM) [166], where each discrete element is discretized into finite elements. In that way the block deformations can also be included in the model. The combined finite-discrete element method (FEM/DEM) has proven highly effective for analyzing non-linear behavior in masonry structures. The method encompasses several key processes, including contact detection, contact interaction, finite strain elasticity, and fracture and fragmentation.

In FEM/DEM simulations, processing contact interaction for all possible contacts involves a number of computational operations proportional to the square of the total number of discrete elements. This could create immense computational challenges for large-scale simulations. To address this, contact detection algorithms are used to reduce CPU requirements by eliminating distant element pairs and detecting actual contacts. CPU efficiency, RAM efficiency, robustness, and ease of implementation are essential for these algorithms.

For example, Munjiza's NBS contact detection algorithm [166, 167], a linear algorithm, is based on space decomposition, with discrete elements mapped onto cells, rows, and columns. This algorithm uses singly connected linked lists for mapping and is efficient in terms of CPU and RAM usage. The total CPU time needed to detect contacts is proportional to the total number of discrete elements and independent of the total number of cells. Moreover, to save CPU time, a buffer can be introduced, controlling the frequency of contact detection analyses based on the maximum traveled distance of elements

The FEM/DEM approach models the fracturing behavior of an initially continuous solid block, represented by a single discrete element. During the collapse process, the

number of discrete elements may change. FEM/DEM allows for modelling the entire structural response, from linear-elastic to non-linear phases, including crack initiation, propagation, and sliding effects. It also tracks particle motion and interaction, considering inertia effects until the structure reaches its final state due to energy dissipation. FEM/DEM is particularly advantageous for cyclic loading situations, where accurate modelling of new contact creation due to system topology redistribution is essential [168].

Applications of the combined FEM/DEM method in masonry structures include the works of Smoljanović et al. [11]. In [11, 169, 172] the FEM/DEM method was applied to dry stone masonry (Figure 2.11a), while in [172] the model is extended further through new constitutive models for the continuum FEM elements and the interface elements, in order to capture the main features of masonry structures. The finite element material model considered the orthotropic and cyclic behavior, as well as compression failure and softening. Meanwhile, the numerical model for an interface element addressed both tension and shear failure, softening, increased shear fracture energy with rising pre-compression stress, reduced friction coefficient with growing shear displacement, and cyclic behavior. In [169] the model was extended to 3D elements for the representation of dry-stone masonry structures.

More application examples of FEM/DEM include the works of Baraldi et al.[173] and Pepe et al. [174], where in-plane masonry walls were modelled both with the DEM and the FEM/DEM approach and the results were compared. Additionally, F-DEM was also used by Ou et al. [175] in the simulation of historic masonry buildings subjected to differential settlements.

A different hybrid model was developed by Azevedo & Lemos [171], named Hybrid Particle/Finite Element Model. In essence, they combined characteristics of particle DEM models with FEM, in order to reduce the computational effort required when modelling stone masonry with particle models. To do so, they descretized the stone units that were expected to remain in the elastic range with FEM, whereas they used particles to model the stone boundaries, maintaining in that way the stone roughness (Figure 2.11c).

Lastly, Malomo & DeJong [13] proposed a Macro-Distinct Element Model (M-DEM), a novel model that combined the efficiency of simplified macroelement approaches, with the accuracy of the interface-based discrete methods. In this new approach, the layout of the interfaces (spring layers) was determined a priori as a function of the masonry texture (i.e. bond pattern), taking into account also the possible out-of-plane failure modes. As a result, each masonry component consisted of six deformable macro-blocks, discretized internally by a tetrahedral mesh, and connected to each other through nonlinear spring layers (interfaces) (Figure 2.11d). Compressive failure was assigned to the macro-blocks, whereas the flexural and shear (sliding or diagonal) failure were accounted for through the spring layers. In [13], the authors validated their approach for the in-plane analysis of masonry walls, and in [176] for the out-of-plane analysis of masonry walls.

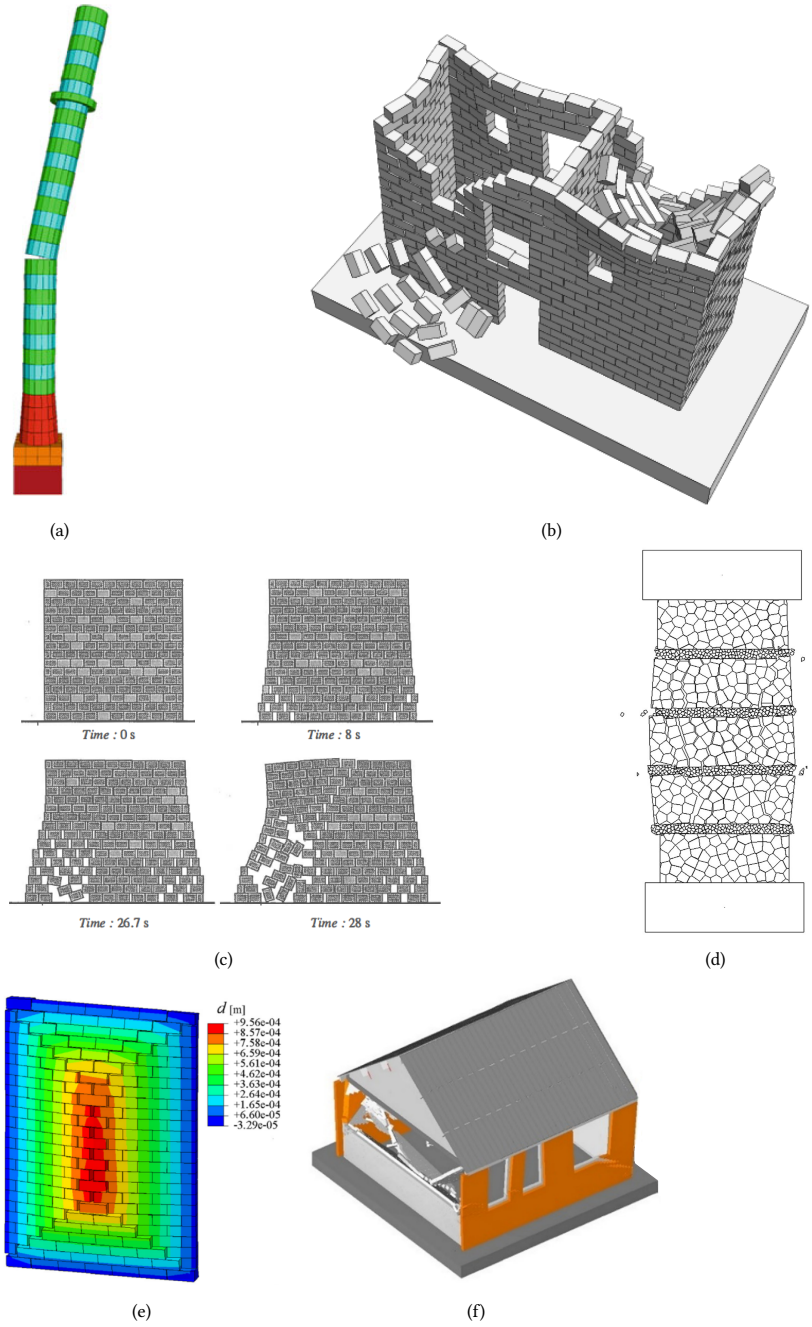

Figure 2.10: Examples of DEM methods: Distinct Element models of (a) [136] and (b) [137], (c) Non-Smooth-Contact-Dynamics model of [138], (d) particle model of [139], (e) DEM model of [17] and (f) Applied Element Method model of [140].

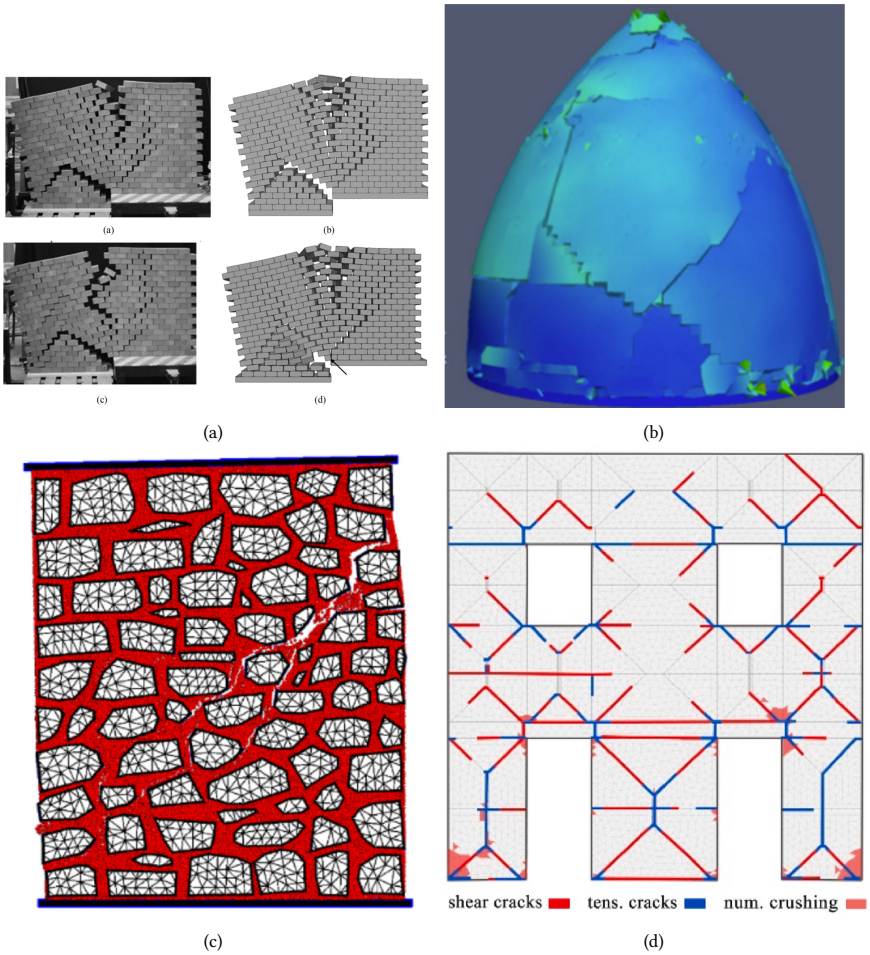

Figure 2.11: Examples of hybrid methods: (a) FEM/DEM model of [169], (b) FEM/DEM model of [170], (c) Hybrid particle-FEM model of [171] and (d) M-DEM model of [13]

2.3 Summary and conclusions

In this chapter, first a short overview of the mechanical behavior of masonry was presented, followed by a review of the different numerical modelling strategies for masonry structures, classified in four major categories: macro-element based methods, FEM methods, including both micromodelling and macromodelling techniques, DEM models and hybrid methods, where characteristics of different methods are combined. Even though an attempt was made to present an overview of the most important and relevant constitutive models, one can find even more information and existing models in the available literature. Moreover, one can also find alternative ways of categorizing the existing numerical approaches, based on the level of detail at which the masonry geometry is modelled, rather than on the numerical method used.

Macroelement models are used commonly by engineers for a fast assessment of a structure's seismic performance. They can provide a quick and easier way to assess ordinary masonry structures, without complex geometries and complicated interactions between different structural elements. However, their performance is hindered in the case of irregular openings, where one needs to make a conscious decision for the macro-element sizes and arrangement for piers and spandrels. Moreover, the main assumption upon which the criteria are formulated, that global failure is caused due to the in-plane behavior, influences their reliability. Ideally, the interaction between in-plane and out-of-plane behavior and damage, as well as other coupling effects between in-plane and out-of-plane elements and diaphragms should be taken into account in the formulation of the failure criteria.

The FE micro-modelling approach has been proven to be very reliable in terms of numerical accuracy. Both the damage pattern and the hysteretic behavior of structures are usually predicted accurately, though in some cases it was observed that material calibration was needed. Their high numerical accuracy, however, comes with a high computational cost, and therefore their application at the moment is limited to academic research, and special cases and projects where extra detail is required. They can also be used as a reference to generate benchmarks for the validation of simpler models in the case that experimental testing is not possible.

Similar to FE micro-modelling, the DEM approach, which is growing fast with new categories of discrete elements and constitutive laws added to it, is representing the behavior of masonry and its progressive failure, at times even explosive, very realistically. Both brick and rubble-stone masonry have been modeled with this approach. Another advantage of DEM is the possibility to capture the interaction between non-neighboring blocks that come in contact later in the loading history (possibly due to collapse). Nevertheless, even though the application to real structures, especially historic buildings, looks promising, many of the models used have not been validated against experimental results. Moreover, as in the case of FE micro-models, the computational effort is significant.

Macro-models could be considered the middle-point between macro-element methods and DEM or FE micro-modelling in terms of numerical accuracy and efficiency. In engineering practice, isotropic models (either from fracture mechanics, plasticity or damage mechanics) are still used, often due to their wide availability in popular software and their ease of application (reduced number of input parameters and simplicity of constitutive relations). However, they should be used with care and sensibility, since they often do

not capture the orthotropic behavior of masonry and can lead to overestimation of the strength and stiffness and/or displacement capacity of the structure. Thankfully, many researchers have contributed to addressing this problem, by developing constitutive models specifically for masonry that take into account the anisotropy of the material, either in a direct approach or through a homogenization procedure. Both models usually require a larger number of input material parameters. In the case of the direct approach, these parameters need to be derived from tests on sufficiently large masonry panels to represent a homogeneous material. On the other hand, the input parameters in the case of constitutive models that follow a homogenization or multiscale approach represent the properties of masonry's constituents (i.e., blocks and mortar joints). From the literature review performed while writing this PhD dissertation, it appears that the majority of continuous constitutive models specifically developed for masonry follow a multiscale or homogenization approach. In general, those have also been validated more against cyclic experimental results than the ones that are based on a direct approach, even if the latter are more commonly used in practice. The main disadvantage of multi-scale approaches is that being formulated based on a RVE, the type of RVE (and the bond pattern of masonry) may limit the applicability of the model to certain geometries, whereas at the same time the computational demand increases with respect to direct continuum models. Moreover, homogenization and multi-scale approaches are usually limited to 2D problems. However, the same can be said for most of the more advanced direct macro-models. A point that requires attention when using continuum models is the mesh sensitivity, which requires the regularization via a crack band approach or the consideration of a characteristic length. Regarding the ability of continuum macro-models to capture the behavior of masonry, it was observed that discrepancies from experimental results arose regarding the hysteretic behavior. More specifically, usually the dissipated energy, as well as the damage localization, were misestimated, especially where more than one failure modes prevail.

Finally, more and more hybrid methods are being developed in the last years: combining DEM with Macro-elements, or FEM/DEM can help achieve better accuracy of the numerical results at a lower computational cost. The results look promising but more validation and guidelines are needed.

To sum up, modelling masonry structures is a challenging task and despite the wide variety in modelling approaches and the great number of options for different constitutive models, there is no one-fit-all solution. Each modelling technique and each constitutive model has its advantages and disadvantages and at the current state of research, the engineers should make an informed decision for the most suitable modelling strategy to their problem, based on the available information (complexity of structure, known properties) and resources.

3

An orthotropic continuum constitutive model for the cyclic nonlinear behavior of unreinforced masonry structures

As it became apparent from Chapter 2, the inclusion of only tensile and compressive failure in a constitutive law is not sufficient to describe the mechanical nonlinear behavior of masonry. Orthotropy and the shear behavior should be considered as well. In this chapter, a new orthotropic continuum constitutive model for the cyclic nonlinear behavior of brick masonry structures is developed and presented. The current model includes orthotropy in two ways: first, both elastic and nonlinear material properties are dependent of the principal angle α_i, which is the angle between the principal strain and the bed joint orientation; secondly, the post-peak softening, as well as the unloading behavior in tension, depend also on the cracking angle α_{crack}, i.e., the angle between the principal strain and the bed joint at the onset of cracking, making a distinction between flexural or shear behavior. Moreover, the shear stress capacity is regulated through an internal iterative loop, to avoid the overestimation of the base shear force often observed in fracture mechanics models. The model and its implementation into the FORTRAN subroutine is discussed in this chapter, whereas in Chapter 4 the validation of the model against experimental results is presented.[1]

[1]This chapter has been adapted from the published paper "Sousamli, M., Messali, F., & Rots, J. G. (2022). A total-strain based orthotropic continuum model for the cyclic nonlinear behavior of unreinforced brick masonry structures. International Journal for Numerical Methods in Engineering, 123(8)".

3.1 Introduction

Masonry is one of the oldest building materials in the world. Due to its aesthetics, availability and ease of construction, it is found in many structures around the world, from historic monuments to residential buildings. It consists of units, such as bricks, stones or blocks, and joints, dry or mortar, arranged in a geometrical pattern. The different material properties of these constituents as well as their geometric arrangement make masonry an inhomogeneous and orthotropic material.

Thanks to the advances in the field of numerical methods, four different approaches have been developed for the numerical modelling of masonry structures: macro-element based methods, like the lumped mass approach and the Equivalent Frame Method [4–6], Discrete Element Methods (DEM) [7–10], Finite Element Methods (FEM), and most recently hybrid methods, like the Finite-Discrete element methods (F-DEM) [11, 12] or the Macro-Distinct Element (M-DEM) [13]. In FEM, which currently is the most commonly used approach, masonry is modelled according to two methods: the micro-modelling, detailed or simplified, and the macro-modelling approach. According to micro-modelling every unit/brick (and every mortar joint in the case of detailed micro-modelling) is modelled individually with its real geometrical and material properties, and it is connected to its surroundings through discontinuous interface elements [14–17]. On the other hand, in the macro-modelling (or continuum models) approach, masonry is considered to be a homogeneous material and the damage is distributed over the continuum. Macro-models can be based either on direct approaches, where the constitutive equations and material properties adopted should represent the behavior of masonry and should be obtained by tests performed on sufficiently large specimens, or on homogenization approaches (e.g. [18–20]), where the constitutive laws are derived through a homogenization process that relates the micro-scale material to the structural-scale. The micro-modelling approach is more accurate and is better able to predict the hysteretic behavior and local failure mechanisms of a structure. However, it is computationally very demanding and its use, up to now, is mostly limited to simulating single structural elements, like walls. On the other hand, macro-models constitute a good compromise between accuracy and computational effort, and are often preferred for modelling large structures, in order to reduce the required computational time.

In order to increase the accuracy of direct macro-models, the orthotropy of the material needs to be included. Currently, a number of constitutive models are available for masonry, based on the frameworks of smeared cracking [21, 22], damage mechanics [23, 24, 26, 128], and plasticity [27, 28]. However, even though these models include orthotropy in the description of the mechanical behavior, more challenges need to be overcome. Firstly, predicted crack patterns are sometimes too diffuse: wide zones of smeared cracked Gauss points have been reported (e.g., [21, 23]) rather than the localized discrete cracks identified in the last stages of tests. This is in part expected, since macro-models do not depict the exact geometry of a structure; however, a realistic damage localization is an important factor to consider when the structure needs to be strengthened. Secondly, most of the existing models have been validated only against experimental results of monotonic tests, whereas the few that have been validated against cyclic tests [21, 23, 28] tend to underestimate the energy dissipation, especially in the case of shear walls. The cyclic hysteretic response may be partially missed because of the unloading/reloading characteristics of the existing

models: either fully secant for damage/smeared cracking models or fully elastic for plasticity models. Damage-plasticity models tackle this issue, but even though such models have been developed for concrete (e.g., [29, 30]), and a few attempts have been made for interface elements [14, 17, 31], only few were developed specifically for macro-modelling of masonry (e.g., [28]). Thirdly, existing models may not always estimate the post-peak part of the load-displacement response correctly, and in general models require the calibration of a large number of material input parameters to obtain accurate predictions. In summary, constitutive models for masonry have progressed significantly over the years, but their accuracy still needs to be improved.

This chapter presents a newly developed orthotropic, continuum constitutive model for macro-modelling applications. The model belongs to the family of smeared crack/crush models and is based on a Total-Strain-Rotating-Crack (TSRC) approach. The novelty of the model lies on two things: first, the way in which shear failure is incorporated through an internal iterative algorithm; second, the unloading/reloading behavior that depends on the cracking angle at the onset of cracking and on the corresponding type of failure. In that way, secant unloading/reloading is adopted when cracking due to flexure occurs, and bilinear unloading/reloading when cracking/sliding due to shear or crushing occur. Moreover, it focuses on the nonlinear cyclic behavior of masonry and on improving the crack localization and hysteretic behavior of masonry structures. In order to validate its accuracy, the model is implemented in a FEM software and is used to simulate four unreinforced brick masonry walls, tested under cyclic, in-plane conditions. Subsequently, in Chapter 4, the numerical results are compared against the experimental results derived from the in-plane tests. The accuracy of the model is evaluated in terms of the envelope force-displacement curve, hysteretic response and energy dissipation, and in terms of crack patterns. It will be demonstrated that the developed model estimates well the base shear capacity of the walls and their post-peak behavior, whereas it predicts the correct failure mechanism and damage localization.

3.2 An orthotropic total-strain based crack model

The constitutive model presented in this chapter is based on a TSRC concept [112] and it incorporates a number of newly implemented characteristics to make its application more suitable for masonry structures. The rotating crack concept describes the constitutive behavior in terms of stress-strain relations in the rotating principal axes. Coaxiality between principal stresses and strains is achieved through a shear stiffness term [22]. A major advantage of rotating crack models over fixed crack models is that they eliminate the difficulty of choosing an appropriate shear retention factor, which can lead to unfavorable stress-locking in crack bands [177]. Moreover, they are usually relatively robust and easily comprehensible from an engineering point of view, since it is sufficient to describe the stress-strain relationships along the principal directions, and it is not required to deal with complicated concepts, such as return-mapping algorithms and corners in yield surfaces. The model is formulated in 2D plane stress, but extension to shell and 3D solid elements is possible.

As aforementioned, orthotropy is one of the main characteristics of masonry, being caused by the geometrical arrangement and the different material properties of its constituents. The developed model incorporates the orthotropic behavior through the different

elastic and inelastic material properties, which are used to describe the constitutive relationships along the two principal directions *i*. In order to define the principal directions *i*, first a distinction should be made between isotropic and anisotropic materials; in isotropic materials, during the elastic phase, the principal direction of the strains coincides with the principal direction of the stresses. On the contrary, for anisotropic materials the principal directions of the stresses and strains are generally not aligned, but it rather depends on the particular elastic properties.

In the presented constitutive model, the principal directions i refer initially to the directions of the principal strains. Coaxiality is ensured through the adopted constitutive relationships. Therefore, the general term principal direction is used consistently both for stresses and strains. The angles α_i are defined as the angles inscribed by the line parallel to the bed joints and the line parallel to the principal strains ε_i, where i=1,2 is the index of the principal direction (Figure 3.1). Due to the symmetric geometrical arrangement of brick masonry, it is sufficient to describe these angles within $-90^o \leq \alpha_i \leq 90^o$, as follows:

$$\alpha_1 = \begin{cases} \theta_1 & \text{if } |\theta_1 - \alpha_{1,0}| \leq 45^o \text{ or } |\theta_2 - \alpha_{2,0}| \leq 45^o \\ \theta_2 & \text{else} \end{cases} \tag{3.1}$$

$$\alpha_2 = \begin{cases} \theta_1 & \text{if } |\alpha_1| = \theta_2 \\ \theta_2 & \text{if } |\alpha_1| = \theta_1 \end{cases} \tag{3.2}$$

with $\theta_1 = 0.5 \arctan\left(\frac{\gamma_{xy}}{\varepsilon_{xx} - \varepsilon yy}\right)$ and $\theta_2 = \begin{cases} \theta_1 - 90^o & \text{if } \theta_1 \geq 0 \\ \theta_1 + 90^o & \text{if } \theta_1 < 0 \end{cases}$.

In the above equation, $\alpha_{i,0}$ refers to the angle in the principal direction i in the previous iteration step. Note that the angles θ_1, θ_2 relate to the directions of the principal strains too. In continuum mechanics there is the general convention that $\varepsilon_1 > \varepsilon_2$. However, here, since the model is orthotropic and focuses on the cyclic behavior of the material where both the loading history and direction matter, the convention that ε_1 (and σ_1) is bigger than ε_2 (and σ_2) is not adopted in the description of the principal stress-strain relationships. Instead, at the very first step of the numerical analysis the principal strains and stresses are defined based on this convention and in all following steps the angles α_1 and α_2 as defined in Equations 3.1 and 3.2 are used to calculate the principal strains ε_1 and ε_2 in a way that allows full cyclicity. The term $|\theta_i - \alpha_{i,0}| \leq 45^o$ ensures that there is a gradual rotation of the principal stresses/strains and that the correct material properties and cyclic behavior are assigned to each principal stress/strain component.

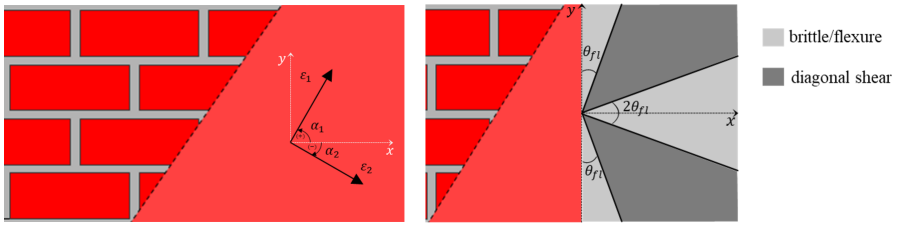

(a) (b)

Figure 3.1: Definition of principal directions and principal angles α_1 and α_2; (b) definition of threshold angle θ_{fl} and zones of assumed flexural and diagonal shear failure.

3.3 Material properties and orthotropy

In order to define the orthotropic behavior of masonry, the material properties alongside its axes should be defined first. To do so, experiments are carried out for the characterization of masonry in tension, compression and shear. Most authors (e.g., [47, 59, 178]) identify the compressive and tensile strengths and their corresponding fracture energies in the directions parallel and/or perpendicular to the bed joints. Additionally, the cohesion and the friction angle for loading parallel to the bed joints can be identified from shear tests [179]. Nevertheless, most experiments are limited to testing parallel to the mortar joints (especially to the head-joints) and there is a lack of mechanical data for loading in different directions. Given this lack of experimental data for different angles, the mechanical properties (with the exception of the tensile strength) are assumed to vary linearly with respect to the principal angles α_i.

Fifteen independent material parameters are required for the definition of the constitutive laws; these are properties defined by experiments carried out parallel to the bed joints (x direction) and head joints (y direction) and include: the Young's moduli ($E_{0,x}, E_{0,y}$), the shear modulus (G) the tensile strengths ($f_{t,x}, f_{t,y}$), the compressive strengths and their corresponding strains ($f_{c,x}, f_{c,y}, \varepsilon_{pc,x}, \varepsilon_{pc,y}$), as well as the fracture energies in tension ($G_{ft,x}, G_{ft,y}$), the fracture energies in compression ($G_{fc,x}, G_{fc,y}$), and finally the cohesion (c_0) and friction coefficient ($\tan\phi$) due to shear friction along the bed joint. The Young's moduli and the compressive strengths, strains and fracture energies can be identified through compression tests, whereas the tensile strength and tensile fracture energy are typically identified through bond wrench tests and/or four-point bending tests. Nevertheless, due to masonry's brittle failure in tension, it is not always easy to measure fracture energy in tension [180], in which case either representative values provided by guidelines [181] or derived by formulas [63], or finally values retrieved indirectly from bending tests (indirect tension) can be used. The shear modulus can be calculated either through the Young's modulus and Poisson's ratios that are measured from compression tests, or it can be directly estimated as a fraction of the Young's modulus (40% according to Eurocode 6-part 1 [182]). Finally, the initial cohesion and friction coefficient are usually defined through shear tests on triplets.

As aforementioned, the experimental data provides little information regarding the material properties of brick masonry under different loading directions. Page [178, 183, 184]

has contributed on this by testing the biaxial tensile and compressive strength properties of brick masonry under different angles. However, further information about the elastic and other inelastic properties along different angles is still scarce. Therefore, it is assumed that the Young's moduli (E_i) (Figure 3.2a), the compressive strain ($\varepsilon_{pc,i}$) corresponding to the compressive strength and the fracture energies in compression ($G_{fc,i}$) along the direction i vary linearly. For simplicity, linear variation is also assumed for the compressive strengths ($f_{c,i}$), although the information from the tests by Page suggests some nonlinear variation. Their definitions are given in Equations 3.3 to 3.6.

$$E_i = E_{0,x} + (E_{0,y} - E_{0,x})\frac{|\alpha_i|}{90^o} \tag{3.3}$$

$$f_{c,i} = f_{c,x} + (f_{c,y} - f_{c,x})\frac{|\alpha_i|}{90^o} \tag{3.4}$$

$$\varepsilon_{pc,i} = \varepsilon_{pc,x} + (\varepsilon_{pc,y} - \varepsilon_{pc,x})\frac{|\alpha_i|}{90^o} \tag{3.5}$$

$$G_{fc,i} = G_{fc,x} + (G_{fc,y} - G_{fc,x})\frac{|\alpha_i|}{90^o} \tag{3.6}$$

The tensile strength ($f_{t,i}$) along the principal direction i is defined such that it fits the pattern of experimental results obtained from [184] for uniaxial tensile loading (Figure 3.2b depicts the comparison between the provided experimental values and the mathematical formula adopted). The corresponding formulation is described by

$$f_{t,i} = f_{t,x} - (f_{t,x} - f_{t,y})\frac{|\alpha_i|}{90^o} + (f_{max} - 0.5(f_{t,x} + f_{t,y}))\sin(4|\alpha_i|) \tag{3.7}$$

where $f_{max} = \sqrt{f_{t,x}^2 + f_{t,y}^2}$.

Finally, once cracking occurs, the material properties are fixed. In essence, when cracking initiates in one of the two principal directions i, a new set of angles $\varepsilon_{crack,i}$ is defined and used in the following steps for the calculation of the material parameters; these are the angles inscribed by the principal tensile strains ε_i in the direction i and the direction parallel to the bed-joints at the onset of cracking. In the context of a TSRC model, the crack (and therefore also the crack plane) can still rotate (α_i changes), but the material properties will no longer change with this rotation (they are now calculated with $\alpha_{crack,i}$). This is a reasonable assumption, since a crack constitutes a weak plane, where future damage will probably localize and no stiffness or stress recovery will be expected.

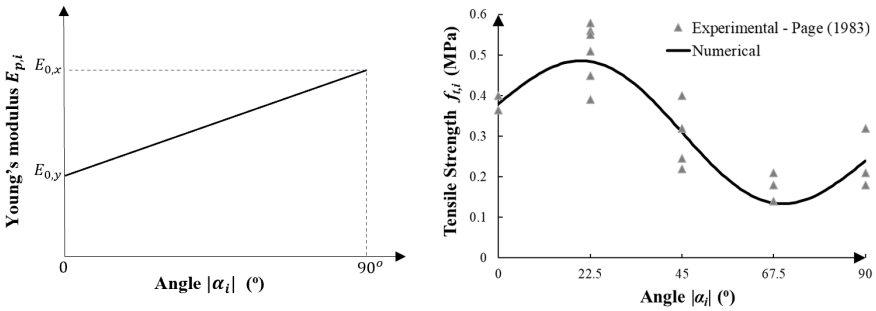

(a) (b)

Figure 3.2: Variation of (a) Young's modulus E_i and (b) tensile strength $f_{t,i}$ with respect to the principal angle α_i.

3.4 Tensile behavior

3.4.1 Envelope curve for tension

Masonry exhibits brittle failure in tension. Most researchers describe the tensile behavior with two branches: a linear pre-peak branch and a softening, post-peak branch, either linear or exponential. The softening rate is usually dependent on the fracture energy in tension, resulting in a more or less brittle failure depending on the value of the fracture energy.

In the current model, a linear ascending and a linear descending branch are used for the pre- and post-peak behavior, respectively. However, a distinction is made on the post-peak behavior (softening rate) based on the cracking angle $\alpha_{crack,i}$. In the case of cracking angles in close proximity to 90^o, horizontal cracks along the bed-joints are expected; this would correspond to bed-joint opening and in-plane flexural failure. Similarly, for $\alpha_{crack,i}$ close to 0^o degrees head-joint failure is expected. Finally, for angles around 45^o diagonal cracking is expected, which is associated to diagonal shear cracking. The post-peak behavior is therefore related to the type of in-plane failure expected: brittle/flexural failure of bed- or head-joints exhibits higher softening rate, whereas diagonal shear failure exhibits a slower softening rate. To distinguish between the two different behaviors a threshold angle (θ_{fl}) is defined to mark the transition from flexural to shear failure (Figure 3.1b). It should be noted that the definitions of the cracking and threshold angles are based on the assumption that the shear failure shows a locally ductile frictional behavior, a condition that is typically obtained when the bricks are sufficiently strong and the mortar is relatively weak, resulting in cracks forming alongside the mortar joints. By observations of the crack patterns presented in [62] for stretcher bond, reasonable values for the threshold angle could vary between 20^o to 30^o. Moreover, the brick pattern can give an indication of the angle of the expected diagonal crack and by considering a reasonable percentage of variation around it (in the case that some cracks might go through the bricks or skip a head joint and pass through the next), a threshold angle can be chosen. The tensile behavior is depicted in Figure 3a and is formulated as:

$$\sigma_i = \begin{cases} E_i \varepsilon_i & \text{for } \varepsilon_{cr,i} \geq \varepsilon_i \geq 0 \\ max(f_{t,i}; \sigma_{un}) \left[1 - \frac{\varepsilon_i - \varepsilon_{cr,i}}{\varepsilon_{ult,i} - \varepsilon_{cr,i}}\right] & \text{for } \varepsilon_{ult,i} \geq \varepsilon_i \geq \varepsilon_{cr,i} \\ E_{res,i} \varepsilon_i & \text{for } \varepsilon_i > \varepsilon_{ult,i} \end{cases} \tag{3.8}$$

where

$$\varepsilon_{ult,i} = \begin{cases} min\left(\frac{f_{t,i}}{\beta_i} + \varepsilon_{cr,i}; 100\varepsilon_{ult,k}\right) & \text{for } \theta_{fl} \geq \left|\alpha_{crack,i}\right| \geq 0 \\ 100\varepsilon_{ult,k} & \text{for } 90^o - \theta_{fl} > \left|\alpha_{crack,i}\right| > \theta_{fl} \\ min\left(\frac{f_{t,i}}{\beta_i} + \varepsilon_{cr,i}; 100\varepsilon_{ult,k}\right) & \text{for } 90^o - \geq \left|\alpha_{crack,i}\right| > 90^o - \theta_{fl} \end{cases} \tag{3.9}$$

In the above equations $\varepsilon_{cr,i}$ are the cracking strains in direction i, given by $\varepsilon_{cr,i} = f_{t,i}/E_i$, whereas $\varepsilon_{ult,k}$ correspond to the ultimate strains along the global direction $k = x, y$, which are expressed as

$$\varepsilon_{ult,k} = \frac{2G_{ft,k}}{f_{t,k} h} \tag{3.10}$$

with $k = x$ when $i = 1$ and $k = y$ when $i = 2$, and h is the crack/crush bandwidth. The softening rate β_i is given by:

$$\beta_i = \begin{cases} \frac{\beta_x \left(\left|\alpha_{crack,i}\right| - \theta_{fl}\right)^2}{\theta_{fl}^2} & \text{for } \theta_{fl} \geq \left|\alpha_{crack,i}\right| \geq 0^o \\ \beta_y \sin\left(4.5\left(\left|\alpha_{crack,i}\right| - (90^o - \theta_{fl})\right)\right) & \text{for } 90^o \geq \left|\alpha_{crack,i}\right| \geq 90^o - \theta_{fl} \end{cases} \tag{3.11}$$

where β_x and β_y are the softening rates for stresses parallel to the x and y directions and are given by:

$$\beta_i = \frac{f_{t,k}}{\varepsilon_{ult,k} - \frac{f_{t,k}}{E_k}} \tag{3.12}$$

Finally, σ_{un} is a stress value that resembles the shear capacity and it is given by Equation 3.13.

$$\sigma_{un} = \begin{cases} \max\left[\omega c_0 - \tan\phi(\sigma_{yy,0} + E_{0,y}\delta\varepsilon_{yy}); \omega c_0\right] & \text{for } 90^o - \theta_{fl} > \left|\alpha_{crack,i}\right| > \theta_{fl} \\ \omega c_0 & \text{else} \end{cases} \tag{3.13}$$

where: $\sigma_{yy,0}$ is the stress normal to the bed joints at the beginning of the step, $\delta\varepsilon_{yy}$ is the incremental strain normal to the bed joint, and ω is a damage factor ranging from 0 and 1, with 0 and 1 referring to a fully cracked and uncracked integration point respectively. It is expressed as $\omega = \max(\omega_1, \omega_2)$, with

$$\omega_i = \min\left[1; \max\left(0; \frac{\varepsilon_{ult,i} - \varepsilon_i}{\varepsilon_{ult,i} - \varepsilon cr, i}\right)\right] \tag{3.14}$$

3.4.2 Unloading/reloading behavior for tension

Even though no experiments exist for the cyclic behavior of masonry subjected to direct tension, from tests on walls it has been observed that the total dissipated energy is higher when the failure mode is governed by shear and smaller when it is governed by flexure [42]. Based on this observation, a distinction is made on the unloading/reloading behavior of masonry subjected to tension, depending on the crack direction (flexural or shear crack). When diagonal shear failure is expected, i.e. for $\theta_{fl} \leq |\alpha_{crack,i}| \leq 90^o - \theta_{fl}$, bilinear unloading/reloading is adopted with elastic stiffness E_i until the critical stress limit σ_{un} (Equation 3.13), which defines the second unloading/reloading branch (Figure 3.3a, is reached. This results in permanent deformations, as often observed in step-wise diagonal cracks. On the other hand, for angles outside this range, corresponding to in-plane flexural failure, secant unloading is adopted (Figure 3.3a).

3.5 Compressive behavior

3.5.1 Envelope curve for compression

The compressive behavior of masonry is described through three curves as formulated in Equation 3.15.

$$\sigma_i = \begin{cases} E_i \varepsilon_i [1 - \frac{1}{n_i} (\frac{\varepsilon_i}{\varepsilon_{pc,i}})^{n_i - 1}] & \text{for } 0 \geq \varepsilon_i \geq \varepsilon_{pc,i} \\ \min[f_{c,i}[1 - (\frac{\varepsilon_i - \varepsilon_{pc,i}}{\varepsilon_{ulc,i} - \varepsilon_{pc,i}})^2]; 0.1 f_{c,i}] & \text{for } \varepsilon_{pc,i} \geq \varepsilon_i \geq \varepsilon_{ulc,i} \\ 0.1 f_{c,i} & \text{for } \varepsilon_i \leq \varepsilon_{ulc,i} \end{cases} \tag{3.15}$$

where σ_i and ε_i are the stress and strain along the principal direction i, respectively, and $n_i = E_i/(E_i - E_{sec})$, with $E_{sec} = f_{c,i}/\varepsilon_{pc,i}$. Knowing that the area under the envelope is equal to $g_{fc,i} = G_{fc,i}/h$, where h is the crack/crush bandwidth that depends on the particular finite element configuration (e.g., [185–188]), inserted to achieve mesh-size objectivity. The ultimate strain in compression $\varepsilon_{ulc,i}$ is calculated as

$$\varepsilon_{ulc,i} = \min \left[\varepsilon_{pc,i} + \frac{3}{2 f_{c,i}} \left(g_{fc,i} - E_i \left(0.5 - \frac{1}{n_i (n_i + 1)} \right) \varepsilon_{pc,i}^2 \right); 1.2 \varepsilon_{pc,i} \right] \tag{3.16}$$

For the pre-peak curve the model proposed by [189] for concrete is used, whereas for the post-peak curve a parabolic curve adopted from [54] is selected. Finally, once the compressive fracture energy is consumed, a residual strength of $0.1 f_{c,i}$ is adopted to avoid numerical instabilities. The envelope curve is depicted in Figure 3.3b.

3.5.2 Unloading/reloading behavior for compression

Experimental research on the behavior of masonry subjected to cyclic compression [26, 48, 50, 51, 57] has shown that the material behaves nonlinearly, with accumulation of non-reversible strains and stiffness degradation. The unloading and reloading branches follow different paths and the reloading stiffness decreases with every new cycle during the post-peak response. Nevertheless, in this model no distinction is made between the unloading and reloading branch. Similar to unloading in tension for diagonal shear cracking, bilinear unloading is adopted with initial stiffness equal to the elastic Young's modulus E_i until the critical value σ_{un} is reached, which defines the upper limit of the second branch, as depicted

in Figure 3.3b and Figure 3.6. In the case of reloading, first, linear elastic stiffness is assumed until the lower limit $\sigma_{fc,i}$ (the stress that corresponds to the minimum compressive strain ever reached during the loading history) is reached, where ideal plastic behavior is adopted. This assumption differs from the cyclic behavior in pure compression. However, since the rotating principal behavior aims to capture indirectly also the shear behavior, the elastic unloading/reloading branch turns out to better represent the overall cyclic behavior, which is of crucial importance in the global hysteretic behavior of masonry walls. This will be explained further in section 3.7 and in the description of the validation examples (Chapter 4).

3.5.3 Reduction of compressive strength with lateral cracking

Similar to concrete, it is assumed that tensile cracks parallel to a compressive strut reduce the compressive strength capacity of that strut [16, 190]. The presented model adopts the reduction model proposed by [191] for concrete. Hence, the compressive strength is reduced after cracking as:

$$f_{c,i} = \min\left(\frac{1}{1+K_{c,i}} f_{c,i}; 0.1 f_{c,i}\right) \tag{3.17}$$

where

$$K_{c,i} = \min\left(0.27\left(\frac{\alpha_{t,j}}{|\varepsilon_{pc,i}|} - 0.37\right); 1\right) \geq 0 \tag{3.18}$$

with $\alpha_{t,j}$ representing the maximum tensile strain reached during the loading history in the direction j perpendicular to i. To simplify, for $i = 1, j = 2$ and for $i = 2, j = 1$. At the same time, no increase in the compressive strength due to biaxial compression is considered, i.e., tension-compression behavior is accounted for but biaxial compression is not.

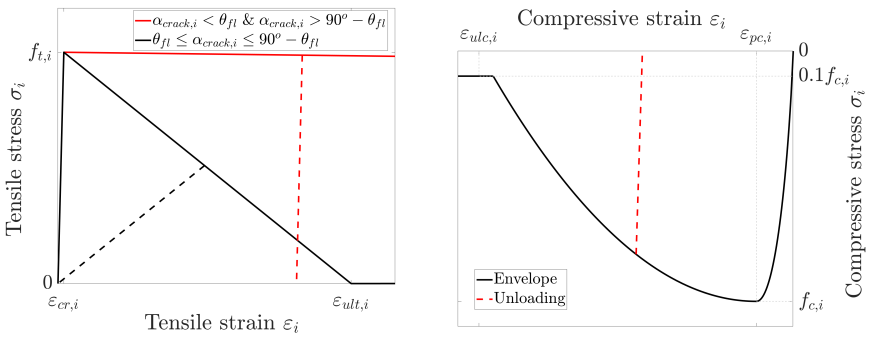

Figure 3.3: (a) Tensile behavior of masonry for the two different types of cracks: steep softening with secant unloading in case of flexural cracking ($\theta_{fl} > |\alpha_{crack,i}|$ and $90^o - \theta_{fl} < |\alpha_{crack,i}|$) and softening with elastic (linear) unloading in case of diagonal shear cracking ($\theta_{fl} \leq |\alpha_{crack,i}| \leq 90^o - \theta_{fl}$); (b) compressive behavior of masonry.

3.6 Indirect inclusion of shear behavior

Many authors have investigated the shear behavior of masonry and concluded that the shear capacity of brick masonry subjected to confinement/compression can be described by Coulomb friction [60, 62, 179]. Some have also highlighted the importance of dilatancy [97, 192]. In damage mechanics and plasticity models, the shear capacity is introduced through the damage or yield surfaces, respectively. However, in smeared crack models there are different ways to describe shear. In fixed smeared crack models the shear capacity along the plane of the fixed crack is explicitly taken into account via a shear retention factor (or function) along that crack plane. Although shear retention can describe aggregate interlock in concrete, it may lead to stress-locking when the crack bands propagate through the mesh in a zig-zag manner [193]. Rotating smeared crack models describe the behavior in the continuously rotating principal direction and, hence, do not explicitly describe shear. However, an implicit shear term is required to guarantee coaxiality between principal stresses and strains [16]. For masonry, the shear behavior along the bed-joints is important and should be considered in the description of the constitutive equations. Ignoring the shear behavior of masonry may lead to overestimation of the structure's base shear capacity (e.g. [21]).

This model introduces the shear capacity via an internal iterative process that ensures that the shear stress τ_{xy} does not exceed the shear capacity $\tau_{\max}(|\tau_{xy}| \leq \tau_{\max})$. This process is indirect: the shear stress τ_{xy} is not described through a total stress-strain relationship. Instead, only the shear stress in the direction of the mortar-joints (which coincide with the global x-y-directions) is limited based on a Coulomb-friction criterion. In order to do so, first the stresses in the global x- and y- coordinates ($\sigma_{xx}, \sigma_{yy}, \tau_{xy}$) are calculated through Equation 3.19. Once the global stresses are known, the shear capacity $\tau_{\max}$ is derived according to Equation 3.21. If the absolute value of the shear stress ($|\tau_{xy}|$) is lower than $\tau_{\max}$ no further action is required; the shear strength computed at the integration point is sufficient to withstand the shear stress τ_{xy}. However, if $|\tau_{xy}|$ exceeds the shear capacity, shear sliding occurs and the shear stress needs to be limited to $|\tau'_{xy}| = \tau_{\max}$. The new global stress σ'_{xx} is calculated via Equation 3.22, with the assumptions that the vertical confinement level (σ_{yy}) does not change, and that coaxiality between principal stresses and strains is maintained. A graphical representation through Mohr's circle is given in Figure 3.4.

$$\begin{Bmatrix} \sigma_{xx} \\ \sigma_{yy} \\ \tau_{xy} \end{Bmatrix} = \left[T_\sigma\right]^{-1} \begin{Bmatrix} \sigma_1 \\ \sigma_2 \\ 0 \end{Bmatrix} \tag{3.19}$$

$$\left[T_\sigma\right]^{-1} = \begin{bmatrix} \cos^2\alpha_1 & \sin^2\alpha_1 & -2\cos\alpha_1\sin\alpha_1 \\ \sin^2\alpha_1 & \cos^2\alpha_1 & 2\cos\alpha_1\sin\alpha_1 \\ \cos\alpha_1\sin\alpha_1 & -\cos\alpha_1\sin\alpha_1 & \cos^2\alpha_1 - \sin^2\alpha_1 \end{bmatrix} \tag{3.20}$$

$$\tau_{\max} = \max[c_0 - \sigma_{yy}\tan\phi; c_0] \tag{3.21}$$

$$\tan 2\alpha_1 = \frac{2|\tau'_{xy}|}{\sigma'_{xx} - \sigma_{yy}} \tag{3.22}$$

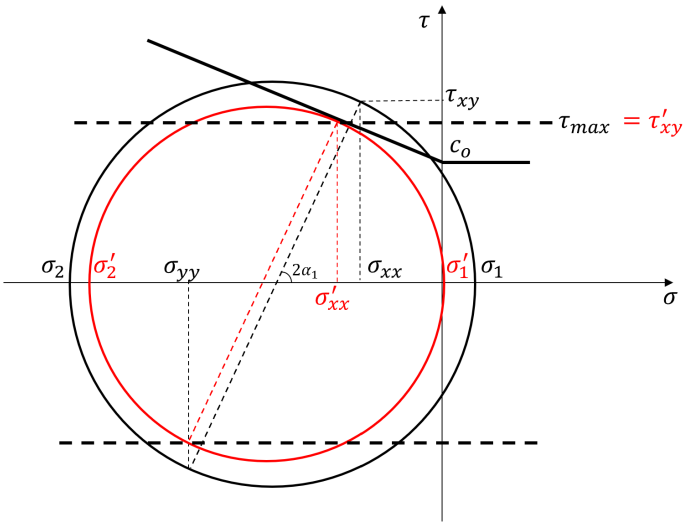

Figure 3.4: Representation of Mohr circle and recalculation of shear stress τ'_{xy}, normal stress (σ'_{xx}) and principal stresses (σ'_1, σ'_2) in the case of shear failure $|\tau_{xy}| > \tau_{\max}$.

Consequently, due to the new set of global stresses ($\sigma'_{xx}, \sigma_{yy}, \tau'_{xy}$), the principal stresses (σ'_1, σ'_2) across the directions α_i need to be recalculated, with the inverse procedure of Equation 3.19. If the new principal stresses (σ'_1, σ'_2) are within the limits set by the envelope for the corresponding principal strains, the shear calculation is completed. However, in the case that one or both of them exceed their corresponding limit, they need to be further reduced. These limits are given by the following equation:

$$\begin{aligned} \sigma_{un} \leq \sigma'_i \leq \sigma_{ft,i} \text{ if } \varepsilon_i \geq 0 \\ \sigma_{fc,i} \leq \sigma'_i \leq \sigma_{un} \text{ if } \varepsilon_i < 0 \end{aligned} \tag{3.23}$$

where $\sigma_{ft,i}$ and $\sigma_{fc,i}$ are the stresses that correspond to the maximum and minimum strain ε_i ever reached during the loading history of the integration point, whereas σ_{un} is the stress value defined in Equation 3.13. The calculation of the new principal stresses is followed by the reevaluation of the global stresses and the check of the shear capacity anew. This procedure is repeated until either all the abovementioned conditions are met or, in the case the conditions cannot be satisfied simultaneously, until a maximum number of 500 iterations is reached. In the latter case, priority is given in maintaining coaxiality and satisfying the criteria of Equation 3.23, resulting therefore in a final shear stress τ_{xy} that may still exceed the shear capacity. The number of maximum iterations was selected after performing a sensitivity study between 50, 100 and 500 iterations, as the latter resulted in the most satisfactory numerical results in terms of numerical stability and damage localization without compromising significantly the computational time. For a graphical representation, one can refer to the flowchart of Figure 3.5. Please note that x and y refer to the directions parallel to bed- and head-joint, respectively; so the model, though it formulates the behavior

in the rotating principal directions, assesses the shear capacity along the predefined joint directions. In other words, the model does not check the shear stresses along the principal directions (their value being null by definition) or in the direction corresponding to the crack initiation (as in existing fixed-crack models), but it rather limits the value of the shear stresses in the predefined x-y (bed joint/head-joint) directions, based on a Coulomb friction formulation. This addresses the specific characteristics of masonry as compared to concrete.

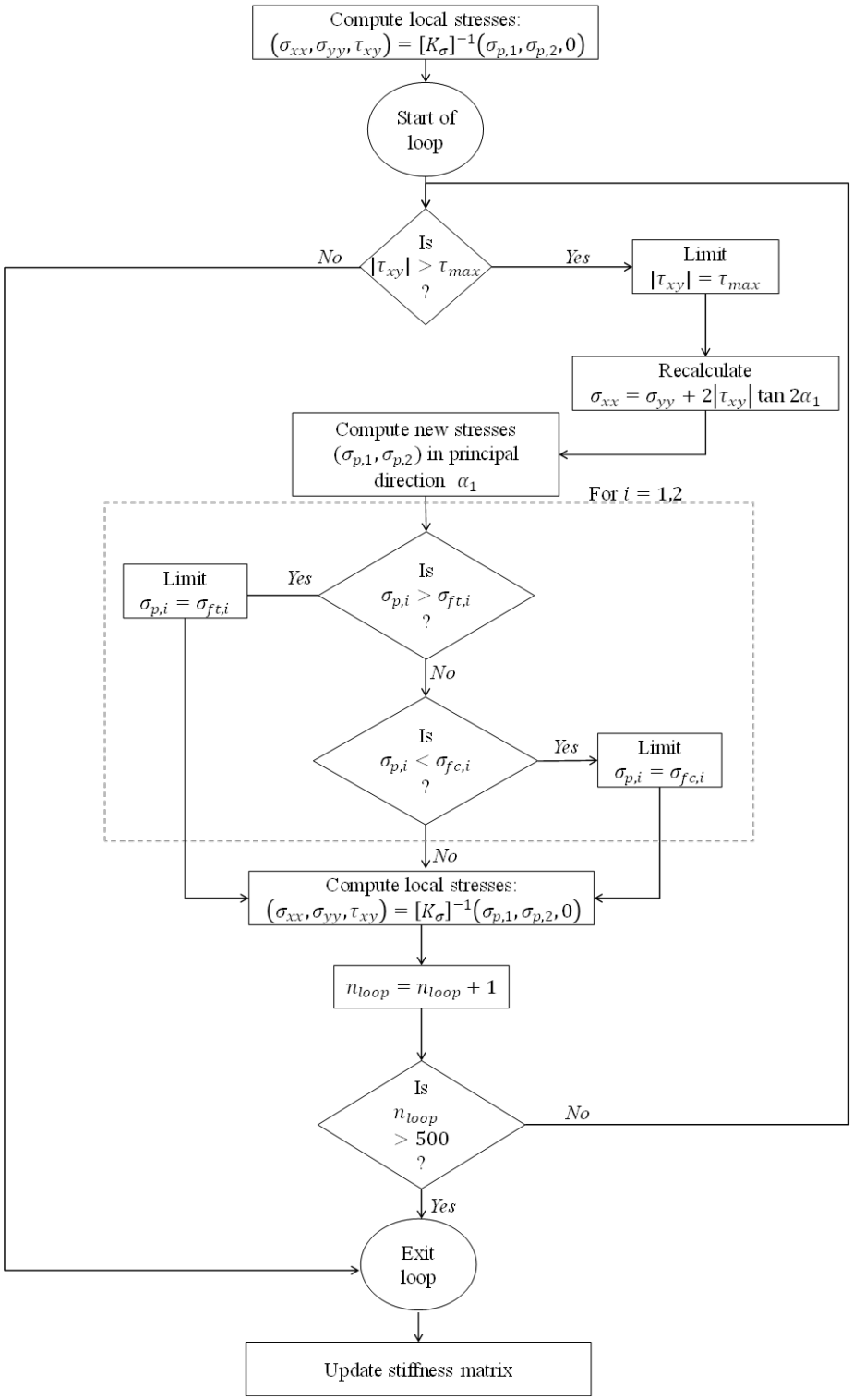

Figure 3.5: Flowchart of internal iterative loop for shear stress limitation.

3.7 Overall cyclic behavior

As mentioned before, linear unloading with elastic stiffness E_i is adopted in compression. In tension two unloading/reloading possibilities are included in the model: when the cracking angle corresponds to a diagonal crack ($90^o - \theta_{fl} \geq |\alpha_{crack,i}| \geq \theta_{fl}$), the unloading/reloading behavior in tension is assumed to be elastic (linear); when the cracking angle relates to a flexural crack, secant unloadingreloading is adopted. Moreover, an upper and lower limit are set when unloading (or reloading) from compression (to tension) and from tension (to compression), respectively. This is the limit $\sigma_u n$ which was defined already in Equation 3.13. In contrast to damage and fracture models, which generally adopt secant unloading and reloading, and often underestimate the dissipated energy, this model allows to increase the dissipated energy, especially when failure is governed by shear. A depiction of the integrated cyclic behavior for compression and tension, including the two options for the types of tensile cracks, is presented in Figure 3.6.

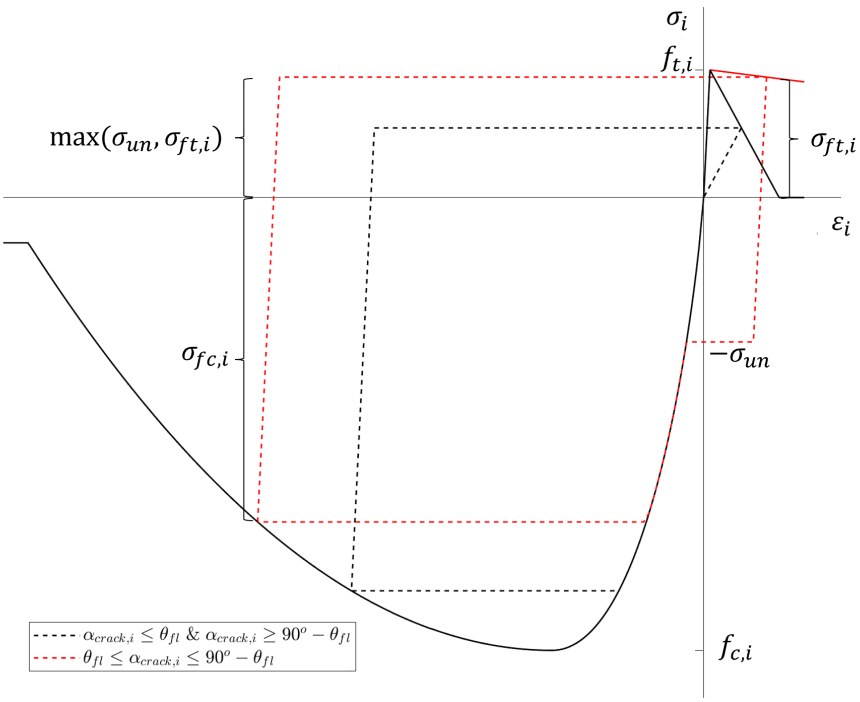

Figure 3.6: Cyclic behavior of masonry as adopted in the presented model. The dashed red lines refer to the unloading when shear cracks are expected, whereas the dashed black lines refer to unloading when flexural cracks are expected. Here it is assumed that the σ_{un} is constant (which means that the vertical compressive stress σ_{yy} remains constant).

3.8 Summary

In this chapter, a new plane-stress orthotropic continuum constitutive model for in-plane behavior of masonry structures was developed and presented. The model is based on a total-strain formulation, assuming coaxiality of stresses and strains (rotating crack model). It includes failures in tension, compression, and, indirectly, shear. The post-peak and the unloading/reloading behaviors for tension depend on the principal strain orientation at the onset of cracking. Brittle failure with steep softening is assumed for angles that correspond to in-plane flexural failure, whereas ductile behavior with softening is assumed for angles that correspond to diagonal shear failure. Reduction of the compressive strength due to lateral cracking is adopted, but the increase of the compressive strength due to lateral compression is not accounted for. Additionally, the shear failure is included through a shear-limitation algorithm that limits the stresses based on a Coulomb friction criterion, while maintaining coaxiality between principal stresses and strains and assuming that the confining vertical stress, normal to the bed-joints, remains unchanged. Fifteen input material parameters are required to define the constitutive equations, derived from standard tests performed perpendicularly and in-parallel to the bed joints.

4

Verification of constitutive model against experimental results

In chapter 3, the developed material model was presented and its assumptions and constitutive equations were discussed. In this chapter, the proposed model will be validated against experimental results, derived by quasi-static tests on in-plane masonry walls. Five different walls are simulated, each one having different geometrical and material properties, boundary and loading conditions, and/or different failure mechanism. The numerical results match satisfactorily the experimental outcomes, estimating with good accuracy the maximum base shear load, the post-peak behavior and the damage localization of each wall. Moreover, the model's sensitivity to the mesh selection is discussed and suggestions are given about the size and type of finite elements to be used to obtain more accurate results.[1]

4.1 Introduction

In order to assess the applicability and validity of the developed constitutive model, the constitutive equations derived and presented in Chapter 3 were inserted in a FORTRAN subroutine and subsequently implemented in the finite element software DIANA FEA, version 10.4. Four walls, tested in the past under cyclic in-plane loading, are modelled; each one differs from the others either in aspect ratio, axial load, boundary conditions or material properties. Two of the modelled walls were tested under cyclic quasi-static conditions at the Joint Research Centre of the European Community in Ispra; these double-wythe walls comprised solid clay bricks and had an aspect ratio of 2 (high wall referred as HIGSTA here) and 1.35 (low wall referred as LOWSTA here) [194, 195]. The vertical precompression level was 0.6 MPa. The remaining two walls, named TUD-COMP-4 and TUD-COMP-6, were built and tested at Delft University of Technology in 2015 [42]; they

[1] Similar to Chapter 3, Chapter 4 is also adapted from the paper: "Sousamli, M., Messali, F., & Rots, J. G. (2022). A total-strain based orthotropic continuum model for the cyclic nonlinear behavior of unreinforced brick masonry structures. International Journal for Numerical Methods in Engineering, 123(8)".

were both single-wythe Calcium Silicate (CS) brick walls with a low aspect ratio of 0.7, and a vertical precompression of 0.5 MPa. Also the boundary conditions at the top varied amongst these benchmark tests; the two Ispra-walls and TUD-COMP-4 were clamped at top and bottom (double clamped), while TUD-COMP-6 was clamped only at the bottom (cantilever). However, for all the walls the top side was allowed to move vertically so that the precompression level would remain constant. The walls exhibited different failure mechanisms: in-plane flexural failure (rocking), diagonal shear failure, and a combination of diagonal shear failure and crushing/splitting. The geometrical properties and failure mechanisms of the walls are presented in Table 4.1.

The material properties adopted are presented in Table 4.2. These properties were obtained by companion material tests that were carried out at the same time period and from the same batch of materials as the large wall tests [42, 196, 197]. For some properties no data from companion tests was available. In that case, representative values were chosen based on literature. Specifically, this related to the fracture energies in tension, where values between 0.005 and 0.02 N/mm were chosen based on the formula $G_{ft,i} = 0.025(2f_{t,i})^{0.7}$. Moreover, for walls LOWSTA and HIGSTA, the same Young's modulus and compressive strength were adopted in both directions, and a reduced tensile strength was applied perpendicular to the bed joints. Finally, the threshold angle θ_{fl} was set to 20^o.

Table 4.1: Geometrical properties and failure mechanisms of the in-plane wall experiments used for validation

Specimen name	Dimensions $l_w \cdot h_w \cdot t_w$ [m]	Vertical pre-compression [MPa]	Boundary Condition	Failure mechanism
LOWSTA	$1.0 \cdot 1.35 \cdot 0.250$	0.60	Double clamped	Diagonal shear
HIGSTA	$1.0 \cdot 2.00 \cdot 0.250$	0.60	Double clamped	Flexure/rocking
TUD-COMP-4	$4.0 \cdot 2.76 \cdot 0.102$	0.50	Double clamped	Diagonal shear
TUD-COMP-6	$4.0 \cdot 2.76 \cdot 0.102$	0.50	Cantilever	Diagonal shear and crushing

All of the presented numerical models adopted 3x3 Gaussian integrated 8-noded quadratic, quadrilateral plane-stress elements with average dimensions of 100mm x 100mm. The Quasi-Newton (Secant) method was selected as the incremental-iterative solution procedure, and either the force or the displacement convergence norm needed to be satisfied, with a tolerance of 0.01. The analyses were permitted to continue in case the convergence criteria were not satisfied, in which case the relevance of the numerical results was examined.

Table 4.3 gives a comparison between the experimental and numerical results in terms of base shear capacity and corresponding displacement at peak, residual shear capacity and its corresponding displacement post-peak, i.e. softening degradation, and energy dissipation for the four walls. The comparison of these key characteristics is subsequently elaborated and discussed in Sections 4.2-4.5.

Table 4.2: Masonry material properties adopted for the continuum numerical models (For the LOWSTA and HIGSTA walls, the corrected values of joint cohesion and friction coefficient, as calculated in [195], are used); unknown and thus assumed material properties are represented in italics, while the other properties were based on the companion material tests

Material properties used in the numerical analyses			TUD-COMP-4 & TUD-COMP-6		LOWSTA & HIGSTA	
			horizontal direction $i = x$	vertical direction $i = y$	horizontal direction $i = x$	vertical direction $i = y$
Modulus of elasticity	E_i	$[MPa]$	3583	5091	1491	1491
Shear Modulus	G	$[MPa]$	1571		1571	
Threshold angle	θ_{fl}	$[^o]$	20		20	
Tensile strength	$f_{t,i}$	$[MPa]$	0.21	0.14	0.10	0.04
Compressive strength	$f_{c,i}$	$[MPa]$	7.55	5.93	6.20	6.20
Compressive strain at peak strength	$\varepsilon_{pc,i}$	$[-]$	*0.01*	*0.01*	*0.01*	*0.01*
Fracture energy in tension	$G_{ft,i}$	$[N/mm]$	*0.02*	*0.012*	*0.01*	*0.005*
Fracture energy in compression	$G_{fc,i}$	$[N/mm]$	43.4	31.3	40.0	40.0
Cohesion	c_0	$[MPa]$	0.14		0.17	
Friction coefficient	$tan\phi$	$[-]$	0.43		0.43	
Density	ρ	$[T/mm^3]$	$1.805 \cdot 10^{-9}$		$1.805 \cdot 10^{-9}$	

Table 4.3: Base shear capacity F_{peak} and its corresponding displacement at peak δ_{peak}, residual base shear F_{res} at the ultimate displacement and total dissipated energy U for the experimental and numerical results of the modelled walls.

Walls	Experimental				Numerical			
	F_{peak} [kN]	δ_{peak} [mm]	F_{red} [kN]	U [10^2 kNmm]	F_{peak} [kN]	δ_{peak} [mm]	F_{red} [kN]	U [10^2 kNmm]
LOWSTA	+81.0	+2.8	+48.4	22.9	+78.2	+2.9	+67.6	20.4
	-83.7	-2.7	-59.0		-78.8	-2.8	-61.2	
HIGSTA	+71.7	+12.5	+67.8	12.9	+77.3	+8.2	+75.0	22.5
	-71.9	-12.0	-71.0		-78.4	-9.1	-74.6	
TUD-COMP-4	+119.1	+2.6	+97.6	55.1	+118.6	+0.9	+70.0	20.6
	-123.4	-0.3	-108.5		-116.2	-1.4	-93.0	
TUD-COMP-6	+109.8	+4.3	+68.1	187.4	+101.5	+1.6	+53.5	157.5
	-109.0	-4.2	-65.6		-104.1	-2.3	-56.1	

4.2 Low wall specimen LOWSTA

The low wall LOWSTA was a double clamped wall, with an aspect ratio of 1.35 and a precompression load of 0.6 MPa. It exhibited brittle failure with diagonal shear cracking. The maximum experimental base shear was 81 kN, whereas the minimum base shear was -83.7 kN. After diagonal cracking, the residual post-peak base shear was measured to be

48.4 kN (-40% reduction) and -59 kN (-57% reduction) for the positive and negative loading direction respectively.

The numerical strength capacity was estimated to be 78.2 kN (3.5% underestimation) and -78.8 kN (5.8% underestimation). The residual post-peak strength of this wall was overestimated with the current numerical model: the remaining strength capacity was 67.6 kN in the positive and -61.2 kN in the negative direction, overestimating the experimental residual base shear by 39% and 3%, respectively. The hysteresis response obtained from the numerical analysis well reproduces the experimental curve (Figure 4.2a). Small dissipation is observed in the pre-peak phase, for top displacements up to 1.5 mm, whereas the increased energy dissipation is clearly visible for the post-peak cycles. The agreement with the experiment is attributed to the inclusion of energy dissipation in the material model through the bilinear unloading/reloading for compression and tension (when shear cracks form). The dissipated energy (area inscribed by the force-displacement hysteretic loops) of the numerical model was 10.7% smaller than the experimental one (Table 4.3), but this is within reasonable accuracy. A model with fully secant unloading/reloading would miss this aspect. As already mentioned, the cyclic behavior of masonry has not received much attention and many constitutive models for masonry have only been tested for monotonic loading. The numerical curves show some small oscillatory irregularities, which are related to local temporary loss of convergence, as will be explained in Section 4.6.1.

The damage localization of the numerical model and the experiment were in agreement, with both of them showing initially horizontal cracks at the corners, and diagonal cracks extending from the corners towards the center of the wall, where they intersected. Subsequently, the two sets of diagonal cracks were connected by a vertical crack (or a slightly inclined crack in the case of the numerical model). A difference was observed regarding the angle of cracks between the experiment and the numerical model. However, this is to be expected in a macro-model, where the brick pattern is not described and where the mesh size and orientation can influence the results. In this research a fixed size (100 x 100 mm) and order (3 x 3) of mesh was chosen for all examined walls, which may be considered rather coarse for this particular wall. A small study on mesh sensitivity regarding the order and size of mesh will be discussed in Section 4.6.3.

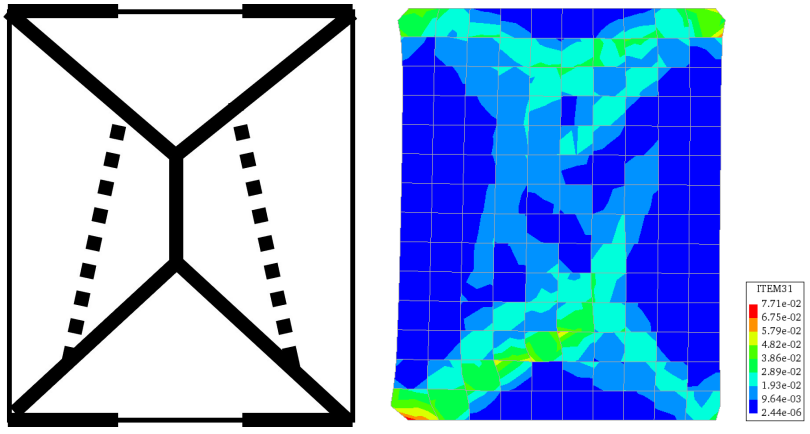

(a) (b)

Figure 4.1: Comparison of (a) experimental crack pattern, and (b) maximum tensile strain ever reached during the loading history, depicted at the end of the numerical analysis, for the wall LOWSTA.

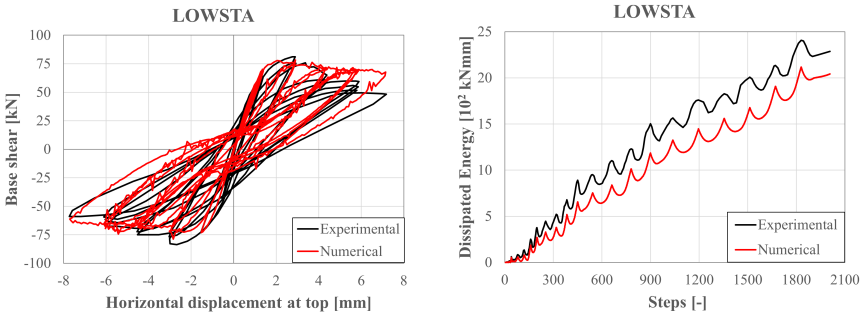

(a) (b)

Figure 4.2: Comparison of experimental (black) and numerical (red) results of (a) hysteretic response (base shear vs displacement) and (b) energy dissipation of shear wall LOWSTA.

4.3 High wall specimen HIGSTA

The high wall HIGSTA had an aspect ratio of 2 and a precompression load of 0.6 MPa. It exhibited flexural behavior with rocking and minimal strength degradation. The maximum and minimum experimental base shear were 71.7 kN and -71.9 kN, respectively. The residual post-peak base shear was only 3.4% and 0.9% smaller than the maximum base shear in the positive and negative direction, respectively.

The numerical model overestimated the base shear capacity, with a maximum capacity of 77.3 kN (7.6% overestimation) and a minimum of -78.4 kN (9% overestimation). This is the only numerical model that overestimated the corresponding experimental capacity. Similarly to the experiment, minimal softening was observed with residual values of 75 kN and -76.4 kN. Again, the model appears to be able to reproduce properly the cyclic behavior,

as compared to other models that either start from secant or elastic unloading/reloading curves (e.g.; [21]). The energy dissipation in the early cycles is close to that of the experiment, while for the last two repetitions an overestimation was observed. The total energy dissipation (Table 4.3 and Figure 4.4b 10b) was overestimated, with the majority of the energy (61%) being released during the last two repetitions. However, the overestimation of the capacity and energy dissipation can be considered within acceptable limits. The overestimation of the energy dissipation was likely caused by the small diagonal shear cracks that developed during the last two loading cycles and their corresponding state of compressive and tensile stresses.

The failure mechanism was rocking, with flexural cracks forming at the top and bottom layers of the wall, both for the experiment and the numerical model. In the case of the numerical model, it seems that some diagonal cracks also started forming at the top and bottom towards the center of the wall. This was not reported after the particular quasi-static experiment. Nevertheless, when the wall was tested again for a higher precompression load of 0.8 MPa, diagonal cracks also formed in the experiment, extending from the corners towards the center of the wall [194]. This indicates that the occurrence of the diagonal cracking mode is close to the occurrence of crack/crush rocking mode, especially when the precompression load increases. In that case softening and higher energy dissipation is observed post-peak as the energy consumption for local constitutive shear and compression cycles is much higher than for tension cycles.

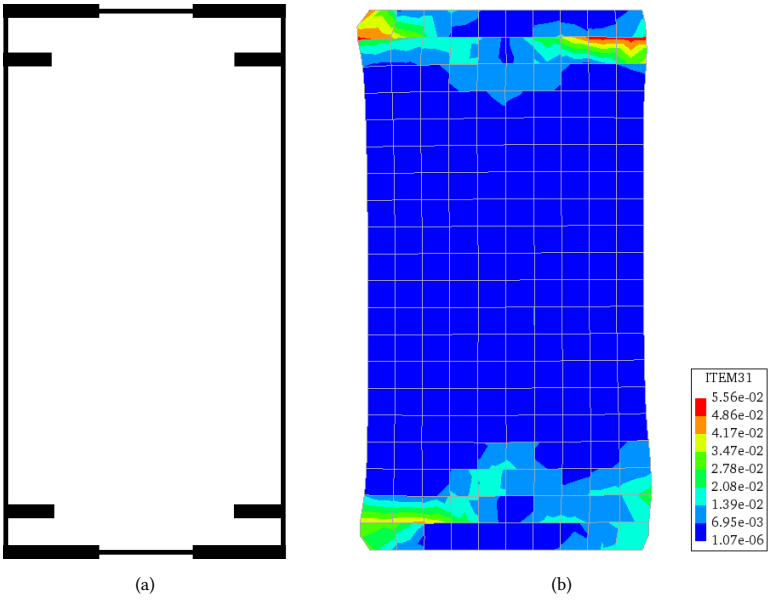

Figure 4.3: Comparison of (a) experimental crack pattern, and (b) maximum tensile strain ever reached during the loading history, depicted at the end of the numerical analysis, for the wall HIGSTA.

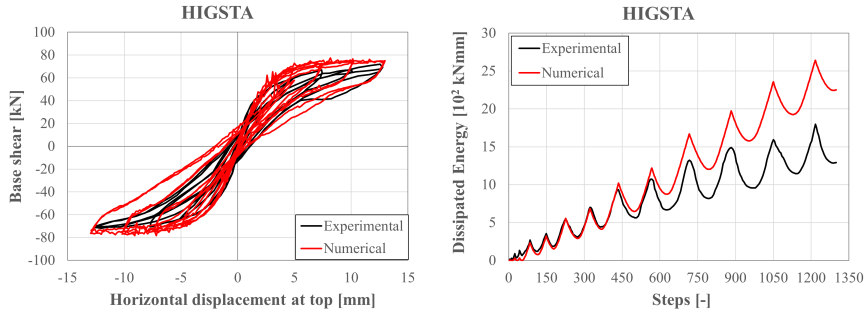

(a) (b)

Figure 4.4: Comparison of experimental (black) and numerical (red) results of (a) hysteretic response (base shear vs displacement) and (b) energy dissipation of slender wall HIGSTA.

4

4.4 Squat wall TUD-COMP-4

Specimen TUD-COMP-4 was a double-clamped squat calcium-silicate brick wall (aspect ratio of 0.7) with a vertical precompression load of 0.5MPa. Brittle shear failure was observed, with diagonal cracks running through the mortar joints approximately along the diagonal of the wall, initially formed at the center of the wall and then expanding towards the corners. In the positive direction the maximum shear force was 119.1 kN; in the negative direction the minimum shear force is slightly higher and equal to -123.4 kN. The wall reached an ultimate displacement of 5.39 mm (0.2% drift) in the positive and -5.35 mm (-0.19% drift) in the negative loading direction at the corresponding shear capacities of 97.6 kN (-18% post-peak reduction) and -108.5 kN (-12% post-peak reduction), respectively. Due to the pure shear failure a large amount of energy was dissipated.

The numerical model estimated the force capacity of the wall with good accuracy, predicting a maximum of 118.6 kN (-0.36% with respect to experimental) and a minimum of -116.2 kN (-5.8% with respect to the experimental value) (Figure 4.7a and Table 4.3). The numerical softening rate was higher than the experimental and more softening occurred in the positive loading direction, with a lowest value of 70 kN (41% reduction of capacity and 28.2% underestimation of experimental value) and -93 kN (19.9% reduction of numerical capacity and 14.2% underestimation of experimental value). This asymmetry in the softening rate could be due to the accumulation of damage and the reduction of the compressive capacity due to lateral cracking, and also due to the indirect shear limitation. The numerical model underestimates significantly (-63.7%) the dissipated energy. (Figure 4.7b). This may be due to the fact that in the experiment pure shear failure occurred with an almost fully elastic unloading/reloading behavior, while in the numerical model a combination of shear-compression failure occurred, affecting the energy consumption in the final cycles.

Regarding the damage localization, the crack pattern of Figure 4.5 is compared to the maximum tensile strain ever reached during the loading history of the wall in Figure 4.6. The similarities in the pattern are apparent: diagonal cracks running from the corners of the walls towards the center were observed in both cases. In the case of the numerical analysis,

the orientation of the cracks in the center was smaller than in the corners but not zero, whereas in the experiment a horizontal crack was present instead. The two main numerical cracks are asymmetric. This is partially due to the different material properties for the involved integration points (depending on the angle of strains at the onset of cracking), but also due to the recalculation and limitation of the stresses because of the indirect shear limitation. Nevertheless, the very localized damage well replicates the experimental outcome. This ability of the model to predict localized patterns, while predicting the correct base shear capacity, is an improvement compared to other existing continuum models that may show too distributed crack patterns (e.g., [21, 27]).

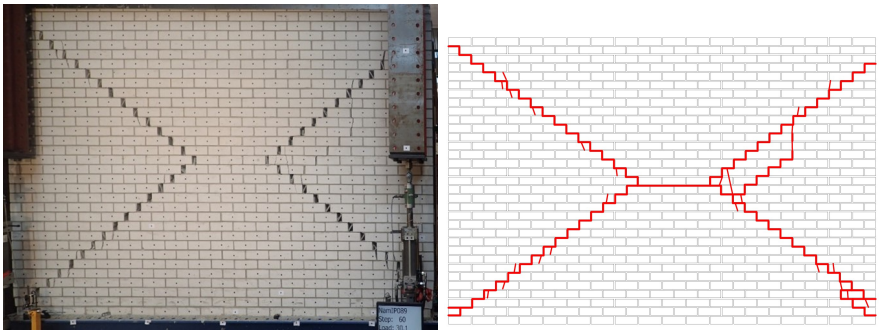

(a) (b)

Figure 4.5: Wall component TUD-COMP-4 (a) accumulated damage and crack at the end of the experiment, (b) crack pattern observed at the end of the experiment.

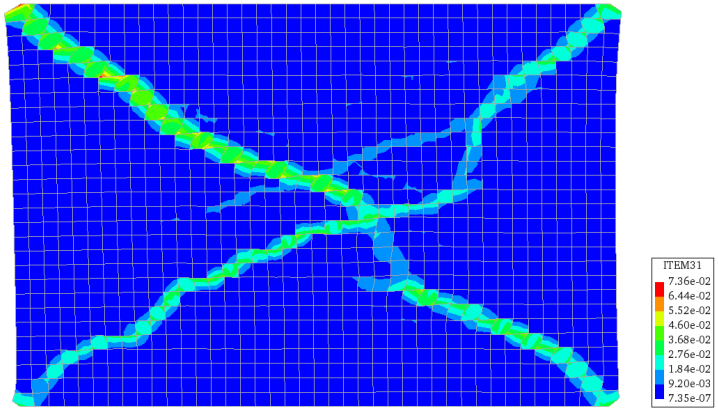

Figure 4.6: Maximum tensile strain ever reached during the loading history of wall TUD-COMP-4, depicted at the end of the numerical analysis.

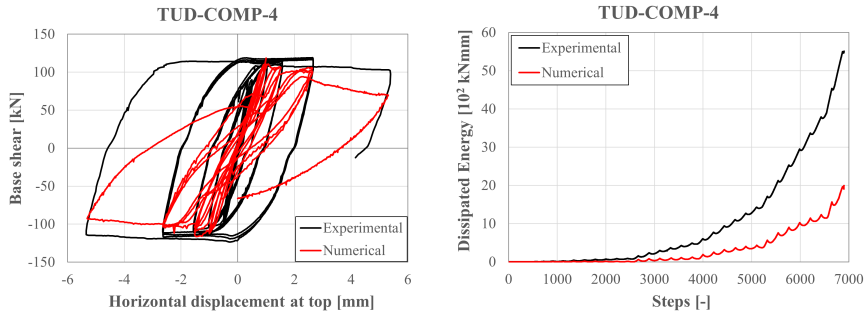

(a) (b)

Figure 4.7: Comparison of experimental (black) and numerical (red) results of (a) hysteretic response (base shear vs displacement) and (b) energy dissipation of squat wall TUD-COMP-4.

4.5 Squat wall TUD-COMP-6

Wall TUD-COMP-6 was a cantilever squat calcium-silicate brick wall (aspect ratio 0.7, same as TUD-COMP-4), with a precompression load of 0.5MPa. The maximum and minimum experimental force capacities were 109.8 kN and -109 kN respectively. The wall exhibited brittle shear failure, with cracks running through the wall diagonally. Two to three parallel step-wise cracks can be observed in Figure 4.8 for each loading direction. Moreover, brick splitting prevailed at the center and at the toes of the wall. The force capacity gradually reduced with every new cycle, with a final value of 68.1 kN for an ultimate displacement of 15.4 mm in the positive direction, and a value of -65.6 kN at a displacement of -15.6 mm.

The numerical model slightly underestimated the force capacity, with a maximum of 101.5 kN (-7.6% with respect to the experimental) and a minimum of -104.1 kN (-4.5%). Similar to component TUD-COMP-4, the peak force capacity was reached in earlier loading cycles and more strength degradation was observed for the numerical model than the experimental (Figure 4.10a and Table 4.3). The maximum and minimum numerical force capacities corresponding to the maximum and minimum drifts were 53.5 kN (-21.5% underestimation) and -56.1 kN (-14.4% underestimation), while the total dissipated energy was 17.4% lower than the experimental. In this case, the simultaneous occurrence of diagonal shear cracks with crushing/splitting of the bricks, both in the experimental and numerical results, resulted in a bigger degradation of the unloading/reloading stiffness during the last three loading cycles. This is well-depicted in the numerical results both in terms of stiffness and strength degradation and energy dissipation, as seen in Figure 4.10.

Comparing Figure 4.8 and Figure 4.9, one can see the similarities in the damage localization. In both cases diagonal cracks were prevailing, a few were parallel to each other and some wider than others. Even though the maximum tensile strains of the numerical model (Figure 4.9) did not follow exactly the same direction as in the experiment, the general crack pattern was well depicted; even the horizontal sliding along the two horizontal cracks at the top left and right of the wall was represented in the numerical results (red localization zone in Figure 4.9). Similar to wall TUD-COMP-4, some asymmetry is observed in the crack pattern. Apart from the reasons already mentioned for wall TUD-COMP-4, an additional

factor that contributed to the asymmetry observed in this wall is the asymmetrically applied external displacement, which was slightly higher when loading in the negative direction.

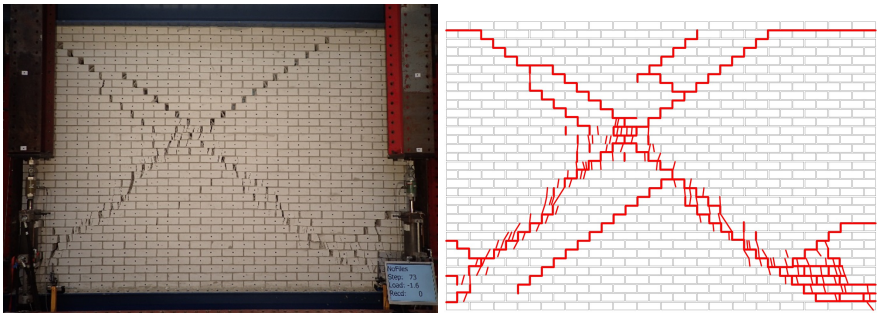

(a) (b)

Figure 4.8: Wall component TUD-COMP-6 (a) accumulated damage and crack at the end of the experiment, (b) crack pattern observed at the end of the experiment.

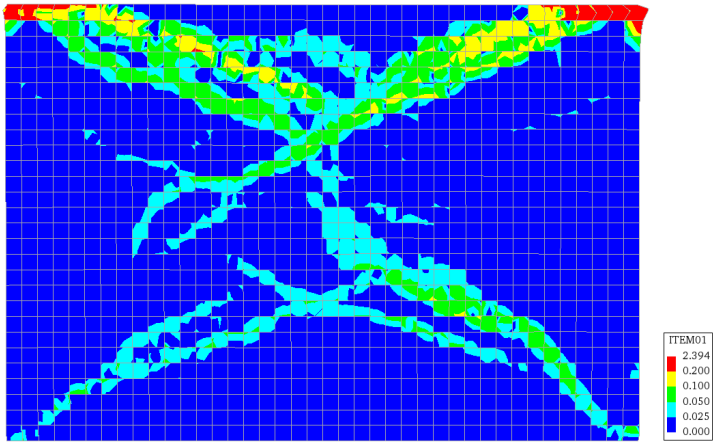

Figure 4.9: Maximum tensile strain ever reached during the loading history of wall TUD-COMP-6, depicted at the end of the numerical analysis.

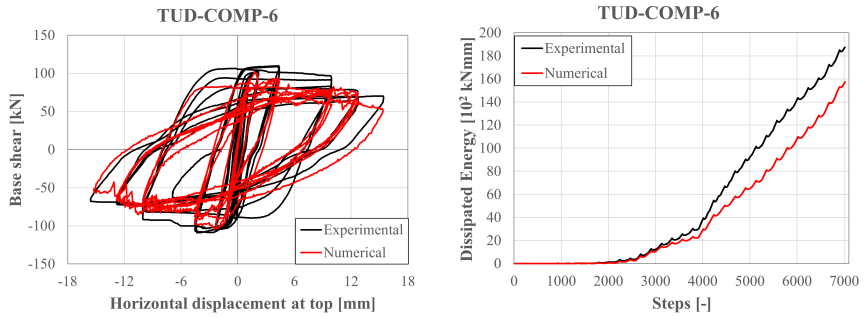

Figure 4.10: Comparison of experimental (black) and numerical (red) results of (a) hysteretic response (base shear vs displacement) and (b) energy dissipation of squat wall TUD-COMP-6.

4.6 Discussion

The comparison between the experimental results and the corresponding numerical predictions shows that the developed constitutive model estimates with good accuracy the base shear capacity of in-plane loaded masonry walls. Additionally, it predicts the correct failure mode and leads to very localized cracks, representative of those observed in the experiments (although the cracks do not perfectly match and their orientation can slightly differ). Compared to other existing macro-models that use implicit solution procedures the damage localization has improved, since it concentrates along few "lines" of elements and is not distributed over many elements, as has been observed in the past (e.g., [19, 23, 72]). Also in terms of cyclicity, the model seems to perform better than models that assume fully secant or fully elastic unloading/reloading. The dissipated energy is best estimated in the cases that a combination of failure mechanisms occurs. Specifically, for walls LOWSTA and TUD-COMP-6 underestimation of 10-17% is observed, which could be considered within acceptable limits for macro-models, but for wall TUD-COMP-4 the underestimation is much bigger. On the other hand, the model overestimated the dissipated energy of HIGSTA. It appears that the numerical estimation is closer to the experimental results when a combination of different failure mechanisms is observed (flexure and shear for LOWSTA, and shear and crushing for TUD-COMP-6), whereas when only one mechanism is observed during the experiment (flexure for HIGSTA and pure shear for TUD-COMP-4) the model still predicts some hybrid mechanism and then is incapable of predicting the precise value. In the case of HIGSTA, the shear cracks that started developing in the numerical model dissipated more energy than the pure rocking cracks of the experiment. As for walls TUD-COMP-4 and TUD-COMP-6, during the experiment a major part of the energy was dissipated due to the shear sliding behavior. Even though the developed model incorporates the ductile energy-absorbing unloading/reloading behavior in shear, this is limited for cracks with initial orientation between $20^o - 70^o$; if a crack forms originally due to flexure, it will always have a brittle behavior with secant unloading and small energy dissipation when unloading/reloading in tension.

4.6.1 Numerical stability and convergence

Figure 4.11 presents the force-displacement curve and the steps that did not converge for each numerical analysis. The maximum number of iterations was set to 100 with a convergence tolerance of 0.01 for both displacement and force norms, and, in the case that convergence was not satisfied, the analysis was permitted to continue to the next step (it is reminded that for convergence either the force or the displacement norm need to be satisfied). The range of the convergence norm is depicted in different colors. Figure 4.11 shows therefore not only the number and location of the unconverged steps, but also the error in the tolerance, to allow for an easier assessment of the accuracy of the numerical results. Some of the spikes and oscillations observed in the force-displacement curve coincide with steps where convergence was not reached, whereas other spikes did not relate with stability issues. Moreover, there are even some points that would not rise suspicion of instability, but did not converge momentarily. For three out of the four walls many steps did not reach convergence, but convergence was reached in the following steps. This was not the case for wall TUD-COMP-4, for which none of the steps on the softening branch converged during the loading in the positive direction of the last cycle. For most of these steps the norm was lower than 0.03, and the force-displacement curve does not show evident signs of such numerical instabilities (such as spikes or sudden drops of capacity).

In general, between 1.5% (TUD-COMP-6) to 7.8% (LOWSTA) of the total number of steps for each analysis had a convergence norm higher than 0.02. These numerical instabilities are probably caused by the internal iterative algorithm defined to limit the shear strength. As a matter of fact, the recalculation of the principal stresses when the shear stress exceeds the shear strength can lead to significant changes in the stiffness matrix of the integration point, which consequently creates numerical instabilities in the Newton-Raphson procedure.

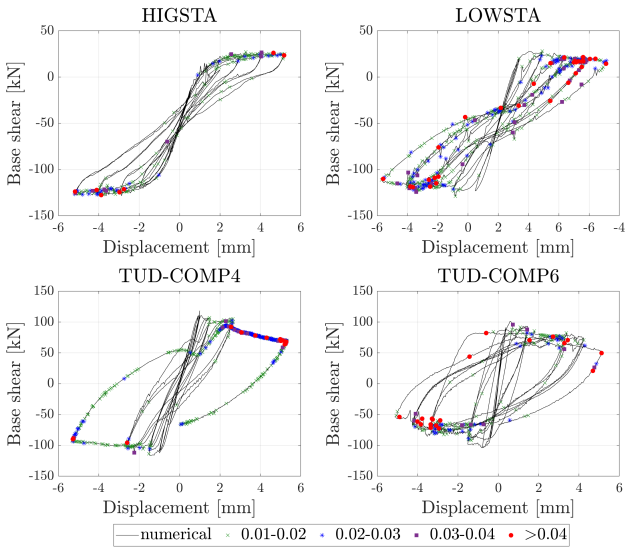

Figure 4.11: Location of unconverged steps on the force-displacement curve and the range of their convergence norm for the modelled walls HIGSTA, LOWSTA, TUD-COMP-4 and TUD-COMP-6.

4.6.2 Compression nonlinearity of squat wall TUD-COMP-6

During the test performed on specimen TUD-COMP-6, reduction of the force capacity and high energy dissipation were observed due to compression nonlinearity. This compression nonlinearity physically emerged in the form of crushing of the mortar joints and splitting of the calcium-silicate bricks. This is illustrated in Figure 4.8b and Figure 4.12a, where splitting of the bricks and crumbling of the mortar joints is observed both at the centre of the wall (where the compressive struts meet) and alongside the compressive struts towards the bottom corners, with most of the crushing and splitting observed at the bottom right corner. To examine if the developed model captures adequately this compression nonlinearity (cracking and crushing) of masonry, a user status ($\alpha_{c,i}$) is defined and set equal to the minimum compressive strain ever reached during the loading history. If the value is smaller than the compressive strain corresponding to the peak strength, crushing/splitting has occurred.

In the numerical model, as seen in Figure 4.12b, crushing occurred in the elements along the compressive-shear strut, but most of it was concentrated at the top of the wall, with only 6 elements being crushed at the bottom two corners. The crushing of the top elements would not normally be expected in a cantilever wall and it was not observed in the experiment either. Lower compressive normal stresses are expected at the bottom of the wall and one would expect that crushing would first appear there. The top side of the wall was free to rotate and move vertically, but the strong bond to the steel beam (modelled as infinitely rigid in the numerical model) forced the top face of the wall to have the same horizontal displacements. In the case of the numerical model, the crushing observed at the top of the wall is due to the combination of two different factors. First, the lower (in absolute terms) normal compressive stresses σ_{yy} at the top of the wall led to a lower shear capacity τ_{max}. Due to the assumption of coaxiality and maintenance of σ_{yy}, the values of σ_1 and σ_2 are recalculated and there is the chance that the compressive principal stress reduces (in absolute value/increases in relative value) before reaching the peak strength. Lower strength resistance leads then to higher deformations. Secondly, even though the minimum ever reached compressive strain is smaller than the compressive strain related to crushing, a major part of the strain is attributed to the shear deformation (γ_{xy}) and not only to the normal deformations ($\varepsilon_{xx}, \varepsilon_{yy}$), as seen in Figure 4.13.

It is therefore recommended to check the stress and strain components both in the principal and global directions, to be able to distinguish if crushing is triggered by the internal shear limitation (and should be therefore ignored) or if it is due to compressive failure. For failure due to flexure or shear, no additional check is required.

4.6.3 Mesh sensitivity

Another problem often encountered in standard strain-softening continua is their potential inobjectivity with respect to the mesh size, mesh order and/or mesh direction. Many researchers tackle this sensitivity by including a mesh-adjusted softening modulus: the crack bandwidth or characteristic length [185–187, 193, 198]. In this work, the crack bandwidth is estimated based on the element area A as: $h_{crack} = \sqrt{A}$ for quadratic elements and $h_{crack} = \sqrt{2A}$ for linear elements [193]. In order to test the sensitivity of the developed model on the mesh size and order, wall TUD-COMP-4 was modelled with elements of different order (quadratic 3x3 vs linear 2x2) and different size (100mm, 200mm, 300mm).

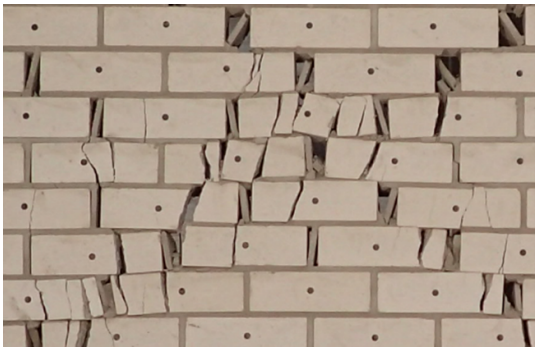

(a)

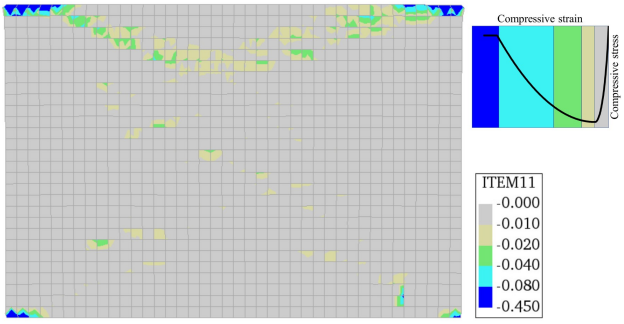

(b)

Figure 4.12: (a) detail of crushing (split bricks and mortar joints) at the center of wall TUD-COMP-6, (b) minimum compressive strain ever reached during the loading history of TUD-COMP-6, depicted at the end of the numerical analysis (scale factor 1).

Note that all the analyses were carried out using the same material properties, solution procedure and convergence criteria as for the model described in Section 4.1. However, only one repetition per cycle was applied.

The force-displacement curve and the damage localization (in terms of $\alpha_{t,1}$) are presented for the different models in Figure 4.14 and Figure 4.15, respectively. All the models estimated the base shear capacity with good accuracy, with a maximum deviation of 5.2% between numerical and experimental capacity, and 9% between the maximum and minimum numerical capacity. Bigger deviations were observed in the post-peak behavior, where the models with quadratic elements exhibited more softening than those with linear elements. Overall, a maximum difference of 28.7% was observed in the residual strength between the numerical models, with the linear-300 element and quadratic-200 element exhibiting the minimum and maximum softening, respectively. In terms of crack pattern, all models predicted shear failure with diagonal cracks, but the crack angle and the point of intersection between the two diagonal cracks differed. Increasing the element size and/or order (quad-200, linear-200, linear-300) resulted in steeper crack angles. This could be attributed to the coarser mesh that offers fewer options for the direction of a diagonal crack. Note that a difference is observed in the crack localization of the wall for the ref-

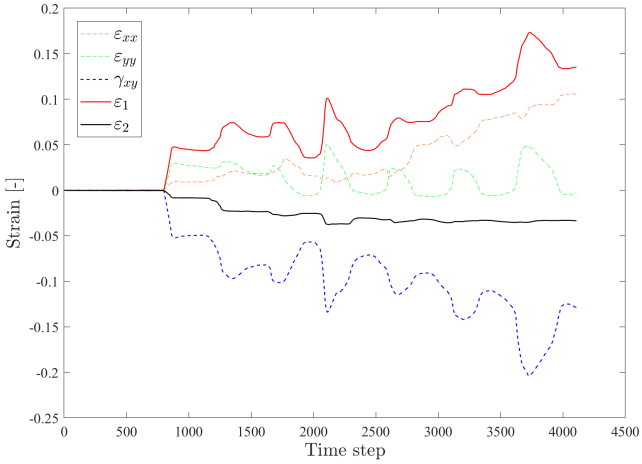

Figure 4.13: Evolution of strains ($\varepsilon_{xx}, \varepsilon_{yy}, \gamma_{xy}$) in global directions (x,y) and principal strains ($\varepsilon_1, \varepsilon_2$) at the top right corner of wall TUD-COMP-6 through its loading history.

erence elements (quad-100) from the analysis of Section 4.4, probably due to the fewer repetitions during the loading procedure and therefore smaller accumulation of permanent deformations.

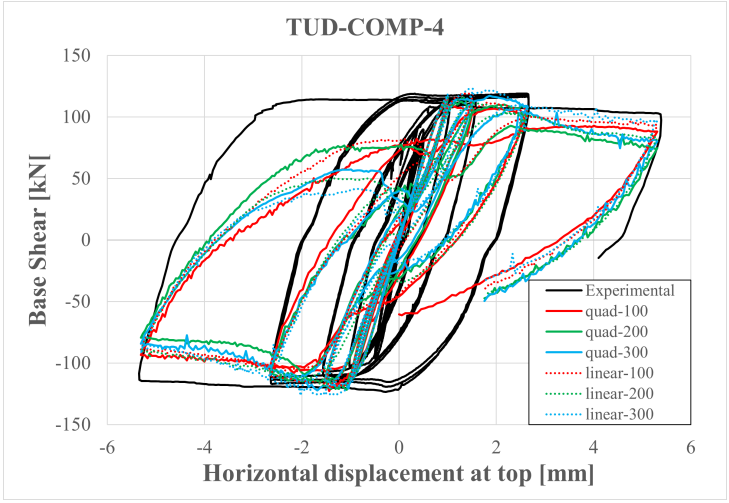

Figure 4.14: Base shear versus horizontal displacement at top for different mesh element size (100mm, 200mm, 300mm) and order (quad for quadratic vs linear).

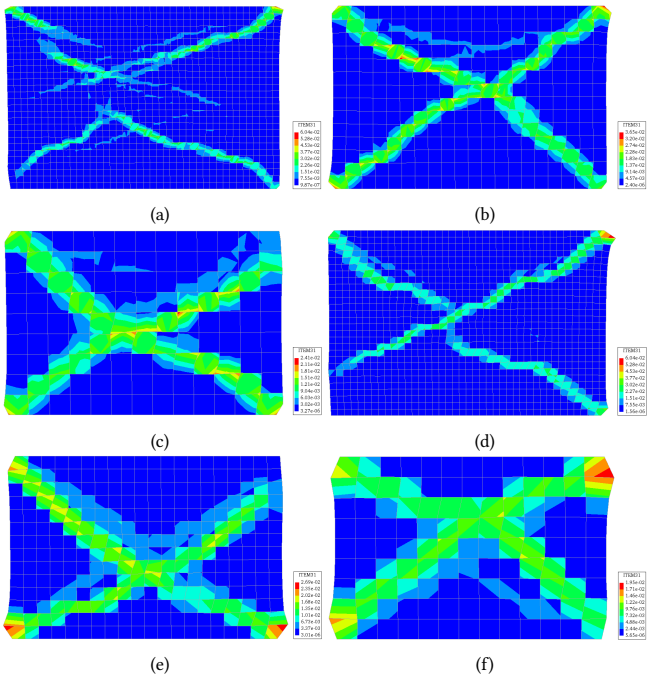

Figure 4.15: Comparison of maximum tensile strains ever reached during the loading history of wall TUD-COMP-4 in the case of (a) quadratic elements of 100mm, (b) quadratic elements of 200mm, (c) quadratic elements of 300mm, (d) linear elements of 100mm, (e) linear elements of 200mm, and (f) linear elements of 300mm.

4.6.4 Threshold angle sensitivity

Finally, a small variation of the model was made to investigate how the threshold angle θ_{fl}, which defines the transition between flexural and shear behavior, influences the global behavior of the walls. Two threshold angles were selected: $\theta_{fl} = 20^o$ which leads to shear behavior for cracking angles between $20^o - 70^o$ (original model), and an angle $\theta_{fl} = 25^o$ for which shear behavior is adopted for cracking angles between $25^o - 65^o$. Wall TUD-COMP-4 was modelled with the two different variations and the results are presented in Figure 4.16 and Figure 4.17. Both models predicted the base shear capacity with good accuracy (less than 5% difference) and only minor differences are observed in the post-peak behavior during the last cycle. On the other hand, the two analyses return different final crack patterns; although both models present diagonal shear cracks, a wider range of "shear angles" ($20^o - 70^o$) leads to steeper angles, more representative of the experiment. Therefore, the choice of a threshold value of 20^o (and an angle range of $20^o - 70^o$ degrees) is considered more appropriate for modelling long shear walls. For walls LOWSTA and HIGSTA, no difference in the numerical results (force-displacement and crack localization) was observed. This proves that these walls, with smaller aspect ratio, were not influenced by a difference of $\pm 5^o$ since flexure was predominant (for HIGSTA) and/or shear cracks were steeper (LOWSTA). Finally, for wall TUD-COMP-6 observations similar to those for

TUD-COMP-4 were made.

The values of the threshold angle in these examples (between 20^o and 30^o) are selected based on observations on the patterns and crack directions from tests performed by Page [183] and on the brick pattern of the modelled walls. For walls LOWSTA and HIGSTA the angle of perfect step-wise diagonal cracks would be 46.12^o, while for walls TUD-COMP-4 and TUD-COMP-6 it would be 37.6^o. The adopted threshold angles ensured that shear behavior would be considered for the angle following from the geometrical brick pattern. Whether the proposed values of the threshold angle are appropriate in the case of bond types other than the stretcher bond considered in the examples herein should be further investigated, because for such bond patterns different angles of the shear cracks may be observed.

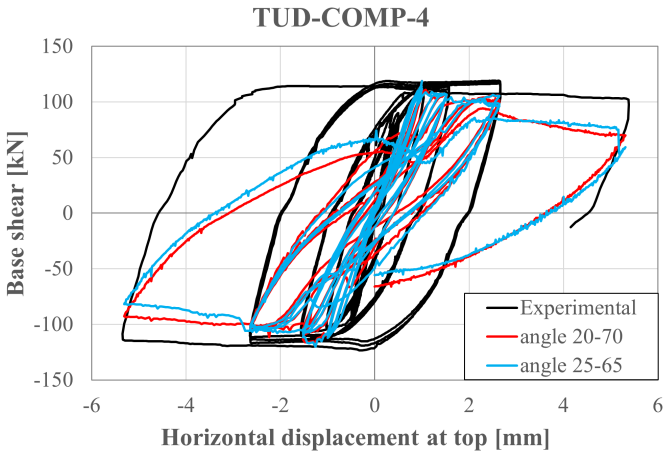

Figure 4.16: Influence of range of cracking angles associated with shear behavior and failure.

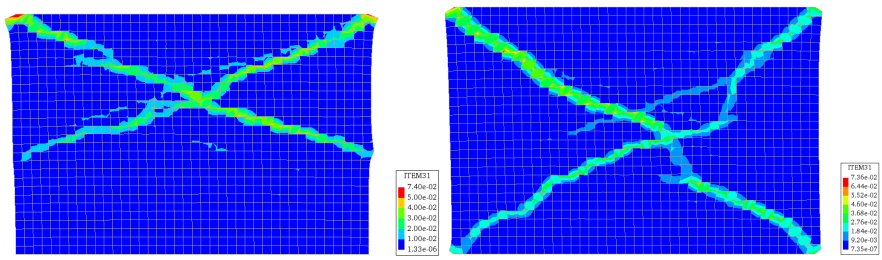

Figure 4.17: Comparison of maximum tensile strains ever reached during the loading history of wall TUD-COMP-4 when shear behavior is adopted for cracking angles between (a) $25^o - 65^o$ and (b) $20^o - 70^o$.

4.7 Conclusions

The model presented in Chapter 3 was validated against cyclic experimental tests performed on walls with different aspect ratios, boundary conditions and precompression levels. Good agreement was found between the numerical and experimental results, especially in terms of base shear capacity (2-8%) and sharpness of the crack localization. The model was demonstrated to be able to capture the cyclic hysteretic response in an adequate manner, compared to the performance of fully secant-driven smeared crack or damage based models, or fully elastic unloading/reloading driven plasticity based models, as presented in previous works (e.g., [21, 23, 25]). The energy dissipation was estimated satisfactorily for walls where a combination of failure modes was observed (flexure and shear cracks, shear and crushing), while the dissipation was underestimated when only pure shear failure was observed, and overestimated when pure rocking was observed. Results were demonstrated to be sufficiently mesh-insensitive. Only small differences were observed in the prediction of the base shear capacity and crack pattern, while some larger differences occurred in the post-peak regime, especially between quadratic and linear elements. Nevertheless, there are aspects of the model that still need to be improved, such as the numerical stability, which is heavily influenced by the internal iterative shear loop, as well as the underestimation of the dissipated energy under pure shear. One more aspect that will be investigated further in the future is the limitation of the compressive capacity due to the internal shear loop that might lead to premature crushing.

Overall, the proposed cyclic constitutive model predicts the correct failure mechanism and accurately computes the load-displacement behavior and presenting realistic localized crack patterns for both slender and squat walls. This makes the model an attractive option for the modelling of in-plane unreinforced masonry walls.

5

Macro-modelling vs. micro-modelling: A comparative study

As discussed in Chapter 2, macro-models, even though less accurate than micro-models, are usually preferred for the modelling of large-scale masonry structures, due to their reduced computational cost and time. Having developed a new Orthotropic Total Strain based Rotating macro-model (OTSRM) in Chapter 3 and having validated it against experimental results in Chapter 4, it is time to evaluate its performance in comparison to other existing macro-models and micro-models. To do so, five different constitutive models commonly used by engineers are selected and compared with the developed one: 3 continuum macro-models and 2 interface micro-models. Two of the constitutive models following the macro-modelling approach are based on a total-strain approach, the isotropic Total Strain Rotating Crack Model (TSRCM) and the Engineering Masonry Model (EMM), and one is based on the theory of plasticity: the Rankine Hill plasticity-based Anisotropy (RHAPM) model. The interface models selected are the plasticity-based Combined Cracking Crushing Shearing (PCCCS) model and a total-displacements based, newly developed micro-model incorporating a sub-stepping iterative algorithm and some characteristics of plasticity theory, called Sub-Stepping Iterative Cracking Crushing Shearing (SI-CCS) model. The OTSRM and these five constitutive models are used to model six unreinforced masonry walls of different aspect ratios and boundary conditions, representative of a wide variety of unreinforced masonry piers. Four of these walls were tested under quasi-static cyclic loading and two under monotonic loading. The numerical results derived by using each constitutive model are compared with the experimental results and with the results from the other constitutive models in Sections 5.2 to 5.7 in terms of numerical accuracy, including the model's ability to accurately predict the failure load, dissipated energy and damage localization. Moreover, a comparison between the different models regarding their numerical stability and computational time is provided in Section 5.8.

5.1 Numerical approach: Six models applied to six walls

In this chapter, six unreinforced masonry (URM) walls are modelled numerically using different modelling techniques and different constitutive models. More specifically, six constitutive models are utilized: four continuum models that are used in the macro-modelling approach, and two interface constitutive models, used in the micro-modelling approach. All six models are implemented in DIANA FEA software, and four of them are commercially available and commonly used when modelling URM structures. These are the following: the Total Strain Rotating Crack Model (TSRCM), the Engineering Masonry Model (EMM), the Rankine-Hill Anisotropy (RHAPM) model, and the Combined Cracking-Shearing-Crushing (PCCCS) model. The remaining two constitutive models are not yet commercially available, but have been developed and implemented as subroutines during this PhD research period; these are the newly developed continuum constitutive model presented in Chapter 3, referred as OTSRM, and the Sub-stepping Iterative constitutive model for cyclic Cracking/Crushing/Shearing in masonry interface elements (SI-CCS) developed by [92], and briefly discussed in Chapter 2. This chapter aims to compare the accuracy and the performance of each modelling approach and constitutive model when modelling URM structures. To this end, six URM walls of different geometrical and material properties, different boundary conditions, and different failure mechanisms are used as benchmark cases. For each wall, the maximum base-shear capacity, the total hysteretic behavior, the energy dissipation and the damage localization that resulted from each of the constitutive models are compared and discussed. Additionally, a comparison is made in terms of computational time and numerical stability.

Five of the six constitutive models have been developed specifically for masonry structures, whereas the sixth, the TSRCM, has been developed for initially isotropic materials, like concrete. The TSRCM is a total-strain crack/crush model based on the Modified Compression Field Theory proposed originally by Vecchio & Collins [199], and it follows a smeared approach for the fracture energy. The "Rotating Crack" term implies that the crack directions are continuously rotating with the principal direction of the strain vector, assuring in this way coaxiality between stresses and strains after cracking. Since this model has been used successfully for many years for the simulation of reinforced concrete, many options are available to describe the tensile and compressive behavior. In the case of application to masonry structures the options most commonly used are the tensile cracking with a linear or exponential softening curve based on fracture energy, and the parabolic curve based on fracture energy for compression. Moreover, it is possible to adjust the compressive capacity in the case of lateral confinement and/or lateral cracking, according to the modified compressive theory [112]. Secant unloading/reloading is adopted. For the definition of the constitutive model with the abovementioned cracking and crushing options, 6 input material parameters are required.

The RHAPM is based on the orthotropic multi-surface plasticity model developed by Lourenço et al. [27], and it comprises an anisotropic Rankine yield criterion for tension combined with an anisotropic Hill criterion for compression. Tensile cracking with exponential softening based on fracture energy is assumed in the orthogonal directions that align with the mortar joint directions, whereas parabolic hardening followed by parabolic/exponential

softening is adopted in compression. The shear stress contribution is included through three parameters (α, β, γ) that are used to define the yield surface. The model requires 17 input material parameters, and adopts elastic unloading/reloading as featured in the standard theory of plasticity.

The EMM is a total-strain based smeared-crack model which describes the constitutive behavior in re-fixed orthogonal directions. It incorporates anisotropy by adopting different stiffness and strength properties along the two pre-defined material directions: parallel to the bed and head-joints. The model provides four different head-joint crack-initiation options, and it is upon the user to choose the most appropriate option for each application. By default, tensile cracking and compressive crushing normal to the bed joints, as well as shear sliding based on a Coulomb friction criterion are included. Based on the choice made for the head-joint failure, tensile cracking and compressive crushing normal to the head-joints may be included or omitted, as well tensile cracking along two pre-defined diagonal crack directions, defined by the user through an input angle parameter. Secant unloading/reloading is adopted in tension, while in compression a nonlinear non-secant unloading/reloading behavior is adopted. Finally, elastic unloading is adopted in shear. The material input parameters for the EMM can therefore vary between 12 and 14. More information about the model can be found in [21, 111].

The last continuum model is the orthotropic total-strain based rotating model (OTSRM) developed and discussed in detail in Chapters 3 and 4. It comprises failures in tension, compression, and indirectly, shear. The behavior in tension after the peak and during unloading/reloading depends on the orientation of principal strain when cracking initiates. For angles corresponding to in-plane flexural failure, brittle failure with steep softening is assumed, while for angles corresponding to diagonal shear failure, ductile behavior with softening is assumed. It also considers a reduction in compressive strength due to lateral cracking. Additionally, shear failure is incorporated using a shear-limitation algorithm based on the Coulomb friction criterion. The model maintains coaxiality between principal stresses and strains and assumes the vertical confining stress, normal to the bed-joints, remains unchanged. To define the constitutive equations, 15 input material parameters are required, which are derived from standard tests conducted perpendicular and parallel to the bed joints.

Regarding the micro-modelling approach, the first of the two interface constitutive models used is the PCCCS model, which is a plasticity-based interface model developed by Lourenço and Rots [33] and later enhanced by Van Zijl [200]. The multi-surface plasticity model includes three types of failure: failure due to tensile cracking with exponential softening dependent on the fracture energy by means of a tension cut-off surface; failure due to crushing with parabolic hardening followed by parabolic/exponential softening by means of a compression cap; and shear slipping through a Coulomb friction yield criterion. Elastic unloading/reloading, as inherent to plasticity theory, is adopted for tension, compression as well as shear, and 13 material input parameters are required for its definition.

The sixth constitutive model is the SI-CCS model, developed by Xie et al. [92]. Based on a total deformation theory, it adopts characteristics of multi-surface plasticity, including a Coulomb friction failure surface for shear, with tension and compression cut-off and softening for all three domains. The model is driven by two damage parameters, one

for compression and one that couples tension and shear. Secant unloading is assumed in tension, whereas bilinear unloading and reloading is assumed in compression, and elastic unloading/reloading in shear. Moreover, a sub-stepping iterative algorithm is used instead of the traditional return-mapping algorithms. The model requires 13 independent input material parameters.

Table 5.1 presents the material properties that are used as input parameters for the six examined constitutive models. In general, the total number of material parameters that are required for the definition of the micro-models are 13 for the properties of the interface (or even more if different properties are assigned to the bed and head-joints) plus at least two elastic parameters for the definition of the brick elements (or more if failure of the bricks is also included).

Table 5.1: Material properties required as input parameters for the numerical analyses of masonry structures for the different constitutive models examined. Where double checkmarks (✓✓) are present, both the material properties parallel to the direction of the head joints and parallel to the direction of the bed-joints are required.

Material Properties required as input for macromodels/micromodels		Macromodels				Micromodels[1]	
		TSRCM[2]	RHAPM	EMM	OTSRM	PCCCS	SI-CCS
Modulus of elasticity / Normal stiffness of interface	E	✓	✓✓	✓✓	✓✓	✓	✓
Shear Modulus/stiffness	G	✓	✓	✓	✓	✓	✓
Threshold angle	θ_{fl}	-	-	-	✓	-	-
Diagonal angle	α_{diag}	-	-	✓	-	-	-
Tensile strength	f_t	✓	✓✓	✓✓[3]	✓✓	✓	✓
Compressive strength	f_c	✓	✓✓	✓	✓✓	✓	✓
Strain/displacement at peak compressive strength	ε_{pc}	-	✓	✓[4]	✓✓	✓	✓
Fracture energy in tension	G_{ft}	✓	✓✓	✓✓	✓✓	✓	✓
Fracture energy in compression	G_{fc}	✓	✓✓	✓✓	✓✓	✓	✓
Cohesion	c_0	-	✓[5]	✓	✓	✓	✓
Friction coefficient	$tan\phi$	-	-	✓	✓	✓	✓
Fracture energy in shear	G_{fs}	-	-	✓[6]	-	✓	✓
Dilatancy angle	ψ	-	-	-	-	✓	-
Additional input parameters required							
Unloading factor in compression	λ	-	-	✓	-	-	✓
Super-hyperbolic Rankine-Hill parameter	m	-	✓	-	-	-	-
Super-hyperbolic Rankine parameter	n	-	✓	-	-	-	-
Shear stress contribution to tensile failure	α_τ	-	✓	-	-	-	-
Biaxial compression control parameter	β	-	✓	-	-	-	-
Shear contribution to failure parameter	γ	-	✓	-	-	-	-
Shear-stress contribution factor for compression	C_s	-	-	-	-	✓	-

[1] In the case of the micro-models, ✓refers to the material properties inserted per interface type (bed-joint or head-joint). It is common to use the same material properties for bed and head-joints when using interface elements, but different material parameters might be used as well, in which case the double amount of input parameters would be required.
[2] The input material parameters for the TSRCM do not necessarily correspond to the ones alongside the mortar joints.
[3] The tensile strength of the head-joints is only required for two out of the four options for head-joint cracking failure.
[4] Taken into account indirectly through the input parameter $n_c = (E\varepsilon_{pc})/f_c$.
[5] Taken into account indirectly through the input parameters $\alpha_\tau = (f_{tx}f_{ty})/c_0$ and $\gamma = (f_{cx}f_{cy})/\tau_{max}$.
[6] The inclusion of fracture energy in shear is optional.

The six walls selected as benchmark for the comparison of the constitutive models have different material properties, boundary conditions, aspect ratios, pre-compression loads and failure mechanisms. The variability in aspect ratios, boundary conditions and material properties were key elements in the selection of the six walls, since this would make more

versatile and unbiased the evaluation of the constitutive models. Four of the six walls were loaded cyclically, so that a comparison of the hysteretic behavior of each constitutive model, an understudied but important topic, could be provided. Moreover, the material properties of these walls were well-documented, hence avoiding material assumptions and calibrations, and making the comparison between numerical and experimental results more objective. In order to make a fair and consistent comparison between the different constitutive models used, only the constitutive model changes in each analysis per wall. The mesh properties and iterative method, including the total number of load-steps, the number of iterations per step, convergence norms are identical for the six different constitutive models for each one of the examined walls. Regarding the finite element discretization of the macro-models 3×3 Gaussian integrated 8-noded quadratic, quadrilateral plane-stress elements were adopted. Their average dimensions were $50\times50mm^2$ for the numerical models of the TU Eindhoven Hollow and Solid walls, and $100\times100mm^2$ for the remaining four walls. In the case of the micro-models the walls were composed of quadrilateral 4-noded, plane stress elements representing the bricks, and line interface elements (2 + 2 nodes) representing the head- and bed-joints. Linear elastic behavior was adopted for the bricks, except for the bricks of TU Eindhoven Solid Wall, where nonlinearities in tension were introduced through a TSRCM. The plane stress elements were integrated by a 2x2 Gauss scheme and the interface elements by a 2-point Newton-Cotes scheme. In the numerical model, the dimensions of the bricks were increased by the thickness of the adjacent mortar layer, in order to ensure geometrical compatibility with the zero-thickness interface elements, following a simplified micro-modelling approach. Where possible, the material properties provided in literature for the corresponding walls were used. In a few cases it was necessary to perform material calibrations; this is reported where applicable. Finally, in the case of the EMM the "Friction Based Head Joint Strength" option was selected to describe the failure of the head-joints for all the examined walls.

Table 5.2: Geometrical properties and loading protocol of the six walls

Specimen name	Aspect ratio h_w/l_w	Boundary Condition	Pre-compression load $[MPa]$	Loading protocol	Number of load-steps	Iterations per step	Number of cycles
TUD-COMP-4	0.70	Double clamped (u_z allowed)	0.50	Displacement control - cyclic	2816	100	17
TUD-COMP-6	0.70	Cantilever	0.50	Displacement control - cyclic	4128	100	17
LOWSTA	1.35	Double clamped (u_z allowed)	0.60	Displacement control - cyclic	2008	200	11.25
HIGSTA	2.00	Double clamped (u_z allowed)	0.60	Displacement control - cyclic	2498	200	12.5
TUe-Hollow	1.01	Double clamped (no u_z allowed)	0.30	Displacement control - monotonic	1010	100	-
TUe-Solid	1.01	Double clamped (no u_z allowed)	0.30	Displacement control - monotonic	1010	100	-

5.2 Shear wall TUD-COMP-4

TUD-COMP-4 was a double-clamped wall with an aspect ratio of 0.7. Its validation against the developed constitutive model has been presented in Chapter 4. The material properties adopted for the macromodels are the ones defined and used in Chapter 4. Regarding the

micro-models, different material properties were adopted for bed and head-joints, based on the work of [92]. The tensile strength used in the macro-models in the horizontal direction is higher than in the vertical direction; this is in line with what was observed in the experiments for vertical out-of-plane bending (cracks forming along bed joints) and horizontal out-of-plane and in-plane bending (step-wise cracks and occasionally splitting of bricks) [46]. On the other hand, the tensile strength of the head-joints in the micro-models is reduced further; a lower value of tensile strength and normal stiffness was given with respect to the bed-joints due to the assumption of lesser pre-compression on the head-joints (and possibly due to poorer filling) during construction. The material properties adopted for the six constitutive models are presented in Table 5.4.

In the case of the macro-models, the contours of the principal strain ε_1 at the maximum applied displacement (+5.31 mm) is used as a means to compare the experimental crack-pattern with the numerical one. The principal strain ε_1 at the current step is used, instead of the maximum ever reached strain throughout the loading history, to represent better the localization of the damage, taking into account the opening and closing of cracks. In the case of the micro-models, the total-relative-displacement of the interface elements is used instead, presenting only displacements higher than 0.5 mm. Figure 5.1 compares the damage localizations for the different constitutive models as depicted at the maximum applied displacement (+5.93 mm). Comparing them with the experimental crack pattern presented in Figure 4.5 of Chapter 4, it can be concluded that the only model truly incapable of capturing the diagonal shear cracks is the EMM, which predicts no less than thirteen steep cracks, parallel to each other (Figure 5.1b). The TSRCM predicts two diagonal cracks, starting at the top left and bottom right corners and extending towards the middle of the wall. The damage localizes over a few lines of elements and the main difference with the experiment is that the two diagonal cracks continue towards the opposite sides, instead of bridging via horizontal line. The RHAPM presents damage along two diagonals, from top left to bottom right, and top right to bottom left. There are also some smaller horizontal cracks alongside the top and bottom rows of elements, as well as at the top and bottom one-third of the wall. This model, with the pure elastic unloading/reloading algorithm is able to predict not only the diagonal cracks, but also the permanent deformations along the shear diagonal crack. The diagonal from top left to bottom right exhibits higher strains, since it is fully open, whereas the opposite diagonal shows lower values since the cracks have slightly closed. A drawback of this model is that the damage is spread over many elements (around six elements per mesh row). The OTSRM, developed in this thesis, has been already discussed in Chapter 4 for its ability to predict the localized damage by comparing the maximum ever reached tensile strains over the loading history of the walls. However, here the principal strains show that one diagonal crack is fully open while loading in the positive direction, whereas in the opposite direction damage is observed on the top right and bottom left corners (Figure 5.1d). The damage localizes over a few elements and the crack pattern resembles the experimental one (Figure 4.5), despite the small differences in the angle orientation. Regarding the micro-models, the PCCCS model predicts three main diagonal cracks open in each direction (X-cracks), with total relative displacement higher than 2mm (Figure 5.1e). More step-wise cracks have been formed parallel to the main ones, but their width is 2.5-5 times smaller than the main ones. This could be due to the small tensile strength of the head-joints. The SI-CCS model also shows diagonal step-wise

Table 5.3: Input material parameters used for the numerical modelling of shear wall TUD-COMP-4 for the six examined constitutive models. The values used for the interface elements represent the material properties resulting from the combination of the mortar joints and the bond between mortar joints and bricks, as is the case in simplified micro-modelling.

Table 5.4:

Material input parameters		TSRCM	RHAPM/EMM/OTSRM		PCCCS/SI-CCS	
			horizontal direction $i = x$	vertical direction $i = y$	head-joints $i = h$	bed-joints $i = b$
Modulus of elasticity / Normal stiffness of interface	$E\ [MPa]$	5091	3583	5091	10.44	121.16
Shear Modulus/stiffness	$G\ [MPa]$	-	1571		16.36	39.31
Poisson's ratio	$\nu\ [-]$	0.14	-	-	-	-
Threshold angle	$\theta_{fl}\ [rad]$	-	0.349		-	-
Diagonal angle	$\alpha_{diag}\ [rad]$	-	0.6304		-	-
Tensile strength	$f_t\ [MPa]$	0.14	0.21	0.14	0.0035	0.105
Compressive strength	$f_c\ [MPa]$	5.93	7.55	5.93	7.55	5.93
Strain/displacement at peak compressive strength	$\varepsilon_{pc}\ [-]$	-	0.012	0.01	3.3082	0.897
Fracture energy in tension	$G_{ft}\ [N/mm]$	0.012	0.02	0.012	$7.75 \cdot 10^{-6}$	$7.75 \cdot 10^{-3}$
Fracture energy in compression	$G_{fc}\ [N/mm]$	31.3	43.4	31.3	34	15
Cohesion	$c_0\ [MPa]$	-	0.14		0.14	0.14
Friction coefficient	$tan\phi\ [-]$	-	0.43		0.43	0.43
Fracture energy in shear	$G_{fs}\ [N/mm]$	-	1		0.1	3
Dilatancy angle	$\psi\ [rad]$	-	-	-	0	0
Density	$\rho\ [T/mm^3]$	$1.805 \cdot 10^{-9}$	$1.805 \cdot 10^{-9}$		-	-
Additional input parameters required						
Unloading factor in compression	λ	-	1[a]		0.95[d]	
Super-hyperbolic Rankine-Hill parameter	m	-	32[b]		-	-
Super-hyperbolic Rankine parameter	n	-	16[b]		-	-
Shear stress contribution to tensile failure	α_τ	-	1[c]		-	-
Biaxial compression control parameter	β	-	-1[c]		-	-
Shear contribution to failure parameter	γ	-	3[c]		-	-
Shear-stress contribution factor for compression	C_s	-	-	-	5	
Input parameters for brick elements						
Modulus of elasticity	$E_{brick}\ [MPa]$	-	-	-	8990	
Poisson's ratio	$\nu_{brick}\ [-]$	-	-	-	0.14	
Density	$\rho_{brick}\ [T/mm^3]$	-	-	-	$1.805 \cdot 10^{-9}$	

[a] This factor is only applicable for the EMM.
[b] These parameters are only applicable for the RHAPM.
[c] The parameters $\alpha_\tau, \beta, \gamma$ are only applicable for the RHAPM, and they are not calculated based on the cohesion c_0.
[d] The unloading factor λ is only applicable in the SI-CCS model.

cracks running from the top left to the bottom right of the wall. The top layer of bricks has slid over the top bed-joint, and the diagonal cracks also initiate from there (Figure 5.1f). Their relative displacement, however, is smaller than for the PCCCS model, and fewer mortar-joints have opened or slid. The difference in the top joint sliding is probably due to the coupling of tensile and shear damage, whereas the fewer open head-joints are due to the secant unloading in tension.

Concerning the hysteretic behavior, the numerical results vary significantly, both in terms of base shear capacity and in terms of energy dissipation, as shown in Figure 5.2 (and in more detail in Appendix A) and Table 5.5. The TSRCM overestimateds the capacity

by 53-67%, while it underestimates the dissipated energy by 93%. Despite its accurate damage localization, it could be concluded that this model is unreliable for modelling this wall. The RHAPM also overestimates the base shear capacity by an average of 82.5% and overestimates the dissipated energy by 59%. The overestimation of the dissipated energy is strongly linked with the overestimation of the capacity, since the RHAPM captures the overall shape of the hysteretic circles well. It should be noted, however, that the parameters (α, β, γ) adopted here are the standard option in the software, and are not derived by using the formulas that include the cohesion c_0. In fact, the numerical analysis was also performed with the (α, β, γ) parameters derived from the formulas, but led to fast strength degradation, with big underestimation of the dissipated energy. Nonetheless, a better calibration of these parameters could lead to numerical results that better match the experimental. The EMM and OTSRM perform similarly in terms of predicting the base shear capacity, with the EMM overpredicting by a maximum of 5% and the OTSRM underestimating by a maximum of 5%. Nevertheless, the OTSRM performs poorer in predicting the dissipated energy and residual base shear, underestimating both by 66% and 12-17%, respectively. Finally, the two micro-models do very good at predicting the total hysteretic behavior, in terms of base shear capacity, residual base shear and dissipated energy. Both micro-models differ only for a few percentage points, but the one that is closest to the experimental results, both in terms of force-displacement capacity, as well crack localization is the PCCCS.

Table 5.5: Base shear capacity F_{peak}, residual base shear F_{res} at the maximum and minimum imposed displacements (± 5.3mm) and total dissipated energy U for the experimental and numerical results of wall TUD-COMP-4. The values in brackets express the difference in percentage between the numerical and experimental results.

	F_{peak} $[MPa]$		F_{res} $[MPa]$		U $[10^2\ kNmm]$	
Experimental	119.07		97.59		54.96	
	-123.40		-108.45			
TSRCM	198.99	(+67.1%)	198.99	(+103.9%)	3.66	(-93.3%)
	-188.90	(+53.1%)	-186.85	(+72.3%)		
EMM	125.48	(+5.4%)	100.94	(+3.4%)	30.92	(-43.7%)
	-126.41	(+2.4%)	-99.65	(-8.1%)		
RHAPM	223.62	(+87.8%)	215.82	(+121.2%)	87.18	(+58.6%)
	-221.87	(+79.8%)	-215.54	(+98.7%)		
OTSRM	113.30	(-4.8%)	80.20	(-17.8%)	18.86	(-65.7%)
	-116.91	(-5.3%)	-95.05	(-12.4%)		
PCCCS	127.57	(+7.1%)	118.26	(+21.2%)	59.38	(+8.0%)
	-128.27	(+3.9%)	-114.70	(+5.8%)		
SI-CCS	129.27	(+8.6%)	122.04	(+25.1%)	60.99	(+11.0%)
	-129.82	(+5.2%)	-125.32	(+15.6%)		

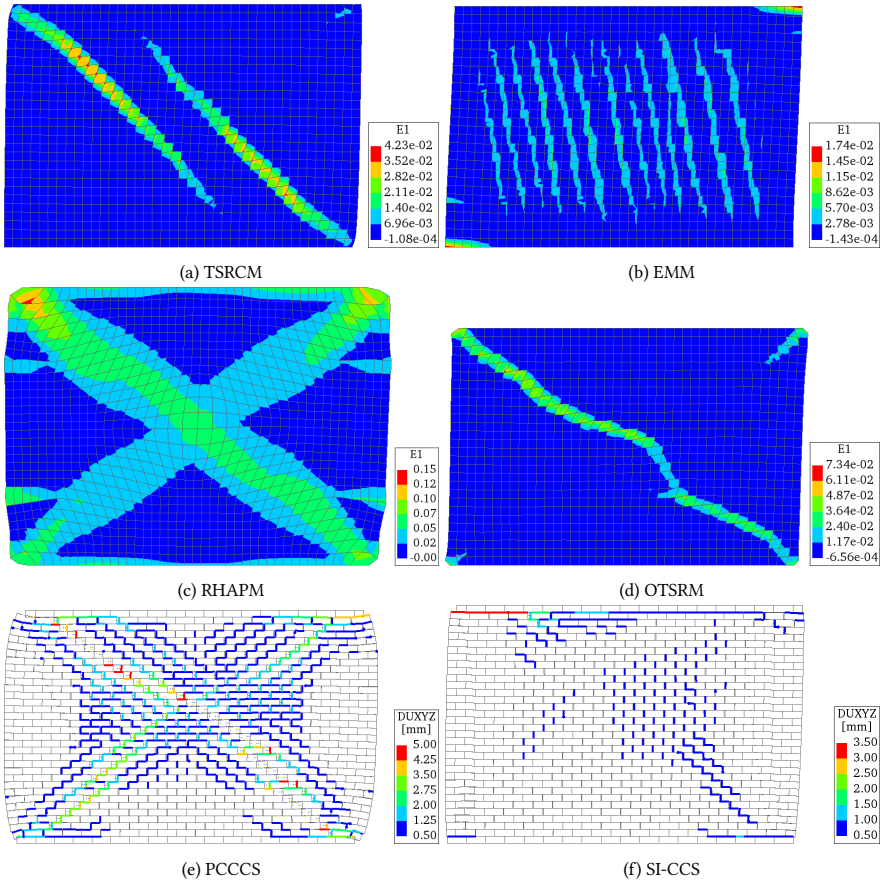

(a) TSRCM (b) EMM

(c) RHAPM (d) OTSRM

(e) PCCCS (f) SI-CCS

Figure 5.1: Principal strain ε_1 for the examined macro-models and total relative displacements for the examined micro-models for the numerical model of wall TUD-COMP-4, depicted at the maximum applied displacement +5.93 mm (scale factor=20 for all models).

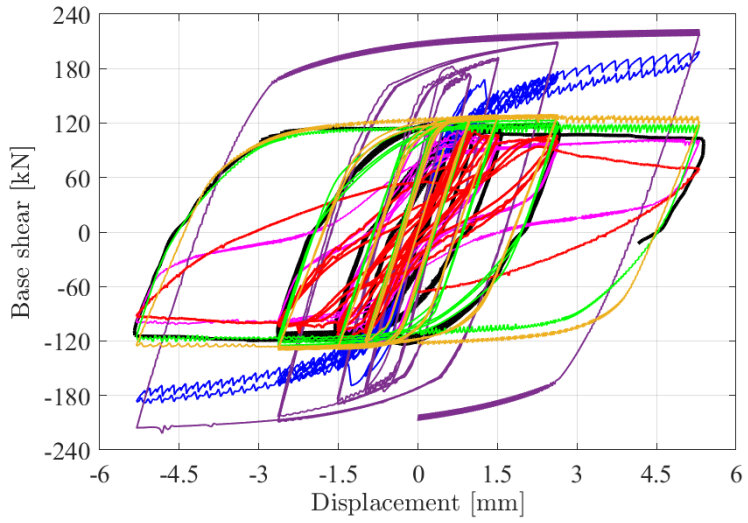

(a)

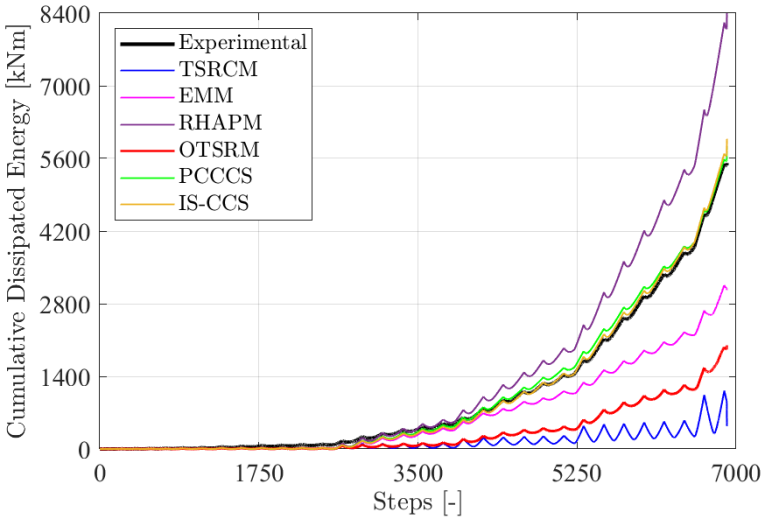

(b)

Figure 5.2: Comparison of (a) force-displacement curve and (b) cumulative dissipated energy between the experimental and numerical results derived from the different constitutive models used for wall TUD-COMP-4.

5.3 Shear wall TUD-COMP-6

The shear wall TUD-COMP-6 was a cantilever wall, tested in TU Delft during the same testing period as the shear wall TUD-COMP-4. More information about its geometry and experimental observations can be found in Chapter 4. The same material properties as for wall TUD-COMP-4 are adopted here for the different examined constitutive models (Table 5.1). The only difference is a reduction in the compressive strength of the bed-joints in the SI-CCS, from 5.9 MPa to 4.5 MPa, and the increase of the friction coefficient from 0.43 to 0.50.

Similar to wall TUD-COMP-4, the experimental and numerical crack patterns are compared by observing the principal strains ε_1 for the macro-models and the total relative displacements for the micro-models. The distribution of strains/displacements depicted in Figure 5.3 corresponds to those reached at the maximum positive displacement (+15.35 mm) during the final loading cycle. The only exception regards the RHAPM, the analysis of which diverged before the application of the final loading cycle; for this model the strains corresponding to the maximum positive displacement ever reached during the last loading cycle before divergence are used instead (Figure 5.3c). During the experiment two to three diagonal step-wise cracks developed parallel to each other in each diagonal (from top left to bottom right corner and bottom left corner towards the top right edge ending in sliding of the bed-joint over the length of 4.5 bricks). Splitting of bricks and mortar was also observed close to the center of the wall, where diagonal cracks met, and along one of the main diagonal cracks, as well as close the bottom right corner of the wall, as depicted in Figure 4.8.

Diagonal cracks can be observed in five out of the six examined constitutive models, except for the EMM, where diffused and incoherent strain localization is observed. In the TSRCM model, diagonal cracks start from the top left and bottom right corners and expand towards the center of the wall, running parallel in part of their length. A smaller crack is also observed on the top left 1/3 of the wall. Unlike for TUD-COMP-4, one of the diagonal cracks developed here is less localized, spreading in average over a width of 6 elements. The RHAPM, diverged before the maximum displacement was reached. Nevertheless high principal strains were already reached in the prior cycles. Two main diagonal cracks are extending from the top to the bottom corners, crossing in the middle of the wall, while two horizontal cracks at a distance of 1/3 of the total wall height from the top of the wall are reaching out towards the diagonals; this is the same position observed for the smaller crack of the TSRCM. High strains are present also in the area around the two bottom corners, as well as along the first row of elements, at the base of the wall. These started as flexural cracks, but because of the elasto-plastic unloading of the RHAPM the cracks never fully closed. The developed OTSRM also predicts diagonal cracks starting from the corners of the walls and expanding towards the center. Unlike wall TUD-COMP-4, where only one of the diagonal cracks appeared open, here we can observe both the main crack running from the top left and bottom right corners towards the center of the wall, as well as the diagonal crack running from the bottom left to the center of the wall. Shear sliding occurs in the top right corner. Though the cracks run towards the center, none of them actually reaches it; instead, they stop before, and two vertical cracks connect them. The micro-models are more capable of predicting the parallel step-wise cracks. Diagonal cracks start from the top left and top right corners and extend towards the bottom side diagonally. More parallel

cracks also start at different locations on the left and right side of the wall. Some crushing is observed in the bottom right and left corners (Figure 5.3e and 5.3f). Nevertheless, the location of the cracks in the numerical models and the experiment do not match. In the numerical models, the diagonal cracks cross in the lower part of the wall, whereas in the experiment they cross in the upper part of the wall (Figure 4.8).

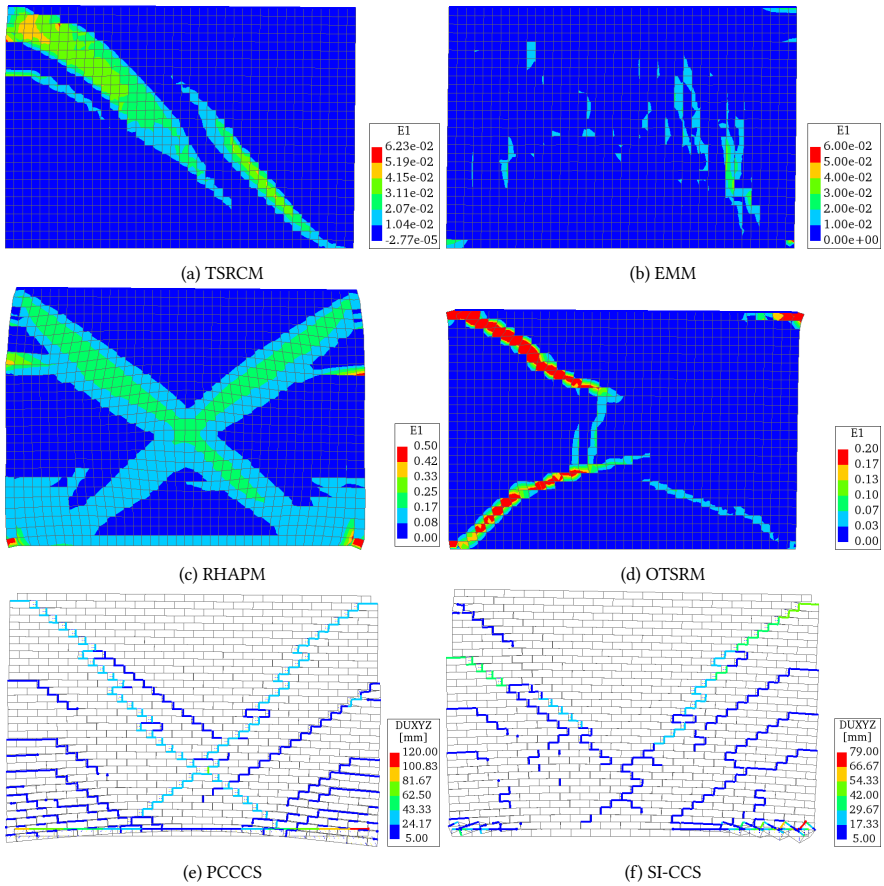

(a) TSRCM (b) EMM

(c) RHAPM (d) OTSRM

(e) PCCCS (f) SI-CCS

Figure 5.3: Principal strain ε_1 for the examined macro-models and total relative displacements for the examined micro-models for the numerical model of wall TUD-COMP-6, depicted at the maximum applied displacement +15.35 mm (scale factor=2 for all models).

Regarding the base shear capacity, the TSRCM and the RHAPM highly overestimate the capacity by 52-59% and 42-43% respectively; their residual strength is also much higher than the experimental one. Softening and strength degradation is observed in the RHAPM in every new cycle and repetition, with a 30% total loss in strength capacity by the time the analysis diverged. The TSRCM severely underestimates the dissipated energy of this wall, whereas the RHAPM overestimates it by at least 70% (and this percentage could be even higher had the analysis not stopped). The overestimation is due to the perfectly elasto-plastic cyclic behavior during unloading/reloading of the wall. On the other hand

the EMM and the OTSRM predict the base shear capacity with better accuracy: the EMM overestimated it between 7.1-12.8%, whereas the OTSRM underestimated it by just 2.3-5.9%, an even smaller error than the micro-models. OTSRM also estimates with good accuracy (4-14%) the residual force capacity; in fact, it is the model with the closest estimation of the peak and residual shear capacities with respect to the experiment. In terms of energy dissipation, both the EMM and the OTSRM simulate properly the experimental data, with an underestimation of 9% and 16.4% respectively (Figure 5.4b). The micro-models are very close to their predictions of maximum base shear capacity, differing from each other only by 2.2%. Nevertheless, bigger differences are observed in the hysteretic behavior: the PCCCS model results in larger and faster strength degradation, both in the positive and negative loading directions. Moreover, the unloading stiffness between the two constitutive models differs, with the SI-CCS model exhibiting more stiffness degradation. This behavior is due to a number of parameters: first, secant unloading/reloading is adopted in tension, and second, bilinear unloading with elastic and secant stiffness is adopted in compression. As compressive failure occurs in the mortar joints at the bottom corners of the wall, the compressive capacity reduces. As a consequence, the contribution of the elastic stiffness in the bilinear unloading reduces and the contribution of the secant stiffness increases. The PCCCS model overestimates the dissipated energy by 16.7%, despite the big overestimation in the strength degradation during the last cycles, this extra overestimation probably occurs due to the high unloading stiffness. The SI-CCS model overestimates the energy dissipation by 9.9%. Notwithstanding, the SI-CCS model has been calibrated to match better the experimental results, according to the compressive strength and friction coefficient proposed in [92]. Without the reduction of the compressive strength and the increase of the friction coefficient, the strength and stiffness degradation are insignificant, while the energy dissipation is overestimated.

Table 5.6: Base shear capacity F_{peak}, residual base shear F_{res} at the maximum and minimum imposed displacements (± 15.35 mm) and total dissipated energy U for the experimental and numerical results of wall TUD-COMP-6. The values in brackets express the difference in percentage between the numerical and experimental results.

	F_{peak} $[MPa]$		F_{res} $[MPa]$		U $[10^2\ kNmm]$	
Experimental	109.84		68.12		198.44	
	-108.99		-65.61			
TSRCM	166.40	(+51.5%)	128.67	(+88.9%)	9.30	(-95.3%)
	-173.97	(+59.6%)	-127.65	(+94.6%)		
EMM	123.89	(+12.8%)	85.68	(+25.8%)	180.18	(-9.2%)
	-116.71	(+7.1%)	-98.14	(+49.6%)		
RHAPM	167.95	(+52.9%)	116.99	(+71.7%)	338.20	(+70.4%)
	-154.45	(+41.7%)	-121.66	(+85.4%)		
OTSRM	103.31	(-5.9%)	65.18	(-4.3%)	165.95	(-16.4%)
	-106.45	(-2.3%)	-74.96	(+14.3%)		
PCCCS	116.46	(+6.0%)	10.84	(-84.1%)	231.67	(+16.7%)
	-117.47	(+7.8%)	-42.64	(-35.0%)		
SI-CCS	119.08	(+8.4%)	12.70	(-81.4%)	178.78	(+9.9%)
	-121.09	(+11.1%)	-67.83	(3.4%)		

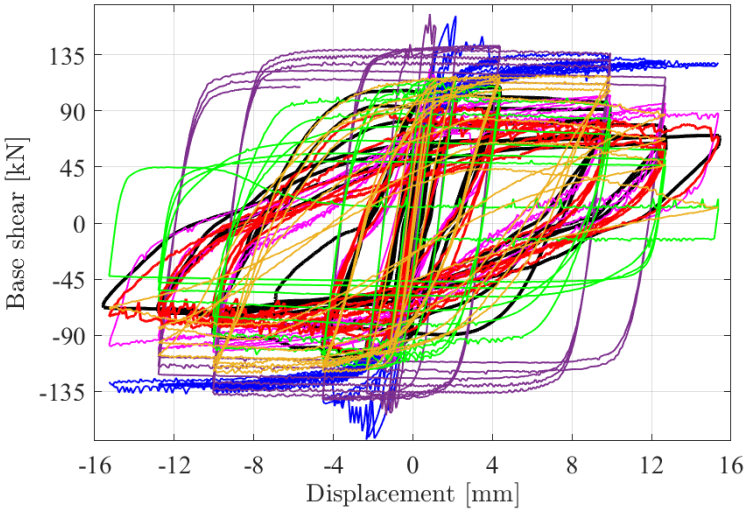

(a)

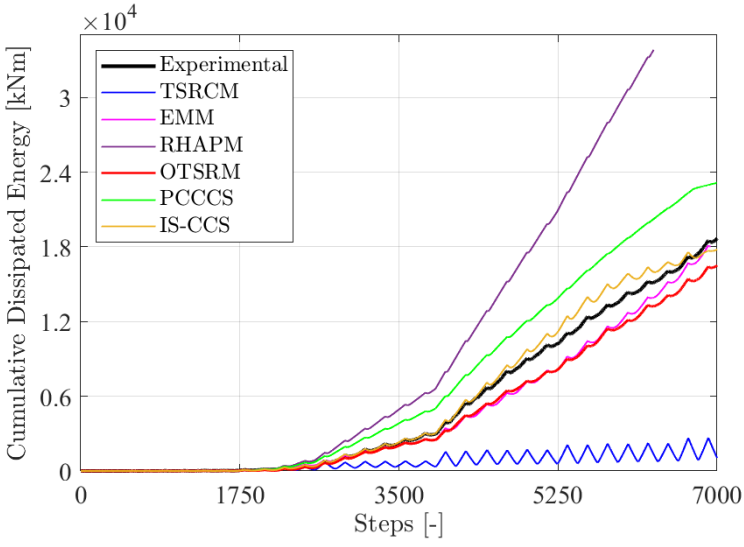

(b)

Figure 5.4: Comparison of (a) force-displacement curve and (b) cumulative dissipated energy between the experimental and numerical results derived from the different constitutive models used for wall TUD-COMP-6.

5.4 Low wall LOWSTA

The low wall LOWSTA was a double-clamped wall with an aspect ratio of 1.35. It has already been used to validate the user developed constitutive model OTSRM in Chapter 4, and its dimensions and damage pattern at failure can be found in Table 4.1 and Figure 4.1a, respectively. The material properties adopted in Chapter 4 are used here for the macro-models as well, whereas in the case of the micro-models the same material properties are adopted for both bed- and head-joints (Table 5.7).

Table 5.7: Input material parameters used for the numerical modelling of low wall LOWSTA and high wall HIGSTA for the six examined constitutive models.

Material input parameters		TSRCM	RHAPM/EMM/OTSRM		PCCCS/SI-CCS	
			horizontal direction $i=x$	vertical direction $i=y$	head-joints $i=h$	bed-joints $i=b$
Modulus of elasticity / Normal stiffness of interface	$E\ [MPa]$	1491	1491	1491	48	48
Shear Modulus/stiffness	$G\ [MPa]$	-	500		21	21
Poisson's ratio	$\nu\ [-]$	0.14	-	-	-	-
Threshold angle	$\theta_{fl}\ [rad]$	-	0.349		-	-
Diagonal angle	$\alpha_{diag}\ [rad]$	-	0.805		-	-
Tensile strength	$f_t\ [MPa]$	0.10	0.10	0.04	0.04	0.04
Compressive strength	$f_c\ [MPa]$	6.20	6.20	6.20	6.20	6.20
Strain/displacement at peak compressive strength	$\varepsilon_{pc}\ [-]$	-	0.01	0.01	0.897	0.897
Fracture energy in tension	$G_{ft}\ [N/mm]$	0.010	0.010	0.005	0.005	0.005
Fracture energy in compression	$G_{fc}\ [N/mm]$	40.0	40.0	40.0	40.0	40.0
Cohesion	$c_0\ [MPa]$	-	0.17		0.17	0.17
Friction coefficient	$tan\phi\ [-]$	-	0.43		0.43	0.43
Fracture energy in shear	$G_{fs}\ [N/mm]$	-	1		0.5	0.5
Dilatancy angle	$\psi\ [rad]$	-	-	-	0	0
Density	$\rho\ [T/mm^3]$	$1.652 \cdot 10^{-9}$	$1.652 \cdot 10^{-9}$		-	-
Additional input parameters required						
Unloading factor in compression	λ	-	1		0.95	
Super-hyperbolic Rankine-Hill parameter	m	-	32		-	-
Super-hyperbolic Rankine parameter	n	-	16		-	-
Shear stress contribution to tensile failure	α_τ	-	1		-	-
Biaxial compression control parameter	β	-	-1		-	-
Shear contribution to failure parameter	γ	-	3		-	-
Shear-stress contribution factor for compression	C_s	-	-	-	5	
Input parameters for brick elements						
Modulus of elasticity	$E_{brick}\ [MPa]$	-	-	-	2991	
Poisson's ratio	$\nu_{brick}\ [-]$	-	-	-	0.14	
Density	$\rho_{brick}\ [T/mm^3]$	-	-	-	$1.652 \cdot 10^{-9}$	

Figure 5.5 presents the deformed shape and the principal strains ε_1 or total relative displacements recorded for each numerical model at the minimum ever reached applied displacement (-7.73 mm) during the loading history. In the experiment, diagonal cracks through the mortar-joints where observed, starting from the corners and expanding towards the center of the wall, where they were connected through a vertical crack crossing through the mortar joints; horizontal cracks at the top and bottom bed-joints were also

present (Figure 4.1a). All the macro-models predict the diagonal shear failure, but there are differences in the number of cracks, orientation and location. The TSRCM predicts a diagonal crack starting close to the bottom left corner and extending towards the top right corner. Close to the two lateral sides also vertical cracks can be seen extending over the height of three-four elements (Figure 5.5a). The EMM predicts flexural cracks at the top (left) and bottom (right) sides of the wall, and three parallel diagonal cracks running along the height of the wall. The angle of these cracks with respect to the bed-joint direction is rather steep, reminding more vertical rather than diagonal cracks. As for the RHAPM, the diagonal cracks observed in the previous walls are also observed here; diagonal cracks starting at the top corners and extending towards the opposite bottom corners, crossing in the middle of the wall. Damage is smeared out over many neighboring elements. The last macro-model, OTSRM, predicts a smaller diagonal crack starting from the bottom left corner and extending towards the middle of the wall, where the direction of the crack changes and becomes steeper, almost vertical. Another vertical crack can be observed, whereas cracked elements can be seen also in the other three corners. From the maximum ever reached tensile strains (α_t) presented in Figure 4.1b, we know that diagonal cracks originating from all four corners occurred throughout the loading history of the wall. This acts as a reminder that the plots in this chapter show the maximum strain at the time step of the maximum imposed displacement, and diagonal or flexural cracks that are activated while loading in the opposite direction, may now be closed, as more evident in the case of EMM and TSRCM. The micro-models exhibited some differences in their damage patterns. They both predicted the vertical crack through the mortar joints observed in the middle of the wall during the experiment, but the length of the crack differed. The bed-joint opening that occurred at the top and bottom of the wall during the first cycles of the two analyses soon transformed: in the case of the PCCCS model diagonal step-wise cracks opened from the cracked bed-joints towards the vertical crack; in the case of the SI-CCS the bed-joints at top and bottom started sliding forming sliding planes rather than step-wise cracks (Figure 5.5f), similar to what was observed in the case of wall TUD-COMP-4. In that aspect, the PCCCS was the model that predicted the experimental crack pattern more accurately. It should also be noted that some of the vertical cracks observed in the macro-models (TSRCM, OTSRM, EMM) could be triggered due to the coarse mesh size.

The force-displacement curves presented in Figure 5.6a show that all models were able to capture the base shear capacity with good accuracy. Nevertheless, big differences are observed when it comes to the post-peak behavior, the stiffness and strength degradation and the total energy dissipation. In more detail, the TSRCM predicted the capacity with an accuracy <10%, a big improvement with respect to the other two walls. Nevertheless, the energy dissipation is once more heavily underestimated, and hardening rather than softening is observed. The RHAPM is overestimating the capacity by 8-15%, but its biggest weakness is that it does not predict any softening and that it overestimates the dissipated energy by 266%, the highest overestimation between the models. The micro-models are predicting the capacity with an error of less than 8%. A drop in the capacity is observed after cracking, but the residual shear is overestimated in both cases. More accurately, the shear capacity seems to slightly increase per cycle for the PCCCS model, while on the other hand it reaches a plateau for the SI-CCS model, exhibiting a behavior observed in pure shear sliding. In both cases the models are overestimating the energy dissipation, especially

the SI-CCS model, which does not show any stiffness degradation. An additional analysis was performed for SI-CCS by reducing the factor λ that defines the bilinear curve used for unloading/reloading in compression. The reasoning behind this was that an unloading curve with smaller participation of the elastic branch and bigger participation of the secant part could help to reduce the dissipated energy. However, no change was observed in the type of hysteretic cycles. A small reduction only occurred in the peak and residual strength capacity, the results are therefore not depicted here. Finally, between the two remaining macro-models, the OTSRM captures the peak and residual capacity with the best accuracy (2-10% difference for the peak and 10-35% for the residual base shear). The energy dissipation is underestimated by 11% and is by far the closest numerical prediction with respect to the experimental value.

Table 5.8: Base shear capacity F_{peak}, residual base shear F_{res} at the maximum and minimum imposed displacements and total dissipated energy U for the experimental and numerical results of wall LOWSTA. The values in brackets express the difference in percentage between the numerical and experimental results.

	F_{peak} $[MPa]$		F_{res} $[MPa]$		U $[10^2\ kNmm]$	
Experimental	81.02		48.39		22.49	
	-83.68		-59.01			
TSRCM	76.40	(-5.7%)	76.40	(+57.9%)	1.77	(-92.1%)
	-75.37	(-9.9%)	-69.10	(+17.1%)		
EMM	74.60	(-7.9%)	74.38	(+53.7%)	40.59	(+80.5%)
	-71.43	(-14.6%)	-71.43	(+21.0%)		
RHAPM	92.73	(+14.4%)	88.07	(+82.0%)	83.11	(+269.5%)
	-91.36	(+9.2%)	-89.48	(+51.6%)		
OTSRM	82.34	(+1.6%)	64.97	(+34.3%)	19.95	(-11.3%)
	-75.38	(-9.9%)	-64.59	(+9.5%)		
PCCCS	78.43	(-3.2%)	63.38	(+31.0%)	64.62	(+187.3%)
	-77.09	(-7.9%)	-64.66	(+9.6%)		
SI-CCS	80.99	(+0.0%)	68.31	(+41.2%)	80.58	(+258.3%)
	-80.75	(-3.5%)	-67.19	(+13.9%)		

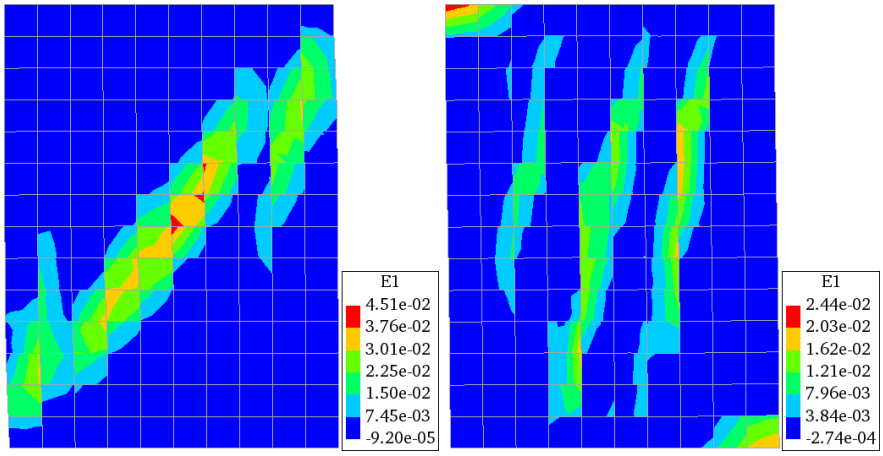

(a) TSRCM

(b) EMM

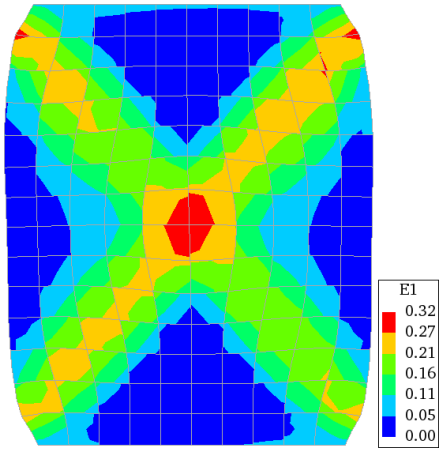

(c) RHAPM

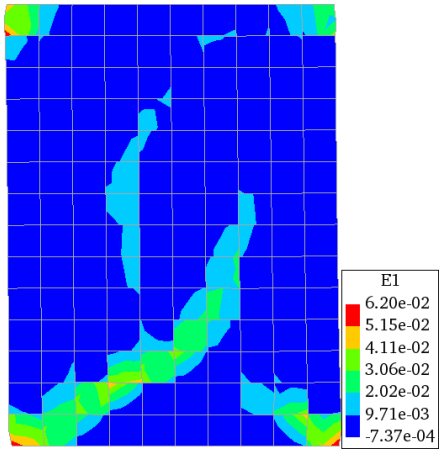

(d) OTSRM

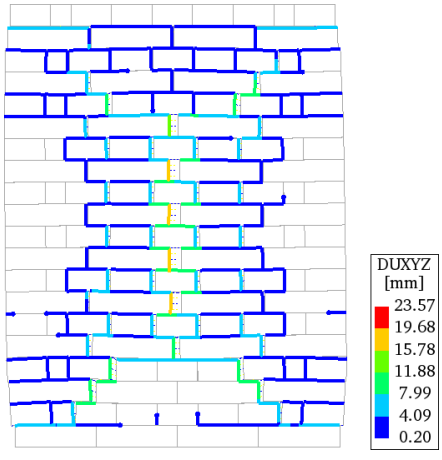

(e) PCCCS

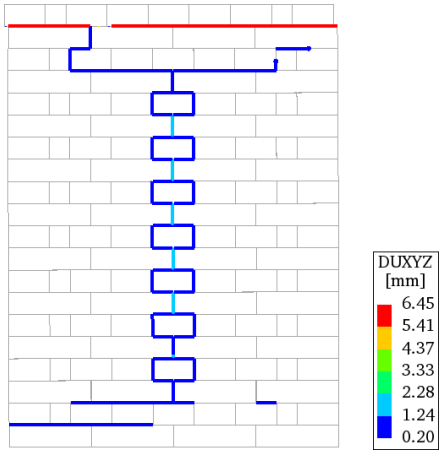

(f) SI-CCS

Figure 5.5: Principal strain ε_1 for the examined macro-models and total relative displacements for the examined micro-models for the numerical model of wall LOWSTA, depicted at the minimum applied displacement -7.7 mm (scale factor=2 for all models).

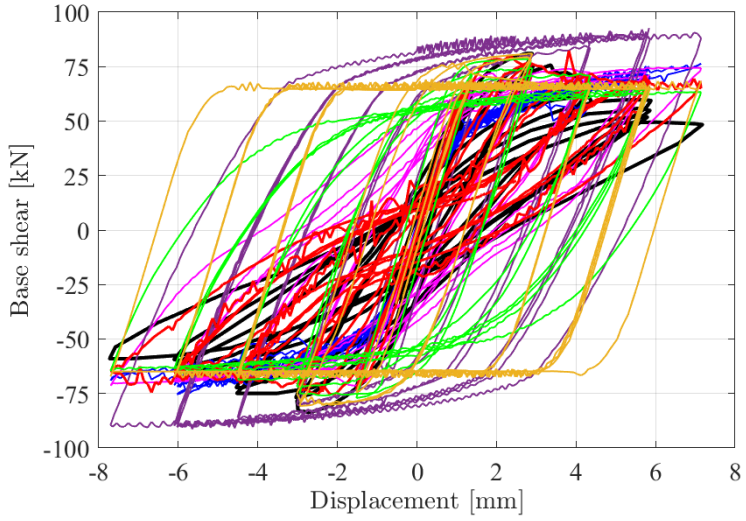

(a)

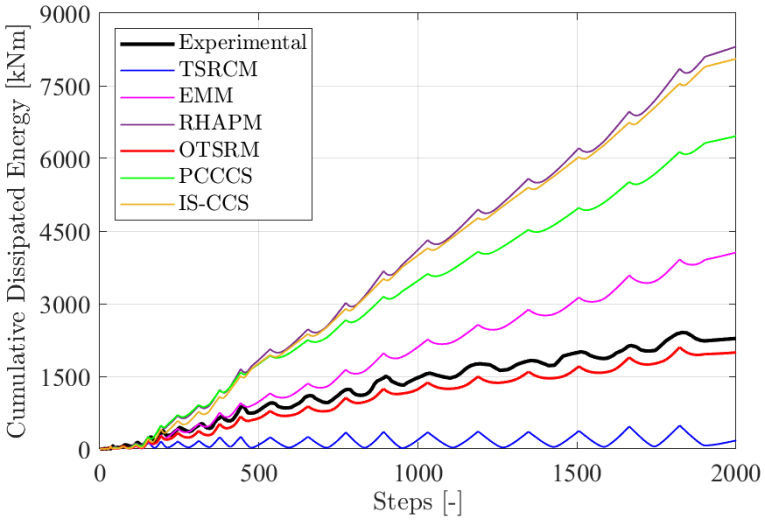

(b)

Figure 5.6: Comparison of (a) force-displacement curve and (b) cumulative dissipated energy between the experimental and numerical results derived from the different constitutive models used for wall LOWSTA.

5.5 High wall HIGSTA

The high wall HIGSTA was a double-clamped wall with an aspect ratio of 2. The same material properties are used as for the low wall LOWSTA, since the two walls were tested in the same lab during the same testing period. The material properties adopted for the six constitutive models are presented in Table 5.7. The type of failure during the experiment was flexural, with horizontal cracks at the top and bottom bed-joints. Surprisingly, most of the constitutive models predicted a different type of failure (Figure 5.7). More specifically, only the TSRCM predicted pure flexural/rocking behavior. The OTSRM shows some flexural cracks at the top and bottom of the wall, but small diagonal cracks start to develop under a small angle as well. The EMM predicts two flexural cracks at the top and bottom of the wall accompanied by a steep diagonal crack. Consistent with the previous walls, the RHAPM led to diagonal shear cracks crossing in the middle of the wall. Even the two micro-models predicted a vertical crack, similar to the one observed in the LOWSTA wall. There is a big difference in the magnitude of total relative displacements between the PCCCS and SI-CCS models, with bigger joint openings in the case of the PCCCS. Horizontal cracks are also observed.

Discrepancies between the different constitutive models were also observed in the force-displacement capacity and cumulative dissipated energy (Figure 5.8 and Table 5.9). The remarks for HIGSTA are similar as the ones of the LOWSTA wall. Strong overprediction of dissipated energy for the RHAPM and PCCCS models (above 400%). It should be mentioned, that although the PCCCS model predicts a very high energy dissipation, this is due to the elastic unloading/reloading path that is adopted in tension, compression and shear. A further refinement of this model to account for the different unloading/reloading paths presented in [31], showed an improved performance for the LOWSTA and HIGSTA walls. The EMM and SI-CCS resulted in similar values for the peak and residual capacity, as well as for the dissipated energy. The TSRCM once more underestimated the dissipated energy, and this time underestimated the capacity by 25-28%. Despite the model looking numerically unstable with many spikes, only a small percentage of steps did not converge, as will be discussed in Section 5.8. Finally, the OTSRM was the most accurate model between the six, estimating both the peak base shear capacity and the residual force with good accuracy (both under 6%). Despite this, it overestimates the dissipated energy by 44% and shows signs of numerical instabilities (spikes) in the force-displacement curve.

Table 5.9: Base shear capacity F_{peak}, residual base shear F_{res} at the maximum and minimum imposed displacements and total dissipated energy U for the experimental and numerical results of wall HIGSTA. The values in brackets express the difference in percentage between the numerical and experimental results.

	F_{peak} $[MPa]$		F_{res} $[MPa]$		U $[10^2\ kNmm]$	
Experimental	71.89		69.40		12.88	
	-71.89		-71.27			
TSRCM	54.15	(-24.7%)	36.43	(-47.5%)	0.45	(-96.5%)
	-51.68	(-28.1%)	-40.88	(-42.6%)		
EMM	62.99	(-12.4%)	58.16	(-16.2%)	28.06	(+117.9%)
	-62.87	(-12.5%)	-60.86	(-14.6%)		
RHAPM	65.26	(-9.2%)	64.32	(-7.3%)	74.53	(+478.6%)
	-64.61	(-10.1%)	-61.72	(-13.4%)		
OTSRM	69.07	(-3.9%)	66.63	(-4.0%)	18.49	(43.5%)
	-73.97	(+2.9%)	-66.86	(-6.2%)		
PCCCS	66.70	(-7.2%)	55.36	(-20.2%)	66.71	(+418.0%)
	-67.45	(-6.2%)	-57.56	(-19.2%)		
SI-CCS	61.77	(-14.1%)	60.84	(-12.3%)	29.27	(+127.3%)
	-61.37	(-14.6%)	-61.37	(-13.9%)		

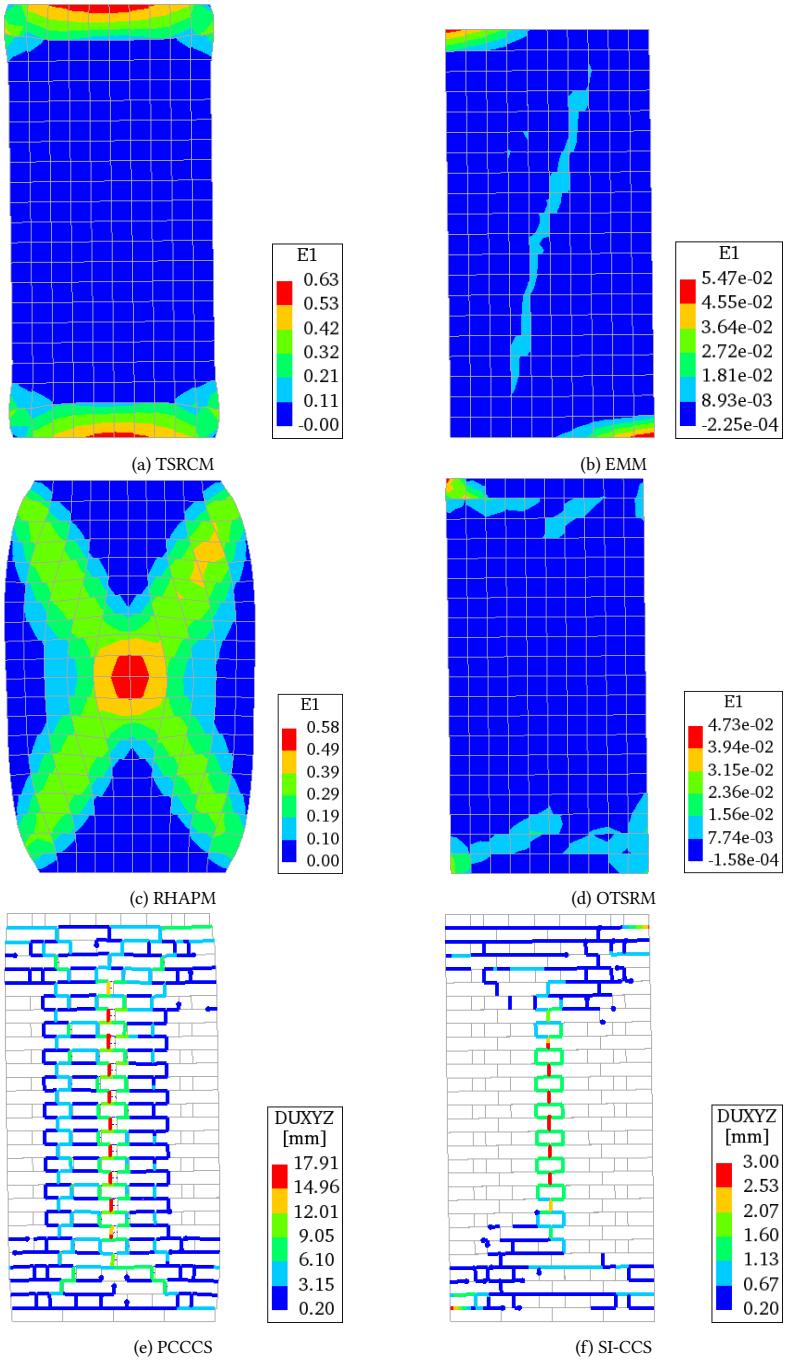

(a) TSRCM (b) EMM

(c) RHAPM (d) OTSRM

(e) PCCCS (f) SI-CCS

Figure 5.7: Principal strain ε_1 for the examined macro-models and total relative displacements for the examined micro-models for the numerical model of wall HIGSTA, depicted at the minimum applied displacement -12.96 mm (scale factor=2 for all models).

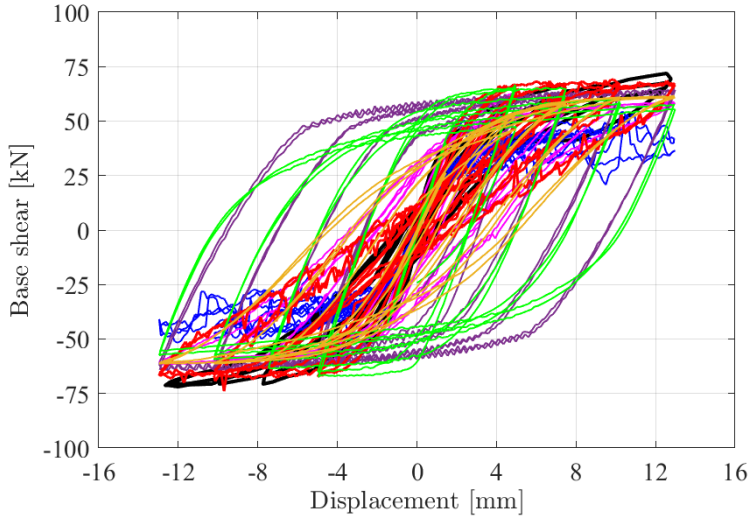

(a)

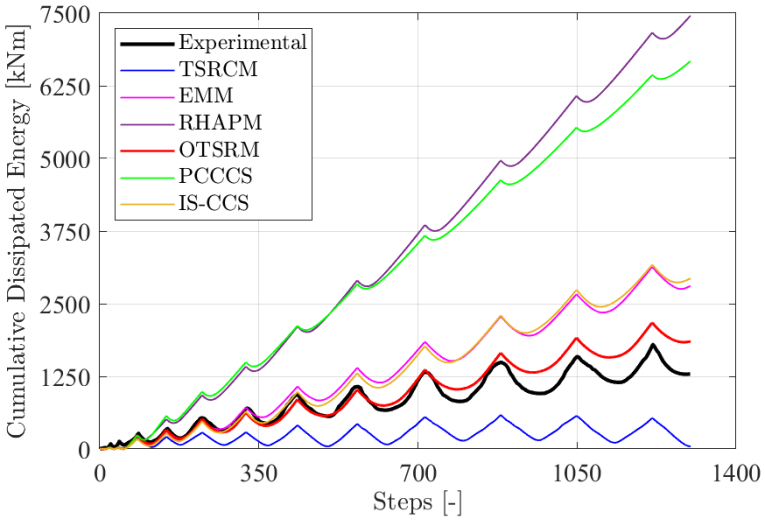

(b)

Figure 5.8: Comparison of (a) force-displacement curve and (b) cumulative dissipated energy between the experimental and numerical results derived from the different constitutive models used for wall HIGSTA.

5.6 TU Eindhoven hollow

Unlike the previous four walls that were tested cyclically, the remaining two walls correspond to monotonic tests, because although big focus was given in developing a new constitutive model with improved hysteretic behavior, the monotonic behavior should be validated too. For this purpose, firstly, two identical double clamped walls with an opening (TUe-Hollow) that were tested in TU Eindhoven [201] are used. Additionally, these two tests present specific boundary conditions that could not be found in other cyclic tests and they were considered also for this reason. The walls had dimensions of $990 \times 1000 mm^2$ with an opening of $204 \times 382 mm^2$ and comprised solid clay bricks of dimensions $204 \cdot 98 \cdot 50 mm^3$ and mortar joints of 10 mm thickness. A vertical pre-compression load of 0.30 MPa was applied at the top of the walls through a steel beam under double clamped conditions, followed by a monotonically increasing horizontal displacement. Unlike the previous walls, during the horizontal loading no vertical displacements were allowed at the top of the wall. The opening resulted in two small piers, and the tests resulted in different load–displacement curves, and different crack patterns. However, for both walls diagonal cracks initiated from the opening's corners and propagated towards the top and bottom of the wall in step-wise patterns (Figure 5.9). Subsequently, horizontal tensile cracks were also formed at the top and bottom of the piers. Eventually, failure due to toe-crushing occurred at the bottom and top of the wall [33]. The material properties adopted by [33] are used for the micro-models. In the case of the SI-CCS model, the compressive strength and its corresponding fracture energy are reduced. This reduction compensates for the absence of the compression cap that would ensure the limitation of shear stresses for high compressive stresses. The compressive strength is limited from 10.4 MPa to 4 MPa, based on the yield surface $f_3 = \sigma_2 + 9\tau^2 - \sigma(\kappa_3)$ describing the cap in the micro-model of Lourenco [33]. Setting $f_3 = 0$ and assuming that $\tau = c_0 - tan\phi\sigma_2$ and $\sigma(\kappa_3) = 10.4$ MPa the new limited value of 4 MPa is derived. For the macro-models, the material properties suggested by [202] and [203] were applied first, but this led to an overestimation of the load capacity of the structure for three out of the four constitutive macro-models. Therefore, some material input parameters were calibrated and the analyses were performed again. In Table 5.10, the calibrated properties are presented in **bold**.

The principal strain localization of the macro-models at ultimate displacement in Figure 5.10 shows the impact of the opening in the damage localization. In three out of the four macro-models, the corners of the windows, where stresses concentrate, also led to crack development. The exception is the TSRCM, where diagonal cracks form from the bottom left and top right corners of the wall and extend through the two piers. However, the cracks are neither starting nor finishing on any corner of the opening; rather they concentrate close to the mid-height of the opening. In the case of the EMM vertical cracks, instead of diagonals, start from the top right and bottom left corners of the opening, extending towards the top and bottom sides. Horizontal cracks at the level of the window can also be observed, in the same locations as in the experiment. The RHAPM resulted in diagonal cracks extending from the bottom left corner of the wall to the top left corner of the window, and from the bottom right corner of the window to the top right corner of the wall. A small concentration of strains is observed in the bottom left corner of the window. The path of the principal strains is not the one observed experimentally, and not the shortest path expected either. As for the OTSRM, diagonal cracks are extending from the bottom

Table 5.10: Input material parameters used for the numerical modelling of monotonic walls TUe-Hollow and TUe-Solid for the six examined constitutive models.

Material input parameters		TSRCM	RHAPM/EMM/OTSRM		PCCCS/SI-CCS	
			horizontal direction $i=x$	vertical direction $i=y$	head-joints $i=h$	bed-joints $i=b$
Modulus of elasticity / Normal stiffness of interface	$E\ [MPa]$	3960	7520	3960	82	82
Shear Modulus/stiffness	$G\ [MPa]$	-	1460		36	36
Poisson's ratio	$\nu\ [-]$	0.36	-	-	-	-
Threshold angle	$\theta_{fl}\ [rad]$	-	0.349		-	-
Diagonal angle	$\alpha_{diag}\ [rad]$	-	0.809		-	-
Tensile strength	$f_t\ [MPa]$	**0.16**	**0.16**	**0.114**	0.25	0.25
Compressive strength	$f_c\ [MPa]$	**4.00**	**4.00**	6.20	**4.0**/10.5	**4.0**/10.5
Strain/displacement at peak compressive strength	$\varepsilon_{pc}\ [-]$	-	0.0035	0.0035	0.897	0.897
Fracture energy in tension	$G_{ft}\ [N/mm]$	0.048	0.05	0.048	0.018	0.018
Fracture energy in compression	$G_{fc}\ [N/mm]$	**16.0**	**16.0**	**16.0**	15.00	15.00
Cohesion	$c_0\ [MPa]$	-	0.35		0.35	0.35
Friction coefficient	$tan\phi\ [-]$	-	0.75		0.75	0.75
Fracture energy in shear	$G_{fs}\ [N/mm]$	-	-		0.125	0.125
Dilatancy angle	$\psi\ [rad]$	-	-	-	0	0
Additional input parameters required						
Unloading factor in compression	λ	-	1		0.95	
Super-hyperbolic Rankine-Hill parameter	m	-	32		-	-
Super-hyperbolic Rankine parameter	n	-	16		-	-
Shear stress contribution to tensile failure	α_τ	-	1		-	-
Biaxial compression control parameter	β	-	-1		-	-
Shear contribution to failure parameter	γ	-	3		-	-
Shear-stress contribution factor for compression	C_s	-	-	-	9	9
Input parameters for brick elements						
Modulus of elasticity	$E_{brick}\ [MPa]$	-	-	-	16700	
Poisson's ratio	$\nu_{brick}\ [-]$	-	-	-	0.15	
Density	$\rho_{brick}\ [T/mm^3]$	-	-	-	$1.805 \cdot 10^{-9}$	
Tensile strength	$f_{t,brick}\ [MPa]$	-	-	-	2	
Fracture energy in tension	$G_{ft,brick}\ [N/mm]$	-	-	-	0.08	

left and top right corners of the opening towards the top and bottom sides of the wall. Nevertheless, they are relatively short and do not reach to the opposite sides. Horizontal cracks are present in this model as well, similar to EMM and the experiment. However, they are not observed at the level of the window bed and head, but two/three elements lower and higher, respectively. The two micro-models resulted in similar crack patterns, resembling the experimental ones. In more detail, they both predicted the horizontal crack at the top of the left pier, observed also in Panel J2G in Figure 5.9; they also predicted the same diagonal crack, starting from the bottom right window corner and extending towards the bottom left corner of the wall, as seen in Panel J3G. Small differences exist regarding the diagonal stepped cracks at the top right of the wall: either one (PCCCS) or two (SI-CCS) diagonal cracks occurred. In both models, a horizontal crack at the base of the left pier formed too, leading to the rocking of the left pier.

The experimental load capacity varied between 36.9 and 47.1 kN. Apart from the TSRCM

that significantly underestimated the load capacity (39-52%), and the PCCCS model that significantly overestimated the load capacity (34-71%), the rest of the numerical predictions were close to the experimental results. The EMM slightly overestimated the maximum of the two provided experimental values (48.8 kN), while the RHAPM, OTSRM and SI-CCS fell within the two experimental values, being closer to the maximum of the two values (Table 5.11). Similarly, the residual forces of the numerical models (except for TSRCM) fell within the experimental results.

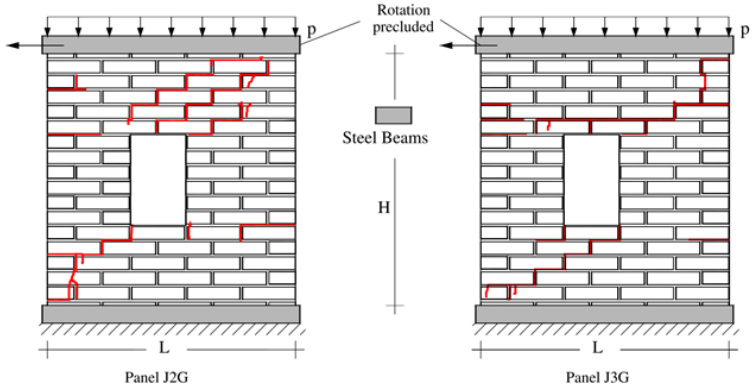

Figure 5.9: Geometry and crack locations of the TU Eindhoven hollow walls observed at the end of the experiment, as taken from [204].

Table 5.11: Base shear capacity F_{peak}, residual base shear F_{res} at the maximum imposed displacement and total dissipated energy U for the experimental and numerical results of TU Eindhoven hollow wall.. The values in brackets express the difference in percentage between the numerical and experimental results.

	F_{peak} $[MPa]$		F_{res} $[MPa]$		U $[10^2\ kNmm]$
Experimental	36.87		28.22		7.34
	47.11		6.45		13.39
TSRCM	22.65	(-51.9/-38.6%)	2.25	(-65.1/-92.0%)	1.44
EMM	48.79	(3.6/32.3%)	20.92	(-25.9/+224.5%)	8.12
RHAPM	42.85	(-9.0/16.2%)	28.50	(-1.0/+342.1%)	8.43
OTSRM	46.41	(-1.5/25.9%)	20.33	(-28.0/+215.4%)	8.11
PCCCS	63.14	(+34.0/+71.3%)	21.19	(-24.9/+228.7%)	9.78
SI-CCS	44.54	(-5.5/20.8%)	21.17	(-24.9/+228.4%)	8.26

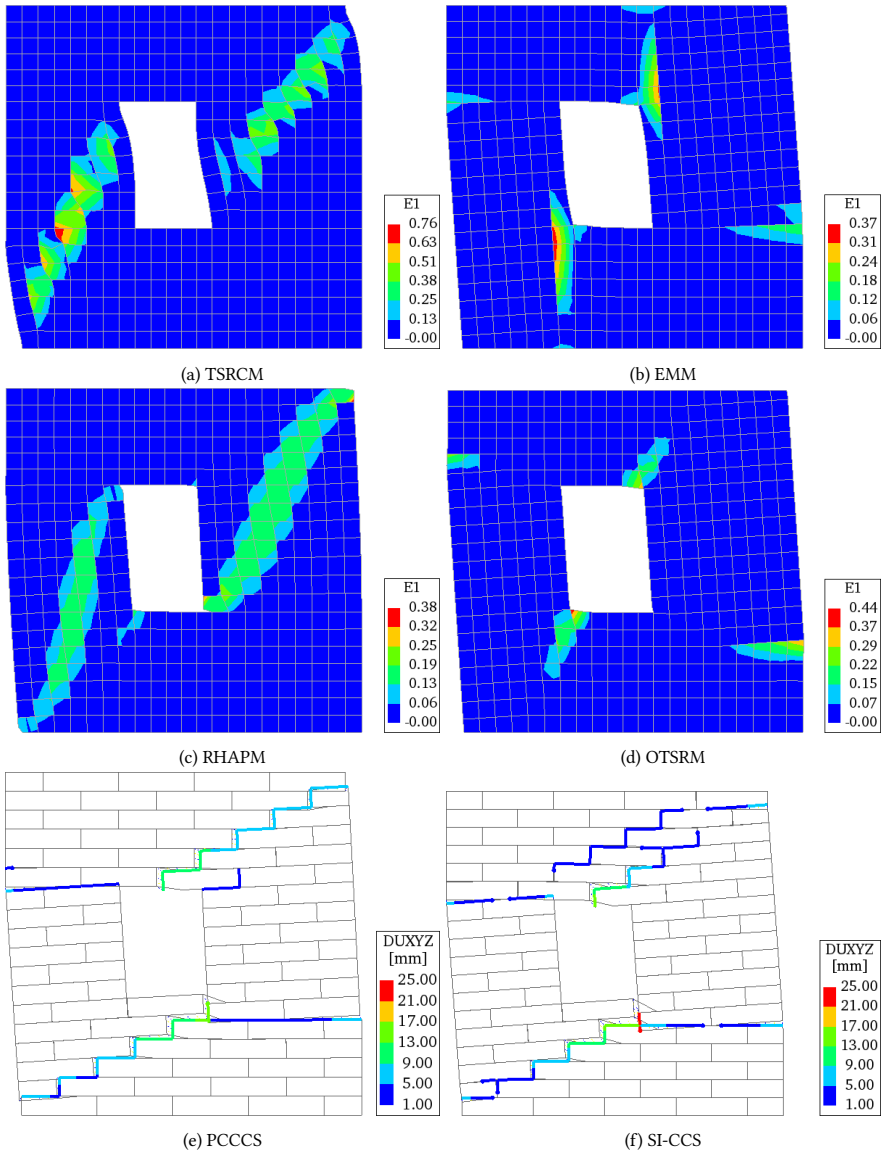

(a) TSRCM (b) EMM

(c) RHAPM (d) OTSRM

(e) PCCCS (f) SI-CCS

Figure 5.10: Principal strain ε_1 for the examined macro-models and total relative displacements for the examined micro-models for the numerical model of the TU Eindhoven Hollow wall, depicted at the end of the numerical analysis at an applied displacement of 24 mm (scale factor=2 for all models).

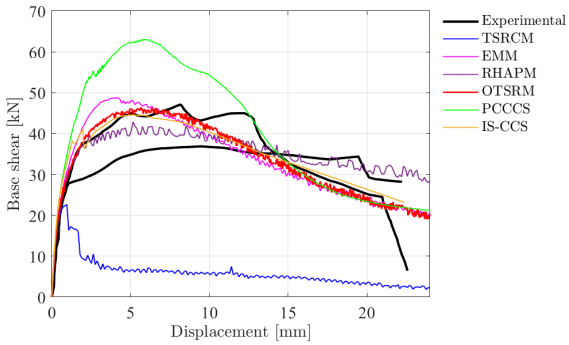

Figure 5.11: Comparison of force-displacement curve between the experimental and numerical results derived from the different constitutive models used for wall TU Eindhoven Hollow.

5.7 TU Eindhoven solid

The TU Eindhoven Solid walls (TUe-Solid) were tested during the same experimental campaign as the hollow walls (TUe-Hollow), under the same loading and boundary conditions. They had dimensions of $990 \times 1000 mm^2$ and were constructed by the same clay bricks and mortar. The tests were performed considering three different levels of vertical pre-compression. Here, the walls relating to a pre-compression level of 0.3 MPa are modelled. The crack pattern of these walls was characterized by initial horizontal cracks along the top and bottom bed-joints of the wall, succeeded by diagonal shear cracks and cracks through the bricks, as well as crushing of the compressed toe. These walls have acted as benchmark for the validation of many constitutive micro-models (e.g., [33],[15],[91],[17]). In most of these validations, the cracks through the bricks are modelled through additional interface elements, otherwise a stiffer behavior and higher collapse load are predicted [205]. Interestingly, the potential cracks through bricks are not modelled in the case of the TUe-Hollow walls, constructed with the same materials and tested in the same period at TU Eindhoven, since cracks were not observed through the bricks. In this study, the cracks through the bricks are not considered through interface elements, but rather the bricks are modelled as inelastic elements, with brittle failure in tension. The material properties adopted by [33] are used for the micro-models, with the modification of compressive strength and fracture energy discussed already in subsection 5.6.

The modelling of the walls using macro-models was more complicated, since not only the input parameters suggested in literature for macro-models [[202],[203]], but also the ones adopted for the simulation of the hollow walls were leading to an overestimation of the load capacity and for some models even in overstiff behavior. The force-displacement curves derived using the same properties as for the hollow walls are presented in Figure 5.15a. The micro-models predict the capacity with good accuracy (Figure 5.15). Between the macro-models, the TSRCM was the only one that predicted a realistic failure load without doing any material calibration; using the calibrated material properties used for the hollow walls led to a decreased failure load. As can be seen in Figure 5.15a the RHAPM overestimated the capacity the most (59-66%), followed by the OTSRM (49-55%), and finally the EMM (36-42%). A difference in the initial stiffness is also observed between the three models, with the OTSRM exhibiting a stiffer behavior. From the graph, it appears that neither the EMM nor the RHAPM have yet reached their peak capacity. The peak capacity for the RHAPM model is reached at a displacement of 5.58 mm and corresponds to 84.7 kN, whereas for the EMM the failure load is equal to 79.6 kN, but for a much higher horizontal displacement of 8.2 mm.

A sensitivity study was conducted to understand the reason behind the overestimation in the capacity. It was observed that due to the boundary conditions, higher compressive stresses were present along the compressive strut. A small compressive strain at peak ($\varepsilon_{pci} = 0.0035$) leads to a more rapid rise in compressive stresses. An increase in the compressive stresses results in an increase in the Coulomb-based shear capacity for the three continuum models. Moreover, a low compressive strain at peak in combination with a high fracture energy in compression leads to slow softening rate, which means slower reduction of compressive stresses, and therefore also of compressive and shear capacity. This has an immediate impact in the load capacity of the wall.

A further calibration of the material properties, based on the abovementioned observa-

tions led to a better match between the numerical and experimental results for the three macro-models. The necessary changes were, first, to reduce the compressive strength from 4 MPa to 3 MPa and, second, to reduce the fracture energy in compression from 16 N/mm to 2 N/mm: this was the most defining factor for obtaining a post-peak behavior. Those modifications led to numerical results that matched better the experimental ones, in terms of load capacity and post-peak behavior (Figure 5.15b). Can, however, such a major calibration of the material properties be accepted? The splitting of the bricks observed during the experiment has always been accounted for in micro-models, either by modelling the potential cracks through interface elements, or assigning nonlinear cracking properties in the continuum bricks. The tensile splitting of the bricks, due to high compressive stresses applied on their top and bottom surfaces is then captured easily. However, most continuum models for masonry based on a phenomenological approach, do not adjust their tensile failure criteria to incorporate this brick splitting. To compensate for this effect, the compressive strength is reduced and the compressive fracture energy is reduced significantly, to trigger the more brittle behavior observed when splitting through the bricks occur.

As for the damage localization, different observations were made in the models. The TSRCM and RHAPM predicted diagonal cracks, whereas the EMM and OTSRM predicted the flexural cracks at the top and bottom of the wall, as well as much thinner diagonal cracks, in different orientations, steeper for the EMM and with small angle for the OTSRM. Regarding the two micro-models, similar behavior is observed in the failure mechanism. They both presented a crack pattern quite representative of the experimental, with horizontal cracks along the top and bottom bed-joints, and diagonal cracks running in parallel from the top right towards the bottom left corner. Overall, in the PCCCS a wider step-wise diagonal crack was observed, whereas in the SI-CCS model the damage is distributed in a few more cracks, resulting in more cracks of smaller width. Cracking occurred in some brick elements as well.

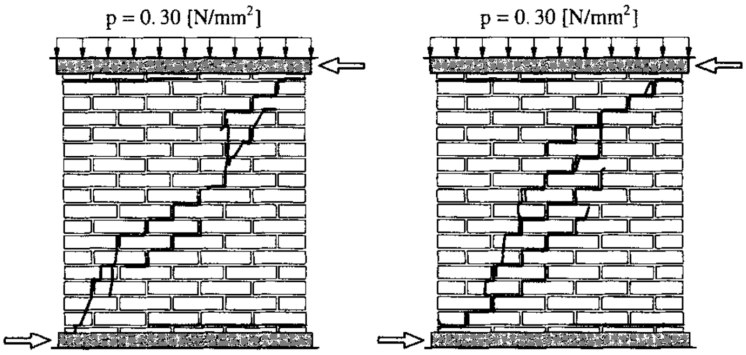

Figure 5.12: Geometry and crack locations of the TU Eindhoven solid walls observed at the end of the experiment, as taken from [33].

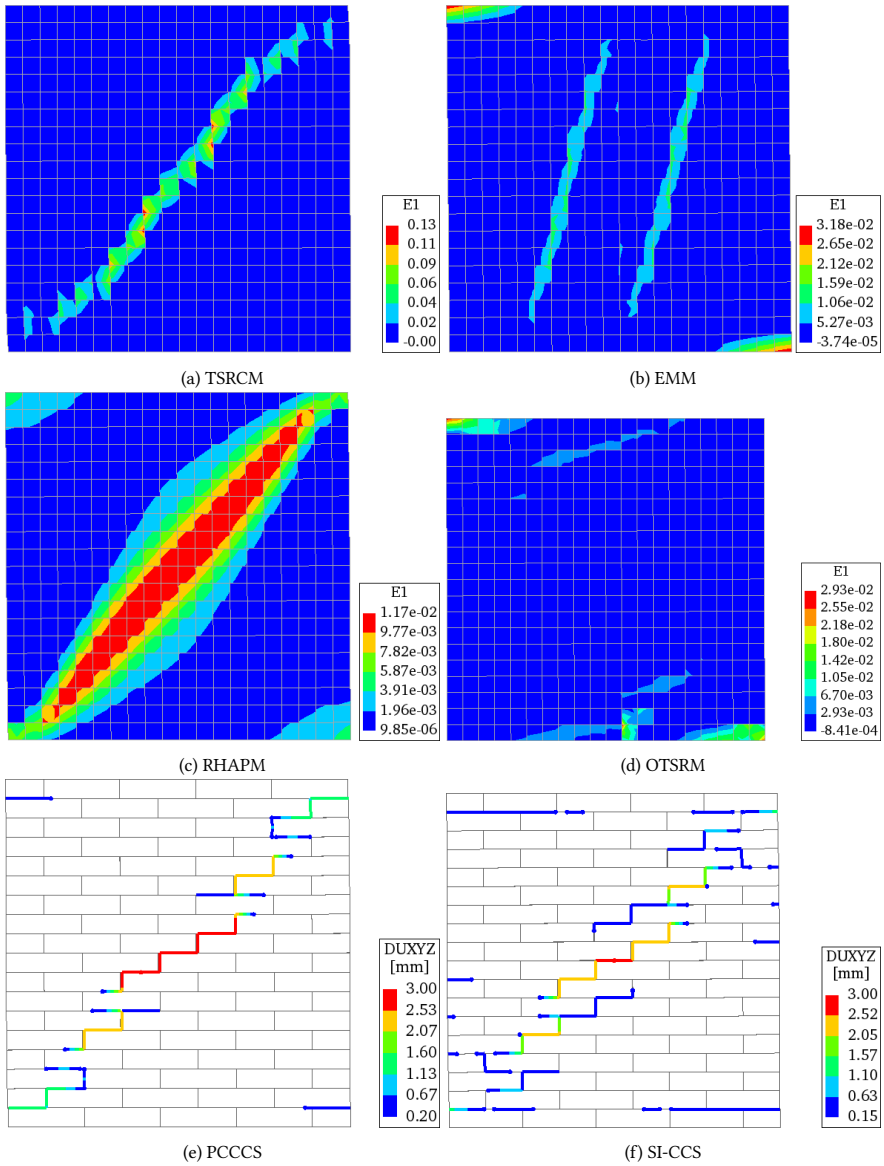

(a) TSRCM (b) EMM

(c) RHAPM (d) OTSRM

(e) PCCCS (f) SI-CCS

Figure 5.13: Principal strain ε_1 for the examined macro-models and total relative displacements for the examined micro-models for the numerical model of the TU Eindhoven Solid wall, before further calibration, depicted at the end of the numerical analysis at an applied displacement of 4 mm (scale factor=2 for all models).

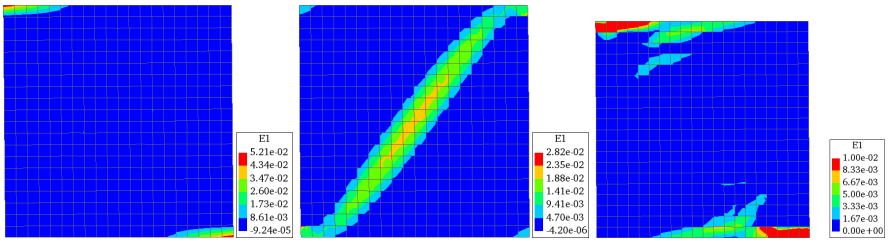

(a) EMM (b) RHAPM (c) OTSRM

Figure 5.14: Principal strain ε_1 for the calibrated models of the EMM, RHAPM and OTSRM after further reduction of the compressive strength and fracture energy of the TU Eindhoven Solid wall, depicted at the end of the numerical analysis at an applied displacement of 24 mm. The plotted tensile strains of OTSRM correspond to a horizontal displacement of 3 mm, before the sudden drop (scale factor=2 for all models).

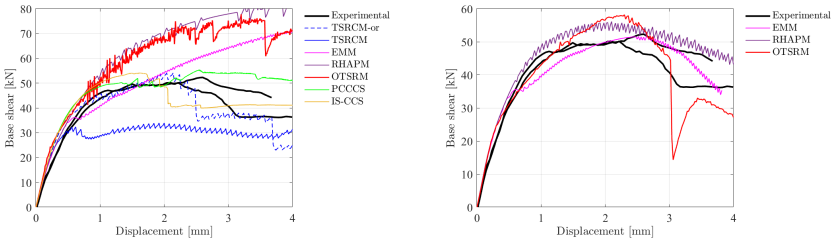

(a) Before calibration (b) After calibration

Figure 5.15: Comparison of force-displacement curve between the experimental and numerical results derived from the different constitutive models used for wall TU Eindhoven Solid before and after further calibration of macro-model parameters for compressive strength, fracture energy in compression and shear coefficient.

Table 5.12: Base shear capacity F_{peak}, residual base shear F_{res} at the maximum and minimum imposed displacements and total dissipated energy U for the experimental and numerical results of TU Eindhoven solid wall. The values presented for the TSRCM and the PCCCS models are corresponding to the numerical analyses with the original material properties as taken from literature [33, 202]. The numerical values of the EMM, RHAPM and OTSRM models are corresponding to the calibrated models, where the compressive strength and fracture energy are reduced further. The values in brackets express the difference in percentage between the numerical and experimental results.

	F_{peak} $[MPa]$		F_{res} $[MPa]$		U $[kNmm]$
Experimental	50.15		36.25		86.46
	52.29		44.15		77.59
TSRCM	54.12	(3.5/7.9%)	25.14	(-43.1/-30.6%)	155.29
EMM	51.76	(-1.0/3.2%)	35.31	(-20.0/-2.6%)	164.62
RHAPM	56.13	(7.3/11.9%)	46.82	(6.0/29.1%)	185.18
OTSRM	58.16	(11.2/16.0%)	27.15	(-38.5/-25.1%)	161.57
PCCCS	42.25	(-19.2/-15.8%)	22.56	(-48.9/-37.8%)	69.79
SI-CCS	54.12	(3.5/7.9%)	41.19	(-6.7/13.6%)	86.59

5.8 Performance and accuracy

An indicator about the reliability and accuracy of the numerical results is the convergence of the incremental-iterative procedure. This is especially relevant when softening is involved, as is the case here for tension, compression as well as shear at local material level, resulting in peaks and valleys in the global force-displacement response. In order to be able to compare the performance of the six studied constitutive models, the same solution procedure was chosen for all the numerical analyses. The Quasi-Newton (also known as secant) iteration scheme was applied to all analyses, and it was required to satisfy either the displacement or the force norm, both set to 0.01. The maximum number of iterations per step was set to 100 or 200 (depending on the wall), and if it was reached without convergence of the force or displacement norm, the analysis was still allowed to continue. As a result, some analyses had temporarily a few non-converged steps, but convergence and force equilibrium were restored in consequent steps without divergence of the analyses. From the 36 numerical analyses two diverged before the end of the imposed loading protocol: the analyses of TUD-COMP-6 for the EMM and RHAPM.

Figure 5.16 presents the percentage of converged steps for all numerical analyses. The color used per constitutive model is consistent with the colors used in the force-displacement curves, so that the comparison can be easier for the reader. To represent the unconverged steps, the same color but with 50% transparency is used. The first observation is that the wall with the most convergence issues (divergence or high percentage of unconverged steps) was the cantilever shear wall TUD-COMP-6. Two of the models diverged, whereas 6% and 18% of the total number of steps (4128) of the TSRCM and the OTSRM models, respectively, did not converge. Another observation is that despite some curves appearing "noisy", only a negligible percentage of their steps did not converge. For example the TSRCM, RHAPM and PCCCS cases of TUD-COMP-4 have small spikes, but less than 0.25% of steps did not converge. On the other hand, some analyses that appear to have no spikes (for example the OTSRM of TUD-COMP-4, as discussed also in Chapter 4) have a high percentage of non-converged steps. Finally, the newly developed constitutive model OTSRM, presented in this dissertation, performs poorer than the other five constitutive models in terms of numerical stability.

One of the strong arguments in favor of using macro-models is the numerical efficiency in terms of computational time, with respect to the micro-models. Table 5.13 summarizes the computational time required for each numerical analysis. To make a fair judgement, the numerical analyses were run in series, and as already mentioned, for each wall the same size of load-steps and total steps were applied. It is surprising how the computational time of each constitutive model was influenced by the properties of the wall modelled. The RHAPM for example took surprisingly longer than expected in the case of LOWSTA and HIGSTA walls, and not for reasons of non-converged steps. As might be expected, the more complicated the definition of a constitutive model and its algorithm, the longer the time required for the solution of the numerical equations. The high number of iterations per step leads to a significant increase in the computational time, in the case that the analysis is not converging (OTSRM for TUD-COMP-4 and TUe-Solid). In fact, in an attempt to decrease the total number of iterations and non-converged steps, the walls were also modeled and analysed with a Full Newton-Raphson iterative scheme. However, only the TSRCM performed better with this solution scheme; the remaining macro-models resulted

in more non-converged steps and more spikes in the force-displacement graph than before. Therefore, the Quasi-Newton method was consistently used for all the analyses and all the constitutive models, for the sake of consistency.

Among the macro-models, the EMM performed consistently better in terms of computational time, followed by the TSRCM. Since a direct relationship between total stresses and strains is provided in the directions of the material, which coincide with the global axes, this is to be expected. The TSRCM still requires the transformation of stresses and strains from the principal to the global directions. The RHAPM and the OTSRM both were slower; since they are both more complicated algorithms. Either the return-mapping algorithm in RHAPM or the iterative internal shear loop for the OTSRM, and the set-up of the local x-y stiffness matrix increase the probability for convergence issues and the computational time as well. Regarding the micro-models, the SI-CCS requires additional time (almost double in some cases) than the PCCCS. The sub-stepping iterative loop and the internal update of the stiffness matrix in each sub-step could be the reasons behind this additional time. Nevertheless, depending on the wall modelled, the micro-models performed better than some macro-models in terms of computational time. For example for TUD-COMP-4, and LOWSTA and HIGSTA walls they ran faster than the OTSRM and RHAPM. It should be noted, however, that for larger systems (e.g., complete buildings) where the number of degrees of freedom increases significantly, the solver time is getting more dominant than the time at the integration point level.

Other factors that can influence the performance of the constitutive models, but were not investigated are the size of the time step (for cyclic analyses, or load step in general), the convergence norm used for reaching equilibrium, and the nonlinear solution procedure and stepping scheme chosen. Here, for example, all the analyses were performed in displacement control, but if load control and/or arc-length control were used the performance would be influenced, probably resulting in additional numerical difficulties and convergence issues.

Table 5.13: Computational time required for the numerical analysis of each wall for each constitutive model used. The elapsed time is presented in h:mm:ss format.

	TUD-COMP-4	TUD-COMP-6	LOWSTA	HIGSTA	TUe-Hollow	TUe-Solid
TSRCM	0:17:49	1:31:34	0:06:48	0:18:07	0:05:23	0:01:25
EMM	0:11:44	0:36:25*	0:03:12	0:04:17	0:02:15	0:00:40
RHAPM	0:45:54	15:37:12*	1:01:35	1:14:54	0:06:57	0:00:56
OTSRM	1:12:53	1:16:27	0:19:20	0:12:25	0:05:17	0:03:31
PCCCS	0:18:30	1:04:54	0:09:05	0:11:56	0:01:15	0:01:35
SI-CCS	0:37:37	1:40:26	0:16:15	0:23:18	0:02:33	0:01:29

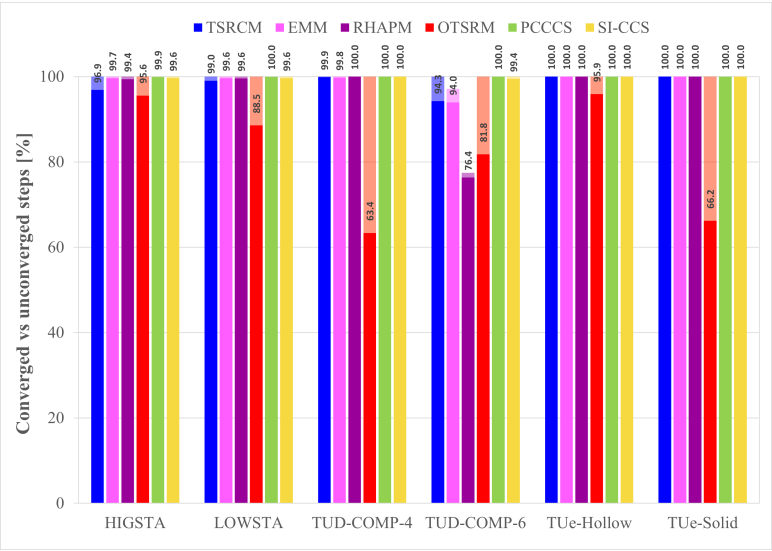

Figure 5.16: Percentage of converged steps (full color) and unconverged steps (50% color transparency) for the numerical analysis of each modelled wall for the different constitutive models.

Table 5.14: Total number of steps, total number of degrees of freedom (DOF) and total number of iterations for the numerical analysis of each wall for each constitutive model used. For the analysis with the asterisk the analysis diverged, and the number of iterations until the divergence is presented instead.

	TUD-COMP-4	TUD-COMP-6	LOWSTA	HIGSTA	TUe-Hollow	TUe-Solid
DOF - macromodels	6994	6994	938	1322	2522	2562
DOF - micromodels	11118	11192	2700	4050	2750	2750
Total number of steps	2816	4128	2008	2002	200	200
TSRCM	10992	70730	16216	40235	6437	1813
EMM	12064	52945*	12803	16535	3337	917
RHAPM	8376	37612*	14076	19095	2834	707
OTSRM	205192	326492	57479	36778	3493	10448
PCCCS	8313	65490	14413	15635	3011	1307
SI-CCS	8345	66958	19681	9187	4298	2728

5.9 Discussion and conclusions

In this chapter, six masonry walls were modelled using six different constitutive models: four continuum macro-models and two interface micro-models. From the six walls, four were loaded cyclically to validate the constitutive models also based on their hysteretic behavior, a topic that has not been researched sufficiently. Where possible, the material properties provided by the experimental campaigns were used, using consistently the same parameters for the two sets of constitutive models: micro and macro-models. Per wall, the numerical results obtained for the six models were compared with each other and with the experimental results, in terms of damage localization, peak base shear capacity, residual base shear capacity, energy dissipation, as well as numerical stability and computational time. Through the comparison of the different cases, one thing became clear: not a single model performed better than the rest consistently in all the examined cases. It is not possible to identify one of the six aforementioned models as the best one for modelling URM structures. Nevertheless, the performance of each model is summarized in the following paragraphs.

The TSRCM is the most simplified of the six constitutive models, and the only not specifically developed for masonry. It performs very poorly in the case of cyclic loading, always severely underestimating the dissipated energy because of the inherent secant unloading/reloading. Regarding the prediction of the failure mechanism it performs adequately, predicting the correct failure mechanism and in most cases a crack pattern representative of the experimental one. Its ability to predict the failure load varies: it led to a significant overestimation of the capacity for shear walls with low aspect ratio, while its prediction improved for higher aspect ratios, but not sufficiently to consider it as an accurate constitutive model.

The EMM performed well in predicting the base shear capacity and even the residual base shear. Overall, it adequately described the dissipated energy, giving a good estimation for one of the walls, and overestimating or underestimating the energy (within reasonable margins) for the rest. It also performed very satisfactorily in terms of computational time and even numerical stability, despite one of the analyses diverging. In most of the examined cases the damage would be diffused over many smaller cracks, rather than concentrate in fewer and bigger ones. This can be identified as the major drawback of the model: its inability to capture the damage localization. In most cases the obtained crack pattern was very diffused, which in not representative of the localized experimental crack pattern at ultimate limit state. Another disadvantage is the expertise required from the engineer when selecting the type of head-joint failure, a choice that, although not shown in this study, can influence heavily the numerical results.

The RHAPM performed less good than the other two macro-models specifically developed for masonry in predicting the hysteretic behavior of the walls tested cyclically. The elastoplastic unloading/reloading leads to an overestimation of the dissipated energy when the failure mechanism is not purely due to shear. The force capacity was also overestimated for the walls tested in TU Delft. The input parameters (α, β, γ) that are chosen to define the yield surfaces for the analyses did not correspond to the same values of cohesion as the other two models. Nevertheless, the analyses with the corresponding values resulted in bigger discrepancy between experimental and numerical values. The damage localization and energy dissipation are connected, since this model favors failure due to shear friction. No matter of the wall aspect ratio, the RHAPM always predicts diagonal failure (flexural

failure/rocking is not predicted in the case of high aspect ratios).

The developed subroutine OTSRM performed well in predicting the base shear capacity, and even the residual shear force. With the exception of wall TUD-COMP-4, it is the macro-model with the most accurate estimation of dissipated energy, performing even better than the micro-models in the case of the LOWSTA and HIGSTA walls. The damage pattern is quite localized, and resembles the experimental one in the majority of the examined walls. This is a big improvement with respect to the EMM and RHAPM. Nevertheless, the implemented algorithm is complex and leads to issues related to numerical stability that the other models did not have. This affects more the computational time and less the numerical results and their accuracy. The source of the numerical instabilities appears to be the internal shear loop and the modification of the local stiffness matrix in each iteration. Using an explicit solver, where the stiffness matrix does not need to be recalculated and inverted in each iteration, could help with these numerical stability issues.

A common drawback of the three macro-models specifically developed for masonry is their inability to capture the behavior of the double clamped shear wall TUe-Solid, that exhibited not only diagonal cracks, but also splitting through the bricks. Significant reduction of the compressive strength and compressive fracture energy was required for the EMM, RHAPM and OTSRM to be able to simulate this wall, in order to prevent over-stiff behavior and overestimating the capacity. Mechanically and physically, it has been observed that splitting of bricks due to vertical compression leads to reduction and softening of the compressive resistance of masonry. This reduction of compression due to lateral cracking has been described by Vecchio & Collins [191, 199] for concrete structures. A reduction of compressive strength due to lateral cracking has also been implemented in the case or the OTSRM, but it appears not sufficient in the case of this wall.

The PCCCS model predicts with high accuracy the failure load of the walls. It estimates with very good accuracy the dissipated energy of the TU Delft shear walls as well. However, the dissipated energy of the slender high wall and low wall are overestimated, since the pure elastic unloading/reloading adopted for both tension/compression and shear is not representative of all the three types of failure in masonry. The predicted crack pattern matched the experimental one with very good accuracy for all six walls.

Finally, the SI-CCS model performs very similar to the PCCCS in terms of peak load estimation. The damage localization is similar but not identical to the one observed for the PCCCS. All applications apart from the HIGSTA predicted the correct failure mechanism, and crack patterns very representative of the experimental ones. The estimated energy dissipation is excellent for the two shear walls of TU Delft, but less accurate for the HIGSTA wall and even less for the LOWSTA wall. A better calibration of the material parameters could lead to better matching numerical results. A point of attention is the need for calibration of the compressive strength when crushing/splitting is present. A further refinement of the model could tackle this issue by including a compression cap.

Unfortunately, there are a few limitations of the current study that need to be addressed. The first is that only constitutive models already implemented in the software DIANA FEA, or specifically developed for DIANA were examined. This makes the cases examined limited to a specific software. Moreover, no damage or damage-plasticity constitutive model was considered in this comparison, due to the unavailability of an appropriate existing model in the considered software. As mentioned in Chapter 2, not many direct

continuum macro-models have been validated against experimental results. Nevertheless, some of the cornestore direct macro-models are the damage-plasticity model of Papa & Nappi [28], and the damage model of Berto et al. [23]. Both models estimated with satisfactory accuracy the base shear capacity, and the failure mechanism of the examined walls, but had trouble capturing the dissipated energy. This chapter did not consider macro-models based on homogenization either, where progress have been made the last years, and where more models have been validated against cyclic experimental results. One such is the model of Calderini & Lagomarsino [19] that was validated against the HIGSTA and LOWSTA walls with very satisfactory results in terms of base-shear capacity, damage localization and even energy dissipation, although the LOWSTA wall analysis stopped early due to loss of convergence. The downside of this model was its inability to describe the stiffness degradation, but also that some of the input parameters were calibrated to match the experimental results. Similarly, no damage, or damage-plasticity model was used in the case of the micro-models, but it has been shown in literature that they can be powerful alternatives too (e.g., [14]). Another point that was not investigated further is the inclusion of potential cracks in the bricks through interface elements. The current models included the potential cracks by modelling the bricks as continuum nonlinear finite elements. However, the presence of a "cracked" interface element could split the brick and allow it to slide over the bed joint, something that would not be possible in the case of bricks modelled as continuum finite elements with nonlinear behavior in tension. Finally, it should be reminded that (1) in the case of the EMM different types of head-joint failure could be chosen, which could lead to a different behavior than the one predicted (either better or worse), and (2) the RHAPM, which is based on [33], only includes elastic unloading/reloading in its current implementation in the selected software, but in further developments of the original constitutive model by [31], the nonlinear unloading/reloading improved the behavior in terms of dissipated energy.

To this end, it was shown that certain models performed better at describing certain types of failure and walls. The newly developed model OTSRM is a good choice when the simulation of the hysteretic behavior and damage localization is of key interest. If only the estimation of the peak capacity is of interest, the EMM could also be a choice when modelling walls. Finally, if the computational time is not an issue, the SI-CCS model performed better among the two micro-models in capturing the hysteretic behavior and crack pattern of the walls. Although it was shown that in the scale of structural walls, the computational time of micro-models vs macro-models was not significantly longer, in the case of complete buildings with significantly more degrees of freedom, modelling exclusively with micro-models could be unfeasible. More parameters influence the performance of a constitutive model though and its suitability to accurately model masonry walls. In the next chapter, the sensitivity of each of the six constitutive models with respect to the variation of the material input parameters will be examined and discussed.

6

Macro-modelling vs. micro-modelling: Material sensitivities

In Chapter 5, six walls were used as benchmark to compare the ability of six different constitutive models to accurately model the hysteretic behavior and damage pattern of unreinforced masonry structures. The numerical results were compared in terms of peak and residual base shear, dissipated energy, crack pattern, numerical stability and computational time. It was concluded that none of the examined constitutive models performed better consistently over the rest in accurately predicting the hysteretic behavior and crack pattern. Each model had its own advantages and disadvantages, and performed better or worse depending on the wall modelled. The majority of these constitutive models requires a large number of material properties as input parameters for their definition. However, the required material properties are not always available, and even if in-situ or lab testing would be possible, some of these properties are hard to measure, while the testing can be costly and even destructive. An educated guess is therefore needed to estimate the unknown material properties. The goals of this chapter are to define which material property variations lead to higher numerical variabilities and which constitutive models are more sensitive to variations of the material properties. To do so, the sensitivity of the six constitutive models with respect to four material properties is investigated: the tensile strength, the compressive strength, the cohesion, and the friction coefficient. The six walls modelled in Chapter 5 are now remodelled by varying these four material parameters for each of the constitutive models. The sensitivity of the numerical simulations is assessed against the analyses performed for each wall and each material model with the original set of material parameters. Averaged peak and residual base shear, dissipated energy, and crack pattern are considered.

6.1 Introduction

Modelling masonry structures is a complicated task that requires a lot of expertise, especially when some data required as input for modelling are unknown. In such cases,

the structural engineers need to make some assumptions during the modelling procedure. These assumptions may relate to the material properties of the masonry walls and other structural elements like floors and roofs, the connections between different structural elements (such as wall-to-floor, wall-to-roof, floor-to-roof, etc.), the boundary conditions, the applied loads and the phased construction. Additionally, engineers need to take into consideration more factors, such as the modelling approach and analysis methods (FEM micro or macro-modeling, DEM, macro-element methods, or hybrid methods) or even the software package used, as stated already in previous chapters. Unfortunately, it has been shown that the modelling assumptions can often lead to significant deviations in the numerical results [82, 206–209].

This chapter examines how sensitive each of the six constitutive models adopted in Chapter 5 is with respect to variations of different material parameters, and how each material variation affects the numerical results in terms of hysteretic load-displacement behavior (here characterized via the averaged peak base shear, averaged residual base shear[1] and dissipated energy), as well as in terms of predicted failure mode and crack pattern. There are two main goals behind this research. First, defining which material properties lead to bigger variabilities in the numerical results will give a strong indication to researchers and engineers about which material properties they should be more mindful with when choosing the input value for an unknown parameter. Once engineers know that a variation of a certain material property can have a significant impact in the numerical predictions, they may have to take further actions if this property is unknown. They can either choose to perform tests to define the relative property experimentally, or to perform adequate sensitivity analyses varying the property, in order to obtain a range of estimated capacities. Second, defining which constitutive models are more sensitive to variations of the input material properties, and to which properties specifically, will allow the engineers to choose the appropriate constitutive model for their analyses, based on the parameters specifically available for their own analyses. For example, if the tensile properties of a masonry structure are not provided and they cannot be defined through tests, the engineers can choose to use one of the constitutive models that are less sensitive to variations of such properties.

The material properties varied in this chapter are the tensile strength ($f_{t,i}$), the compressive strengths ($f_{c,i}$), the cohesion (c_0) and the friction coefficient ($tan\phi$); these are all properties that can be calculated directly or indirectly from tests. The tensile and compressive strength are required as input for all six examined constitutive models, while the cohesion and friction coefficient are direct input for four out of the six models (EMM, OTSRM, PCCCS and SI-CCS). The tensile and compressive strength can be either of the composite masonry (for the continuum macro-models) or of the brick-mortar interface (for the interface micro-models), whereas the cohesion and friction coefficient are the material properties of the brick-mortar bed joint interface. Other material properties that could have an impact on the numerical results are the Young's modulus and the fracture energies in tension and compression, and the shear modulus and fracture energy in shear. As shown in Chapter 5, the compressive fracture energy had big impact in the response of

[1]Averaged peak base shear and averaged residual base shear refer to the average of the absolute peak base shear recorded in the positive and negative loading directions, and the average of the residual base shear recorded in the two loading directions, respectively.

the double-clamped shear wall TUe-Solid. However, it is not always easy to measure the fracture energy in compression, and even harder to measure the fracture energy in tension [46]. In this chapter, only the material properties that relate to the strength of the material are varied and investigated, as they are expected to influence the base shear capacity of the wall more than other material properties; the stiffness parameters are not varied as they are expected to affect more the pre-peak behavior and less the ultimate post-peak behavior of the walls.

For all the numerical variations, one material parameter is varied per time, and where applicable in both directions simultaneously. In reality, correlations have been observed between different material properties (e.g., [210]), but these have not been taken into account here, for the sake of simplicity and to allow for more straightforward comparisons. To be more precise, in the models where compressive and tensile strength are assigned both in the direction parallel to the bed and head-joints, the corresponding strength values are increased or reduced simultaneously in both directions, by the same percentage. For the remaining unvaried material properties, the values presented in Chapter 5 are used. The corresponding fracture energies and compressive strain at peak are not modified, which could result to faster or slower softening rate, as depicted in Figure 6.1.

The tensile strength is varied by ±40%, the compressive strength by ±20% and the cohesion by ±18%. These percentages were chosen based on the range observed in the experiments [42, 195]. In fact, the range observed in compression was smaller, between 2-9% for the TU Delft walls (TUD-COMP-4 and TUD-COMP-6) and 12.2% for the Ispra walls (LOWSTA and HIGSTA), but a higher range was selected to amplify the effect on the results. As for the friction coefficient, the variation was not performed in terms of percentage, since the coefficient of variation was not provided for any of the examined cases. Rather, different friction coefficients suggested for calcium silicate masonry and clay masonry were gathered from the literature [42, 46, 195, 211–213], and the maximum and minimum values of each dataset were used. For both types of masonry the minimum value was 0.43, whereas the maximum value for clay masonry was 1.03 and for calcium silicate 0.82.

In the following sections, the numerical results derived per material variation for each of the walls and constitutive models are summarized in terms of percentage of deviation of the sensitivity models from the benchmark model. Three numerical outcomes are presented: the averaged percentage difference in peak shear capacity, the averaged percentage difference in residual capacity and the percentage difference in dissipated energy. The averaged percentage difference in peak shear capacity (and likewise in residual shear capacity) is calculated by computing the percentage difference between the two peak base shears in the positive loading direction and averaging it with the percentage difference between the two peak base shears in the negative loading direction. Naturally, for the monotonic walls, there is no averaging, and the percentage difference is calculated directly for the loading direction.

The results are presented both in the form of tables for all three numerical outcomes, as well as in the form of 3D bar charts for the case of the averaged percentage difference in peak shear capacity. The 3D bar charts give a fast indication on which variations led to an increase and which to a decrease of the base shear capacity, and for which cases (walls or constitutive models) a larger difference was observed. The 3D bar charts for the

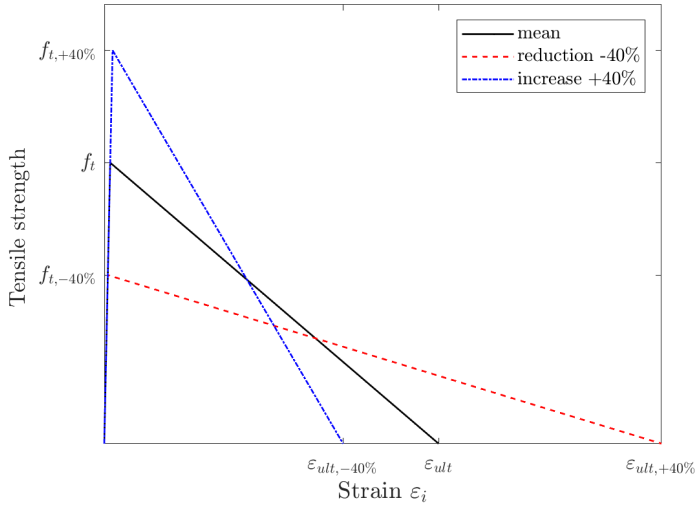

Figure 6.1: Tensile behavior in the case of reducing and increasing the tensile strength by 40% while keeping the Young's modulus and fracture energy constant.

averaged percentage difference in the residual base shear and the percentage difference in dissipated energy are presented in Appendix B. In Appendix B the damage localization plots for each material variation for all six walls and six constitutive models can be found as well. Finally, if a numerical analysis diverged, the percentage differences for the three numerical outcomes are calculated by considering only the load steps fully run and shared in both models before divergence occurred in one (or both) of the models. Those analyses have been presented using different format (different color of plotted bars and asterisks in the tables). However, in the case an analysis diverged before the peak base capacity is reached, those results are omitted from the comparison.

6.2 Tensile strength variation

The first material property examined was the tensile strength. According to codes (e.g., [181, 182]), the base shear capacity of a wall is a function of the geometry and compressive strength for flexural failure and the geometry and the compressive and shear strength for shear failure. From that perspective, the peak base shear should not be significantly influenced by a change in the tensile strength. That being said, in numerical analyses an increase of the tensile strength could be expected to lead to an increase in the peak base shear capacity when cracking determines the peak load.

Overall, regarding the peak shear capacity most of the constitutive models predicted a difference of less than ±5% from the benchmark value, except for the two micro models for which higher difference (up to 10.9%) was obtained for the two Eindhoven walls, and particularly the TSRCM that led to significant variations of the averaged peak capacity between -36% to 28% for the TU Eindhoven walls, and smaller variations between -1%

to 11% for the rest of the walls (Table 6.1). As for the average residual shear strength, generally a wider variation is observed than for the peak shear strength capacity. Moreover, a negative difference between the benchmark case and the variation is more probable, even when there is a positive difference in the peak shear capacity. The reason behind this is that the fracture energy in tension is not varied alongside the tensile strength, leading to a steeper softening when the tensile strength increases, and consequently a faster softening of the base shear of the wall.

The dissipated energy appears more sensitive to a variation of the tensile strength than the peak capacity, and in specific cases also than the residual strength. It is especially sensitive in the case of the slender wall HIGSTA, where an overestimation and an underestimation of around 13% is observed for the cases of the EMM and the OTSRM, respectively, regardless increasing or decreasing the tensile strength. Moreover, huge differences in the dissipated energies are predicted in the case of the TSRCM. However, especially for walls HIGSTA and LOWSTA, the increase could be attributed to spikes of the force-displacement curve (similar to the ones observed in Figure 5.8a). Furthermore, it should also be reminded that in general the dissipated energy predicted by the TSRCM is significantly lower than the one of the other constitutive models, so even though the difference in dissipated energy is large in relative terms, it is still small in absolute terms and therefore may not be of interest.

Another point of comparison is the influence of the tensile strength's variation in the damage localization of the walls. For the vast majority of the analyses, the crack pattern does not significantly change from the one observed during the benchmark case. Some differences are observed in the orientation of certain cracks, e.g., for an increase of 40% in the case of TUD-COMP-4 (Figure 6.3d) and TUD-COMP-6 for OTSRM, or even the total number of main cracks, e.g., when reducing the tensile strength in the case of HIGSTA for the EMM (Figure 6.3f). However, the failure mechanisms remain the same as the benchmark cases for all the sensitivity models apart for one: increasing the tensile strength of the cantilever squat wall TUD-COMP-6 in the case of the TSRCM leads to a flexural failure mechanism (Figure 6.3b). This is accompanied by an increase in the peak and residual base shear capacity, as well as in the dissipated energy. It should also be noted that five analyses diverged: three of them corresponded to an increase of 40% of the tensile strength for the cases of TUD-COMP-6 for the EMM and RHAPM (it is reminded that these analyses also diverged for the benchmark models), as well as for TUe-Solid for the micro-model SI-CCS. All these analyses reached their peak capacity, but diverged before the completion of the loading protocol. The other two analyses that diverged corresponded to the tensile strength reduction of the LOWSTA and HIGSTA walls in the case of the RHAPM. However, in these two variations divergence occurred even before the peak capacity was reached, and their numerical results are therefore not included in this section. These walls had the lowest tensile strengths in the benchmark case (0.10 and 0.04 MPa in horizontal and vertical direction respectively) and a relatively coarse mesh ($100x100mm^2$) for the dimension of the walls ($1000x1300mm^2$ and $1000x2000mm^2$, for LOWSTA and HIGSTA respectively). The further reduction of the tensile strength led to a fast divergence, and despite performing two variations regarding the input parameters (α, β, γ) no better solution was achieved.

To conclude, from the six constitutive models examined, the one that is the most sensitive to variations of the tensile strength, in other words the one that exhibits a wider

range in the numerical results when varying the input tensile strength, is the TSRCM. Since the TSRCM only has a few input parameters and does not describe the sliding/shear failure, it is expected that the variation of its tensile strength would affect the results more than for other models. In fact, the TSRCM displayed the largest variation not only for the peak shear capacity, but also for the residual base shear, as well as for the total dissipated energy. For three out of the six walls (LOWSTA, HIGSTA, TUD-COMP-4), a variation of the tensile strength by 40% led up to a 10% of difference in the base shear capacity, whereas for the two TU Eindhoven walls that had more restricted boundary conditions, the variation in the predicted value was even larger (up to -36% for a reduction of the tensile strength). Finally, the percentage of deviation from the benchmark case is not analogous to the percentage of tensile strength variation: if a tensile strength reduction of -40% leads to a peak base shear reduction of -7%, a tensile strength increase of 40% will not necessarily lead to an increase of 7% in the peak shear capacity. Generally, it could be argued that a very accurate estimation of the tensile strength is not essential for the remaining five constitutive models, as the differences in the base shear capacities are small.

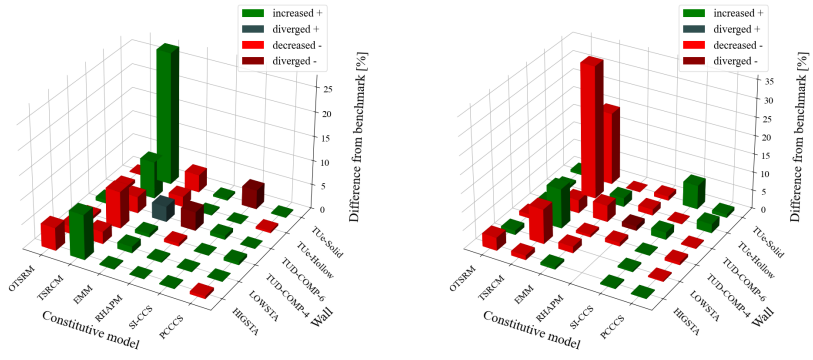

(a) +40% (b) -40%

Figure 6.2: Difference of the peak shear strength (average of positive and negative direction) between the original material properties and (a) an increase of 40% of the tensile strength, and (b) a decrease of 40% of the tensile strength.

Table 6.1: Difference of the average peak shear strength, average residual shear strength and dissipated energy with respect to the original material properties caused by an increase of 40% of the tensile strength (f_t) and a decrease of 40% of the tensile strength.

			HIGSTA	LOWSTA	TUD-COMP-4	TUD-COMP-6	TUe-Hollow	TUe-Solid
Difference in average peak capacity [%]	EMM	$+40\%f_t$	+0.2	+1.3	+0.7	+3.2	-2.1	-3.6
		$-40\%f_t$	+0.7	-1.8	-0.7	-4.5	+2.4	-0.1
	RHAPM	$+40\%f_t$	0.0	+0.2	-0.6	-3.9	+0.2	+0.4
		$-40\%f_t$	-	-	-1.0	-1.3	-1.7	-1.2
	TSRCM	$+40\%f_t$	+9.2	-2.5	-7.6	-3.4	+7.7	+27.4
		$-40\%f_t$	-1.2	-9.4	+10.8	-3.6	-36.1	-19.7
	OTSRM	$+40\%f_t$	-4.7	-1.6	-0.6	+0.8	-0.7	-0.1
		$-40\%f_t$	-3.5	+1.2	-1.2	+0.4	+0.7	+0.7
	SI-CCS	$+40\%f_t$	+0.1	+0.1	+0.1	+0.8	0.0	-4.0
		$-40\%f_t$	+0.3	+0.4	+0.2	+2.0	-0.2	+6.5
	PCCCS	$+40\%f_t$	-0.6	+0.1	+0.6	0.0	-0.4	+0.2
		$-40\%f_t$	+0.2	-0.3	-0.8	-0.3	+2.5	+0.9
Difference in residual shear capacity [%]	EMM	$+40\%f_t$	-7.6	-4.5	-1.1	-0.5	-0.5	-3.6
		$-40\%f_t$	-5.6	-3.9	-1.6	+5.5	+2.0	-0.1
	RHAPM	$+40\%f_t$	-0.3	+2.1	-0.1	0.0	+1.9	+0.4
		$-40\%f_t$	-	-	+2.2	+0.5	-3.9	-1.2
	TSRCM	$+40\%f_t$	0.0	-0.2	-7.9	+11.8	+9.5	-4.8
		$-40\%f_t$	-15.6	-15.2	+8.0	+1.2	-46.7	-8.9
	OTSRM	$+40\%f_t$	-4.9	+12.3	+1.8	+4.8	-2.9	+5.2
		$-40\%f_t$	-0.3	+6.1	-22.0	-37.1	-7.0	+2.4
	SI-CCS	$+40\%f_t$	-0.3	-2.5	-1.8	+363.3	-0.6	+6.8
		$-40\%f_t$	+0.2	-2.6	+3.9	+64.3	0.0	-6.2
	PCCCS	$+40\%f_t$	+0.5	+0.2	-1.3	-20.4	+0.1	+1.1
		$-40\%f_t$	-0.6	+0.1	-1.4	+0.3	+7.7	-0.4
Difference in dissipated energy [%]	EMM	$+40\%f_t$	+12.3	-6.2	-0.9	+2.2	-0.5	-2.5
		$-40\%f_t$	+13.8	+0.2	+1.7	-1.6	+0.7	-0.1
	RHAPM	$+40\%f_t$	+0.3	-0.1	-0.1	+0.3	+0.3	+1.8
		$-40\%f_t$	-	-	-1.4	-0.4	-2.2	-2.8
	TSRCM	$+40\%f_t$	+203.5	+33.9	-19.5	+43.3	+6.5	+4.9
		$-40\%f_t$	+306.4	+92.7	+27.7	+26.7	-42.9	-26.7
	OTSRM	$+40\%f_t$	-12.5	+6.6	+3.7	-2.9	-1.3	-0.4
		$-40\%f_t$	-13.0	+2.0	-7.0	-14.3	-1.9	+2.0
	SI-CCS	$+40\%f_t$	-0.8	0.0	+0.9	+42.9	-0.4	-1.7
		$-40\%f_t$	+4.0	-2.4	-1.7	+1.5	+0.5	+3.0
	PCCCS	$+40\%f_t$	+0.8	-0.3	-0.2	-0.1	-0.1	-0.4
		$-40\%f_t$	-0.3	+0.4	+0.1	+0.4	+3.8	+1.3

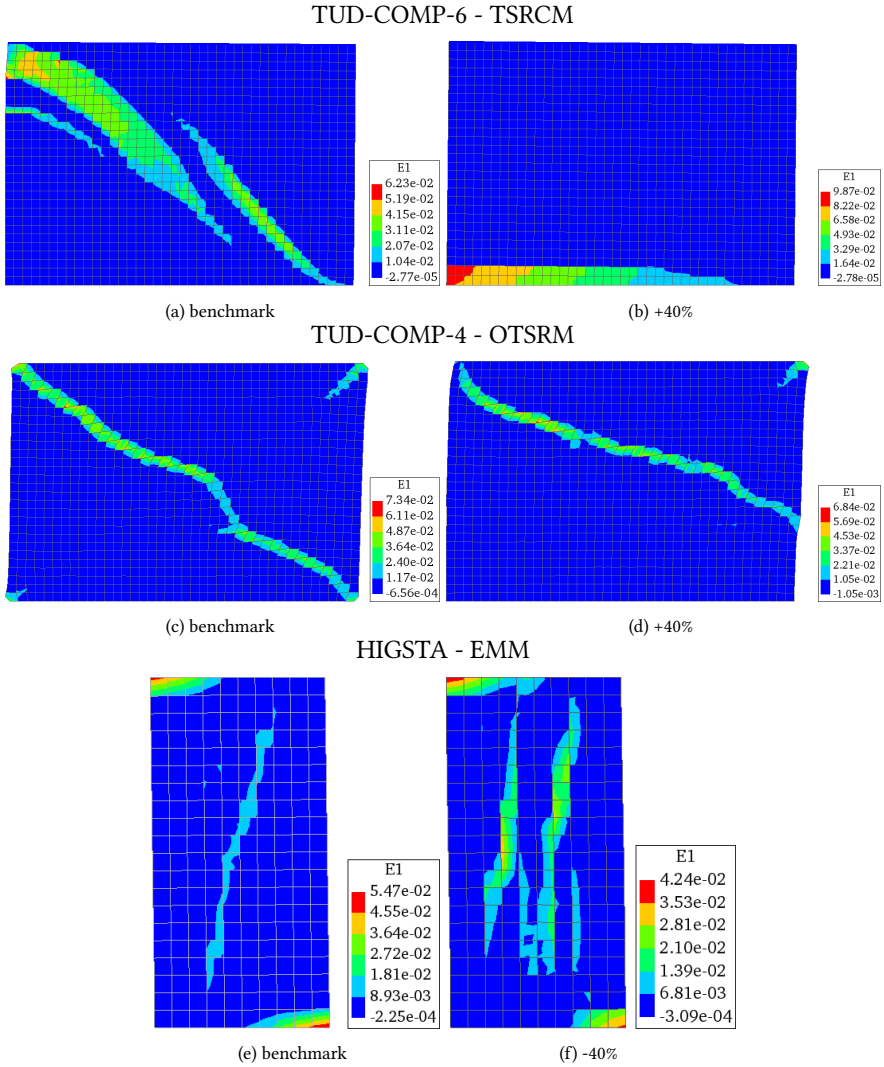

Figure 6.3: Principal strain ε_1 for a variation of the tensile strength by 40% and its impact on walls (a) TUD-COMP-6 for the TSRCM, where a shift in the failure mechanism occurred from diagonal shear cracking to rocking for an increase of the tensile strength, (b) on wall TUD-COMP-4 for the OTSRM, where the orientation of the diagonal crack changed and (c) on wall TUD-COMP-4 for the OTSRM, where the number of cracks increased, (scale factor is 2 for TUD-COMP-6 and HIGSTA walls and 20 for TUD-COMP-4 wall).

6.3 Compressive strength variation

The second sensitivity study regards the variation of the compressive strength. Figure 6.4 presents the averaged percentage difference that a variation of ±20% of the compressive strength has on the peak shear capacity of the walls modelled with the six different constitutive models. This variation satisfies with more evidence the assumption that an increase of the compressive strength leads to a higher peak base shear, with few exceptions predicting the opposite. These exceptions are mostly observed for the orthotropic constitutive model developed and presented in this PhD dissertation (OTSRM), where an increase of the compressive strength leads to a decrease of the shear capacity (Figure 6.4a) in four of the walls (HIGSTA, LOWSTA, TUD-COMP-4 and TUD-COMP-6), as well as for two analyses of the TSRCM (HIGSTA and TUD-COMP-4) and one of the SI-CCS model, which also diverged (TUe-Hollow). Nevertheless, the percentage differences computed for these seven analyses are less than -3.7%. Similarly, when the compressive strength is reduced, the shear capacity of the wall reduces too for most of the analyses. An exception is observed for the doubled-clamped squat wall TUD-COMP-4, where four of the constitutive models (OTSRM, EMM, SI-CCS and PCCCS) predicted an increase of the shear capacity upon decreasing compressive strength. Of these, the EMM had the highest estimation of +5.5%, but the rest had a much smaller estimation (less than 2% of difference from the benchmark case). One more exception is the case of TUe-Solid modelled with the TSRCM, where an increase of the capacity by 4.3% is observed upon decreasing compressive strength.

Another apparent observation is the high influence that the variation of the compressive strength has on the two double-clamped TU Eindhoven walls. This was already discussed in Section 5.7 of Chapter 5, where the reduction of the compressive strength was necessary for the three macro-models (EMM, RHAPM and OTSRM) to capture the splitting of the bricks, otherwise the shear capacity of the wall was significantly overestimated. During this sensitivity study, it was observed that not only the TUe-Solid wall is sensitive to the input compressive strength, but also the TUe-Hollow wall, which had not exhibited splitting of the bricks, but had also diagonal shear cracks. The macro-models are more influenced, showing wider ranges of variation than the micro-models. More specifically, the RHAPM and the OTSRM showed the highest deviation from the benchmark case, whereas the model least influenced was the TSRCM. Something to be expected, probably, since the TSRCM is the only model for which the capacity in compression does not influence the capacity in shear (a Coulomb friction shear criterion is not included in the TSRCM).

Regarding the averaged percentage difference in the residual base shear, in general higher variations are observed than in the peak base shear. The big differences in the TUe-Solid wall are expected, as toe-crushing/splitting dominate the post-peak behavior of this confined double clamped wall. Many integration points reach the compressive strength and enter the softening curve, the slope of which is modified in order to maintain the same fracture energy in compression as the benchmark model. Similarly, variations are expected also for wall TUD-COMP-6 that displayed some crushing even in the benchmark case. Although in 75% of the analyses the difference in the residual shear capacity would have the same sign as the difference in the peak shear capacity (meaning an increase or a decrease in both the peak shear strength and the residual strength), similar trend was not observed for the dissipated energy. As for the percentage difference in dissipated energy, big and untrustworthy values are observed for the TSRCM in the case of the HIGSTA wall, due to

spikes in the force-displacement curve. A bigger variation is observed than for the peak base shear, with the TSRCM and the OTSRM resulting in higher deviations. In any case, the small absolute values of dissipated energy of the TSRCM make the variation of the energy less significant. High values are observed for the SI-CCS model in the case of the HIGSTA wall, possibly because there is crushing in the interface elements at the bottom and top corners of the wall and the energy dissipated due to the bilinear unloading/reloading once crushing occurred (softening compressive curve) is larger (with large compressive relative displacements of the interface). On the other hand, this big difference is not observed in the case of the PCCCS model, because the linear elastic unloading from compression and tension leads in general to higher dissipated energy, and hence a difference in the compressive capacity will not lead to equally large compressive relative displacements and energy dissipation in the interface.

From the 72 analyses performed, 7 diverged: 5 after having reached their peak capacity and towards the end of the loading protocol (last cycle of TUD-COMP-6); the remaining two diverged before reaching the peak capacity. Those pertained to the models of the LOWSTA and HIGSTA walls for an increase of the compressive strength for the RHAPM constitutive model. Similar to what was observed when reducing the tensile strength of these two walls for the RHAPM, the material model diverged rapidly; possibly a better calibration of the parameters (α, β, γ) that define the yield surfaces is required.

Finally, minor differences were observed with respect to the damage localization. In all the cases the failure mode remains the same and even the crack location does not change, except for a few constitutive models for which the crack orientation or crack length might differ. For example, for wall TUD-COMP-6 an increase of the compressive strength by 20% for the OTSRM leads also to diagonal shear cracks, like in the benchmark case, but the two main open cracks appear on the opposite side of the wall, for the same loading step; in one case a part of the wall enclosed by the cracks shears out to the left, whereas in the other it shears out towards the right (Figures 6.5a and 6.5b). Additionally, for the same wall and material variation, the SI-CCS model leads to fewer but larger cracks; more diagonal shear sliding over the bed joints is observed, in comparison to the benchmark case (Figures 6.5c and 6.5d). The rest of the damage plots can be found in Appendix B.

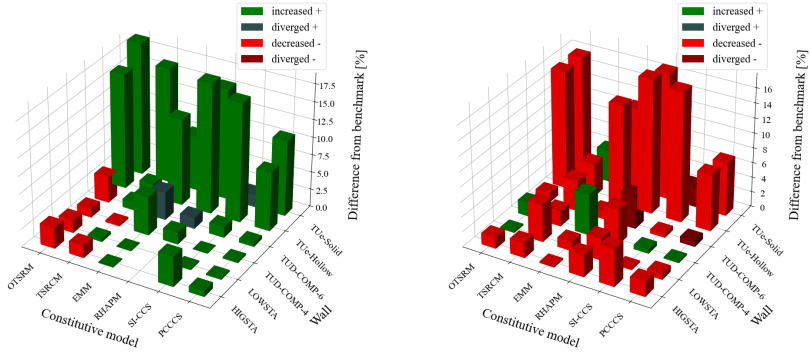

(a) +20% (b) -20%

Figure 6.4: Difference of the peak shear strength (average of positive and negative direction) between the original material properties and (a) an increase of 20% of the absolute compressive strength, and (b) a decrease of 20% of the compressive strength.

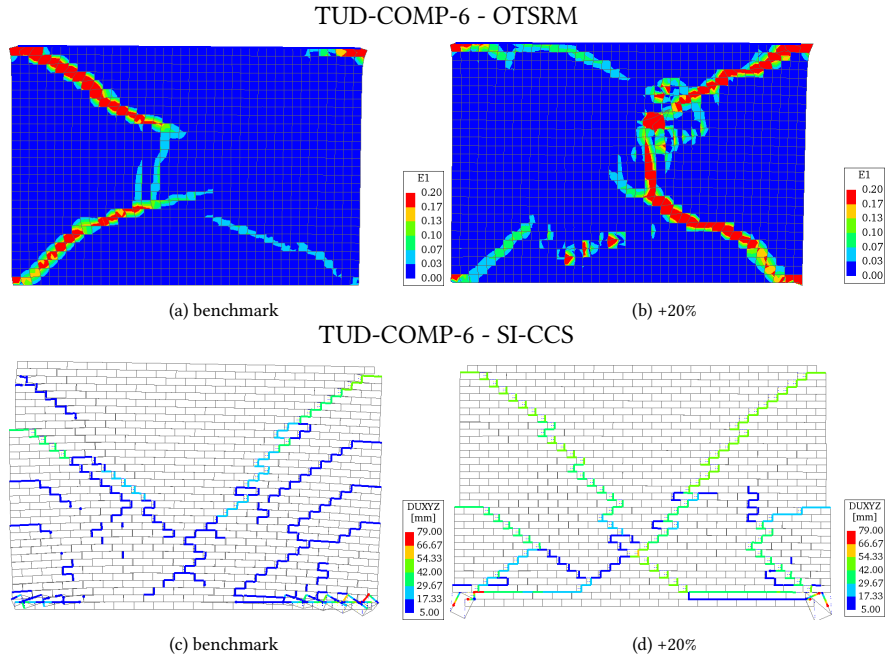

(a) benchmark (b) +20%

(c) benchmark (d) +20%

Figure 6.5: Principal strain ε_1 for a variation of the compressive strength by +20% and its impact on wall TUD-COMP-6 for the OTSRM (a), and interface total relative displacements for a variation of the compressive strength by +20% and its impact on wall TUD-COMP-6 for the SI-CCS (b) (scale factor is 2 for all models).

Table 6.2: Difference of the average peak shear strength, average residual shear strength and dissipated energy with respect to the original material properties caused by an increase of 20% of the compressive strength (f_c) and a decrease of 20% of the compressive strength.

			HIGSTA	LOWSTA	TUD-COMP-4	TUD-COMP-6	TUe-Hollow	TUe-Solid
Difference in average peak capacity [%]	EMM	+20% f_c	+0.1	+0.1	+5.5	+4.0	+12.3	+7.8
		−20% f_c	-0.2	-1.3	+5.5	-1.1	-13.5	-11.1
	RHAPM	+20% f_c			+1.7	+1.6	+18.4	+15.7
		−20% f_c	-2.9	-3.0	-4.7	-4.5	-17.9	-16.9
	TSRCM	+20% f_c	-1.8	+0.4	-0.3	+1.2	+1.8	+16.4
		−20% f_c	-2.1	-5.0	-2.1	-4.2	-4.5	+4.3
	OTSRM	+20% f_c	-3.0	-1.8	-1.3	-3.7	+16.4	+19.0
		−20% f_c	-1.5	+0.2	+1.9	-1.3	-15.8	-16.0
	SI-CCS	+20% f_c	+4.3	+0.2	+0.1	+1.6	+16.9	+1.8
		−20% f_c	-5.0	-0.2	+0.6	-0.6	-17.4	-2.8
	PCCCS	+20% f_c	+0.9	+0.2	+0.2	+0.5	+8.4	+10.7
		−20% f_c	-2.0	-0.8	+0.2	-0.8	-7.6	-7.2
Difference in residual shear capacity [%]	EMM	+20% f_c	-0.1	-3.1	+2.5	+4.3	+1.9	+7.8
		−20% f_c	-1.8	-4.6	+3.5	+5.2	-3.1	-11.2
	RHAPM	+20% f_c			+2.6	+6.1	+1.8	+15.7
		−20% f_c	-1.6	-2.4	-3.6	-9.5	-20.9	-16.9
	TSRCM	+20% f_c	+16.5	-0.2	-0.8	+2.3	-40.5	+32.1
		−20% f_c	+25.2	-4.4	-4.0	-4.3	-35.2	-19.9
	OTSRM	+20% f_c	-3.9	+7.8	-11.0	-5.4	-12.2	+22.5
		−20% f_c	-0.9	+10.6	-0.9	+8.1	-3.9	-17.2
	SI-CCS	+20% f_c	+4.2	-2.1	+0.5	+406.5	-7.2	+13.8
		−20% f_c	-5.5	-2.5	+3.8	+176.1	+4.4	+14.4
	PCCCS	+20% f_c	+2.3	+1.3	-1.6	+184.2	+4.9	+11.1
		−20% f_c	-3.3	-2.1	+0.2	-26.2	-15.9	-11.2
Difference in dissipated energy [%]	EMM	+20% f_c	+8.4	-1.8	+2.0	-5.0	+8.5	+4.2
		−20% f_c	+10.4	+0.5	+1.7	+3.4	-10.0	-6.8
	RHAPM	+20% f_c			-0.3	+2.3	+14.4	+10.6
		−20% f_c	-0.9	0.0	+0.8	-4.0	-16.1	-12.7
	TSRCM	+20% f_c	+209.9	-5.5	+0.7	-13.0	-13.1	+9.2
		−20% f_c	+350.8	+26.1	+10.1	+18.9	-16.0	-11.0
	OTSRM	+20% f_c	-1.1	+4.2	+15.6	-12.8	+7.6	+15.3
		−20% f_c	+6.7	-9.7	-11.3	-9.6	-10.7	-14.5
	SI-CCS	+20% f_c	+33.5	+0.3	-1.0	+85.4	+9.4	+4.9
		−20% f_c	-22.8	-1.9	-2.1	-14.7	-12.1	+5.9
	PCCCS	+20% f_c	-4.7	-0.5	-2.4	+16.3	+8.0	+5.4
		−20% f_c	+2.3	+3.3	+4.1	-8.5	-11.0	-7.5

6.4 Cohesion variation

The third sensitivity study presented in this chapter concerned the variation of the cohesion, i.e. the initial shear strength at zero confinement. From the six constitutive models, four of them include the value of the cohesion as a direct input parameter: the EMM, the OTSRM, and the two micro-models SI-CCS and PCCCS . No variation of the material property was performed for the TSRCM and RHAPM as for them the cohesion is not an input parameter. In the case of cohesion, an increase in the input value leads to a corresponding increase in the base shear reaction (and a decrease of the input cohesion to a decrease of the output shear as well), this not being the case for only four analyses in total, all of which have a negligible percentage difference of less than 1.4% from the benchmark case (Table 6.3). The averaged peak base shear of the walls differs less than 10% from the benchmark case. The biggest variations are observed for the two squat walls TUD-COMP-4 and TUD-COMP-6. Specifically, for wall TUD-COMP-4 all the constitutive models predict a difference between 5.2-7.8% in absolute values. As for the wall TUD-COMP-6, there is a wider range, between 2.8-9.2% for the macro-models and around 4% for the PCCCS , while the SI-CCS shows a very small variation. The walls that exhibited the smallest variation were the HIGSTA wall and the TUe-Hollow wall. More specifically, the HIGSTA wall presented the smallest variation for the macro-models as well as for the SI-CCS model that exhibited mainly flexural cracks, with a vertical crack forming at later loading cycles. The PCCCS model had exhibited more shear sliding and therefore a variation in cohesion affected it more, even though the variation is still considered very small (less than 3.5%). As for the TUe-Hollow, the micro-models had negligible variation in their capacities, since many of the cracks were opening in mode-I under flexure (bed-joint opening), rather than mode-II. The micro-model SI-CCS also exhibited relatively big variation for wall TUe-Solid (-4.9% and 7.5% for a decrease and increase of the cohesion, respectively). This difference is not observed in the PCCCS model, for which there are two possible explanations. First, the compressive strength used for the benchmark in the case of the SI-CCS model is lower than for the PCCCS model to compensate for the lack of interaction between the compression cap and the shear failure envelope, leading to a lower shear strength capacity. Second, the common damage parameter for tension and cohesion influences also the overall performance of the wall under mode-I failure, since exceeding the cohesion would lead to a decreased capacity for tensile damage.

Regarding the residual base shear, the OTSRM leads to larger averaged percentage difference, followed by the EMM. When reducing the cohesion, the PCCCS model predicts a faster reduction of the residual base shear, reaching the same minimum residual base shear as the benchmark case half a loading cycle earlier; the averaged percentage difference then appears higher and equal to -35.7%, standing out between the rest deviations.

The only model that predicted a different crack localization than the benchmark case is the OTSRM for wall HIGSTA, where a vertical crack along the height of the wall now emerges from the small diagonal cracks observed in the benchmark case (Figures 6.7b and Figure 6.7c). In fact, this vertical crack, which is also predicted in all the other constitutive models, occurs in all the material variations of the constitutive model. More differences can be seen also in the case of the LOWSTA wall for an increase of the cohesion, where now the diagonal cracks on the opposite corners are visible, and more damage occurs also in the middle of the wall, between the diagonal cracks (Figure 6.7e).

It can be concluded that among the four constitutive models, the most sensitive one to the cohesion parameter is the OTSRM, since it results in wider deviations from the benchmark case for the three comparison measures, and it leads to a different localization of the cracks for the HIGSTA wall too.

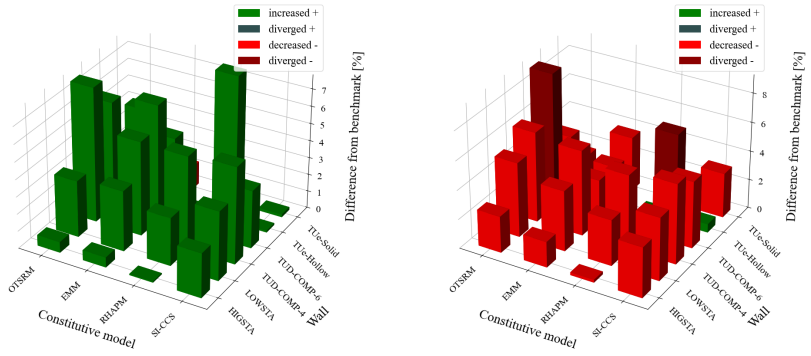

(a) +18% (b) -18%

Figure 6.6: Difference of the peak shear strength (average of positive and negative direction) between the original material properties and (a) an increase of 18% of the cohesion, and (b) a decrease of 18% of the cohesion.

Table 6.3: Difference of the average peak shear strength, average residual shear strength and dissipated energy with respect to the original material properties caused by an increase of 18% of the initial cohesion (c_0) and a decrease of 18% of the initial cohesion.

			HIGSTA	LOWSTA	TUD-COMP-4	TUD-COMP-6	TUe-Hollow	TUe-Solid
Difference in average peak capacity [%]	EMM	$+18\%c_0$	+0.6	+3.5	+5.5	+6.7	+4.0	-1.3
		$-18\%c_0$	-1.8	-4.2	-5.9	-2.8	-2.7	-3.8
	OTSRM	$+18\%c_0$	+0.6	+3.3	+7.8	+6.1	+2.8	+4.1
		$-18\%c_0$	-2.5	-5.1	-6.2	-9.2	-3.9	-1.6
	SI-CCS	$+18\%c_0$	+0.1	+2.8	+5.4	+1.3	-0.4	+7.5
		$-18\%c_0$	-0.2	-3.2	-5.1	-0.2	+0.2	-4.9
	PCCCS	$+18\%c_0$	+2.6	+4.0	+5.6	+3.4	+0.1	+0.2
		$-18\%c_0$	-3.4	-4.3	-5.5	-4.6	+0.6	-3.1
Difference in residual shear capacity [%]	EMM	$+18\%c_0$	+1.6	-0.4	+1.1	+10.6	-0.2	-1.3
		$-18\%c_0$	-6.6	-9.8	-4.7	+1.3	+1.3	-3.8
	OTSRM	$+18\%c_0$	+0.3	+10.1	+7.3	-18.1	+2.8	+5.3
		$-18\%c_0$	-8.9	+11.4	-5.4	+1.0	-8.6	+0.7
	SI-CCS	$+18\%c_0$	+0.1	-2.5	+6.0	-42.5	0.0	-0.3
		$-18\%c_0$	-0.5	-2.6	-1.8	+4.5	0.0	-0.3
	PCCCS	$+18\%c_0$	+0.3	+0.4	+0.4	-35.7	+0.3	-5.0
		$-18\%c_0$	-0.4	-0.6	-4.4	+1.9	-0.4	-4.3
Difference in dissipated energy [%]	EMM	$+18\%c_0$	-1.4	+4.3	+2.0	+0.8	+2.0	+1.5
		$-18\%c_0$	+11.1	-2.1	-3.5	-3.6	-2.4	-4.6
	OTSRM	$+18\%c_0$	+5.4	-7.0	+8.1	-4.0	+3.7	+3.9
		$-18\%c_0$	+3.1	-0.4	-0.2	-14.1	-5.7	-3.1
	SI-CCS	$+18\%c_0$	-3.5	+0.1	+1.4	+2.3	+0.3	+5.5
		$-18\%c_0$	+4.7	-0.7	-2.8	-4.4	-0.3	-2.8
	PCCCS	$+18\%c_0$	+3.3	+1.3	+2.9	-2.8	+0.4	-0.1
		$-18\%c_0$	-3.3	-0.8	-3.2	+1.2	-0.4	-5.3

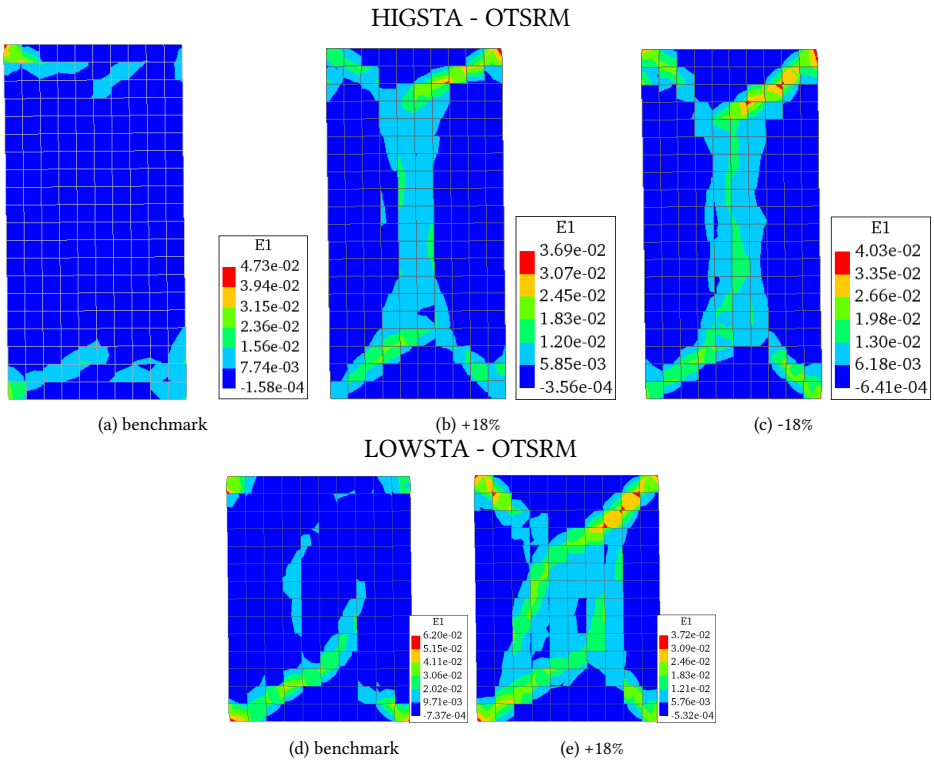

Figure 6.7: Comparison of principal strain ε_1 between the benchmark case and a variation of the cohesion by ±18% for the case of OTSRM for wall HIGSTA (a-c) and for wall LOWSTA (d-e) (scale factor is 2 for all models).

6.5 Friction coefficient variation

The final sensitivity study regards the friction coefficient. This sensitivity differs from the previously presented ones in that the friction coefficient is not varied by the same percentage around its benchmark value. Instead, the maximum and minimum friction coefficients available in the literature relative to each type of considered masonry (clay or calcium silicate brick masonry) [42, 46, 195, 211–213] are used. Coincidentally, for two of the three wall sets, the friction coefficient measured in the experiments and used in the numerical benchmark cases is the minimum value reported in the literature. Consequently, for these walls the difference presented is the one between the minimum and maximum friction coefficients. The values of the coefficient have increased from 0.43 to 0.82 (+93%) for walls TUD-COMP-4 and TUD-COMP-6, consisting of Calcium Silicate bricks, and from 0.43 to 1.03 (+139%) for walls HIGSTA and LOWSTA, made of clay bricks. For the TU Eindhoven walls, also consisting of clay bricks, the minimum and maximum adopted values are 0.43 (-42% from the benchmark value) and 1.03 (+37% from the benchmark value). The comparison therefore is not straightforward and the numerical results should be compared within each set of properties, and not as a whole.

Similarly to the variation of cohesion, only the two micro-models and the EMM and

OTSRM adopt the friction coefficient as an input parameter in their constitutive equations. Increasing the friction coefficient to its extreme value leads to a significant increase of the base shear, both the peak and the residual, for all the walls (Figure 6.8 and Table 6.4). But, even more important, the type of cracks and their localization change: for the HIGSTA wall flexural damage is observed for all four of the constitutive models when the maximum friction coefficient is adopted; for the LOWSTA wall less sliding is observed at the top of the wall for the SI-CCS model and less wide and shorter diagonal cracks for the macro-models (see Appendix B); for the TUD-COMP-4 wall more and wider diagonal shear sliding cracks appear for the two micro-models (Figure 6.9b); for the TUe-Hollow walls the micro-models predict a different mechanism when the friction coefficient is reduced: the left pier does not crack in the bottom and does not rock, and the top part of the wall slides over it (Figure 6.9h); finally, only flexural horizontal cracks are now predicted for the HIGSTA wall, and the vertical crack does not open for any of the four models (Figures 6.9d and 6.9f).

Interestingly, despite the difference in the crack pattern, the HIGSTA wall is the least sensitive in terms of changes in the hysteretic behavior, showing the smallest difference with respect to the amount of increase in the input friction coefficient. This is not surprising as flexural cracks were predominant in the benchmark case too. For the two TU Eindhoven walls, decreasing the friction coefficient leads to a bigger change in the peak and residual shear capacity than increasing it. One of the reasons is that the percentage of reduction is 5% more than the one of increase, but another reason is that the reduction of the shear coefficient can trigger shear sliding or diagonal shear cracks before flexural cracks are formed. In terms of residual base shear, big difference with respect to the benchmark case is observed as well for most of the walls. The difference is smaller in the case of the TUe-Hollow wall for the two micro-models.

As for the dissipated energy, a reduction of the dissipated energy is observed in the case of the EMM and the SI-CCS models. This reduction can be explained when considering the constitutive equations. The EMM has a direct relationship between shear stresses τ_{xy} and (relative) shear strains $\delta\gamma_{xy}$, given by $\tau_{xy} = min(\tau_{xy,0} + G \cdot \delta\gamma_{xy}, \tau_{max})$, where τ_{max} is defined through a Coulomb friction criterion $\tau_{max} = \omega \cdot c_0 - \sigma_{yy} \cdot tan\phi$. If the maximum shear stress capacity is not reached, the shear stress is behaving elastically, not dissipating any energy. In the case of the SI-CCS model, the same principle holds. The difference with the plasticity-based PCCCS model is once again the linear elastic unloading/reloading of plasticity models and the compression cap, that limits the maximum shear strength for high compression stresses.

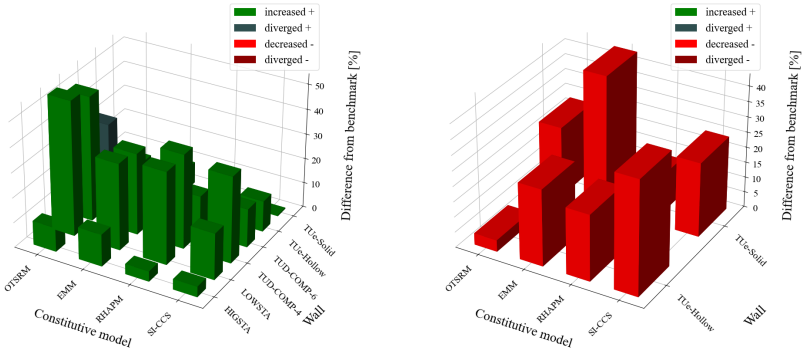

(a) maximum (b) minimum

Figure 6.8: Difference of the peak shear strength (average of positive and negative direction) between the original material properties and (a) the maximum and (b) the minimum friction coefficient provided for each masonry type (clay or calcium silicate bricks).

Table 6.4: Difference of the average peak shear strength, average residual shear strength and dissipated energy with respect to the original material properties caused by adopting the maximum ($tan\phi_{max}$) and minimum ($tan\phi_{max}$) friction coefficients.

			HIGSTA	LOWSTA	TUD-COMP-4	TUD-COMP-6	TUe-Hollow	TUe-Solid
Difference in average peak capacity [%]	EMM	$tan\phi_{max}$	+12.9	+34.8	+32.8	+8.9	-9.4	+8.6
		$tan\phi_{min}$					-25.0	-43.9
	OTSRM	$tan\phi_{max}$	+9.7	+54.1	+50.1	+33.4	+0.3	+6.2
		$tan\phi_{min}$					-3.8	-23.0
	SI-CCS	$tan\phi_{max}$	+4.1	+37.2	+37.9	+15.0	+2.0	+10.8
		$tan\phi_{min}$					-21.6	-12.5
	PCCCS	$tan\phi_{max}$	+4.2	+18.7	+34.8	+15.5	+12.4	+0.4
		$tan\phi_{min}$					-37.3	-24.3
Difference in residual shear capacity [%]	EMM	$tan\phi_{max}$	+18.2	+34.1	+23.4	+36.2	0.0	+8.3
		$tan\phi_{min}$					+46.3	-43.9
	OTSRM	$tan\phi_{max}$	+11.0	+69.2	+7.7	+92.0	-2.0	+8.8
		$tan\phi_{min}$					-12.9	-21.7
	SI-CCS	$tan\phi_{max}$	+4.7	+63.1	+34.8	-56.3	-0.3	+44.1
		$tan\phi_{min}$					-26.1	-36.7
	PCCCS	$tan\phi_{max}$	+16.6	+3.8	+23.7	-28.6	-2.4	-3.1
		$tan\phi_{min}$					+4.8	-56.4
Difference in dissipated energy [%]	EMM	$tan\phi_{max}$	-74.3	-41.6	-17.5	-10.3	-7.1	+0.9
		$tan\phi_{min}$					-9.6	-50.7
	OTSRM	$tan\phi_{max}$	+45.7	+41.0	+30.0	-81.1	-1.0	+6.5
		$tan\phi_{min}$					-6.3	-20.7
	SI-CCS	$tan\phi_{max}$	-85.5	-61.9	-38.5	-35.6	+1.7	+30.1
		$tan\phi_{min}$					-39.8	-4.6
	PCCCS	$tan\phi_{max}$	+39.0	+29.7	+11.7	-6.4	-1.5	0.0
		$tan\phi_{min}$					-26.2	-42.9

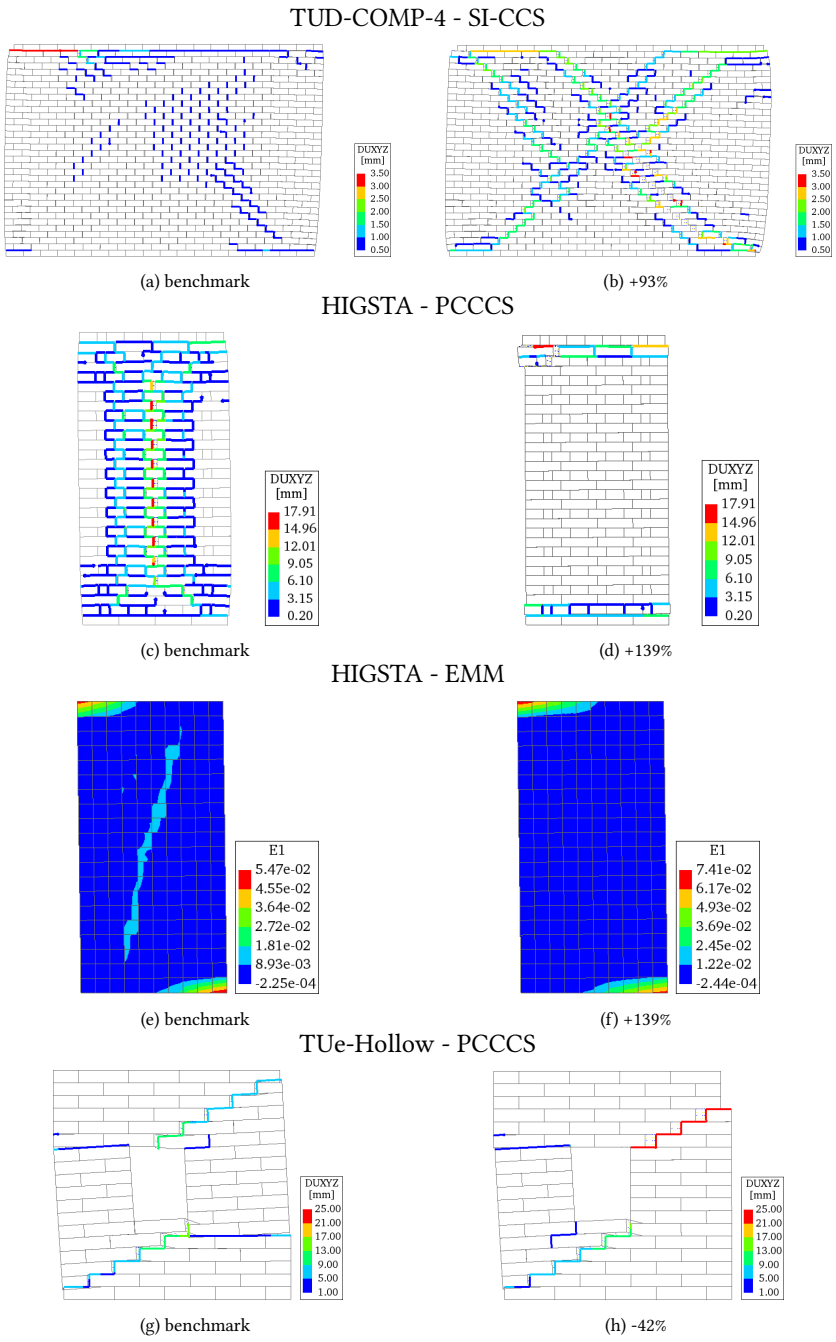

(a) benchmark (b) +93%

(c) benchmark (d) +139%

(e) benchmark (f) +139%

(g) benchmark (h) -42%

Figure 6.9: Comparison of damage pattern between the benchmark case and a variation of the friction coefficient for the case of (a-b) TUD-COMP-4 wall and SI-CCS model, (c-d) HIGSTA wall and PCCCS model, (e-f) HIGSTA wall and EMM and (g-h) TUe-Hollow wall and PCCCS model (scale factor is 20 for TUD-COMP-4 and 2 for all the other models).

6.6 Discussion, conclusions and limitations

In this chapter the results of a total of 224 sensitivity analyses were presented, focusing on the effect of four material parameters on the performance of six masonry walls tested under combined axial and shear loading. Specifically, variations in peak and residual base shear capacity, dissipated energy, prevailing failure mechanism and damage pattern were analyzed. The four material parameters selected were the tensile strength, compressive strength, and the two parameters defining the shear strength: the cohesion and friction coefficient. This chapter aimed at two goals: to identify (i) which input material properties have a bigger impact on the behavior of the walls, and (ii) which of the examined constitutive models are more sensitive to variations of the aforementioned material properties.

In order to answer the first question: "which material parameters, once varied, influence the behavior of the walls the most?", the results of the numerical analyses were arranged per wall and material property. For each wall the absolute values of the percentage differences in peak base shear between the maximum and minimum material variation for the six constitutive models are used to find their average percentage range per material variation. For example, to find the range of the peak base shear capacity for a variation of the tensile strength by ±40% for wall HIGSTA, the values of the *averaged percentage differences in peak capacity* presented in Table 6.1 for the maximum (+40%) and minimum (-40%) variation for each constitutive model (EMM, RHAPM, TSRCM, OTSRM, SI-CCS and PCCCS) are used to find the range of percentage difference for each constitutive model. Then, the ranges between minimum and maximum for the six constitutive models (expressed in percentage) are averaged, in order to find the *average percentage range in* $F_{peak,av}$ *due to a tensile variation of ±40%* for wall HIGSTA. In this way the ranges of each wall's shear capacity and energy dissipation are found for the variations of each material parameter.

Table 6.5 shows that the material property that influences the most the response of the walls is the *friction coefficient*, which led to the highest percentages for all the walls. Varying the *compressive strength* influenced significantly the response of the TU Eindhoven walls, as seen also in sections 5.6 and 5.7 of Chapter 5. These walls were doubled clamped and did not allow any vertical displacement on the top and bottom edges, leading to high compressive stresses along the strut and hence crushing along the diagonal compressed strut and at toes. Wall TUD-COMP-6, where local crushing occurred during the experiment, exhibited higher ranges of peak base shear, residual base shear and dissipated energy than the other three remaining walls. Even though the range in peak capacity is small, less than 4%, the range of the residual base shear and dissipated energy for TUD-COMP-6 are significantly high. Overall, the range remains small for the peak and residual base shear (less than 5%) for the three walls: HIGSTA, LOWSTA and TUD-COMP-4.

The level of sensitivity due to a variation of the *cohesion* seems to depend on the geometry of the wall and the type of failure. Where diagonal shear failure prevails (squat walls LOWSTA, TUD-COMP-4, TUD-COMP-6 and TUe-Solid) the range of percentage difference is higher (more than 6% and up to 12% for the peak shear capacity). However, in the case of slender walls with flexural failure (rocking), the range is lower than 4%. The average percentage range is also small in the case of the residual base shear (except for wall TUD-COMP-6) and dissipated energy (<7.4%). The *tensile strength* variation also led to overall small averaged percentage ranges, with the exception of the two TU Eindhoven walls, similar to what was observed in the case of compression. In more detail, the averaged

range for TUe-Hollow and TUe-Solid's peak base shear is 9.1% and 10.7%, respectively, and all other ranges lower than 3.7%. Furthermore, the residual base shear and dissipated energy presented also small ranges. A few exceptions are the residual base shear of TUD-COMP-6, which similar to the case of compression and cohesion is significantly higher than the rest. The higher averaged percentage ranges in the residual base shear are due to the big difference in the percentage change of the TSRCM, which, however, presents small changes in the dissipated energy in absolute terms.

One could argue that comparing ranges that resulted from different percentages of variation for the tensile strength (±40%), compressive strength (±20%), cohesion (±18%) and friction coefficient could lead to subjective results. Besides, the absolute range of tensile strength and cohesion considered is significantly lower than the absolute range of compressive strengths (for example for the HIGSTA/LOWSTA walls the range of tensile strength is 0.08MPa, of cohesion is 0.11MPa and of compression 2.48MPa). On top of that, the friction coefficient cannot be directly related to a stress range, since it is a coefficient multiplied by the normal stress. Nevertheless, if one would divide the averaged percentage ranges with the range of absolute strengths (for cohesion, tension and compression) per wall, similar observations would be made for the tensile strength and cohesion, whereas the influence of the compressive strength would have a lower impact. In any case, those different variations for each material property were obtained from experimental results performed in the past, and they are representative ranges that the user would anyhow reasonably consider.

In order to answer the second question: "to which material properties are the examined constitutive models more sensitive?", the average percentage difference (range) between the minimum and maximum variation for the six walls is calculated per material parameter for each different constitutive model. This is done similarly to the procedure described above. To give an example, in order to calculate how much the analyses performed with the RHAPM would vary when the tensile strength is varied by ±40% around the mean value, the ranges of the numerical results (peak and residual base shear, and dissipated energy) are calculated as the difference between the minimum (-40%) and maximum (+40%) tensile strength variation for each of the six walls; then, the average of these ranges is calculated and is used to express the average range of numerical results in the case of tensile strength variation.

The resulting Table 6.6 can be read in two ways. Comparing the values of each row horizontally gives an indication about the sensitivity of a specific constitutive model to the four examined input parameters. Comparing the values of each column vertically shows which of the six constitutive models is more likely to lead to a wider range of results for the variation of a given material parameter. Consistent with the findings presented above, the governing material property is the *friction coefficient*, which is included as an input parameter in four of the constitutive models: EMM, OTSRM, PCCCS and SI-CCS. The most sensitive model to *tensile strength* variations is the TSRCM. Not only was the peak base shear influenced a lot (21.1%), but also the failure mode of one of the squat walls switched from diagonal cracks to flexural cracks at the bottom of the wall. This sensitivity though is somewhat expected, since it is a model that accounts for failure purely in tension or in compression; failure in shear is not included through a direct (like in EMM, SI-CCS, PCCCS) or indirect (OTSRM) shear friction criterion or through yield surfaces

Table 6.5: Average percentage difference in base shear capacity, residual base shear and dissipated energy between the minimum and maximum material variation for the six walls in the case of variations in the: tensile strength ($0.6f_t$-$1.4f_t$), compressive strength ($0.8f_c$-$1.2f_c$), cohesion ($0.82c_0$-$1.18c_0$) and friction coefficient (0.43-0.82 for TUD-COMP-4 and TUD-COMP-6, and 0.43-1.04 for remaining four walls).

		HIGSTA	LOWSTA	TUD-COMP-4	TUD-COMP-6	TUe-Hollow	TUe-Solid
Tensile strength f_t	$F_{peak,av}$	2.2%	2.3%	3.7%	2.1%	9.1%	10.7%
	$F_{res,av}$	4.0%	4.0%	8.1%	63.1%	12.8%	4.4%
	$U_{diss,av}$	18.5%	12.2%	10.8%	12.4%	9.8%	7.9%
Compressive strength f_c	$F_{peak,av}$	2.9%	2.2%	2.0%	3.8%	25.2%	20.2%
	$F_{res,av}$	5.1%	2.5%	4.3%	79.6%	12.3%	27.7%
	$U_{diss,av}$	35.8%	9.0%	7.6%	29.1%	18.5%	16.4%
Cohesion $\pm 18\%c_0$	$F_{peak,av}$	3.0%	7.6%	11.8%	8.6%	3.6%	6.0%
	$F_{res,av}$	4.7%	3.0%	7.8%	28.3%	3.4%	2.0%
	$U_{diss,av}$	7.4%	4.0%	6.0%	6.3%	3.8%	6.7%
Friction coefficient tan_ϕ	$F_{peak,av}$	7.7%	36.2%	38.9%	18.2%	23.3%	32.4%
	$F_{res,av}$	12.6%	42.6%	22.4%	53.3%	22.6%	54.2%
	$U_{diss,av}$	61.1%	43.6%	24.4%	33.4%	18.5%	39.1%

(RHAPM). There is an option to reduce the compressive strength due to lateral tensile cracking, according to different formulations provided for reinforced concrete mechanics, but this option was not utilized in the analyses. The big percentage change in dissipated energy though still corresponds to small absolute values. Generally, the tensile strength is not a critical parameter for the remaining five examined constitutive models, as long as its value is kept within expected and reasonable limits; the peak base shear ranged less than 4%, and even the dissipated energy and residual base shear exhibited low percentage ranges (lower than 10%, except for the residual base shear of SI-CCS).

According to Table 6.6, the *compressive strength* influences the response of the five constitutive models more than the tensile strength and the cohesion. The two models that are influenced the most are the RHAPM and the OTSRM. In reality, not all five constitutive models were largely influenced by changes of the compressive strength. Depending on the walls' geometry, loading and boundary conditions, the models resulted in higher or lower deviations, with the more restricting boundary conditions leading to higher capacities. *Cohesion* comes third in order of influence, and the bigger influence is observed for the OTSRM (8.9%), followed by the EMM(6.7%), in the case of the peak base shear. However, for the residual base shear the OTSRM and the SI-CCS model lead to the biggest variations, staying nevertheless below 10%.

This study is limited in examining the sensitivity of the six aforementioned constitutive

models in four key material input parameters: the tensile strength, compressive strength, cohesion and friction coefficient. Other parameters that could influence the response of the walls and the performance of each constitutive model, such as the fracture energy in tension, compression or shear, have not been examined herein. Moreover, the sensitivity study focused on the cyclic behavior of walls in their ultimate limit state, where in the majority of cases shearing and crushing were the governing failure mechanisms. This explains why the friction coefficient, compressive strength and cohesion influenced most the results. However, in the case of light damage or settlement problems, where the pre-compression levels are lower and where most cracks observed are usually tensile and/or shear cracks, the impact of the performed material variations could differ significantly; a bigger influence of the tensile strength variation might be expected. Therefore, it is strongly advised to consider the presented results within the context of ultimate limit state for walls of similar geometry and boundary conditions and not to generalize the findings of this research for other types of problems.

Finally, we can draw conclusions about which material property leads to wider dispersion of the base shear capacity and dissipated energy when the six different constitutive models are considered, but these conclusions are based solely on numerical observations. Within the realm of this study, it was neither the scope nor possible to perform experiments where the material strengths would vary too, and compare the effect of the experimental variations with the one of the numerical variations. Such an experimental study would be of great interest and would confirm which material properties govern the response of walls. Nevertheless, with masonry being an inhomogeneous material that exhibits large variabilities in its properties, not only due to the variability in the properties of its constituents, but also due the quality of construction, consciously varying its material properties for experiments is a very challenging task. It is, therefore, only possible to discuss which constitutive models are more sensitive to material variations and not which of these deviations due to sensitivities are more realistic.

Table 6.6: Average percentage change in base shear capacity, residual base shear and dissipated energy between the minimum and maximum material variation for the six constitutive models, in the case of variations in the: tensile strength ($0.6f_t$-$1.4f_t$), compressive strength ($0.8f_c$-$1.2f_c$), cohesion ($0.82c_0$-$1.18c_0$) and friction coefficient (0.43-0.82 for TUD-COMP-4 and TUD-COMP-6, and 0.43-1.04 for remaining four walls).

		Tensile strength f_t	Compressive strength f_c	Cohesion c_0	Friction coefficient $tan\phi$
Average change in peak shear capacity [%]	EMM	3.5	8.6	6.7	26.3
	RHAPM	1.1	14.6	-	-
	TSRCM	21.1	5.2	-	-
	OTSRM	1.2	12.7	8.9	30.1
	SI-CCS	2.1	8.6	5.2	23.5
	CCCS	1.1	6.5	6.2	24.6
Average change in residual shear capacity [%]	EMM	2.5	4.9	6.1	35.1
	RHAPM	2.1	13.5	-	-
	TSRCM	19.6	13.3	-	-
	OTSRM	13.9	12.9	9.7	36.9
	SI-CCS	53.2	42.7	9.3	44.3
	CCCS	5.2	44.1	7.6	22.2
Average change in dissipated energy [%]	EMM	3.0	7.1	6.6	33.0
	RHAPM	1.6	10.4	-	-
	TSRCM	51.1	39.5	-	-
	OTSRM	5.0	16.7	7.3	38.4
	SI-CCS	9.5	30.4	4.8	49.6
	CCCS	1.4	12.3	4.1	25.7

7

Conclusions

The goal of this research was the development of a cyclic, nonlinear and orthotropic continuum constitutive model for masonry structures, its evaluation against experimental results and its comparison with other existing and commonly used constitutive models. This research started by reviewing existing constitutive models used for the numerical analysis of masonry structures. In Chapter 2 the mechanical behavior of masonry as a material was briefly discussed, and an overview of the different modelling approaches that can be used for the analysis of masonry structures was presented. These were classified as: macroelement models, finite element models (including micro-models and macro-models), discrete element models, and hybrid models. Additionally, the chapter listed some representative constitutive models for each modelling approach, focusing on the available continuum constitutive models for macro-modelling analyses. The strengths and weaknesses of the available modelling approaches were discussed and can be summarized as follows:

- Macroelement models provide a quick and fast assessment of a structure's performance. They can be quite accurate for structures with regular geometries, but may be inaccurate for structures with irregular openings. Additionally, their main assumption that global failure occurs due to in-plane behavior, and the fact that they do not consider the interaction between in-plane and out-of-plane elements and diaphragms also affects the accuracy of the results.

- Finite element micro-models provide high numerical accuracy, but their high computational cost limits their applicability to special cases where detailed modelling is required.

- Discrete element methods are a powerful tool to model the cyclic behavior of masonry and its brittle failure. One big advantage is their capability to capture the interaction between non-neighboring blocks as well if they would come in contact. However, they have been validated less against experimental results in comparison to the other methods reviewed.

- Direct macro-models describe the behavior of masonry in a phenomenological approach. The constitutive formulations are usually based on a plasticity or damage mechanics formulation, though damage-plasticity models and models based on fracture mechanics have also been developed. A crucial characteristic that influenced the accuracy of the models is the inclusion of initial orthotropy, and the description of the compression and shear stress behavior. Overall, a large number of material input parameters is required, and the numerical results are less accurate than in the case of micro-models. Their main disadvantage is the representation of damage and the difficulty in capturing the hysteretic behavior, especially in terms of post-peak behavior and dissipated energy. Moreover, only few of the available direct macro-models have been validated against cyclic tests.

- Macro-models based on homogenization or multiscale approaches have the advantage of taking into account in their constitutive formulations the texture of the masonry. In general, they have been validated more against cyclic experimental tests during their development phase, and their numerical accuracy may be considered higher compared to direct macro-models. However, being formulated based on RVE means that their applicability is limited to the specific masonry bond, while the computational cost increases with respect to direct macro-models. This, in combination with the fact that in general macro-models based on homogenization or multiscale approaches are not commercially available, leads researchers and engineers to most often use direct macro-models when modelling masonry structures subjected to cyclic loads.

- Hybrid models combine characteristics of the other approaches, mainly discrete element methods with macro-elements, and finite element with discrete element methods. This combination of different numerical approaches can help to achieve more accurate results while reducing the computational cost. However, being a relatively new approach means that more validations and guidelines are required.

Identifying the advantages and disadvantages of the existing continuum models acted as the catalyst for the development of the constitutive model that this dissertation entails. Chapter 3 presented the mechanical behavior and the constitutive equations that describe the tensile, compressive and indirect shear behavior of the developed model, referred to as Orthotropic Total Strain Rotating Model (OTSRM). Its main characteristics can be summarized as follows:

- The OTSRM is based on a Total Strain Rotating Crack concept, adopting coaxiality between principal stresses and strains.

- The OTSRM is an orthotropic model, adopting different elastic and inelastic characteristics in the two rotating principal stress/strain directions.

- Before cracking, the material properties adopted vary with respect to the principal angle, i.e., the angle between the principal stresses and the bed joints. This variation is based on linear and nonlinear interpolations between the material properties corresponding to the directions parallel to the bed and head joints. After cracking, the elastic and inelastic properties are kept constant and equal to the ones corresponding

to the cracking directions, i.e., the principal stress/strain direction at the onset of cracking.

- The OTSRM adopts two different post-peak and unloading/reloading behaviors in tension based on the cracking angle: brittle behavior with a steep softening rate and secant unloading/reloading for cracking angles that correspond to flexural cracks; and a ductile behavior with slow softening rate and elasto-plastic unloading/reloading for cracking angles that correspond to diagonal shear cracks. The range of sub-horizontal and sub-vertical angles for which flexural behavior is adopted are defined through a threshold angle, used as an additional material input parameter.

- The compressive behavior is described through three curves, a nonlinear pre-peak hardening and a nonlinear post-peak softening curve, ending at a residual plateau of small compressive strength once the compressive fracture energy has been consumed, in order to avoid numerical problems. The compressive unloading/reloading behavior is idealized with a bilinear curve, with the aim to resemble to the elastoplastic unloading/reloading observed in shear sliding behavior. The compressive strength reduces with lateral cracking, as for some concrete models.

- The OTSRM accounts for the shear behavior indirectly, by applying a Coulomb-friction limit to the shear stress τ_{xy} parallel to the mortar bed-joints. The main assumption during this indirect inclusion, is that the stress σ_{yy} normal to the bed-joint is kept constant, and that the coaxiality between the principal stresses and strains is maintained. If the shear stress exceeds the maximum shear capacity, the principal stresses are recalculated and limited appropriately through an internal iterative loop.

In Chapter 4, the constitutive model was implemented in a FEM software (DIANA FEA), using incremental-iterative solution procedures, and was validated against experimental results. Four walls of different dimensions, pre-compression load, boundary conditions and material properties were modelled. The numerical and experimental results were compared in terms of peak and residual shear capacity, dissipated energy, and crack pattern. Moreover, two sensitivity studies were performed and discussed: a mesh sensitivity study, varying the element size (100mm, 200mm, 300mm) and the element order (quadratic 3x3, linear 2x2); and a sensitivity study on the influence of the threshold angle, comparing the results for threshold angles of 20^o and 25^o. Additionally, the numerical stability and convergence of the models were discussed. The main conclusions regarding the applicability of the OTSRM constitutive model and its performance in terms of accuracy and numerical efficiency are the following:

- The model predicts with good accuracy (between 2-8%) the base shear capacity of the examined walls.

- The model estimates the dissipated energy sufficiently well when a combination of failure modes is present ($\pm 10-17\%$), whereas it underestimates the capacity when pure shear failure occurs (-65%), and overestimates it in the case of pure flexural/rocking failure (+43.5%).

- The model predicts consistently the failure mechanism observed during the experiments. Moreover, it leads to localized cracks that resemble well the experimental crack pattern.

- Regarding the mesh sensitivity, the model estimates the base shear capacity with a good estimation, deviating less than 5.2% from the experimental results and each other. Nevertheless, bigger deviations occur for the post-peak behavior. The linear elements with larger mesh size exhibit the least softening, and the quadratic elements exhibit more softening. The crack pattern is representative of the experimental one, but the different mesh sizes and order lead to differences in the crack orientation and point of intersection of the diagonal cracks.

- A small variation of $\pm 5^o$ in the threshold angle leads to negligible differences in terms of force capacity and post-peak behavior. However, the orientation of the cracks changes; a wider range of angles where shear behavior is adopted leads to steeper cracks.

After having compared the accuracy of the developed constitutive model OTSRM against experimental results in Chapter 4, Chapter 5 compared the performance of the OTSRM with another five constitutive models available in the same software package and commonly used for the numerical analysis of masonry structures. The selected models included four macromodels: the developed OTSRM, the Total Strain Rotating Crack Model (TSRCM), the Engineering Masonry Model (EMM), and the Rankine-Hill-Anisotropy model (RHAPM), and two micro-models: the Combined Cracking Crushing Shearing model (PC-CCS) and the Sub-stepping Iterative model for Cracking-Crushing-Shearing (SI-CCS). The walls of Chapter 4 and two additional walls were modelled using the six constitutive models. All models adopted the material properties provided by the corresponding experiments, and where some properties were unknown, the same values were assumed for all models. The performance of each constitutive model was evaluated in terms of failure mode, damage pattern at peak applied displacement, hysteretic behavior (including force-displacement capacity and dissipated energy), and numerical efficiency, discussing both convergence rate and computational time. The conclusions can be summarized as follows:

- The TSRCM, which was originally developed for concrete, is the most simplified model, with only six required input parameters. It predicts the correct failure mechanism, and in most cases provides a representative crack pattern. Its performance regarding the force capacity varies; it overestimates significantly the capacity for squat walls with low aspect ratio, and underestimates it for the wall with the highest aspect ratio. Moreover, it consistently underestimates the dissipated energy and is therefore considered inappropriate for capturing cyclicity. All in all, it is the constitutive model least appropriate for the (cyclic) modelling of masonry walls.

- The EMM, with twelve to fourteen material input parameters, and four different options for representing the head-joint failure, estimates the force capacity with good accuracy. It performs well in terms of computational time and numerical stability, even though one of the analyses diverged. Regarding the dissipated energy, it estimated with good accuracy (-9.2%) the results of one of the walls (TUD-COMP-6),

but overestimated (at least by +80%) or underestimated (-44%) the rest. However, the biggest drawback of this constitutive model is its inability to localize the damage, leading to diffused cracks, not representative of the localized and brittle nature of masonry.

- The RHAPM, an orthotropic plasticity model with elastic unloading/reloading, fails to predict the correct failure mechanism in the case of flexural failure, and consistently leads to a significant overestimation of the dissipated energy when the failure mechanism is not due to pure diagonal shear sliding. Both of the disadvantages are related to the elastic unloading/reloading, inherent to plasticity based formulations, that fails to capture the brittle tensile failure of masonry.

- The interface micro-model PCCCS predicts with good accuracy both the force capacity and the crack pattern of the examined walls. Only for the wall HIGSTA a different failure mechanism was predicted. For the scale of walls examined, it is even very efficient numerically, with a computational time comparable to the one of the most efficient macro-models and the highest convergence rate. However, the dissipated energy was overestimated significantly in the cases of flexural failure, since the elastic unloading/reloading adopted both in tension, compression and shear is not representative of the brittle behavior of mortar joints in tension.

- The SI-CCS model predicts accurately the response of the walls. The model failed to predict the correct failure mechanism in the case of the slender wall HIGSTA. In terms of hysteretic behavior it captures better the dissipated energy than the PCCCS model, since it includes secant unloading/reloading in the case of tensile stresses. An important point is the need to calibrate the compressive strength, in order to limit the shear stresses in an indirect way via the compression cap.

- The developed OTSRM predicts with good accuracy both the peak and the residual base shear. It estimates the dissipated energy adequately, being the constitutive macro-model with the smallest difference from the experimental results. Furthermore, not only it predicts the correct failure mechanism consistently, but it also leads to localized damage and representative crack patterns, even if the exact location or orientation of cracks does not match the experimental ones. Nevertheless, it exhibits more numerical difficulties in achieving convergence; the percentage of converged steps in an analysis ranged between 63% and 96% for the OTSRM, whereas for the other models the percentage of converged steps was at least 94%, with the exception of one case for RHAPM that diverged.

- There is no model that outperforms the others consistently in all the examined parameters.

Having compared the numerical with the experimental results for the six constitutive models and the six walls, the next step is to assess how sensitive are these results with respect to variations of the input material parameters. Four material parameters were varied, the tensile strength, the compressive strength, the cohesion and the friction coefficient. Each of the six walls was modelled with the six different constitutive models, this time varying one of the four abovementioned material parameters per analysis. The goal was to

determine (a) which material properties, once varied, influence the behavior of the walls the most, and (b) to which material property variation are the constitutive models more sensitive. Regarding the first question, the findings can be summarized as:

- For all six walls, the material property that leads to higher variances of the peak base shear, residual shear and energy dissipation is the friction coefficient.

- The compressive strength influences significantly the results of the two TU-Eindhoven walls, where double-clamped conditions with no vertical movement of the top boundary were applied. A variation of the compressive strength also influenced more the TUD-COMP-6 wall, which had exhibited also crushing during the experiment.

- Variations in cohesion have a bigger impact in the case of squat walls that exhibit diagonal shear failure. In the case of slender walls or piers that exhibit rocking failure, cohesion has a negligible effect on the hysteretic behavior.

- The tensile strength variation overall leads to small variations in the base shear capacity, consistent with what is suggested in literature for the in-plane walls. The exceptions are the two TU-Eindhoven walls in the case of the TSRCM. The dissipated energy and residual base shear are influenced more from a change in the tensile strength than the peak base shear.

Regarding the second question, the findings can be summarized as:

- The friction coefficient is the material parameter that influences the most the numerical results for the four constitutive models where it is used as an input: EMM, OTSRM, PCCCS and SI-CCS. Not only the force-displacement curve is influenced, but in some cases the failure mechanism switches from shear failure to flexural failure.

- The tensile strength has a significant impact only on the TSRCM, where a high range in the predicted numerical results is found both for the base shear capacity, residual base shear and the dissipated energy, with average percentage changes between the minimum and maximum tensile variation of 21.1%, 13.9% and 51.1%, respectively.

- The cohesion is a direct input parameter in only four of the constitutive models (EMM, OTSRM, PCCCS and SI-CCS). The constitutive model that is more sensitive to cohesion variations is the OTSRM, with an average percentage change between minimum and maximum cohesion variation of 8.9% for the peak shear strength and 9.7% for the residual shear strength.

- The compressive strength influences the numerical results more than the tensile strength and cohesion. Even though all three examined outputs (peak base shear, residual base shear, dissipated energy) are influenced in a greater or lesser degree, and the location or orientation or width of cracks varied, the failure mechanism remains the same.

Limitations

As all studies, this dissertation also had some limitations and points that require further research and attention.

Regarding the developed constitutive model, the following limitations are observed:

- The inclusion of the internal iterative shear loop has a big impact on the numerical stability of the OTSRM. Many iterations are required to reach convergence and for a number of (consecutive or nonconsecutive) steps convergence is not reached. Although in the examined cases a good match between numerical and experimental results was found, in the case where no experimental results are available a more careful assessment of the numerical results might be required.

- The inclusion of the internal iterative shear loop and its consequences in the numerical stability have also an impact on the computational time, which is increased in comparison to other total-strain based macro-models.

- The dissipated energy, even though significantly improved in comparison to other models, does not match the experimental one for all the examined walls, differing between 10%-65% from the experimental values.

- The indirect inclusion of a shear limit through the internal iterative loop leads to a limitation of the compressive strength, which might lead to premature crushing.

- The validation of the OTSRM against experimental results was done using only displacement-control. Its accuracy and numerical performance has not been assessed in the case of force-control and arc-length methods or in the case of dynamic nonlinear time history analyses.

Regarding the comparison between the different constitutive models, the following limitations are observed:

- The study conducted included only constitutive models that are already implemented in the DIANA FEA software. This not only makes the study specific to the software used, but also it limits the comparison to the types of available constitutive models. All macro-models considered followed a direct approach; no macro-models based on homogenization or multiscale approaches were examined. Moreover, no damage nor damage-plasticity constitutive macro-model was included in the comparisons either.

- Some of the constitutive models had additional failure criteria that could have led to a better estimation of the hysteretic behavior, but they were not considered. For example, the TSRCM gives a variety of choices for the tensile and compressive stress-strain relationship, and an option to include reduction of the compressive strength due to lateral cracking. Similarly, the EMM provides four different options for how the head-joint failure should be expressed. In both models, only one of the available options was compared.

- The study of the material sensitivities was limited to the variation of four main material parameters. However, these parameters are often correlated. The correlation

between each of them was neither examined nor taken into account. Additionally, the choice of keeping the fracture energies constant while increasing the strengths, may lead to more brittle post-peak behavior than in reality.

- The comparison between the different constitutive models to assess which is more sensitive and to which material parameter, and how each material variation affects the behavior of each wall may be interesting from a numerical point of view, but there are no experimental data to support that indeed such an influence is valid.

- The results drawn regarding the material sensitivity are specific to the type of analysis performed (lateral cyclic quasi-static). For other problems and applications, such as settlements, different sensitivities may be observed.

Future research

During the development of the OTSRM and the numerical analyses and comparisons with other constitutive models, as well as during the material sensitivity investigation, some aspects of modelling arose that would be worth further investigation, but time limitations did not allow doing so. With regard to the developed constitutive model, the following suggestions for future research are made:

- Modifications in the compressive capacity to include the increase of compressive strength in the case of biaxial compression.

- Modeling and validation of masonry walls with different types of bonds to define a set of threshold angles representative for each type of bond.

- Implementing the constitutive laws in an explicit solver could help reduce the numerical instabilities observed when using the implicit solve. Since many of the convergence issues were caused due to the internal iterative shear loop, which would limit and recalculate the principal stresses (and therefore also the local stiffness matrix), not requiring to evaluate this stiffness matrix could omit the convergence problems.

- Extending the constitutitve equations from 2D plane-stress elements to shell elements and even 3D solid elements would make OTSRM applicable also to the modelling of entire buildings, in addition to single walls.

When it comes to the modelling strategy used for the comparison of the different constitutive models and their sensitivity to material parameters, the following aspects could be of interest:

- Considering different cases for the post-peak behavior of the tensile and compressive strength. For example, keeping the softening rate constant instead of keeping the fracture energies constant.

- Making more consistent variations in the case of the friction coefficient to find the friction angle that would act as a threshold value between flexural and shear failure.

- Considering constitutive models that belong to different modelling approaches, for example continuum models based on homogenization approach, or damage-plasticity theory, or even macro-element models.
- Conducting experiments complimentary to the numerical variations perform, in order to validate what is the actual impact on the wall's behavior when one or more of the material properties is varied.

Finally, although this dissertation focused on the cyclic behavior of structures under lateral loads, it is worth investigating the applicability of the developed constitutive model and the other existing models on other types of problems as well, such as climate-induced damage and settlements. Only when all different types of loads are considered for the different numerical approaches and different constitutive models, can guideline recommendations regarding uncertainty quantification be considered complete.

A

Appendix A

A

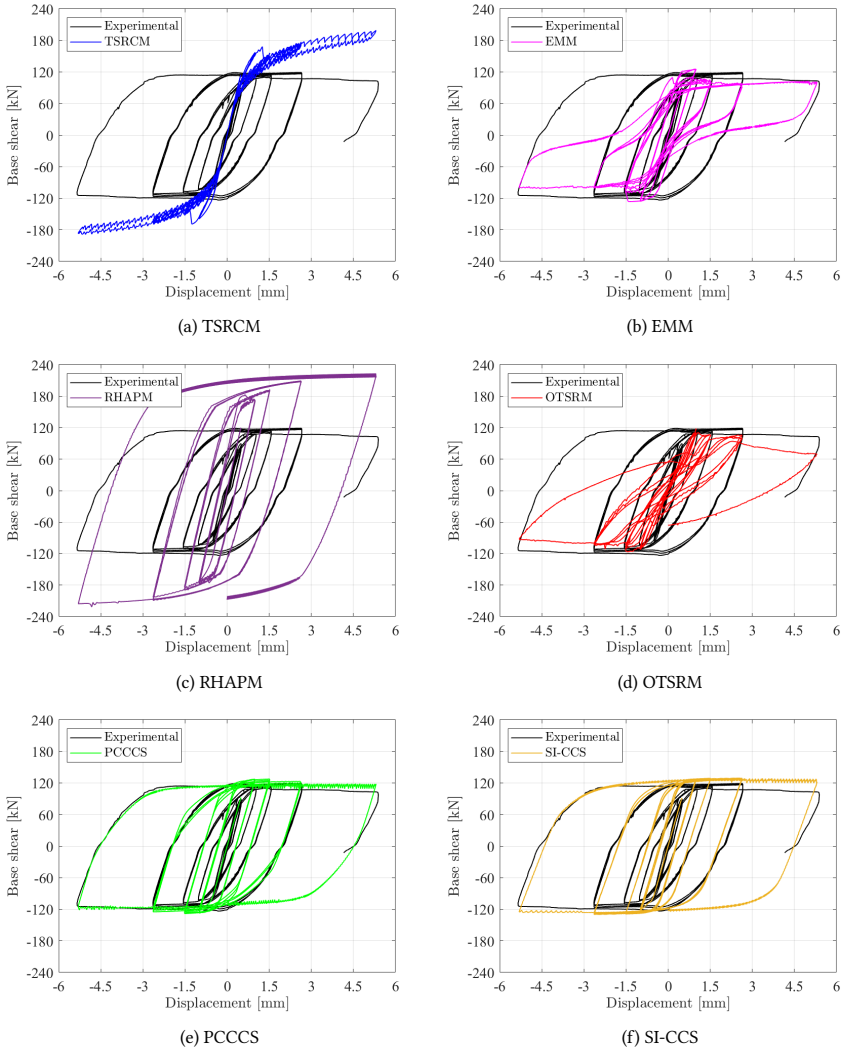

Figure A.1: Comparison of force-displacement curve between the experimental and the numerical results of wall TUD-COMP-4 for the examined constitutive models (a) Total-Strain-Rotating-Crack model (TSRCM), (b) Engineering Masonry Model (EMM), (c) Rankine Hill Anisotropy model (RHAPM), (d) User developed constitutive model (OTSRM), (e) Combined Cracking Crushing Shearing interface model (PCCCS), and (f) Substep-Iterative Cracking Crushing Shearing model (SI-CCS).

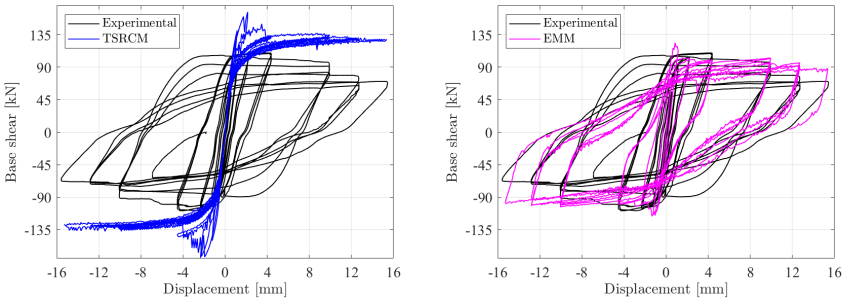

(a) TSRCM

(b) EMM

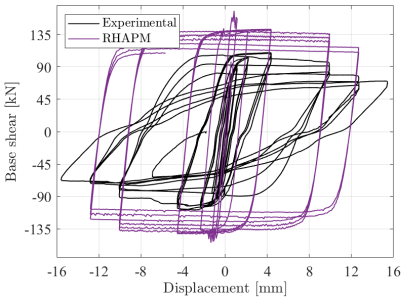

(c) RHAPM

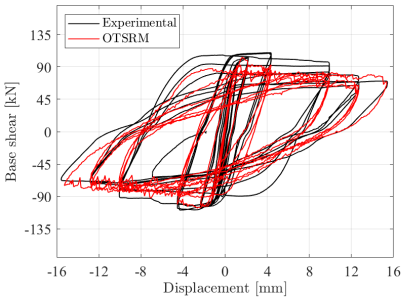

(d) OTSRM

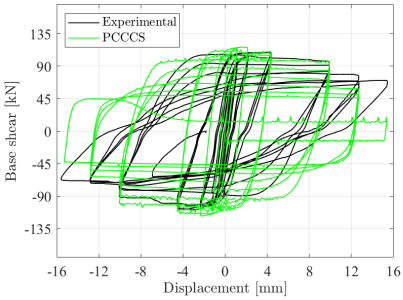

(e) PCCCS

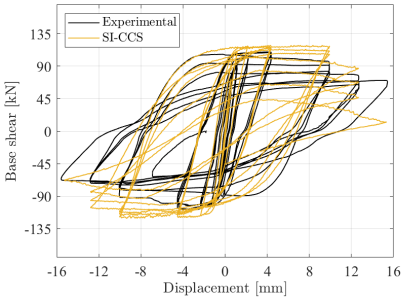

(f) SI-CCS

Figure A.2: Comparison of force-displacement curve between the experimental and the numerical results of wall TUD-COMP-6 for the examined constitutive models (a) Total-Strain-Rotating-Crack model (TSRCM), (b) Engineering Masonry Model (EMM), (c) Rankine Hill Anisotropy model (RHAPM), (d) User developed constitutive model (OTSRM), (e) Combined Cracking Crushing Shearing interface model (PCCCS), and (f) Substep-Iterative Cracking Crushing Shearing model (SI-CCS).

A

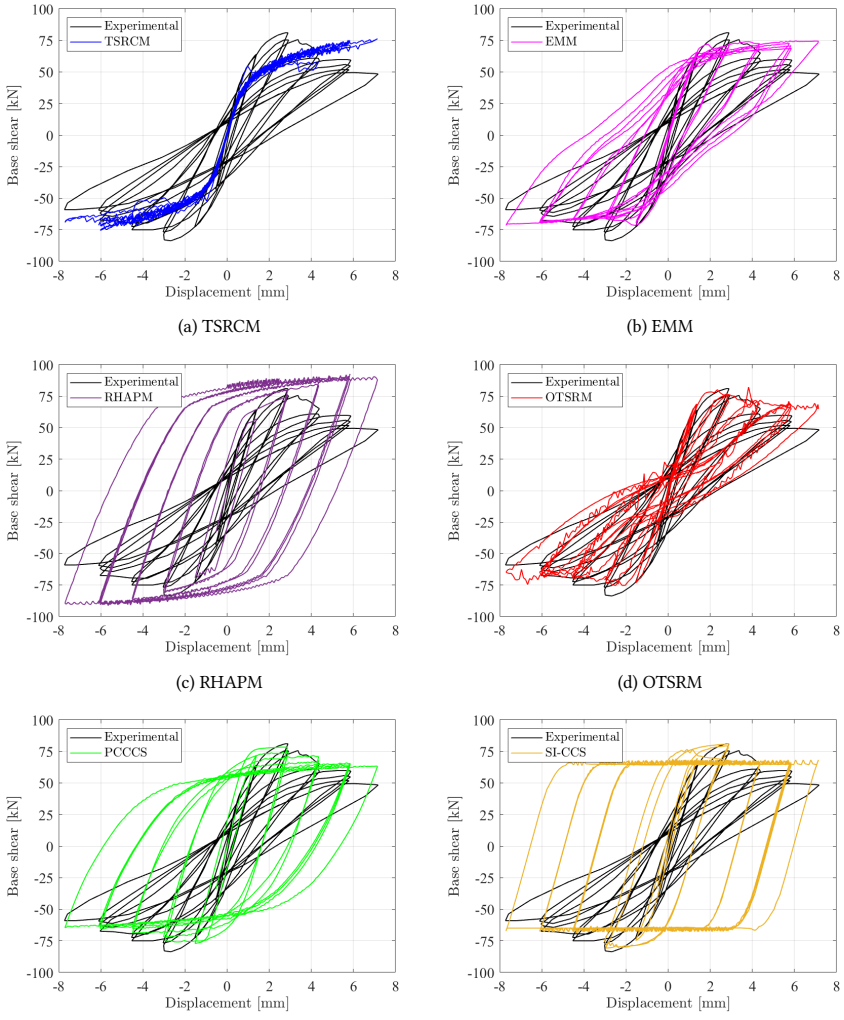

Figure A.3: Comparison of force-displacement curve between the experimental and the numerical results of wall LOWSTA for the examined constitutive models (a) Total-Strain-Rotating-Crack model (TSRCM), (b) Engineering Masonry Model (EMM), (c) Rankine Hill Anisotropy model (RHAPM), (d) User developed constitutive model (OTSRM), (e) Combined Cracking Crushing Shearing interface model (PCCCS), and (f) Substep-Iterative Cracking Crushing Shearing model (SI-CCS).

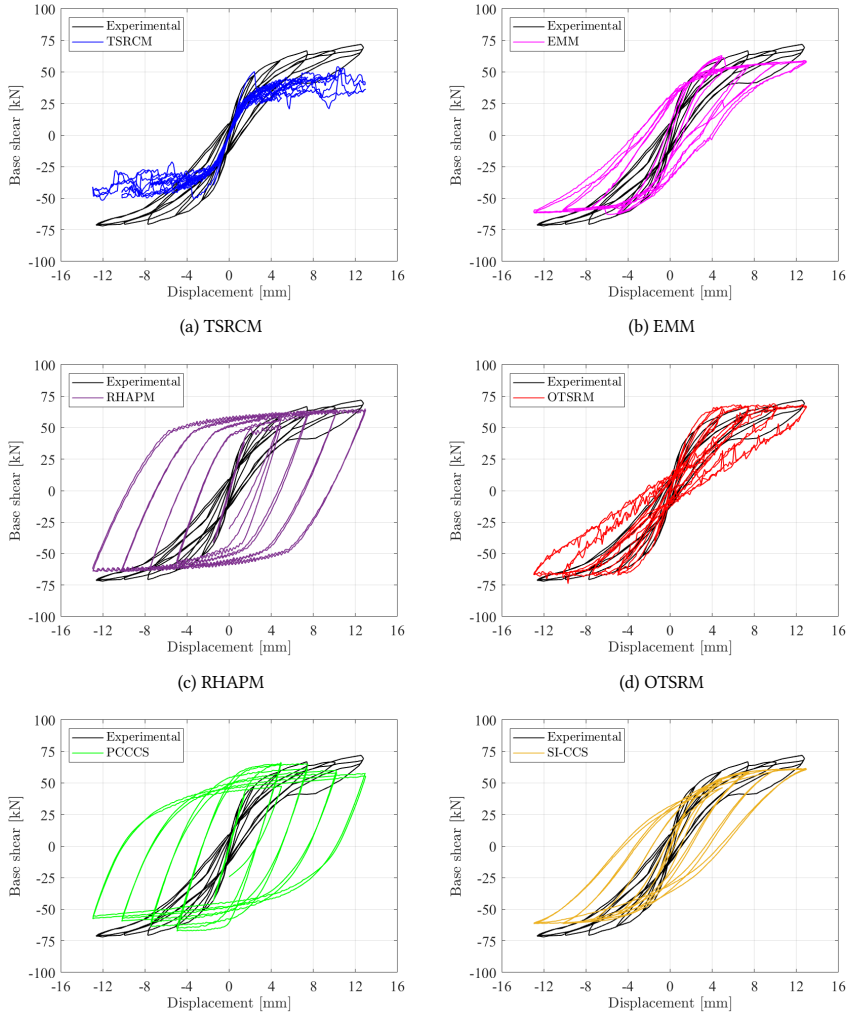

Figure A.4: Comparison of force-displacement curve between the experimental and the numerical results of wall HIGSTA for the examined constitutive models (a) Total-Strain-Rotating-Crack model (TSRCM), (b) Engineering Masonry Model (EMM), (c) Rankine Hill Anisotropy model (RHAPM), (d) User developed constitutive model (OTSRM), (e) Combined Cracking Crushing Shearing interface model (PCCCS), and (f) Substep-Iterative Cracking Crushing Shearing model (SI-CCS).

A

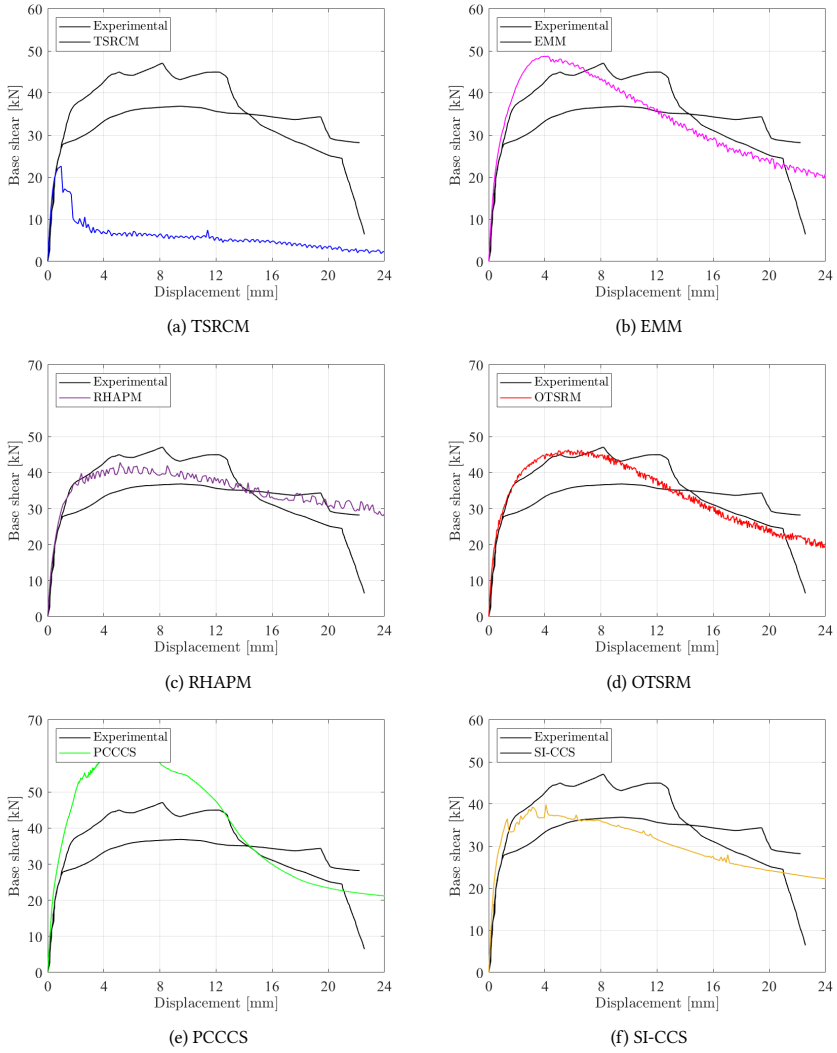

Figure A.5: Comparison of force-displacement curve between the experimental and the numerical results of wall TUe-Hollow for the examined constitutive models (a) Total-Strain-Rotating-Crack model (TSRCM), (b) Engineering Masonry Model (EMM), (c) Rankine Hill Anisotropy model (RHAPM), (d) User developed constitutive model (OTSRM), (e) Combined Cracking Crushing Shearing interface model (PCCCS), and (f) Substep-Iterative Cracking Crushing Shearing model (SI-CCS).

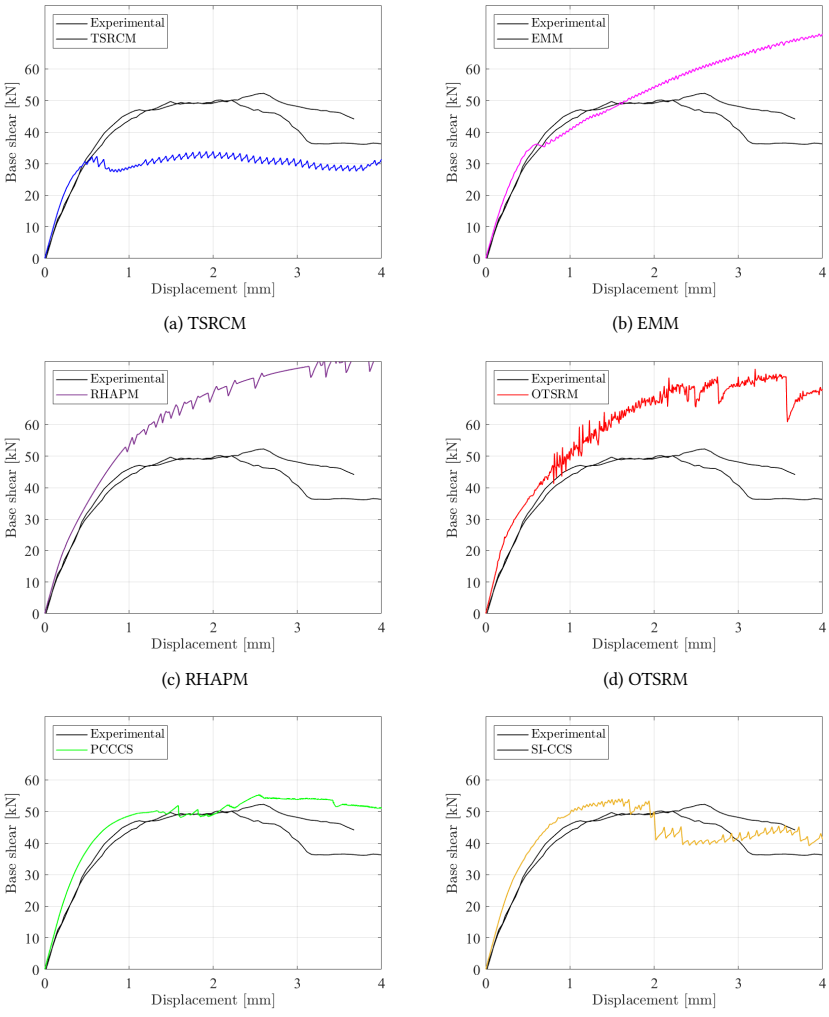

Figure A.6: Comparison of force-displacement curve between the experimental and the numerical results of wall TUe-Solid before calibration for the examined constitutive models (a) Total-Strain-Rotating-Crack model (TSRCM), (b) Engineering Masonry Model (EMM), (c) Rankine Hill Anisotropy model (RHAPM), (d) User developed constitutive model (OTSRM), (e) Combined Cracking Crushing Shearing interface model (PCCCS), and (f) Substep-Iterative Cracking Crushing Shearing model (SI-CCS).

A

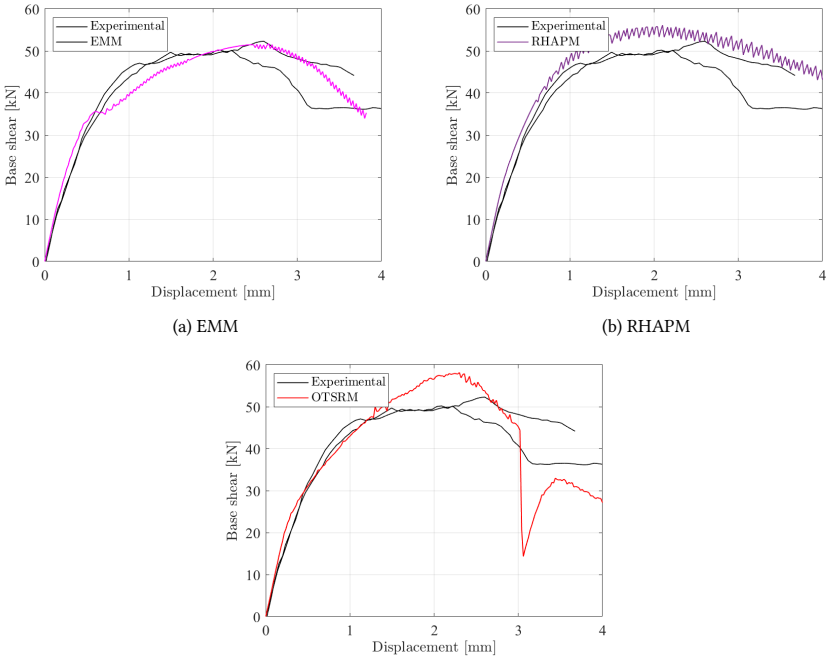

(a) EMM

(b) RHAPM

(c) OTSRM

Figure A.7: Comparison of force-displacement curve between the experimental and the numerical results of wall TUe-Solid after calibration for the examined constitutive models (a) Engineering Masonry Model (EMM), (b) Rankine Hill Anisotropy model (RHAPM), (c) User developed constitutive model (OTSRM)

B

Appendix B

B

Difference in average residual base shear due to tensile strength variation

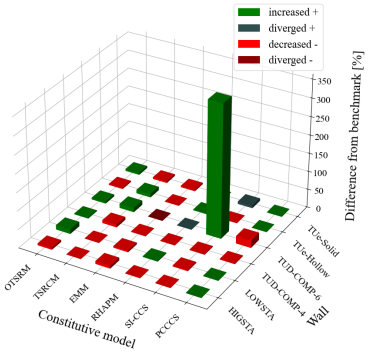

(a) +40%

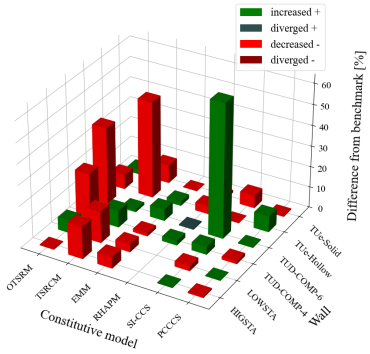

(b) -40%

Difference in dissipated energy due to tensile strength variation

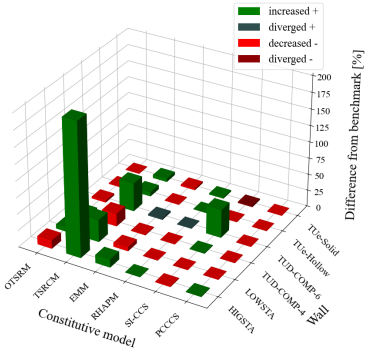

(c) +40%

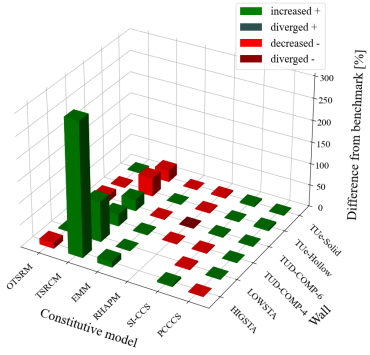

(d) -40%

Figure B.1: Difference in the residual base shear capacity (average of positive and negative direction) and dissipated energy between the original material properties and a variation of the tensile strength by 40% ((a) and (c)), and -40% ((b) and (d)).

Difference in average residual base shear due to compressive strength variation

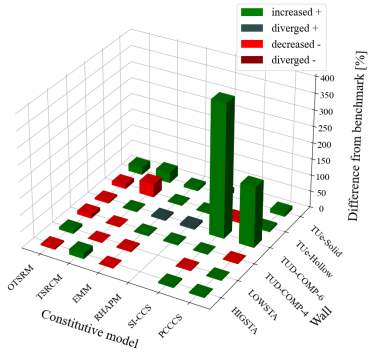

(a) +20%

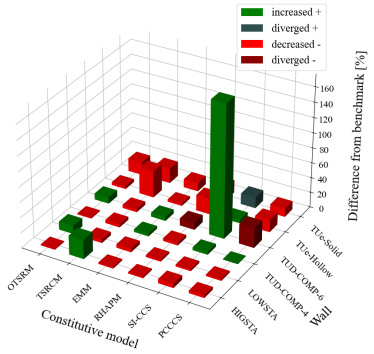

(b) -20%

Difference in dissipated energy due to compressive strength variation

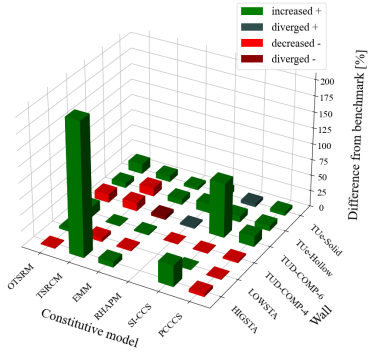

(c) +20%

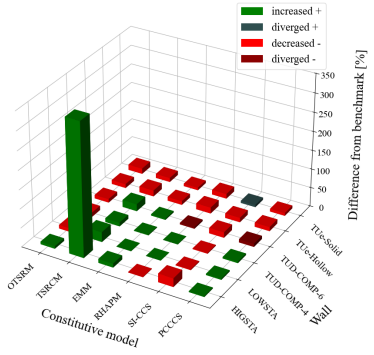

(d) -20%

Figure B.2: Difference in the residual base shear capacity (average of positive and negative direction) and dissipated energy between the original material properties and a variation of the absolute compressive strength by 20% ((a) and (c)), and -20% ((b) and (d)).

B

Difference in average residual base shear due to cohesion variation

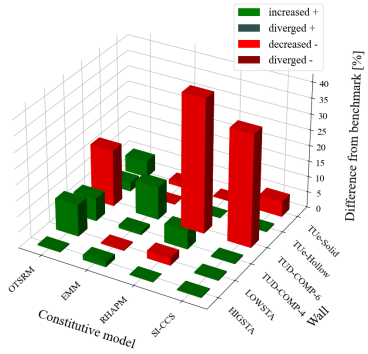

(a) +18%

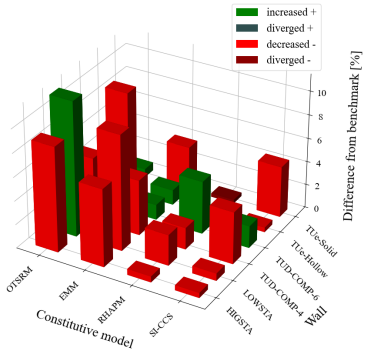

(b) -18%

Difference in dissipated energy due to cohesion variation

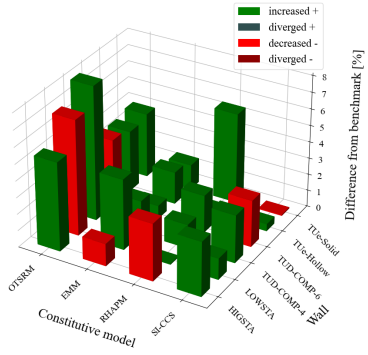

(c) +18%

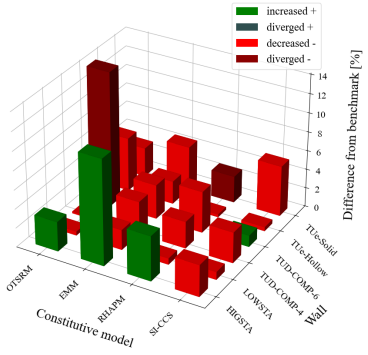

(d) -18%

Figure B.3: Difference in the residual base shear capacity (average of positive and negative direction) and dissipated energy between the original material properties and a variation of the cohesion by 18% ((a) and (c)), and -18% ((b) and (d)).

Difference in average residual base shear due to friction coefficient variation

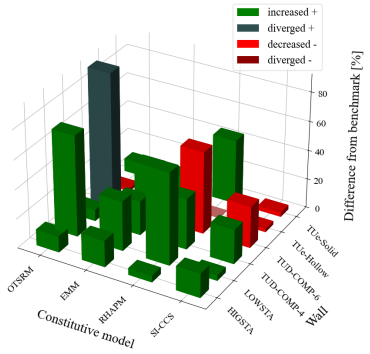

(a) maximum $tan\phi$

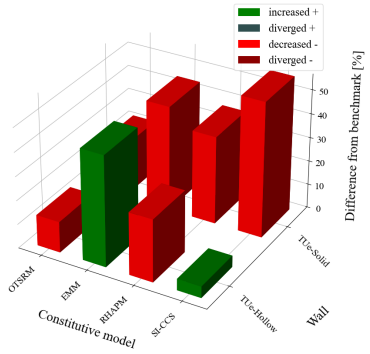

(b) maximum $tan\phi$

Difference in dissipated energy due to cohesion variation

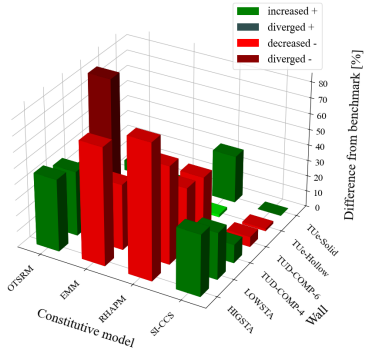

(c) +18%

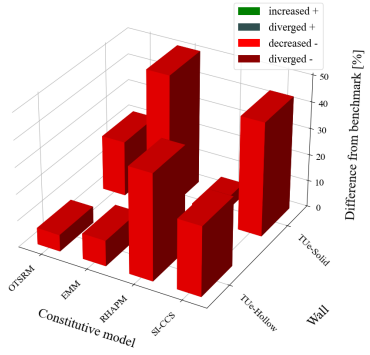

(d) -18%

Figure B.4: Difference in the residual base shear capacity (average of positive and negative direction) and dissipated energy between the original material properties and the maximum available friction coefficint ((a) and (c)), and minimum available friction coefficient ((b) and (d)).

B

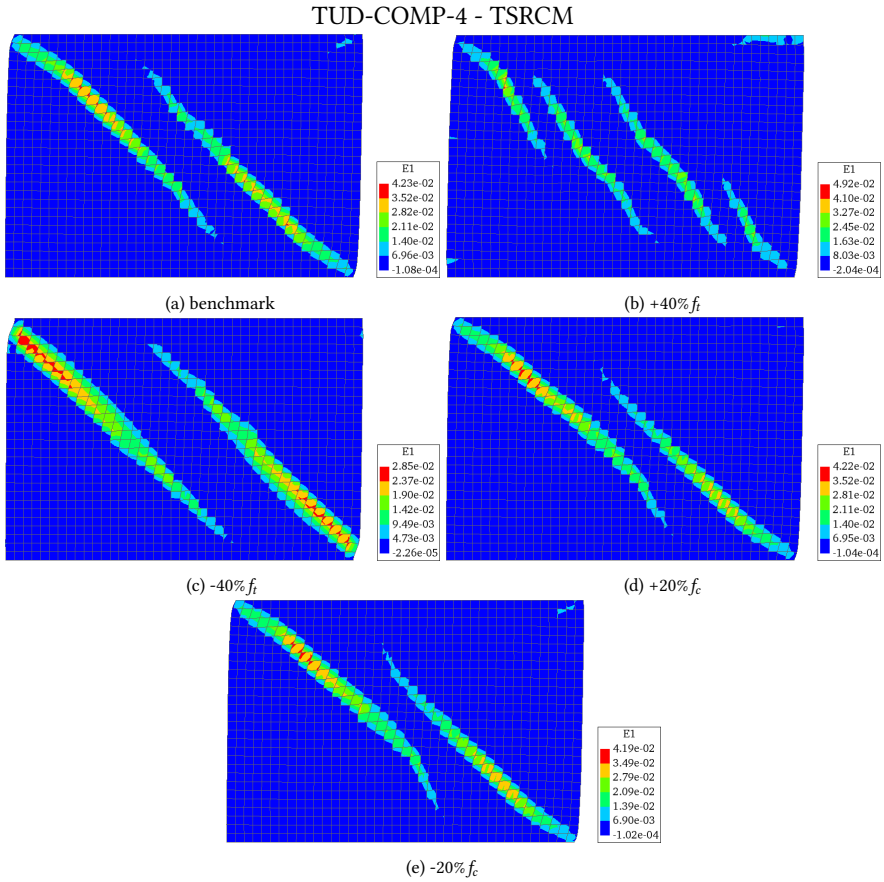

(a) benchmark (b) +40% f_t

(c) -40% f_t (d) +20% f_c

(e) -20% f_c

Figure B.5: Principal strain ε_1 for the material variations of the Total-Strain-Rotating-Crack Model (TSRCM) for the numerical model of wall TUD-COMP-4, depicted at the maximum applied displacement +5.93 mm (scale factor=20 for all models).

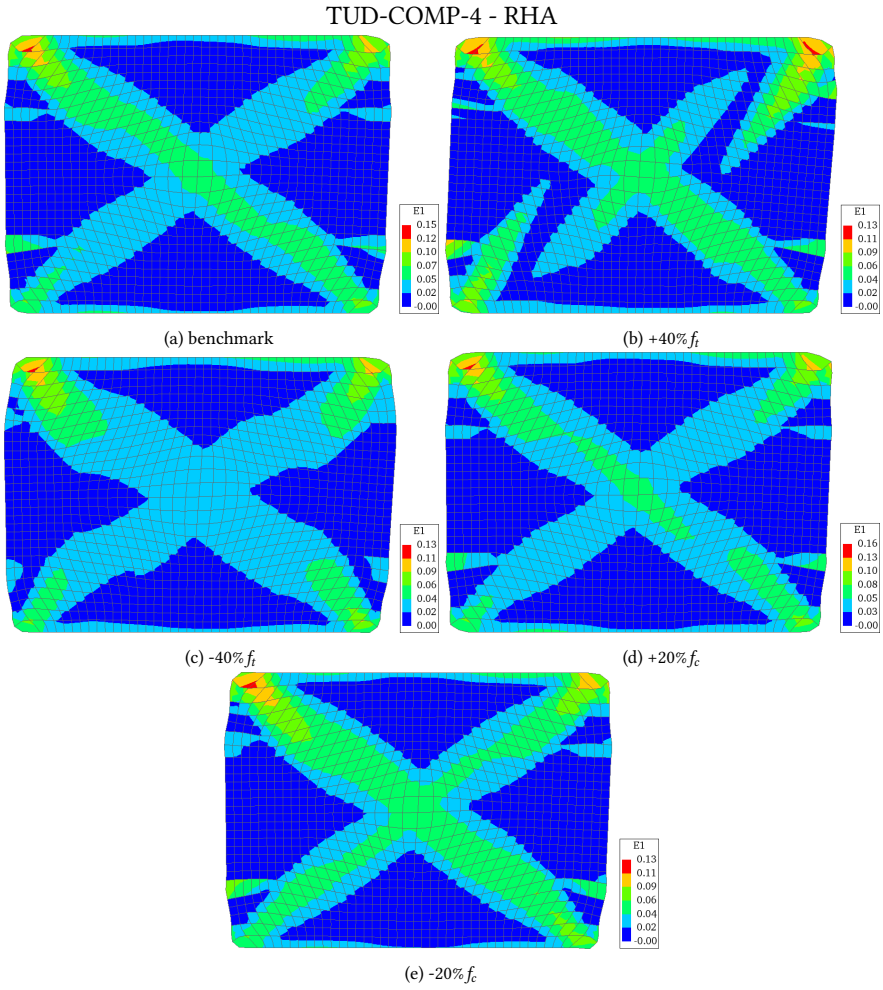

Figure B.6: Principal strain ε_1 for the material variations of the Rankine-Hill Anisotropy model (RHA) for the numerical model of wall TUD-COMP-4, depicted at the maximum applied displacement +5.93 mm (scale factor=20 for all models).

B

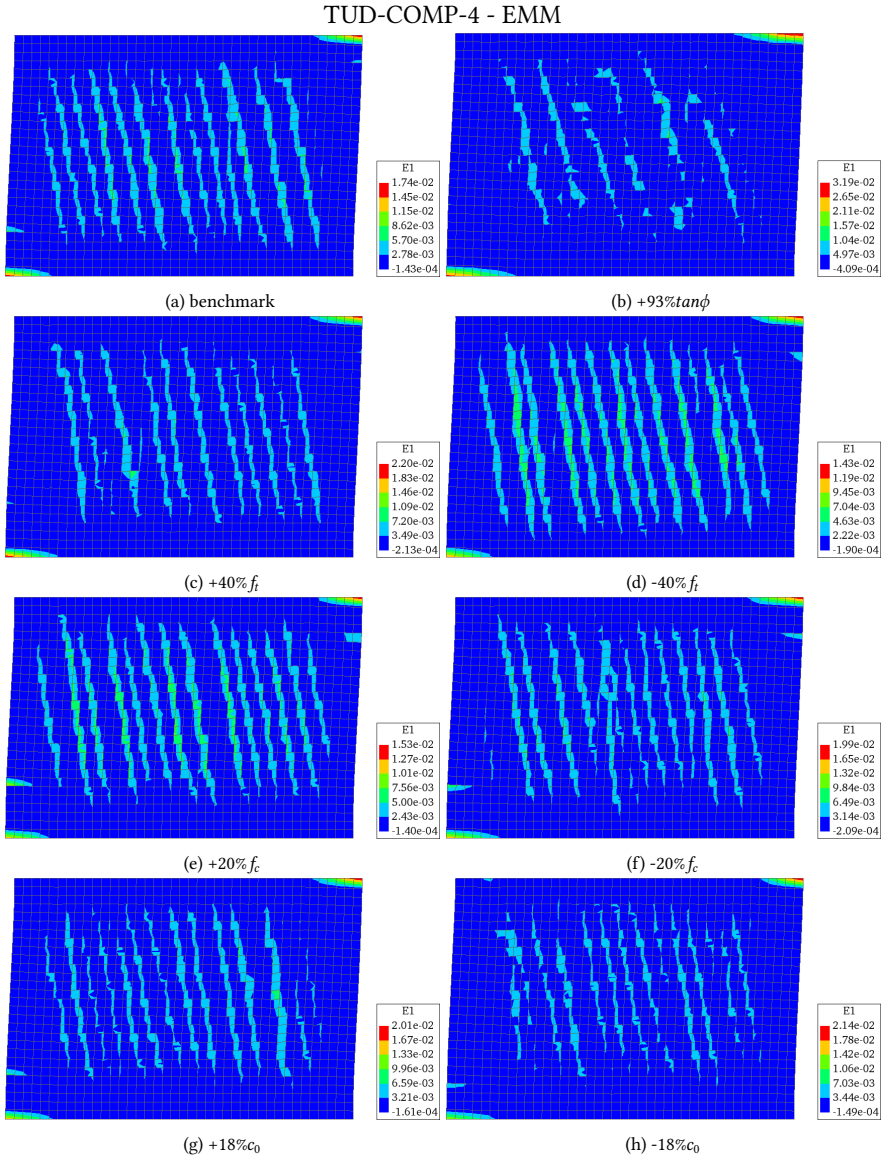

(a) benchmark (b) +93%$tan\phi$

(c) +40%f_t (d) -40%f_t

(e) +20%f_c (f) -20%f_c

(g) +18%c_0 (h) -18%c_0

Figure B.7: Principal strain ε_1 for the material variations of the Engineering Masonry Model (EMM) for the numerical model of wall TUD-COMP-4, depicted at the maximum applied displacement +5.93 mm (scale factor=20 for all models).

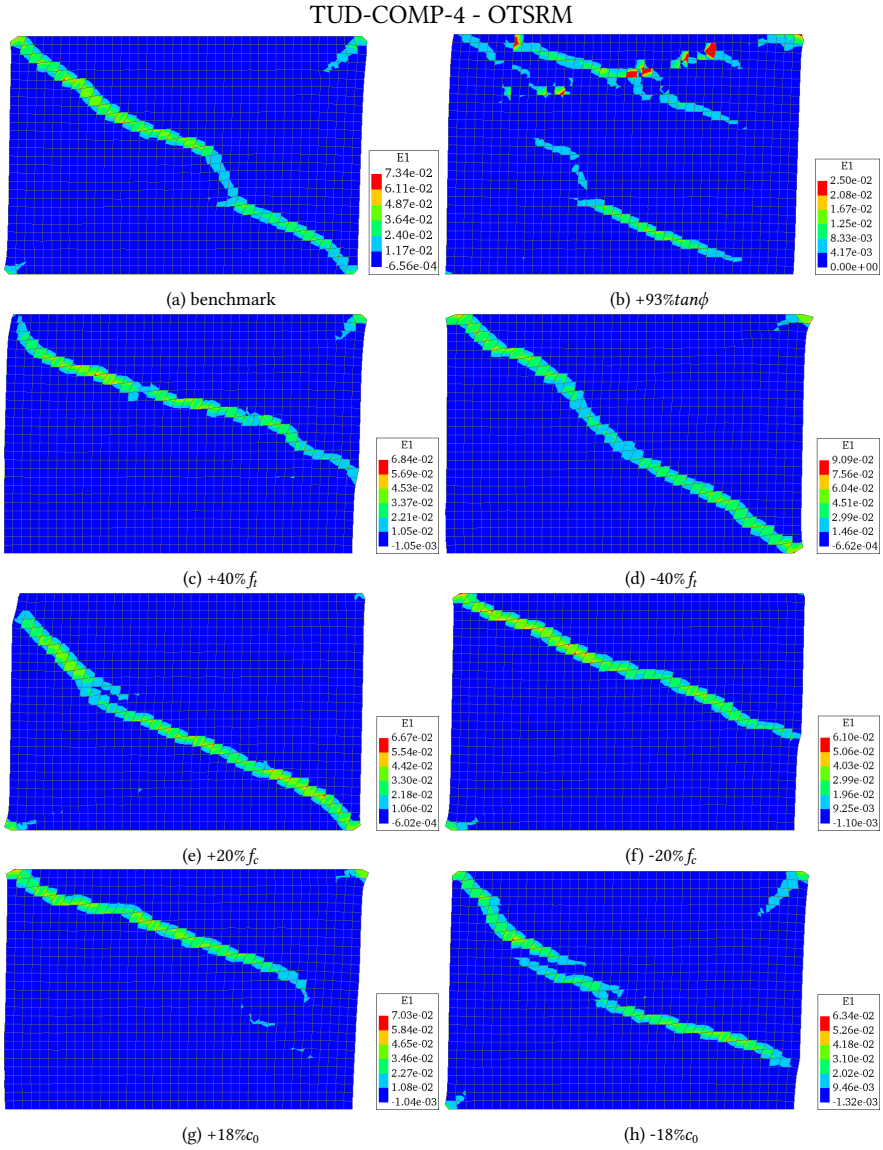

Figure B.8: Principal strain ε_1 for the material variations of the Orthotropic Total-Strain-Rotating Model (OTSRM) for the numerical model of wall TUD-COMP-4, depicted at the maximum applied displacement +5.93 mm (scale factor=20 for all models).

B

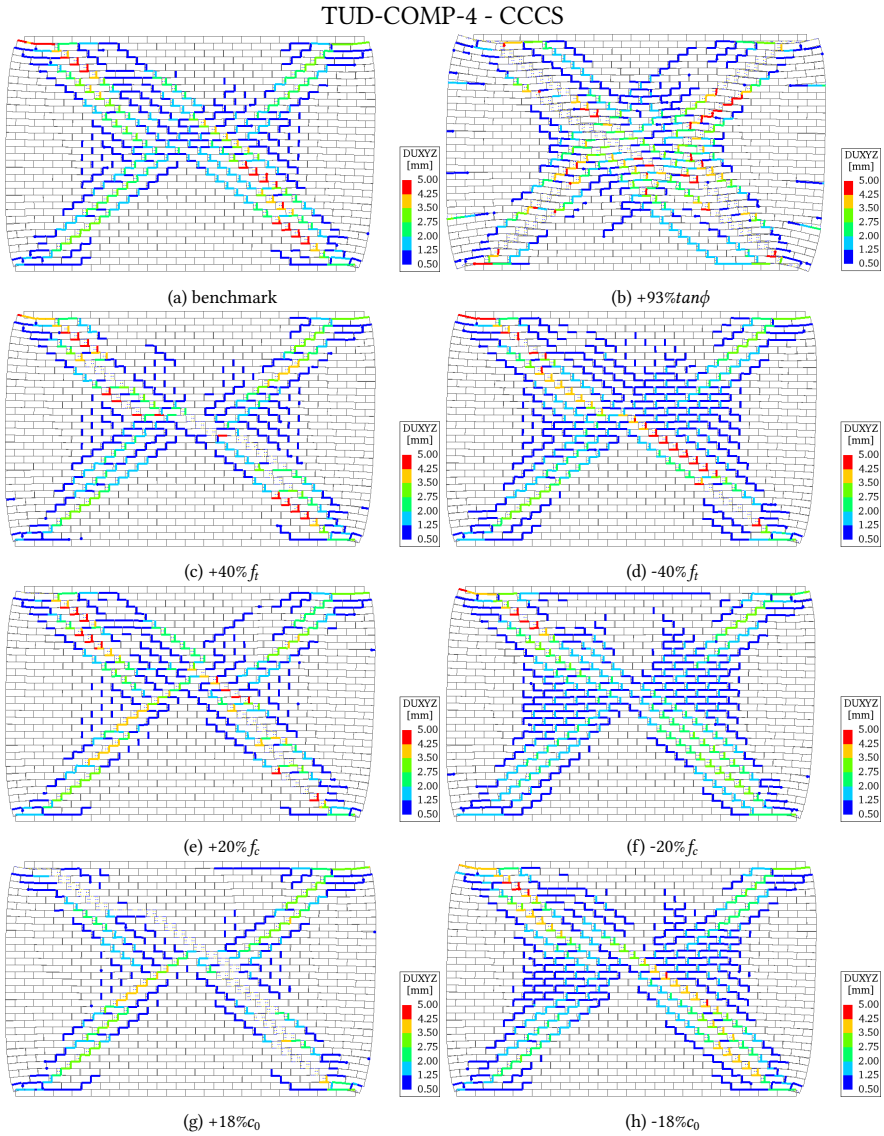

Figure B.9: Principal strain ε_1 for the material variations of the Combined Cracking, Crushing, Shearing micro-model (CCCS) for the numerical model of wall TUD-COMP-4, depicted at the maximum applied displacement +5.93 mm (scale factor=20 for all models).

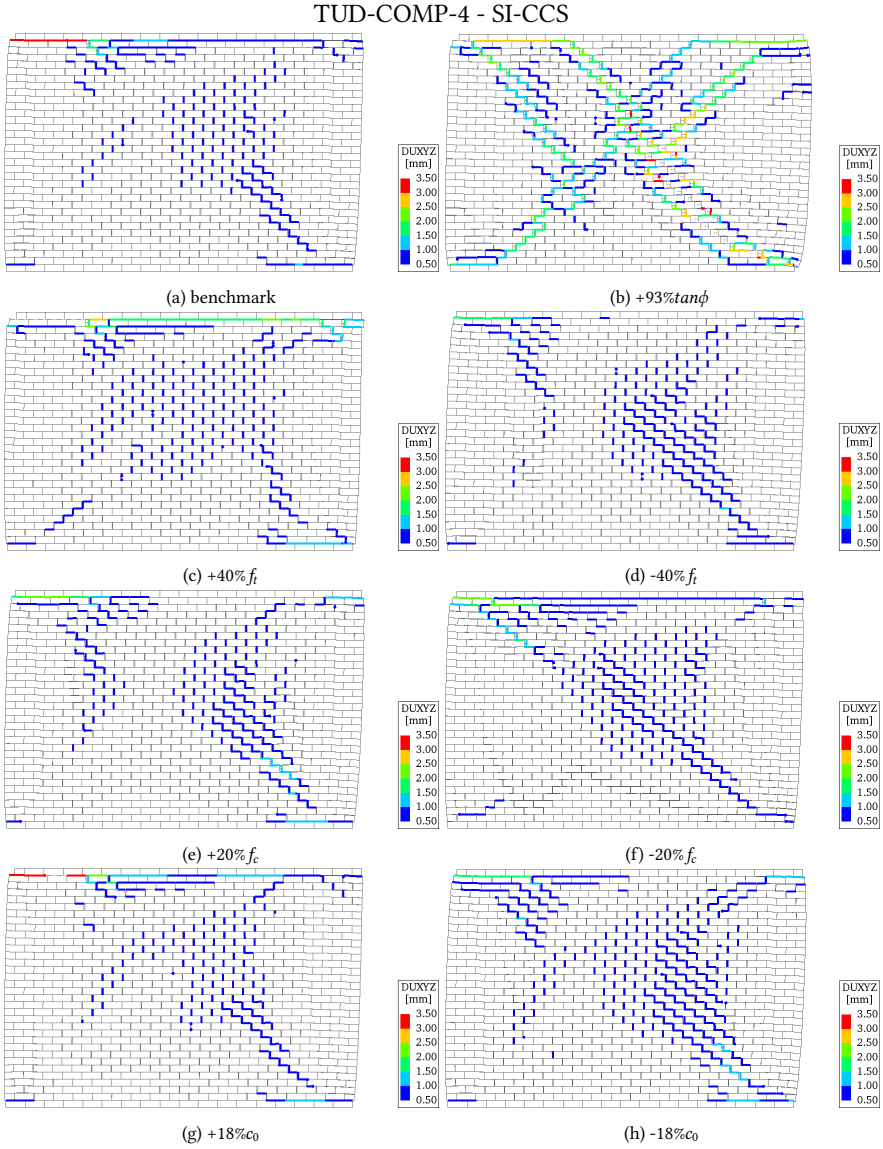

Figure B.10: Principal strain ε_1 for the material variations of the Sub-stepping Iterative- Cracking, Crushing, Shearing micro-model (SI-CCS) for the numerical model of wall TUD-COMP-4, depicted at the maximum applied displacement +5.93 mm (scale factor=20 for all models).

B

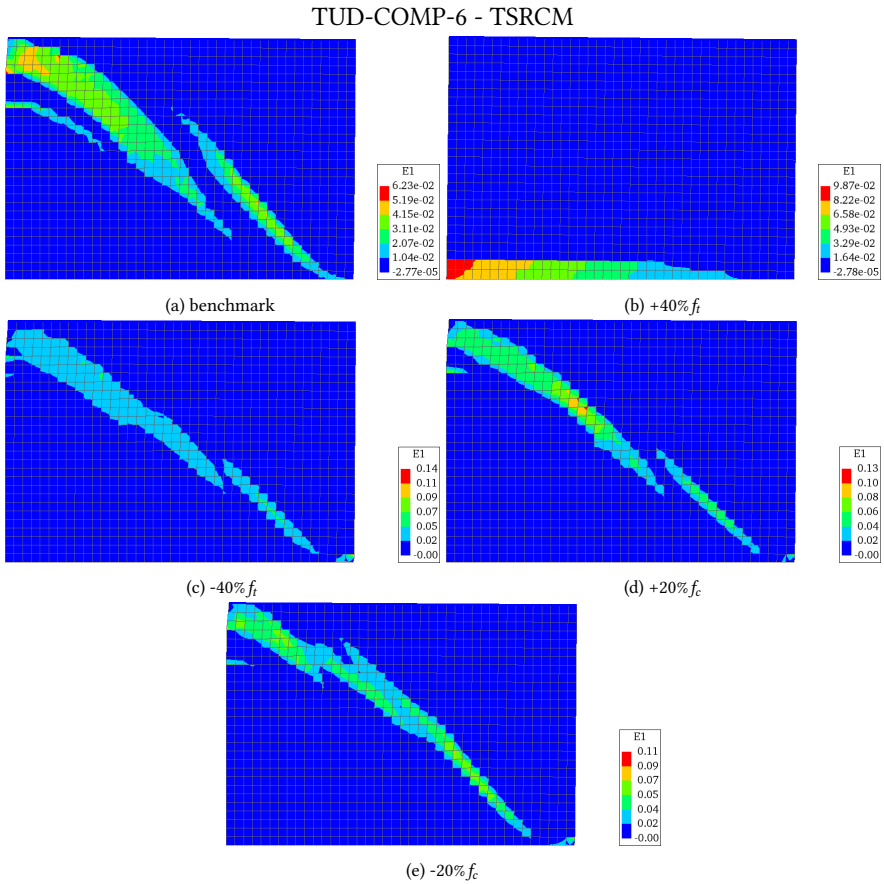

(a) benchmark (b) +40% f_t

(c) -40% f_t (d) +20% f_c

(e) -20% f_c

Figure B.11: Principal strain ε_1 for the material variations of the Total-Strain-Rotating-Crack Model (TSRCM) for the numerical model of wall TUD-COMP-6, depicted at the maximum applied displacement +15.35 mm (scale factor=2 for all models).

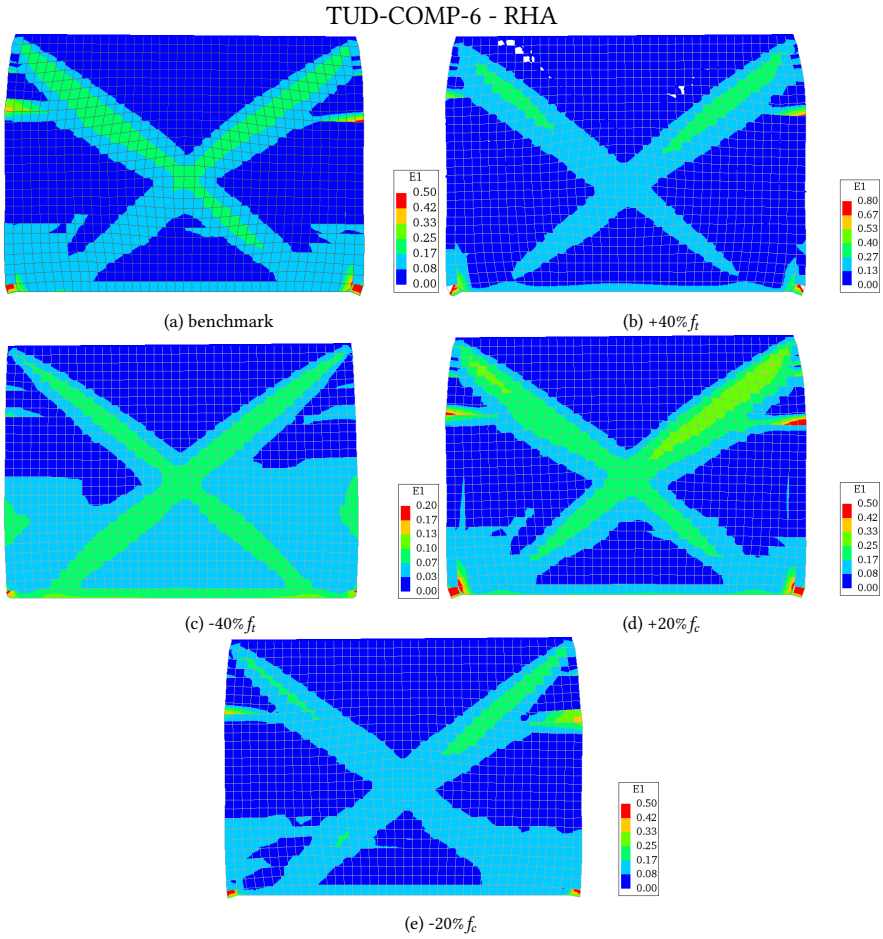

(a) benchmark

(b) +40% f_t

(c) -40% f_t

(d) +20% f_c

(e) -20% f_c

Figure B.12: Principal strain ε_1 for the material variations of the Rankine-Hill Anisotropy model (RHA) for the numerical model of wall TUD-COMP-6, depicted at the maximum applied displacement +15.35 mm (scale factor=2 for all models).

B

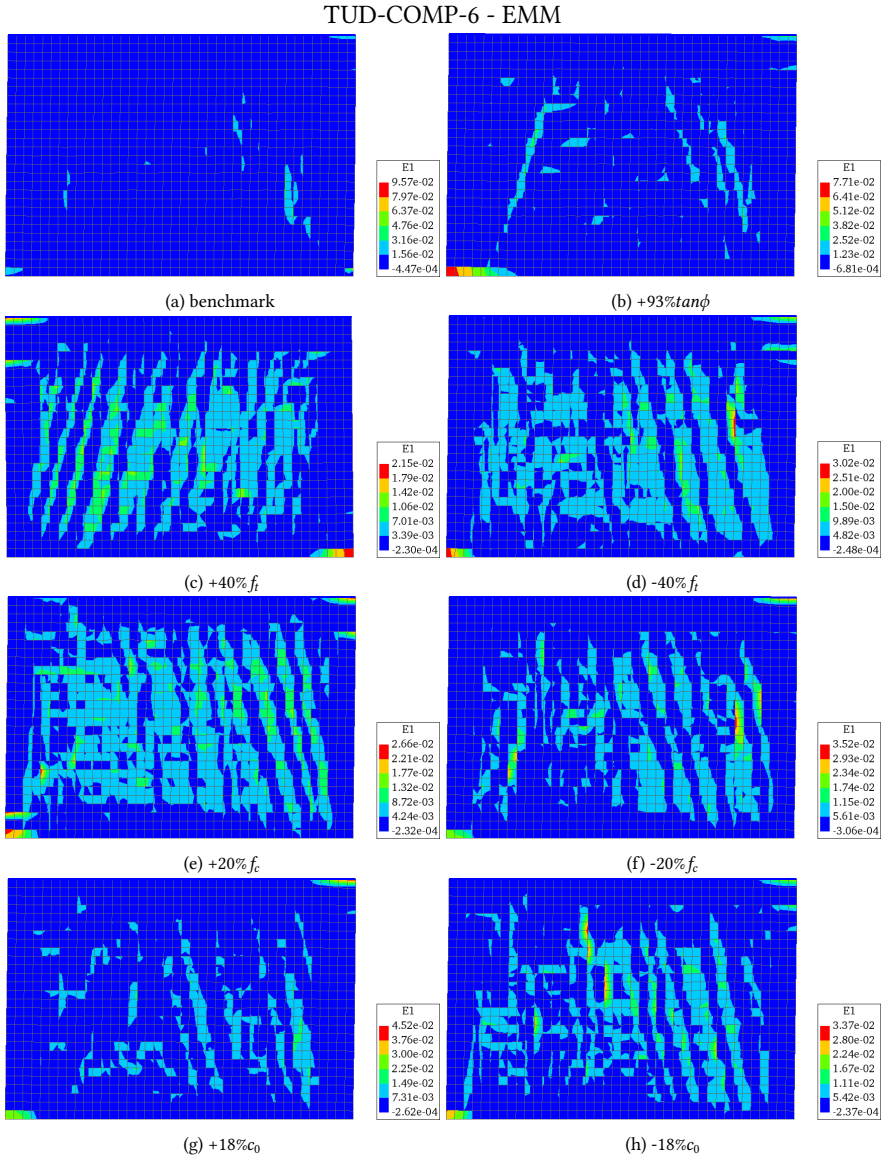

Figure B.13: Principal strain ε_1 for the material variations of the Engineering Masonry Model (EMM) for the numerical model of wall TUD-COMP-6, depicted at the maximum applied displacement +15.35 mm (scale factor=2 for all models).

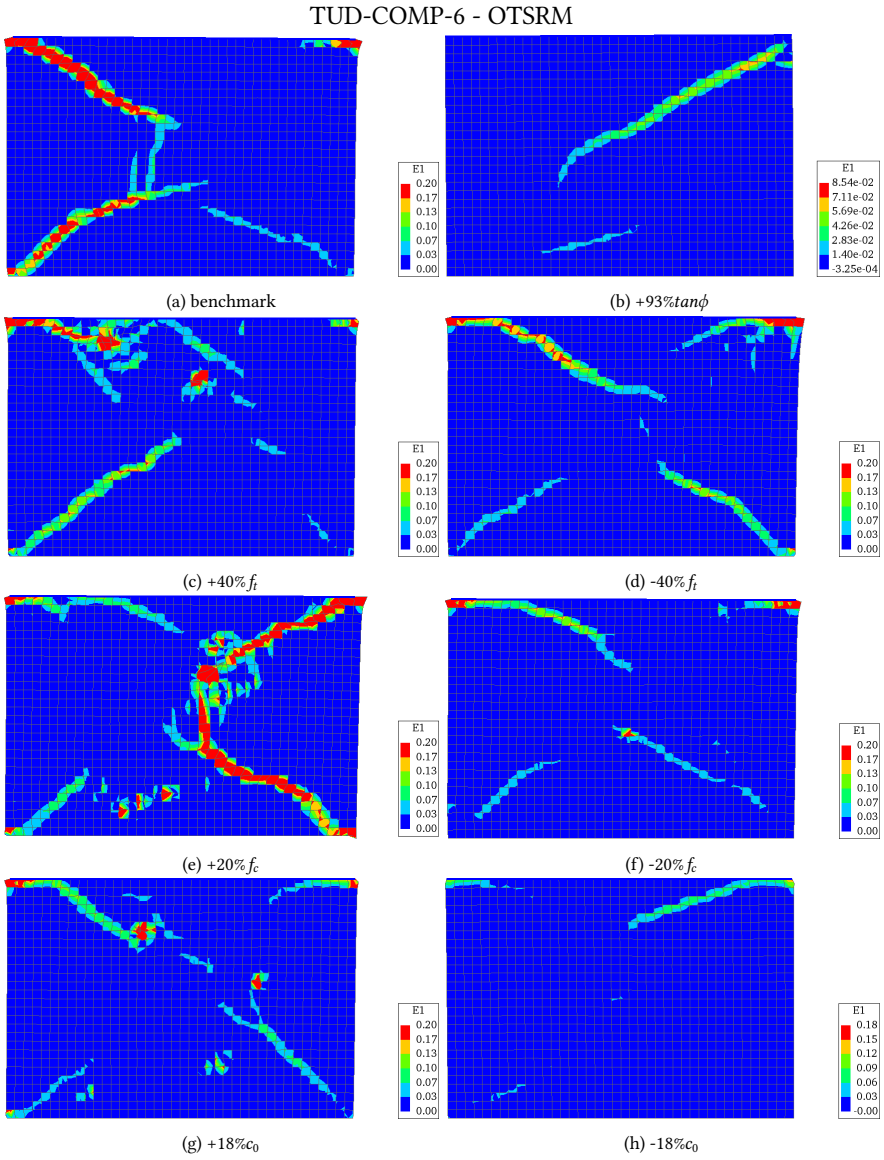

(a) benchmark (b) +93%$tan\phi$

(c) +40%f_t (d) -40%f_t

(e) +20%f_c (f) -20%f_c

(g) +18%c_0 (h) -18%c_0

Figure B.14: Principal strain ε_1 for the material variations of the Orthotropic Total-Strain-Rotating Model (OTSRM) for the numerical model of wall TUD-COMP-6, depicted at the maximum applied displacement +15.35 mm (scale factor=2 for all models).

B

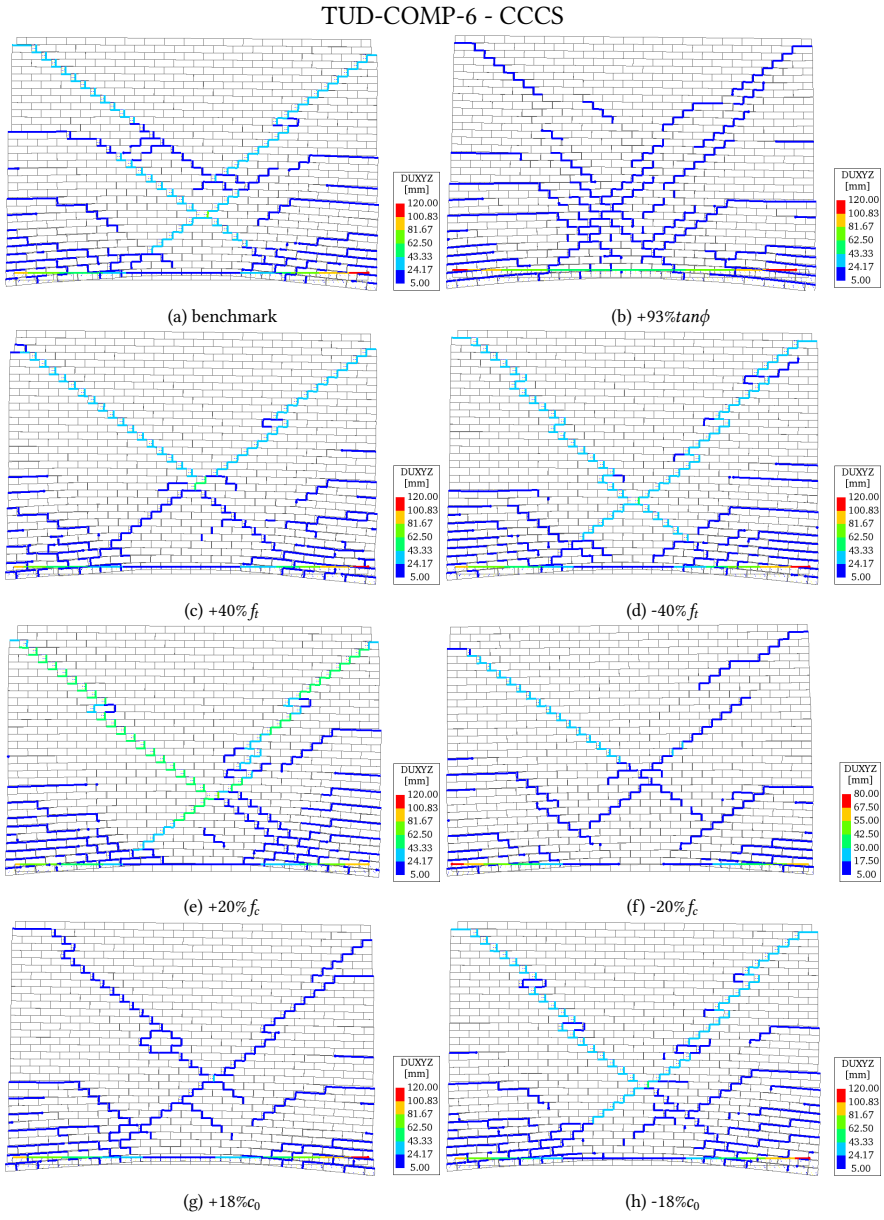

Figure B.15: Principal strain ε_1 for the material variations of the Combined Cracking, Crushing, Shearing micro-model (CCCS) for the numerical model of wall TUD-COMP-6, depicted at the maximum applied displacement +15.35 mm (scale factor=2 for all models).

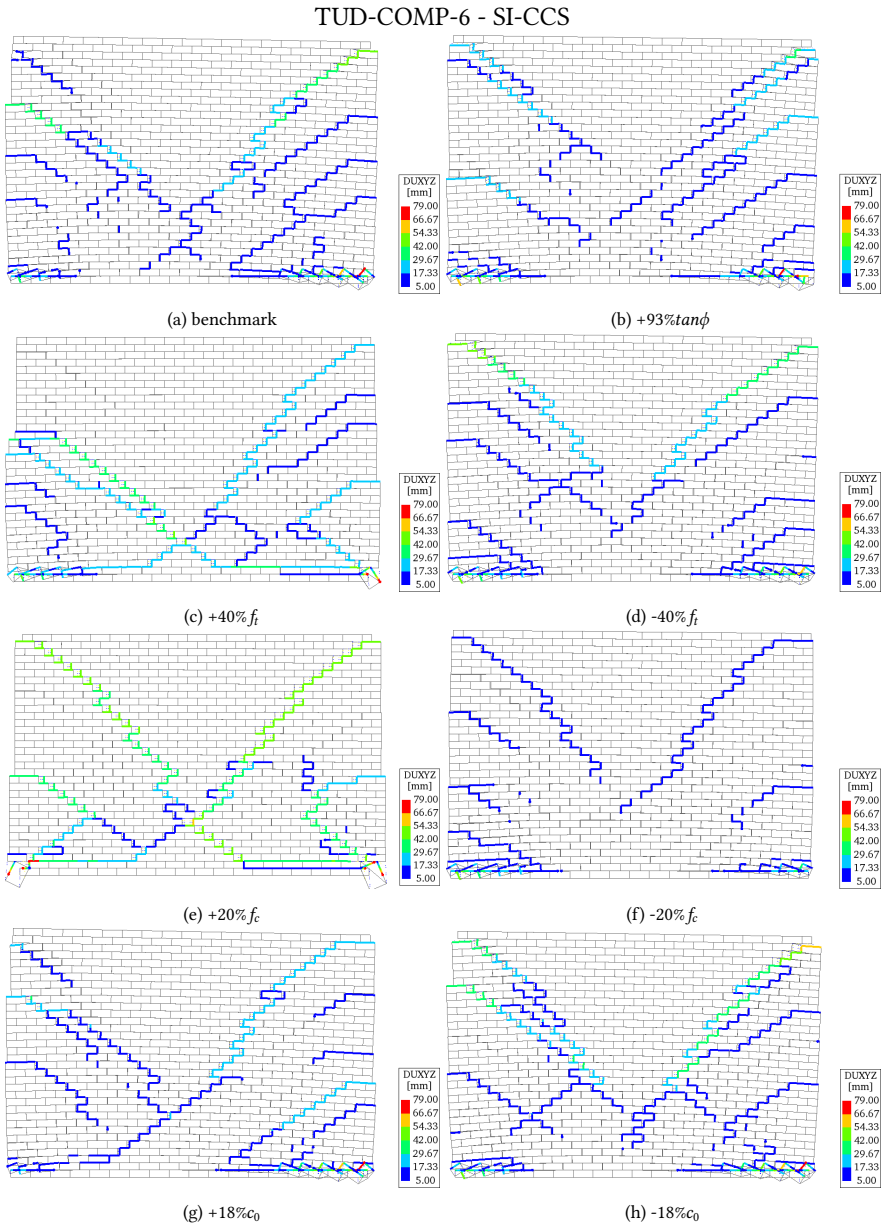

Figure B.16: Principal strain ε_1 for the material variations of the Sub-stepping Iterative- Cracking, Crushing, Shearing micro-model (SI-CCS) for the numerical model of wall TUD-COMP-6, depicted at the maximum applied displacement +15.35 mm (scale factor=2 for all models).

B

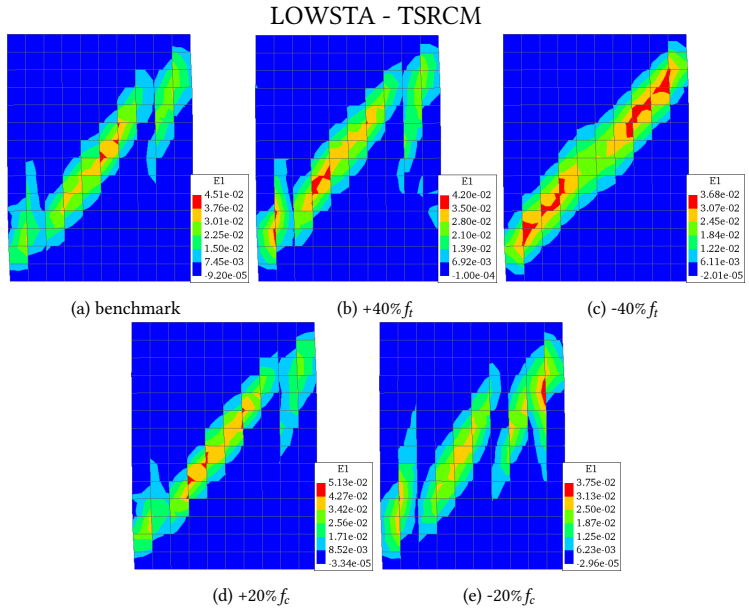

(a) benchmark (b) +40%f_t (c) -40%f_t

(d) +20%f_c (e) -20%f_c

Figure B.17: Principal strain ε_1 for the material variations of the Total-Strain-Rotating-Crack Model (TSRCM) for the numerical model of wall LOWSTA, depicted at the minimum applied displacement -7.7 mm (scale factor=2 for all models).

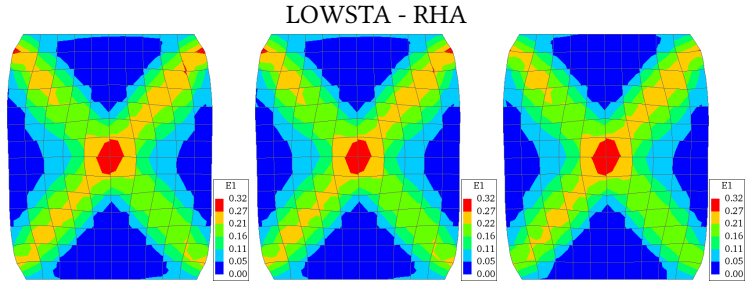

(a) benchmark (b) +40%f_t (c) -20%f_c

Figure B.18: Principal strain ε_1 for the material variations of the Rankine-Hill Anisotropy model (RHA) for the numerical model of wall LOWSTA, depicted at the minimum applied displacement -7.7 mm (scale factor=2 for all models).

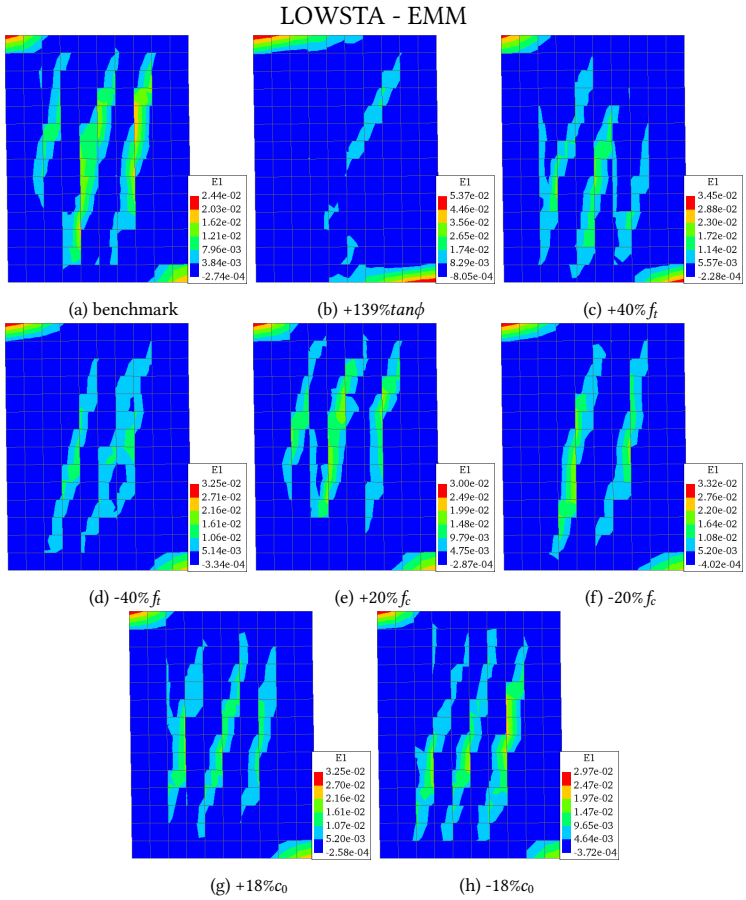

Figure B.19: Principal strain ε_1 for the material variations of the Engineering Masonry Model (EMM) for the numerical model of wall LOWSTA, depicted at the minimum applied displacement -7.7 mm (scale factor=2 for all models).

B

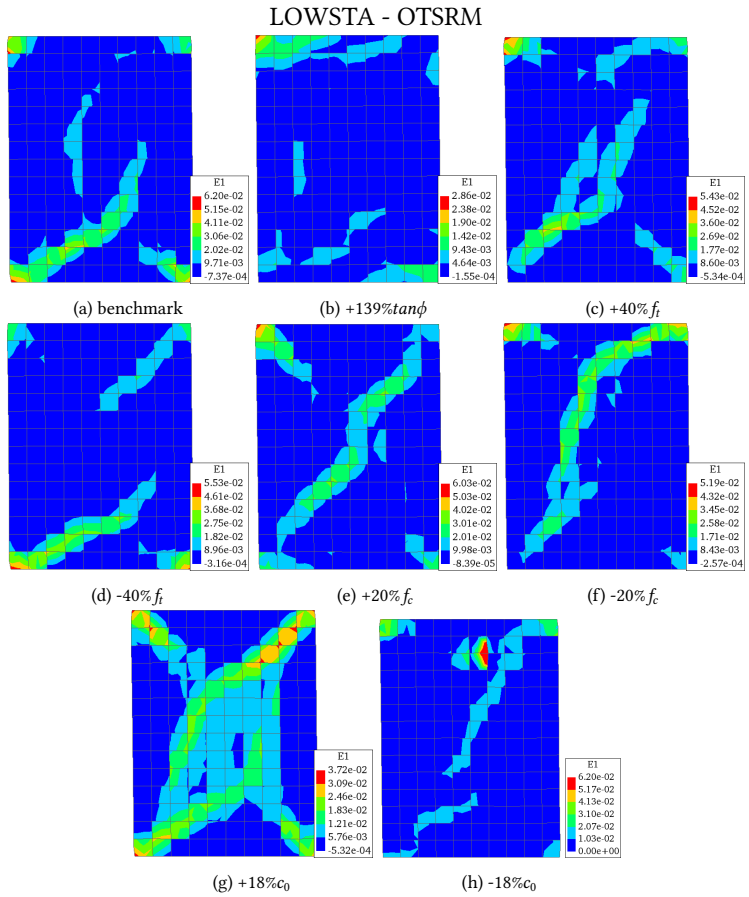

Figure B.20: Principal strain ε_1 for the material variations of the Orthotropic Total-Strain-Rotating Model (OTSRM) for the numerical model of wall LOWSTA, depicted at the minimum applied displacement -7.7 mm (scale factor=2 for all models).

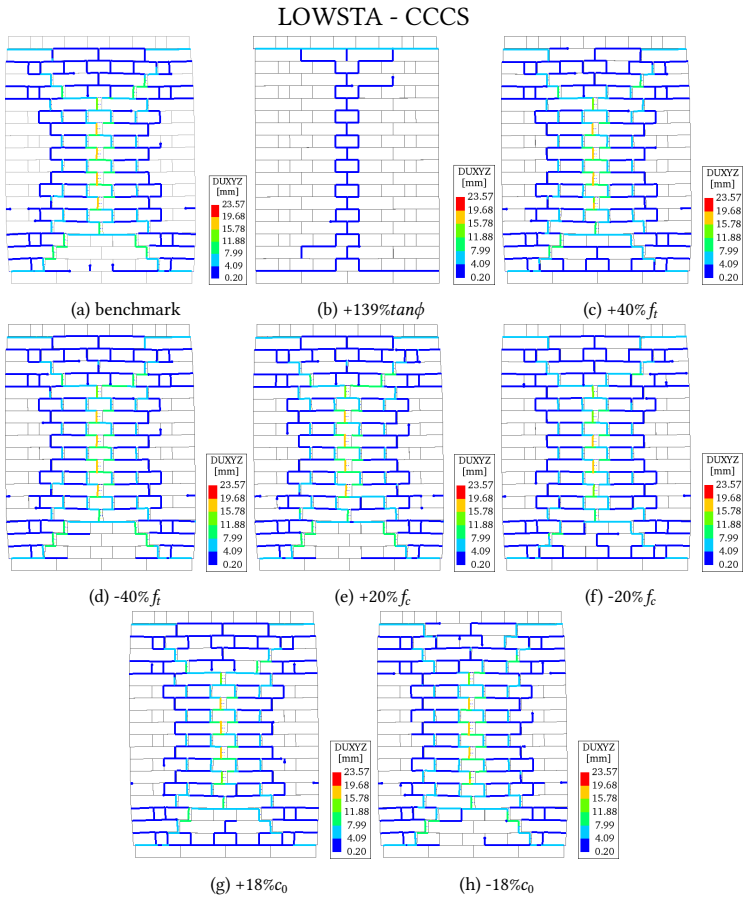

Figure B.21: Principal strain ε_1 for the material variations of the Combined Cracking, Crushing, Shearing micro-model (CCCS) for the numerical model of wall LOWSTA, depicted at the minimum applied displacement -7.7 mm (scale factor=2 for all models).

B

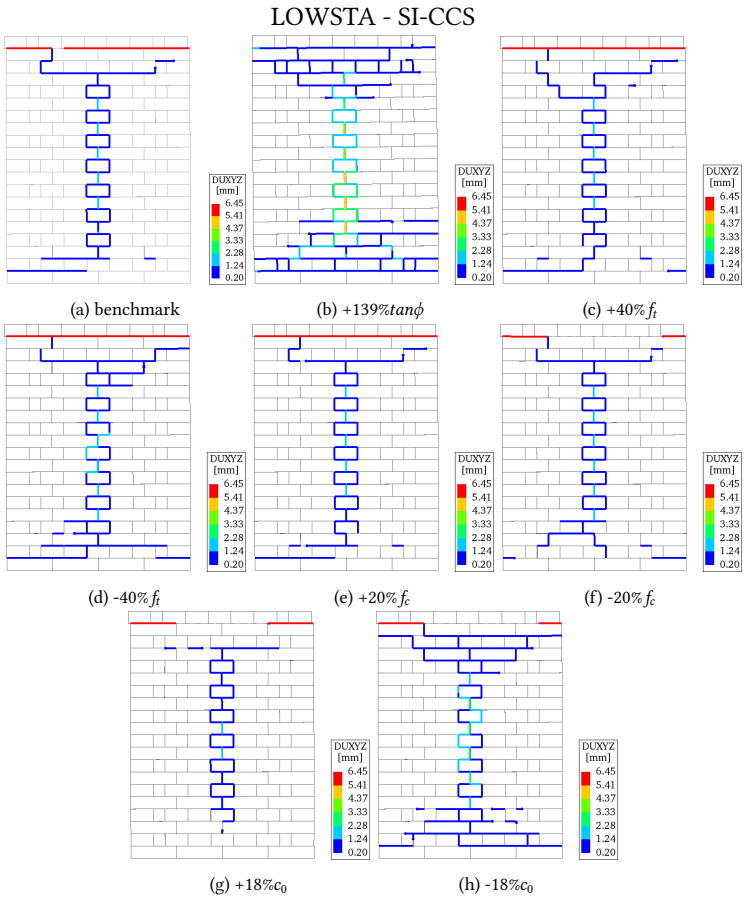

Figure B.22: Principal strain ε_1 for the material variations of the Sub-stepping Iterative- Cracking, Crushing, Shearing micro-model (SI-CCS) for the numerical model of wall LOWSTA, depicted at the minimum applied displacement -7.7 mm (scale factor=2 for all models).

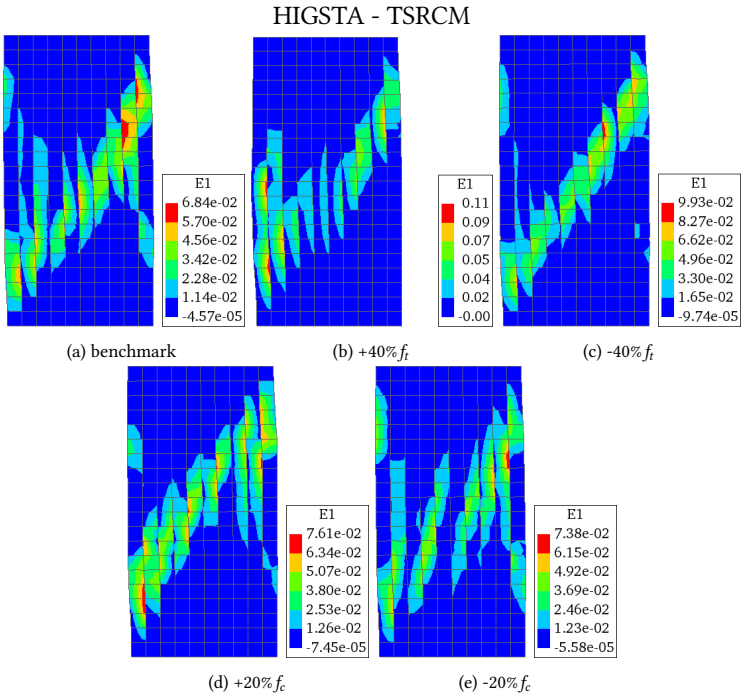

Figure B.23: Principal strain ε_1 for the material variations of the Total-Strain-Rotating-Crack Model (TSRCM) for the numerical model of wall HIGSTA, depicted at the minimum applied displacement -12.96 mm (scale factor=2 for all models).

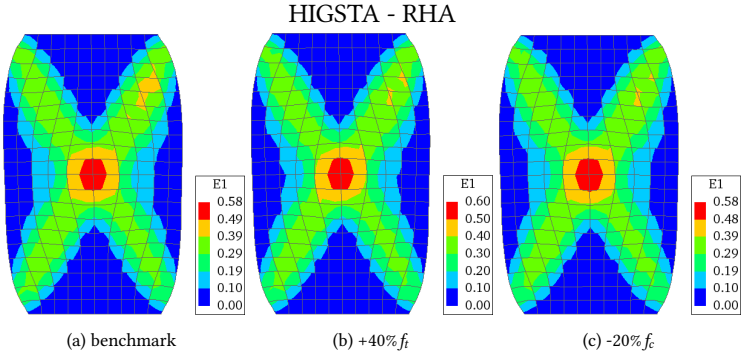

Figure B.24: Principal strain ε_1 for the material variations of the Rankine-Hill Anisotropy model (RHA) for the numerical model of wall HIGSTA, depicted at the minimum applied displacement -12.96 mm (scale factor=2 for all models).

B

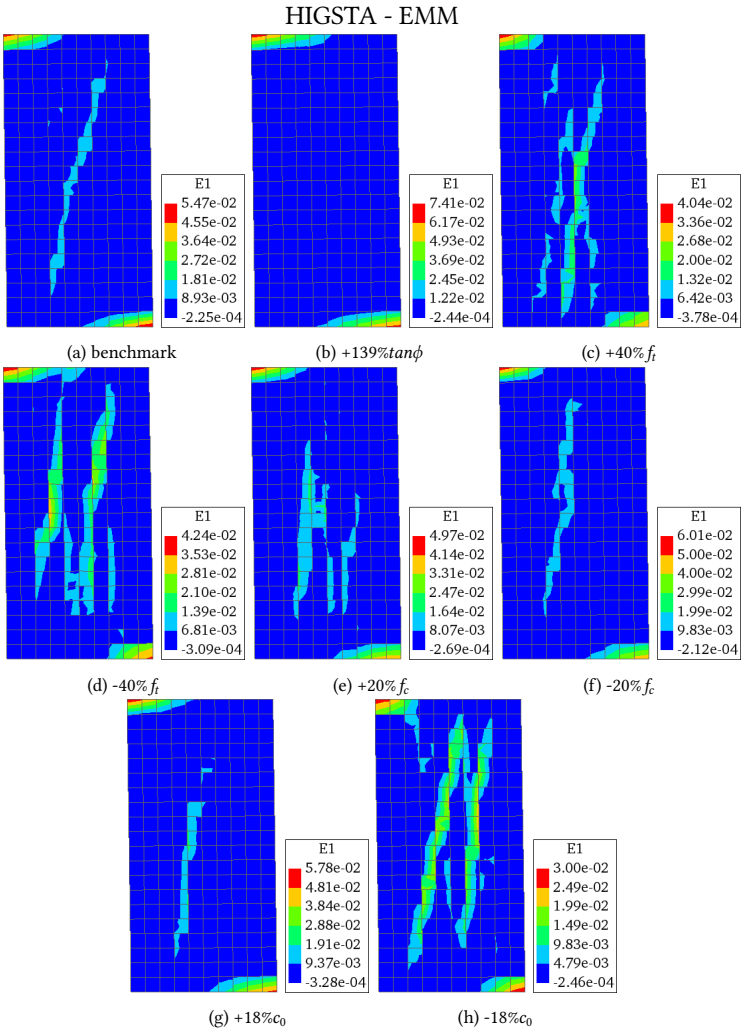

Figure B.25: Principal strain ε_1 for the material variations of the Engineering Masonry Model (EMM) for the numerical model of wall HIGSTA, depicted at the minimum applied displacement -12.96 mm (scale factor=2 for all models).

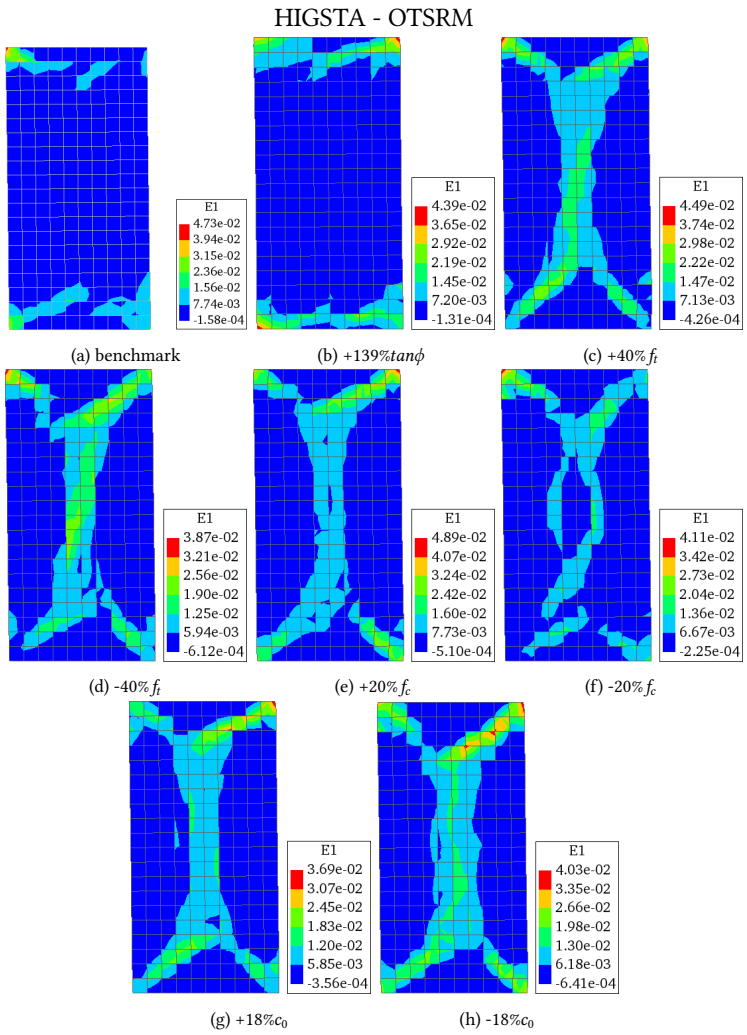

Figure B.26: Principal strain ε_1 for the material variations of the Orthotropic Total-Strain-Rotating Model (OTSRM) for the numerical model of wall HIGSTA, depicted at the minimum applied displacement -12.96 mm (scale factor=2 for all models).

B

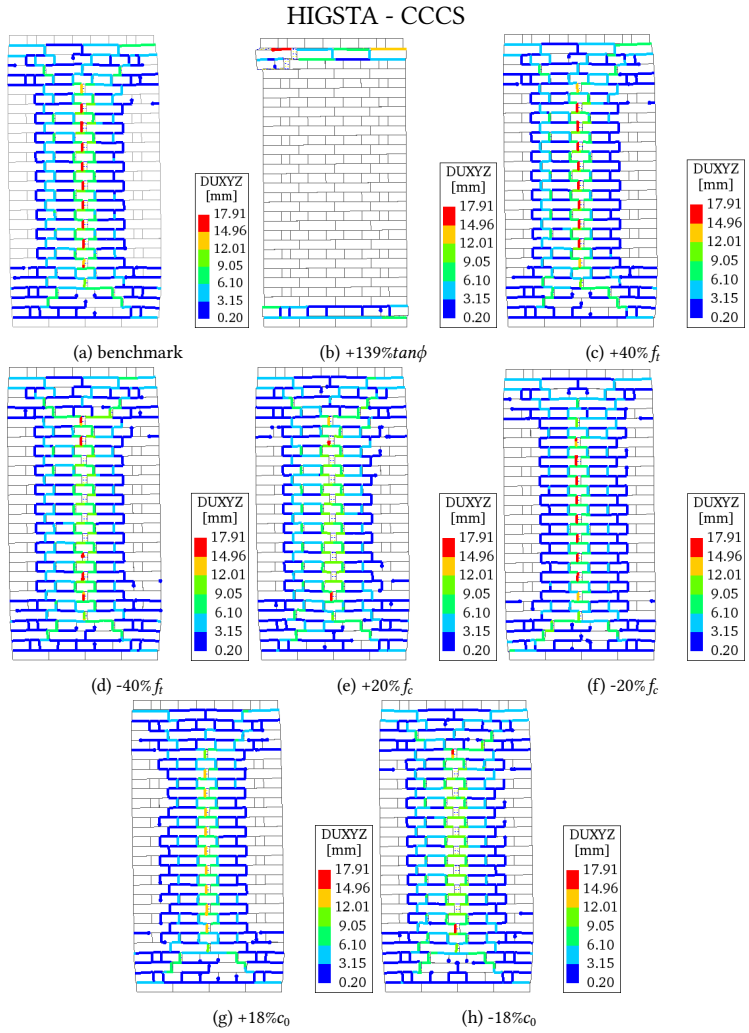

Figure B.27: Principal strain ε_1 for the material variations of the Combined Cracking, Crushing, Shearing micro-model (CCCS) for the numerical model of wall HIGSTA, depicted at the minimum applied displacement -12.96 mm (scale factor=2 for all models).

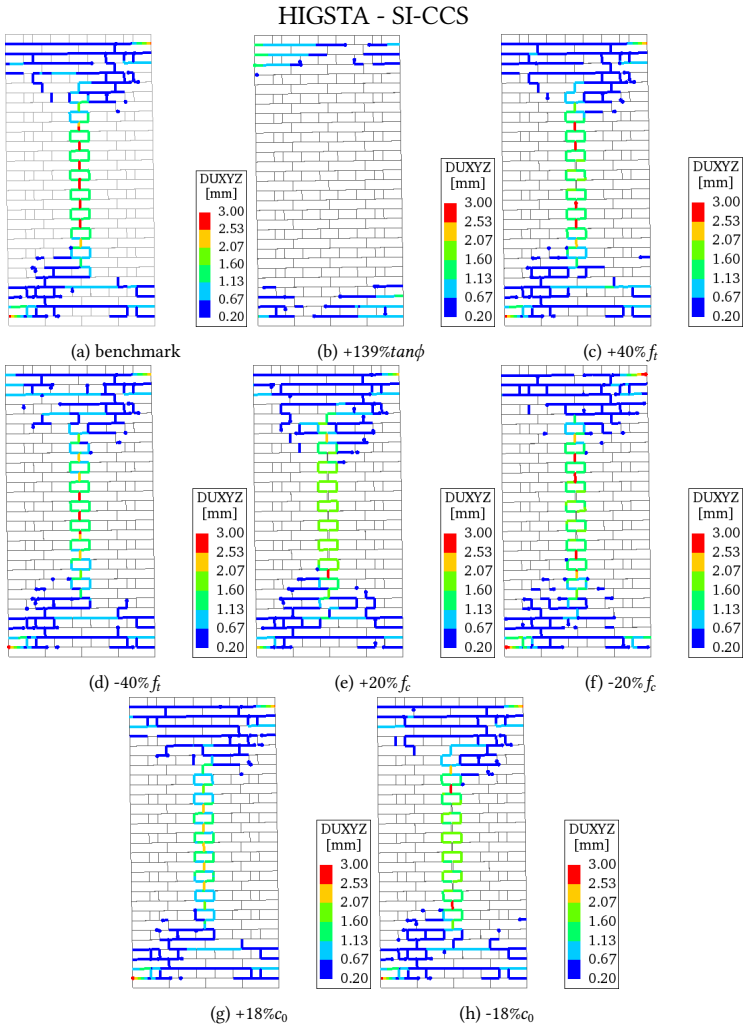

Figure B.28: Principal strain ε_1 for the material variations of the Sub-stepping Iterative- Cracking, Crushing, Shearing micro-model (SI-CCS) for the numerical model of wall HIGSTA, depicted at the minimum applied displacement -12.96 mm (scale factor=2 for all models).

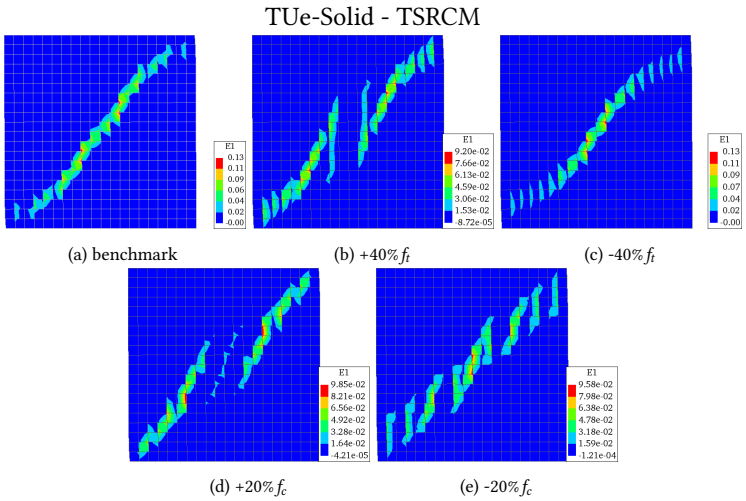

Figure B.29: Principal strain ε_1 for the material variations of the Total-Strain-Rotating-Crack Model (TSRCM) for the numerical model of wall TUe-Solid, depicted at the maximum applied displacement +4 mm (scale factor=2 for all models).

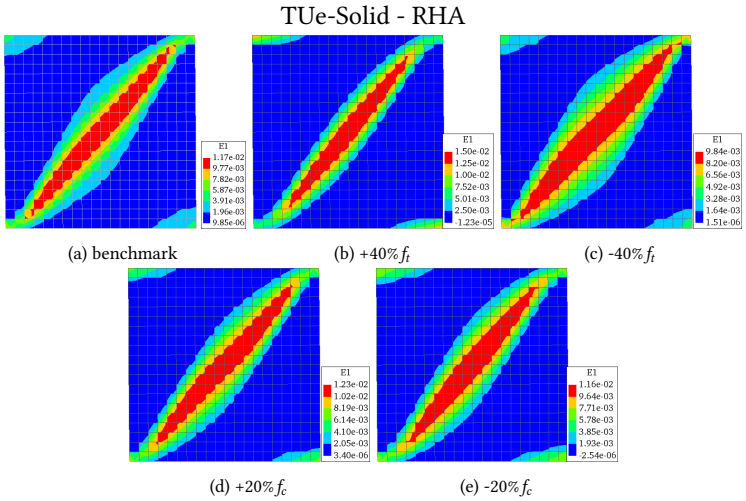

Figure B.30: Principal strain ε_1 for the material variations of the Rankine-Hill Anisotropy model (RHA) for the numerical model of wall TUe-Solid, depicted at the maximum applied displacement +4 mm (scale factor=2 for all models).

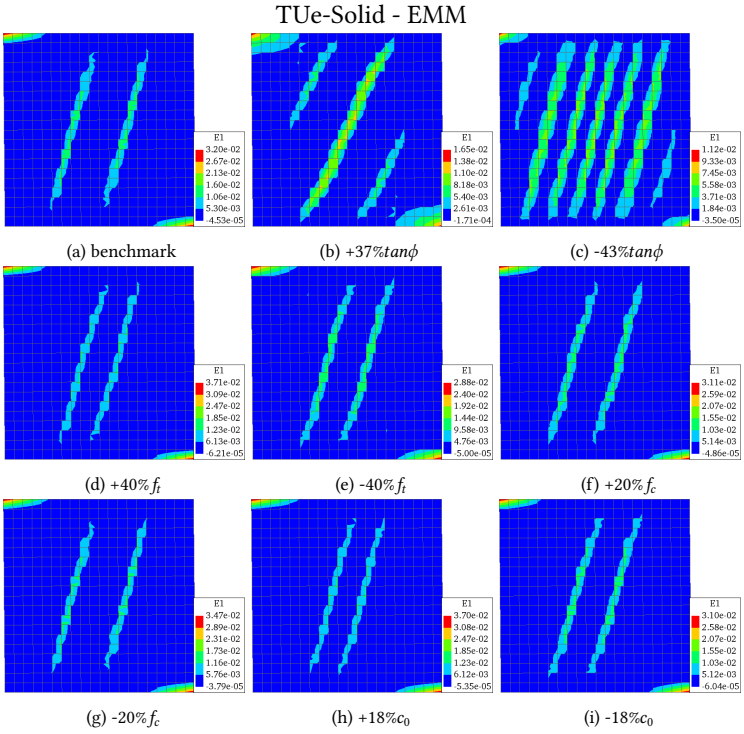

Figure B.31: Principal strain ε_1 for the material variations of the Engineering Masonry Model (EMM) for the numerical model of wall TUe-Solid, depicted at the maximum applied displacement +4 mm (scale factor=2 for all models).

B

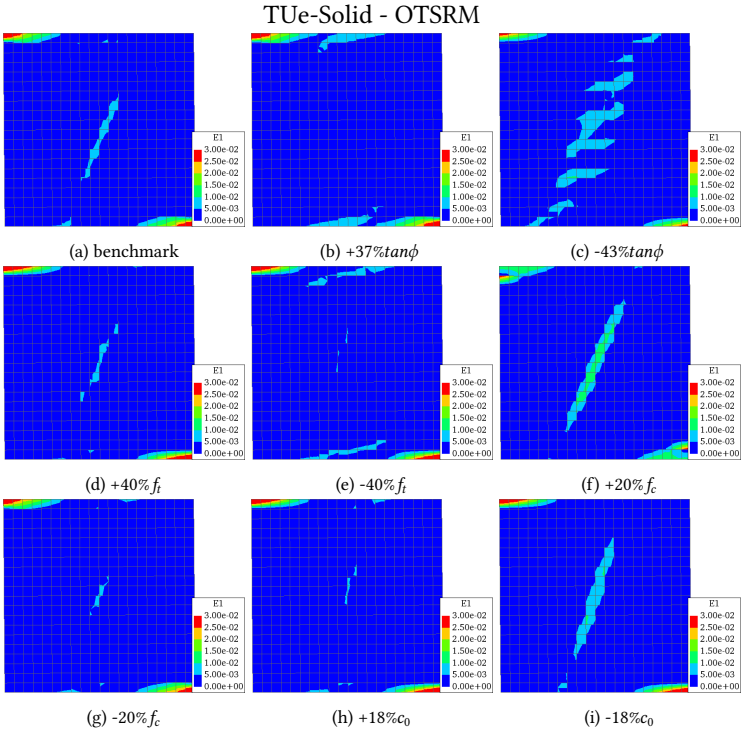

(a) benchmark (b) +37%$tan\phi$ (c) -43%$tan\phi$

(d) +40%f_t (e) -40%f_t (f) +20%f_c

(g) -20%f_c (h) +18%c_0 (i) -18%c_0

Figure B.32: Principal strain ε_1 for the material variations of the Orthotropic Total-Strain-Rotating Model (OTSRM) for the numerical model of wall TUe-Solid, depicted at the maximum applied displacement +4 mm (scale factor=2 for all models).

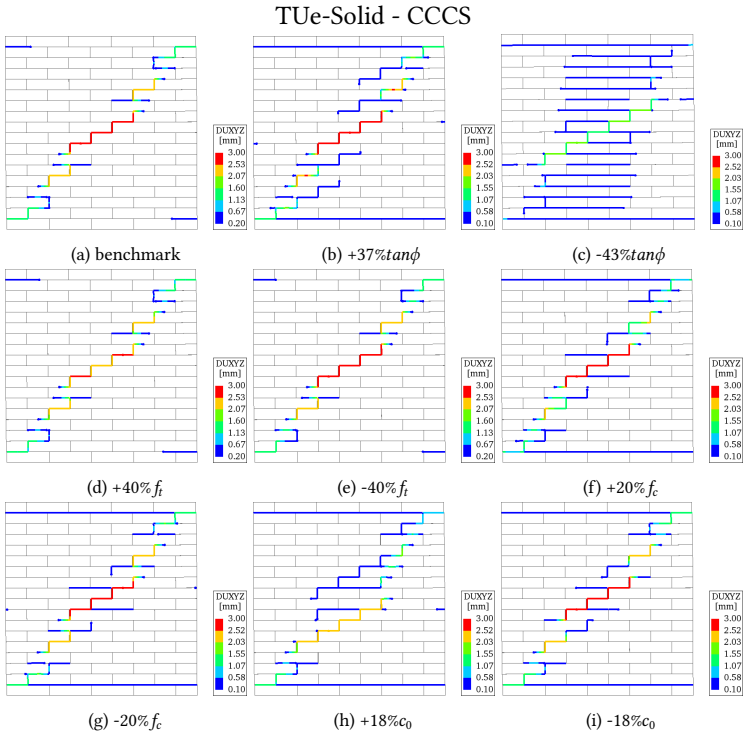

Figure B.33: Principal strain ε_1 for the material variations of the Combined Cracking, Crushing, Shearing micro-model (CCCS) for the numerical model of wall TUe-Solid, depicted at the maximum applied displacement +4 mm (scale factor=2 for all models).

B

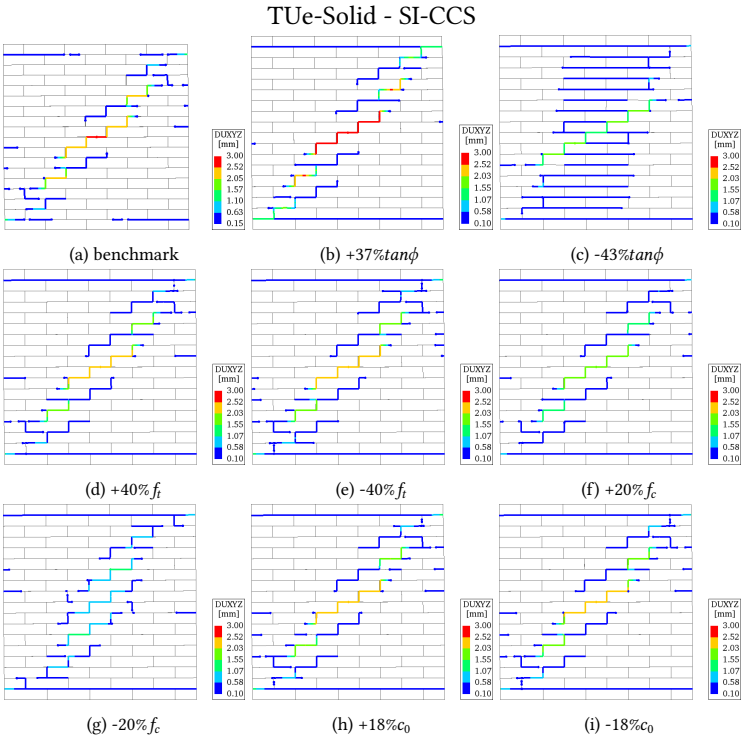

Figure B.34: Principal strain ε_1 for the material variations of the Sub-stepping Iterative- Cracking, Crushing, Shearing micro-model (SI-CCS) for the numerical model of wall TUe-Solid, depicted at the maximum applied displacement +4 mm (scale factor=2 for all models).

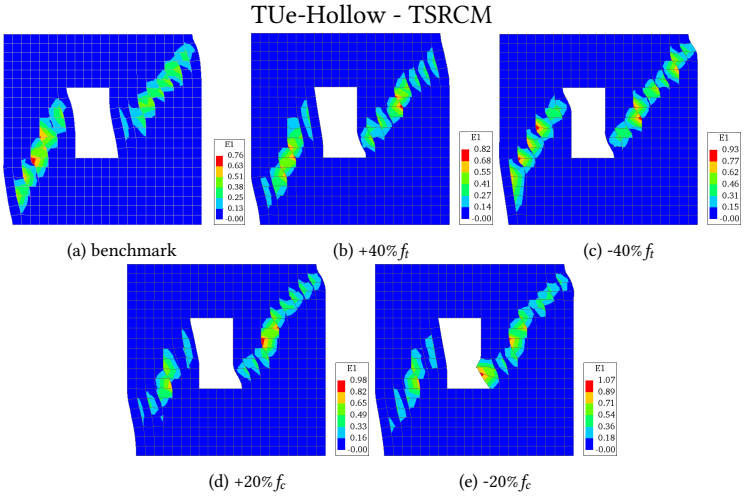

Figure B.35: Principal strain ε_1 for the material variations of the Total-Strain-Rotating-Crack Model (TSRCM) for the numerical model of wall TUe-Hollow, depicted at the maximum applied displacement +24 mm (scale factor=2 for all models).

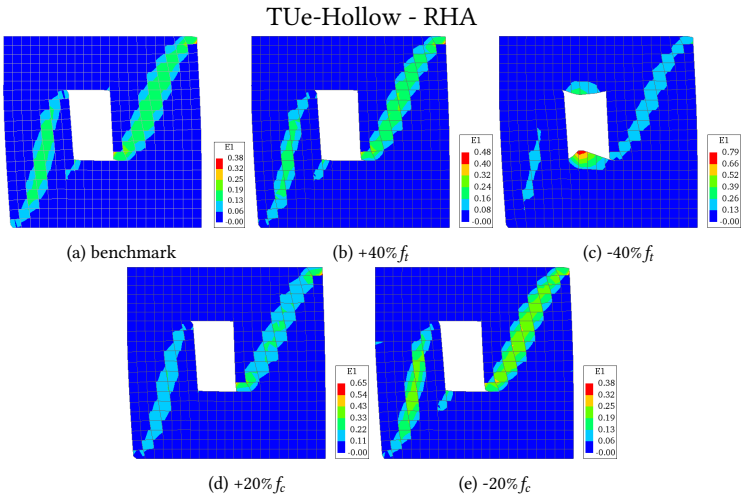

Figure B.36: Principal strain ε_1 for the material variations of the Rankine-Hill Anisotropy model (RHA) for the numerical model of wall TUe-Hollow, depicted at the maximum applied displacement +24 mm (scale factor=2 for all models).

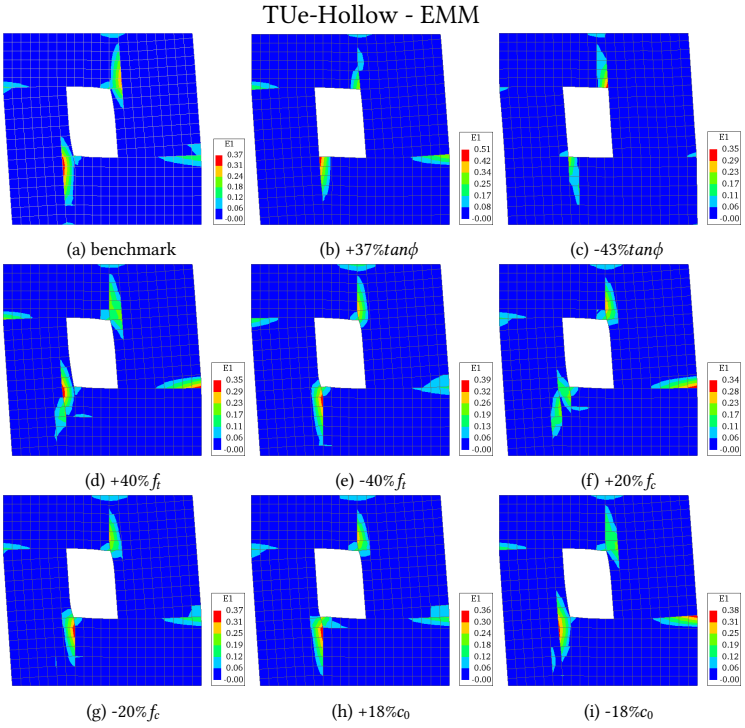

Figure B.37: Principal strain ε_1 for the material variations of the Engineering Masonry Model (EMM) for the numerical model of wall TUe-Hollow, depicted at the maximum applied displacement +24 mm (scale factor=2 for all models).

B

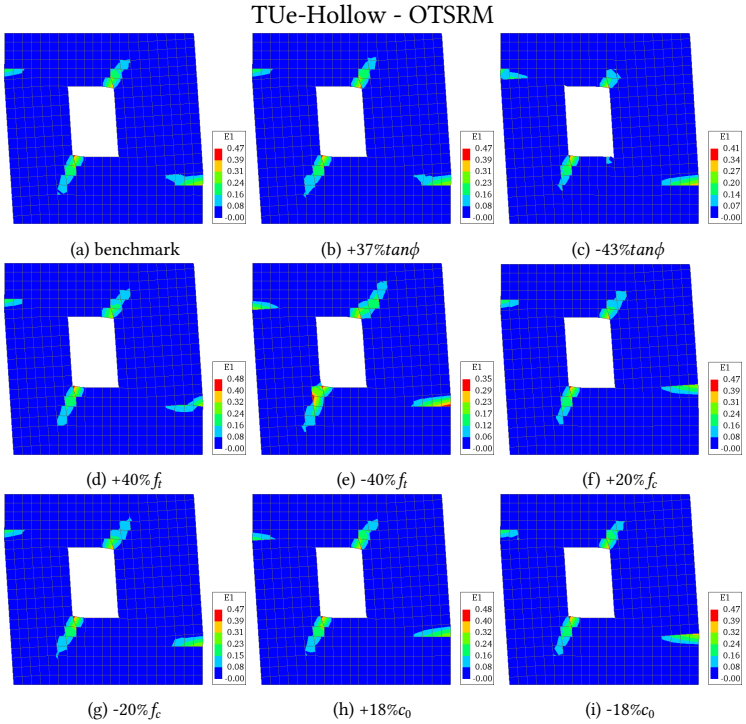

(a) benchmark (b) +37%$tan\phi$ (c) -43%$tan\phi$

(d) +40%f_t (e) -40%f_t (f) +20%f_c

(g) -20%f_c (h) +18%c_0 (i) -18%c_0

Figure B.38: Principal strain ε_1 for the material variations of the Orthotropic Total-Strain-Rotating Model (OTSRM) for the numerical model of wall TUe-Hollow, depicted at the maximum applied displacement +24 mm (scale factor=2 for all models).

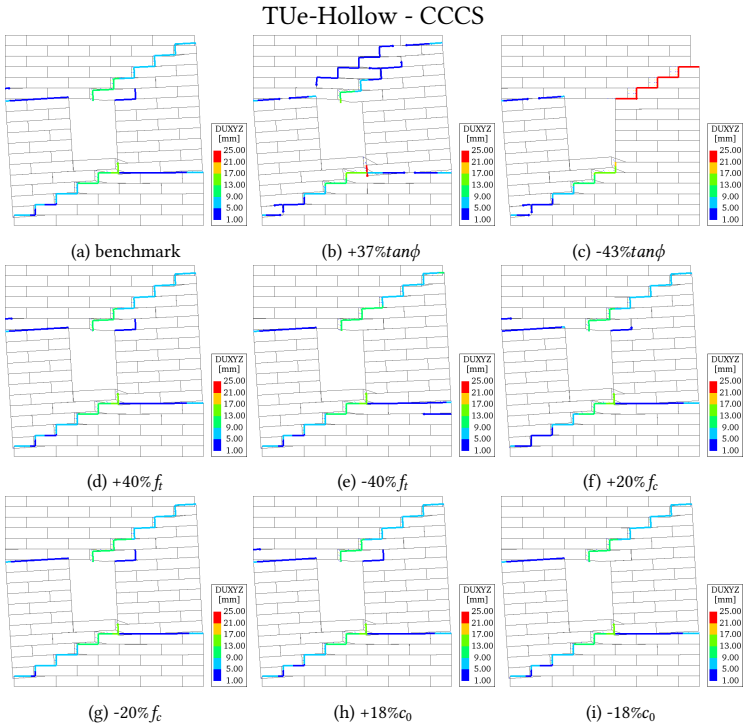

Figure B.39: Principal strain ε_1 for the material variations of the Combined Cracking, Crushing, Shearing micro-model (CCCS) for the numerical model of wall TUe-Hollow, depicted at the maximum applied displacement +24 mm (scale factor=2 for all models).

B

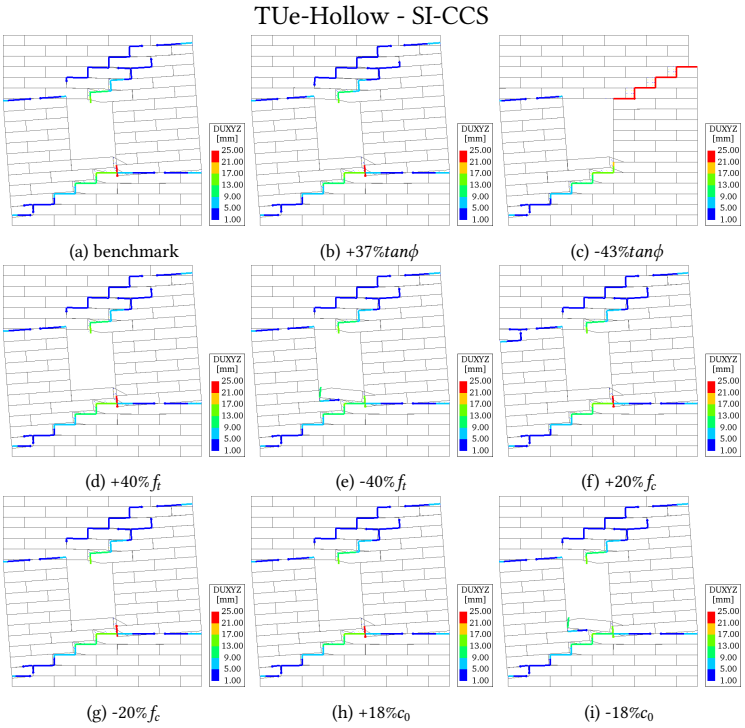

Figure B.40: Principal strain ε_1 for the material variations of the Sub-stepping Iterative- Cracking, Crushing, Shearing micro-model (SI-CCS) for the numerical model of wall TUe-Hollow, depicted at the maximum applied displacement +4 mm (scale factor=2 for all models).

Bibliography

URLs in this thesis have been archived on Archive.org. Their link target in digital editions refers to this timestamped version.

References

[1] A. M. D'Altri, V. Sarhosis, G. Milani, J. Rots, S. Cattari, S. Lagomarsino, E. Sacco, A. Tralli, G. Castellazzi, and S. de Miranda. Modeling strategies for the computational analysis of unreinforced masonry structures: Review and classification. *Archives of Computational Methods in Engineering*, 2019.

[2] N. Zamani. Testing anchors in cracked masonry, Sep 2019.

[3] T. White. 3,000 groningen farmers demand damage compensation - the northern times, 2018.

[4] S. Lagomarsino, A. Penna, A. Galasco, and S. Cattari. Tremuri program: An equivalent frame model for the nonlinear seismic analysis of masonry buildings. *Engineering Structures*, 56:1787–1799, 2013.

[5] R. Siano, V. Sepe, G. Camata, E. Spacone, P. Roca, and L. Pelà. Analysis of the performance in the linear field of equivalent-frame models for regular and irregular masonry walls. *Engineering Structures*, 145:190–210, 2017.

[6] S. Bracchi, F. Graziotti, F. Messali, and A. Penna. Seismic assessment of dutch URM buildings according to npr9998:2018 code with an equivalent-frame approach. pages 3028–3039, 2021.

[7] P. A. Cundall and R. D. Hart. Numerical modelling of discontinua. *Engineering Computations*, 9(2):101–113, 1992.

[8] J. V. Lemos. Discrete element modeling of masonry structures. *International Journal of Architectural Heritage*, 1(2):190–213, 2007.

[9] D. Malomo, R. Pinho, and A. Penna. Using the applied element method for modelling calcium silicate brick masonry subjected to in-plane cyclic loading. *Earthquake Engineering & Structural Dynamics*, 47(7):1610–1630, 2018.

[10] D. Malomo, M. J. DeJong, and A. Penna. Distinct element modelling of the in-plane cyclic response of urm walls subjected to shear-compression. *Earthquake Engineering & Structural Dynamics*, 48(12):1322–1344, 2019.

[11] H. Smoljanović, N. Živaljić, and Z. Nikolić. A combined finite-discrete element analysis of dry stone masonry structures. *Engineering Structures*, 52:89–100, 2013.

[12] M. Paola Costanza, C. B. Evan, and G. Giovanni. Finite/discrete element modelling of reversed cyclic tests on unreinforced masonry structures. *Engineering Structures*, 138:159–169, 2017.

[13] D. Malomo and M. J. DeJong. A macro-distinct element model (m-dem) for simulating the in-plane cyclic behavior of urm structures. *Engineering Structures*, 227:111428, 2021.

[14] E. Minga, L. Macorini, and B. A. Izzuddin. A 3d mesoscale damage-plasticity approach for masonry structures under cyclic loading. *Meccanica*, 53(7):1591–1611, 2018.

[15] G. Alfano and E. Sacco. Combining interface damage and friction in a cohesive-zone model. *International Journal for Numerical Methods in Engineering*, 68(5):542–582, 2006.

[16] H. R. Lotfi and P. B. Shing. Interface model applied to fracture of masonry structures. *Journal of structural engineering*, 120(1):63–80, 1994.

[17] A. M. D'Altri, S. de Miranda, G. Castellazzi, and V. Sarhosis. A 3d detailed micro-model for the in-plane and out-of-plane numerical analysis of masonry panels. *Computers & Structures*, 206:18–30, 2018.

[18] E. Bertolesi, G. Milani, and P. B. Lourenço. Implementation and validation of a total displacement non-linear homogenization approach for in-plane loaded masonry. *Computers and Structures*, 176:13–33, 2016.

[19] C. Calderini and S. Lagomarsino. Continuum model for in-plane anisotropic inelastic behavior of masonry. *Journal of Structural Engineering-ASCE*, 134(2):209–220, 2008.

[20] A. Zucchini and P. B. Lourenço. A micro-mechanical homogenisation model for masonry: Application to shear walls. *International Journal of Solids and Structures*, 46(3):871–886, 2009.

[21] G. Schreppers, A. Garofano, F. Messali, and J. Rots. Diana validation report for masonry modelling. Report, DIANA FEA BV & TU Delft, 2016.

[22] H. Lotfi and P. Shing. An appraisal of smeared crack models for masonry shear wall analysis. *Computers & structures*, 41(3):413–425, 1991.

[23] L. Berto, A. Saetta, R. Scotta, and R. Vitaliani. An orthotropic damage model for masonry structures. *International Journal for Numerical Methods in Engineering*, 55(2):127–157, 2002.

[24] L. Pelà, M. Cervera, S. Oller, and M. Chiumenti. A localized mapped damage model for orthotropic materials. *Engineering Fracture Mechanics*, 124:196–216, 2014.

[25] L. Gambarotta and S. Lagomarsino. Damage models for the seismic response of brick masonry shear walls. part ii: The continuum model and its applications. *Earthquake Engineering & Structural Dynamics*, 26(4):441–462, 1997.

[26] S. Saloustros, L. Pelà, M. Cervera, and P. Roca. An enhanced finite element macro-model for the realistic simulation of localized cracks in masonry structures: A large-scale application. *International Journal of Architectural Heritage*, 12(3):432–447, 2018.

[27] P. Lourenço, R. de Borst, and J. Rots. A plane stress softening plasticity model for orthotropic materials. *International Journal for Numerical Methods in Engineering*, 40(21):4033–4057, 1997.

[28] E. Papa and A. Nappi. Numerical modelling of masonry: A material model accounting for damage effects and plastic strains. *Applied Mathematical Modelling*, 21(6):319–335, 1997.

[29] J. Lee and G. L. Fenves. Plastic-damage model for cyclic loading of concrete structures. *Journal of engineering mechanics*, 124(8):892–900, 1998.

[30] J. Lubliner, J. Oliver, S. Oller, and E. Oñate. A plastic-damage model for concrete. *International Journal of solids and structures*, 25(3):299–326, 1989.

[31] D. V. Oliveira and P. B. Lourenço. Implementation and validation of a constitutive model for the cyclic behaviour of interface elements. *Computers & Structures*, 82(17-19):1451–1461, 2004.

[32] J. Wambacq, J. Ulloa, G. Lombaert, and S. François. A variationally coupled phase field and interface model for fracture in masonry. *Computers & Structures*, 264:106744, 2022.

[33] P. B. Lourenço and J. G. Rots. Multisurface interface model for analysis of masonry structures. *Journal of engineering mechanics*, 123(7):660–668, 1997.

[34] A. Rahman and T. Ueda. In-plane shear performance of masonry walls after strengthening by two different frps. *Journal of Composites for Construction*, 20:04016019, 2016.

[35] T. Celano, L. U. Argiento, F. Ceroni, and C. Casapulla. Literature review of the in-plane behavior of masonry walls: Theoretical vs. experimental results. *Materials*, 14(11):3063, 2021.

[36] H. Choi, C. Quan, and K. Jin. Nonlinear performance curve estimation of unreinforced masonry walls subjected to in-plane rocking behavior. *Applied Sciences*, 13(12), 2023.

[37] M. Javed, G. Magenes, B. Alam, A. Khan, Q. Ali, and M. Syed. Experimental seismic performance evaluation of unreinforced brick masonry shear walls. *Earthquake Spectra*, 2013.

[38] S. Adanur. Performance of masonry buildings during the 20 and 27 december 2007 bala (ankara) earthquakes in turkey. *Natural Hazards and Earth System Sciences*, 10, 2010.

[39] *Standard Test Method for Compressive Strength of Masonry Prisms*. 2016.

[40] *EN 1052-1:1998 - Methods of test for masonry - Part 1: Determination of compressive strength.* 1998.

[41] A. H. Salmanpour, N. Mojsilović, and J. Schwartz. Displacement capacity of contemporary unreinforced masonry walls: an experimental study. *Engineering Structures*, 89:1–16, 2015.

[42] F. Messali, R. Esposito, G. Ravenshorst, and J. Rots. Experimental investigation of the in-plane cyclic behaviour of calcium silicate brick masonry walls. *Bulletin of Earthquake Engineering*, pages 1–32, 2020.

[43] P. B. Lourenco and A. Gaetani. *Finite Element Analysis for Building Assessment: Advanced Use and Practical Recommendations.* Taylor & Francis, 2022.

[44] K. Gumaste, K. Nanjunda Rao, B. Venkatarama Reddy, and K. Jagadish. Strength and elasticity of brick masonry prisms and wallettes under compression. *Materials and structures*, 40(2):241–253, 2007.

[45] H. B. Kaushik, D. C. Rai, and S. K. Jain. Stress-strain characteristics of clay brick masonry under uniaxial compression. *Journal of materials in Civil Engineering*, 19(9):728–739, 2007.

[46] J. Samira. *Material characterisation of existing masonry: A strategy to determine strength, stiffness and toughness properties for structural analysis.* Doctoral thesis, 2021.

[47] K. Naraine and S. Sinha. Behavior of brick masonry under cyclic compressive loading. *Journal of Structural Engineering-Asce*, 115(6):1432–1445, 1989.

[48] K. Naraine and S. Sinha. Cyclic behavior of brick masonry under biaxial compression. *Journal of Structural Engineering*, 117(5):1336–1355, 1991.

[49] M. M. AlShebani and S. N. Sinha. Stress-strain characteristics of brick masonry under uniaxial cyclic loading. *Journal of Structural Engineering*, 125(6):600–604, 1999.

[50] D. V. Oliveira, P. B. Lourenço, and P. Roca. Cyclic behaviour of stone and brick masonry under uniaxial compressive loading. *Materials and Structures*, 39(2):247–257, 2006.

[51] M. Ispir and A. Ilki. Behavior of historical unreinforced brick masonry walls under monotonic and cyclic compression. *Arabian Journal for Science and Engineering*, 38(8):1993–2007, 2013.

[52] J. Segura, L. Pelà, and P. Roca. Monotonic and cyclic testing of clay brick and lime mortar masonry in compression. *Construction and Building Materials*, 193:453–466, 2018.

[53] N. Mojsilović. Masonry subjected to semi-cyclic compression: Inelastic response modelling. *Construction and Building Materials*, 263:120147, 12 2020.

[54] L. Facconi, F. Minelli, and F. J. Vecchio. Predicting uniaxial cyclic compressive behavior of brick masonry: New analytical model. *Journal of Structural Engineering*, 144(2), 2018.

[55] Nonlinear response of masonry wall structures subjected to cyclic and dynamic loading. *Engineering Structures*, 33(6):1955–1965, 2011.

[56] K. V. Subramaniam and S. Sinha. Analytical model for cyclic compressive behavior of brick masonry. *Structural Journal*, 92(3):288–294, 1995.

[57] J. Thamboo, J. Bandara, S. Perera, S. Navaratnam, K. Poologanathan, and M. Corradi. Experimental and analytical study of masonry subjected to uniaxial cyclic compression. *Materials*, 13(20):4505, 2020.

[58] A. Vermeltfoort. *Brick-mortar interaction in masonry under compression.* Phd thesis, Built Environment, 2005.

[59] S. Jafari, J. G. Rots, R. Esposito, and F. Messali. Characterizing the material properties of dutch unreinforced masonry. *Procedia Engineering*, 193:250–257, 2017.

[60] A. Rahman and T. Ueda. Experimental investigation and numerical modeling of peak shear stress of brick masonry mortar joint under compression. *Journal of Materials in Civil Engineering*, 26(9), 2014.

[61] K. Chaimoon and M. M. Attard. Experimental and numerical investigation of masonry under three-point bending (in-plane). *Engineering Structures*, 31(1):103–112, 2009.

[62] M. Dhanasekar, A. Page, and P. Kleeman. The failure of brick masonry under biaxial stresses. *Proceedings of the Institution of Civil Engineers*, 79(2):295–313, 1985.

[63] R. Pluijm, van der. *Out-of-plane bending of masonry: behaviour and strength.* Doctoral thesis, 1999.

[64] M. Maalej and V. C. Li. Flexural/tensile-strength ratio in engineered cementitious composites. *Journal of Materials in Civil Engineering*, 6:513–528, 1994.

[65] R. Lumantarna, D. T. Biggs, and J. M. Ingham. Compressive, flexural bond, and shear bond strengths of in situ new zealand unreinforced clay brick masonry constructed using lime mortar between the 1880s and 1940s. *Journal of Materials in Civil Engineering*, 26(4):559–566, 2014.

[66] J. A. Thamboo, M. Dhanasekar, and C. Yan. Flexural and shear bond characteristics of thin layer polymer cement mortared concrete masonry. *Construction and Building Materials*, 46:104–113, 2013.

[67] C. Culmann. *Die graphische statik*, volume 1. Meyer & Zeller, 1875.

[68] W. J. M. Rankine. *A manual of applied mechanics.* Griffin, 1877.

[69] J. Heyman. The stone skeleton. *International Journal of solids and structures*, 2(2):249–279, 1966.

[70] G. G. Ungewitter. *Lehrbuch der gotischen Konstruktionen*, volume 2. Weigel, 1892.

[71] M. Pari. *Simulating quasi-brittle failure in structures using Sequentially Linear Methods: Studies on non-proportional loading, constitutive modelling, and computational efficiency.* doctoral thesis, 2020.

[72] P. B. Lourenço. Computations on historic masonry structures. *Progress in Structural Engineering and Materials*, 4(3):301–319, 2002.

[73] P. G. Asteris, V. Sarhosis, A. Mohebkhah, V. Plevris, L. Papaloizou, P. Komodromos, and J. V. Lemos. *Numerical Modeling of Historic Masonry Structures*, book section chapter 7, pages 213–256. Advances in Civil and Industrial Engineering. 2015.

[74] K. M. Dolatshahi and M. Yekrangnia. Out-of-plane strength reduction of unreinforced masonry walls because of in-plane damages. *Earthquake Engineering & Structural Dynamics*, 44(13):2157–2176, 2015.

[75] A. Brencich, L. Gambarotta, and S. Lagomarsino. A macroelement approach to the three-dimensional seismic analysis of masonry buildings. In *11th European Conference on Earthquake Engineering*, volume 90, pages 1–10, 1998.

[76] S.-Y. Chen, F. Moon, and T. Yi. A macroelement for the nonlinear analysis of in-plane unreinforced masonry piers. *Engineering Structures*, 30(8):2242–2252, 2008.

[77] H. Xu, C. Gentilini, Z. Yu, H. Wu, and S. Zhao. A unified model for the seismic analysis of brick masonry structures. *Construction and Building Materials*, 184:733–751, 2018.

[78] M. Tomaževič. The computer program POR. *Report ZRMK*, 846, 1978.

[79] D. Addessi, A. Mastrandrea, and E. Sacco. An equilibrated macro-element for nonlinear analysis of masonry structures. *Engineering Structures*, 70:82–93, 2014.

[80] D. Addessi, D. Liberatore, and R. Masiani. Force-based beam finite element (fe) for the pushover analysis of masonry buildings. *International Journal of Architectural Heritage*, 9(3):231–243, 2015.

[81] D. Liberatore and D. Addessi. Strength domains and return algorithm for the lumped plasticity equivalent frame model of masonry structures. *Engineering Structures*, 91:167–181, 2015.

[82] S. Cattari and G. Magenes. Benchmarking the software packages to model and assess the seismic response of unreinforced masonry existing buildings through nonlinear static analyses. *Bulletin of Earthquake Engineering*, 20(4):1901–1936, 2022.

[83] S. Cattari, B. Calderoni, I. Caliò, G. Camata, S. de Miranda, G. Magenes, G. Milani, and A. Saetta. Nonlinear modeling of the seismic response of masonry structures: critical review and open issues towards engineering practice. *Bulletin of Earthquake Engineering*, 20(4):1939–1997, 2022.

[84] E. Quagliarini, G. Maracchini, and F. Clementi. Uses and limits of the equivalent frame model on existing unreinforced masonry buildings for assessing their seismic risk: A review. *Journal of Building Engineering*, 10:166–182, 2017.

[85] C. Morandini, D. Malomo, and A. Penna. Equivalent frame discretisation for urm façades with irregular opening layouts. *Bulletin of Earthquake Engineering*, 03 2022.

[86] A. Penna, S. Lagomarsino, and A. Galasco. A nonlinear macroelement model for the seismic analysis of masonry buildings. *Earthquake Engineering & Structural Dynamics*, 43(2):159–179, 2014.

[87] L. Gambarotta and S. Lagomarsino. On dynamic response of masonry panels. In *Proc. of the National Conference "Masonry Mechanics Between Theory and Practice*, 1996.

[88] A. Brencich and S. Lagomarsino. A macroelement dynamic model for masonry shear walls. *Computer methods in structural masonry*, 4:67–75, 1998.

[89] S. Bracchi, A. Galasco, and A. Penna. A novel macroelement model for the nonlinear analysis of masonry buildings. part 1: Axial and flexural behavior. *Earthquake Engineering & Structural Dynamics*, 50(8):2233–2252, 2021.

[90] S. Bracchi and A. Penna. A novel macroelement model for the nonlinear analysis of masonry buildings. part 2: Shear behavior. *Earthquake Engineering & Structural Dynamics*, 50(8):2212–2232, 2021.

[91] K. Chaimoon and M. M. Attard. Modeling of unreinforced masonry walls under shear and compression. *Engineering Structures*, 29(9):2056–2068, 2007.

[92] Z. Xie, M. Sousamli, F. Messali, and J. G. Rots. A sub-stepping iterative constitutive model for cyclic cracking-crushing-shearing in masonry interface elements. *Computers & Structures*, 257:106654, 2021.

[93] E. Sacco and J. Toti. Interface elements for the analysis of masonry structures. *International Journal for Computational Methods in Engineering Science and Mechanics*, 11(6):354–373, 2010.

[94] D. Addessi and E. Sacco. Nonlinear analysis of masonry panels using a kinematic enriched plane state formulation. *International Journal of Solids and Structures*, 90:194–214, 2016.

[95] A. W. Page. Finite element model for masonry. *Journal of the Structural Division*, 104(8):1267–1285, 1978.

[96] G. Giambanco, S. Rizzo, and R. Spallino. Numerical analysis of masonry structures via interface models. *Computer methods in applied mechanics and engineering*, 190(49-50):6493–6511, 2001.

[97] G. P. A. G. van Zijl. Modeling masonry shear-compression: Role of dilatancy highlighted. *Journal of Engineering Mechanics*, 130(11):1289–1296, 2004.

[98] N. Kumar and M. Barbato. New constitutive model for interface elements in finite-element modeling of masonry. *Journal of Engineering Mechanics*, 145, 02 2019.

[99] Y. Nie, A. Sheikh, P. Visintin, and M. Griffith. A robust computational strategy for failure prediction of masonry structures using an improved multi-surface damage-plastic based interface model. *International Journal for Numerical Methods in Engineering*, 2023.

[100] S. Zhang, S. M. Taheri Mousavi, N. Richart, J.-F. Molinari, and K. Beyer. Micro-mechanical finite element modeling of diagonal compression test for historical stone masonry structure. *International Journal of Solids and Structures*, 112:122–132, 2017.

[101] G. Andreotti, F. Graziotti, and G. Magenes. Detailed micro-modelling of the direct shear tests of brick masonry specimens: The role of dilatancy. *Engineering Structures*, 168:929–949, 2018.

[102] M. Petracca, L. Pelà, R. Rossi, S. Zaghi, G. Camata, and E. Spacone. Micro-scale continuous and discrete numerical models for nonlinear analysis of masonry shear walls. *Construction and Building Materials*, 149:296–314, 2017.

[103] J. G. Rots and R. De Borst. Analysis of mixed-mode fracture in concrete. *Journal of engineering mechanics*, 113(11):1739–1758, 1987.

[104] J. Lopez, S. Oller, E. Oñate, and J. Lubliner. A homogeneous constitutive model for masonry. *International journal for numerical methods in engineering*, 46(10):1651–1671, 1999.

[105] L. Pelà, M. Cervera, and P. Roca. An orthotropic damage model for the analysis of masonry structures. *Construction and Building Materials*, 41:957–967, 2013.

[106] P. Bilko and L. Małyszko. An orthotropic elastic-plastic constitutive model for masonry walls. *Materials (Basel, Switzerland)*, 13, 2020.

[107] E. Bertolesi, G. Milani, and S. Casolo. Homogenization towards a mechanistic rigid body and spring model (hrbsm) for the non-linear dynamic analysis of 3d masonry structures. *Meccanica*, 53:1819–1855, 2018.

[108] G. Milani. Simple lower bound limit analysis homogenization model for in-and out-of-plane loaded masonry walls. *Construction and Building Materials*, 25(12):4426–4443, 2011.

[109] S. Marfia and E. Sacco. Multiscale damage contact-friction model for periodic masonry walls. *Computer Methods in Applied Mechanics and Engineering*, 205-208:189–203, 2012.

[110] T. J. Massart, R. H. J. Peerlings, and M. G. D. Geers. An enhanced multi-scale approach for masonry wall computations with localization of damage. *International Journal for Numerical Methods in Engineering*, 69(5):1022–1059, 2007.

[111] J. G. Rots, F. Messali, R. Esposito, S. Jafari, and V. Mariani. Computational modelling of masonry with a view to groningen induced seismicity. *Structural Analysis of Historical Constructions: Anamnesis, Diagnosis, Therapy, Controls*, pages 227–238, 2016.

[112] P. Feenstra, J. Rots, A. Arnesen, J. Teigen, and K. Hoiseth. A 3d constitutive model for concrete based on a co-rotational concept. In *Euro-C Conference Computational Modelling of Concrete Structures*. Balkema, 1998.

[113] M. Cervera, J. Oliver, and R. Faria. Seismic evaluation of concrete dams via continuum damage models. *Earthquake engineering & structural dynamics*, 24(9):1225–1245, 1995.

[114] P. B. Lourenço. *Recent Advances in Masonry Modelling: Micromodelling and Homogenisation*, pages 251–294. Computational and Experimental Methods in Structures. 2009.

[115] S. Pietruszczak and X. Niu. A mathematical description of macroscopic behaviour of brick masonry. *International journal of solids and structures*, 29(5):531–546, 1992.

[116] A. Anthoine. Derivation of the in-plane elastic characteristics of masonry through homogenization theory. *International journal of solids and structures*, 32(2):137–163, 1995.

[117] A. Cecchi and K. Sab. A multi-parameter homogenization study for modeling elastic masonry. *European Journal of Mechanics-A/Solids*, 21(2):249–268, 2002.

[118] M. Mistler, A. Anthoine, and C. Butenweg. In-plane and out-of-plane homogenisation of masonry. *Computers & Structures*, 85(17-18):1321–1330, 2007.

[119] A. Drougkas, P. Roca, and C. Molins. Analytical micro-modeling of masonry periodic unit cells–elastic properties. *International Journal of Solids and Structures*, 69:169–188, 2015.

[120] R. Masiani and P. Trovalusci. Cosserat and cauchy materials as continuum models of brick masonry. *Meccanica*, 31:421–432, 1996.

[121] I. Stefanou, J. Sulem, and I. Vardoulakis. Three-dimensional cosserat homogenization of masonry structures: elasticity. *Acta Geotechnica*, 3:71–83, 2008.

[122] A. Zucchini and P. B. Lourenço. A micro-mechanical model for the homogenisation of masonry. *International Journal of Solids and Structures*, 39(12):3233–3255, 2002.

[123] G. Milani, P. B. Lourenço, and A. Tralli. Homogenised limit analysis of masonry walls, part i: Failure surfaces. *Computers & structures*, 84(3-4):166–180, 2006.

[124] G. Milani, P. B. Lourenço, and A. Tralli. Homogenised limit analysis of masonry walls, part ii: Structural examples. *Computers & structures*, 84(3-4):181–195, 2006.

[125] S. Casolo. Modelling in-plane micro-structure of masonry walls by rigid elements. *International Journal of Solids and Structures*, 41(13):3625–3641, 2004.

[126] S. Casolo and F. Pena. Rigid element model for in-plane dynamics of masonry walls considering hysteretic behaviour and damage. *Earthquake engineering & structural dynamics*, 36(8):1029–1048, 2007.

[127] E. Sacco. *Micro, Multiscale and Macro Models for Masonry Structures*, pages 241–291. Springer Vienna, Vienna, 2014.

[128] L. Gambarotta and S. Lagomarsino. Damage models for the seismic responce of brick masonry shear walls. part 1: the mortar joint model and its applications. *Earthquake engineering & structural dynamics*, 26(4):423–439, 1997.

[129] C. Calderini and S. Lagomarsino. A micromechanical inelastic model for historical masonry. *Journal of Earthquake Engineering*, 10(4):453–479, 2006.

[130] E. Sacco. A nonlinear homogenization procedure for periodic masonry. *European Journal of Mechanics - A/Solids*, 28(2):209–222, 2009.

[131] S. Casolo. Macroscopic modelling of structured materials: relationship between orthotropic cosserat continuum and rigid elements. *International Journal of Solids and Structures*, 43(3-4):475–496, 2006.

[132] G. Salerno and G. De Felice. Continuum modeling of periodic brickwork. *International Journal of Solids and Structures*, 46(5):1251–1267, 2009.

[133] D. Addessi and E. Sacco. A multi-scale enriched model for the analysis of masonry panels. *International Journal of Solids and Structures*, 49(6):865–880, 2012.

[134] D. Addessi, P. Di Re, C. Gatta, and E. Sacco. Multiscale analysis of out-of-plane masonry elements using different structural models at macro and microscale. *Computers & Structures*, 247:106477, 2021.

[135] P. Cundall. A computer model for simulating progressive large scale movements in blocky system. In *Proc. Int. Symp. on Rock Fractures.*, pages II–8, 1971.

[136] E. Çaktı, C. S. Oliveira, J. V. Lemos, Ö. Saygılı, S. Görk, and E. Zengin. Ongoing research on earthquake behavior of historical minarets in istanbul. *Seismic Assessment, Behavior and Retrofit of Heritage Buildings and Monuments*, pages 321–339, 2015.

[137] A. Alexandris, E. Protopapa, and I. Psycharis. Collapse mechanisms of masonry buildings derived by the distinct element method. In *Proceedings of the 13th world conference on earthquake engineering*, volume 59, 2004.

[138] M. Jean and J. J. Moreau. Unilaterality and dry friction in the dynamics of rigid body collections. In *1st Contact Mechanics International Symposium*, pages 31–48, 1992.

[139] V. Sarhosis and J. Lemos. A detailed micro-modelling approach for the structural analysis of masonry assemblages. *Computers & Structures*, 206:66–81, 2018.

[140] D. Malomo, R. Pinho, and A. Penna. Numerical modelling of the out-of-plane response of full-scale brick masonry prototypes subjected to incremental dynamic shake-table tests. *Engineering Structures*, 209:110298, 2020.

[141] I. Itasca Consulting Group. Udec - universal distinct element code, ver. 7.0., 2019.

[142] I. Itasca Consulting Group. 3dec - three-dimensional distinct element code, ver. 7.0., 2020.

[143] N. Ambraseys and I. N. Psycharis. Earthquake stability of columns and statues. *Journal of Earthquake Engineering*, 15(5):685–710, 2011.

[144] M. J. DeJong and C. Vibert. Seismic response of stone masonry spires: Computational and experimental modeling. *Engineering Structures*, 40:566–574, 2012.

[145] G. Lengyel and K. Bagi. Numerical analysis of the mechanical role of the ribs in groin vaults. *Computers & Structures*, 158:42–60, 2015.

[146] G. De Felice. Out-of-plane seismic capacity of masonry depending on wall section morphology. *International Journal of Architectural Heritage*, 5(4-5):466–482, 2011.

[147] I. N. Psycharis, A. E. Drougas, and M.-E. Dasiou. *Seismic Behaviour of the Walls of the Parthenon A Numerical Study*, pages 265–283. Springer Netherlands, Dordrecht, 2011.

[148] N. Mendes, S. Zanotti, and J. V. Lemos. Seismic performance of historical buildings based on discrete element method: An adobe church. *Journal of Earthquake Engineering*, 24(8):1270–1289, 2020.

[149] G.-H. Shi. *Discontinuous Deformation Analysis–A New Model for the Statics and Dynamics of Block Systems (Ph. D. thesis)*. PhD thesis, 1988.

[150] G.-h. Shi. Discontinuous deformation analysis: a new numerical model for the statics and dynamics of deformable block structures. *Engineering computations*, 1992.

[151] M. Ma, A. Pan, M. Luan, and J. M. Gebara. Seismic analysis of stone arch bridges using discontinuous deformation analysis. In *Proceedings of the 11th world conference on earthquake engineering. Elsevier, Amsterdam, paper*, number 1551, 1996.

[152] N. Bićanić, C. Stirling, and C. Pearce. Discontinuous modelling of masonry bridges. *Computational Mechanics*, 31:60–68, 2003.

[153] E. Rizzi, F. Rusconi, and G. Cocchetti. Analytical and numerical dda analysis on the collapse mode of circular masonry arches. *Engineering Structures*, 60:241–257, 2014.

[154] H. Jiang, L. Wang, L. Li, and Z. Guo. Safety evaluation of an ancient masonry seawall structure with modified dda method. *Computers and Geotechnics*, 55:277–289, 2014.

[155] R. Kamai and Y. H. Hatzor. Dynamic back analysis of structural failures in archeological sites to obtain paleo-seismic parameters using dda. In *Proceedings of 7th International Conference on the Analysis of Discontinuous Deformation (ICADD-7)*, pages 121–136, 2005.

[156] R. Kamai and Y. H. Hatzor. Numerical analysis of block stone displacements in ancient masonry structures: a new method to estimate historic ground motions. *International Journal for Numerical and Analytical Methods in Geomechanics*, 32(11):1321–1340, 2008.

[157] J. J. Moreau. Unilateral contact and dry friction in finite freedom dynamics. *Nonsmooth mechanics and Applications*, pages 1–82, 1988.

[158] K. Bagi. The contact dynamics method. In *Computational Modeling of Masonry Structures Using the Discrete Element Method*, pages 103–122. IGI Global, 2016.

[159] A. Rafiee, M. Vinches, and C. Bohatier. Application of the nscd method to analyse the dynamic behaviour of stone arched structures. *International Journal of Solids and Structures*, 45(25-26):6269–6283, 2008.

[160] A. Rafiee and M. Vinches. Mechanical behaviour of a stone masonry bridge assessed using an implicit discrete element method. *Engineering Structures*, 48:739–749, 2013.

[161] A. Isfeld and N. Shrive. Discrete element modeling of stone masonry walls with varying core conditions: Prince of wales fort case study. *International Journal of Architectural Heritage*, 9(5):564–580, 2015.

[162] G. Lancioni, S. Lenci, Q. Piattoni, and E. Quagliarini. Dynamics and failure mechanisms of ancient masonry churches subjected to seismic actions by using the nscd method: The case of the medieval church of s. maria in portuno. *Engineering Structures*, 56:1527–1546, 2013.

[163] V. Beatini, G. Royer-Carfagni, and A. Tasora. A regularized non-smooth contact dynamics approach for architectural masonry structures. *Computers & Structures*, 187:88–100, 2017.

[164] K. Meguro and H. Tagel-Din. Applied element method for structural analysis theory and application for linear materials. *Doboku Gakkai Ronbunshu*, 2000(647):31–45, 2000.

[165] S. Sharma, A. Marasca, M. Ponte, and R. Bento. Modelling the in-plane cyclic behaviour of typical portuguese rubble stone masonry using the applied element method. *Structures*, 46:1224–1242, 2022.

[166] A. A. Munjiza. *The combined finite-discrete element method.* John Wiley & Sons, 2004.

[167] A. Munjiza and K. Andrews. Nbs contact detection algorithm for bodies of similar size. *International Journal for Numerical Methods in Engineering*, 43(1):131–149, 1998.

[168] M. Hazay and A. Munjiza. Introduction to the combined finite-discrete element method. In *Computational Modeling of Masonry Structures Using the Discrete Element Method*, pages 123–145. IGI Global, 2016.

[169] H. Smoljanović, N. Živaljić, Ž. Nikolić, and A. Munjiza. Numerical analysis of 3d dry-stone masonry structures by combined finite-discrete element method. *International Journal of Solids and Structures*, 136:150–167, 2018.

[170] D. Lorenzi-Venneri, R. C. Lee, D. J. Luscher, C. A. Bronkhorst, E. Rougier, E. E. Knight, Z. Lei, E. C. Milner, J. D. Bacon, E. Guardincerri, et al. Proceedings of the workshop on the structural cracking of the cupola of santa maria del fiore. Technical report, Los Alamos National Lab.(LANL), Los Alamos, NM (United States), 2014.

[171] N. M. Azevedo and J. V. Lemos. A hybrid particle/finite element model with surface roughness for stone masonry analysis. *Applied Mechanics*, 3(2):608–627, 2022.

[172] H. Smoljanović, Ž. Nikolić, and N. Živaljić. A combined finite–discrete numerical model for analysis of masonry structures. *Engineering fracture mechanics*, 136:1–14, 2015.

[173] D. Baraldi, E. Reccia, and A. Cecchi. In plane loaded masonry walls: Dem and fem/dem models. a critical review. *Meccanica*, 53:1613–1628, 2018.

[174] M. Pepe, M. Pingaro, P. Trovalusci, E. Reccia, L. Leonetti, et al. Micromodels for the in-plane failure analysis of masonry walls: Limit analysis, fem and fem/dem approaches. *Frattura e Integrità Strutturale*, 14(51):504–516, 2020.

[175] W. Ou, X. Chen, A. Chan, Y. Cheng, and H. Wang. Fdem simulation on the failure behavior of historic masonry heritages subjected to differential settlement. *Buildings*, 12(10):1592, 2022.

[176] D. Malomo and M. DeJong. A macro-distinct element model (m-dem) for out-of-plane analysis of unreinforced masonry structures. *Engineering Structures*, 244:112754, 2021.

[177] M. Jirásek and T. Zimmermann. Analysis of rotating crack model. *Journal of Engineering Mechanics*, 124(8):842–851, 1998.

[178] A. Page. An experimental investigation of the biaxial strength of brick masonry. In *Proceedings of the Sixth International Brick Masonry Conference (Rome)*, pages 3–15, 1982.

[179] R. H. Atkinson, B. P. Amadei, S. Saeb, and S. Sture. Response of masonry bed joints in direct shear. *Journal of Structural Engineering-Asce*, 115(9):2276–2296, 1989.

[180] R. Van der Pluijm. Non-linear behaviour of masonry under tension. *HERON-ENGLISH EDITION-*, 42:25–54, 1997.

[181] *NPR 9998:2020 en. Assessment of structural safety of buildings in case of erection, reconstruction and disapproval - Induced earthquakes - Basis of design, actions and resistances.* 2021.

[182] *Eurocode 6: design of masonry structures—part 1-1: general rules for reinforced and unreinforced masonry structures.* CEN, Brussels, 2001.

[183] A. W. Page. The biaxial compressive strength of brick masonry. *Proceedings of the Institution of Civil Engineers*, 71(3):893–906, 1981.

[184] A. Page. The strength of brick masonry under biaxial tension-compression. *International journal of masonry construction*, 3(1):26–31, 1983.

[185] Z. P. Bazant and B. H. Oh. Crack band theory for fracture of concrete. *Materiaux et Construction*, 16(3):155–177, 1983.

[186] S. Govindjee, G. J. Kay, and J. C. Simo. Anisotropic modelling and numerical simulation of brittle damage in concrete. *International Journal for Numerical Methods in Engineering*, 38(21):3611–3633, 1995.

[187] J. Oliver. A consistent characteristic length for smeared cracking models. *International Journal for Numerical Methods in Engineering*, 28(2):461–474, 1989.

[188] J. Rots, P. Nauta, G. Kuster, and J. Blaauwendraad. Smeared crack approach and fracture localization in concrete. *HERON, 30 (1), 1985*, 1985.

[189] J. Hoshikuma, K. Kawashima, K. Nagaya, and A. W. Taylor. Stress-strain model for confined reinforced concrete in bridge piers. 123(5):624–633, 1997.

[190] S.-J. Lee, T.-S. Eom, and E. Yu. Investigation of diagonal strut actions in masonry-infilled reinforced concrete frames. *International Journal of Concrete Structures and Materials*, 15(1), 2021.

[191] F. J. Vecchio and M. P. Collins. Compression response of cracked reinforced-concrete. *Journal of Structural Engineering-Asce*, 119(12):3590–3610, 1993.

[192] P. B. Lourenço and R. J. G. Understanding the behaviour of shear walls: A numerical approach. In *10 th international Brick/Block Masonry Conference*, 1994.

[193] J. Rots. *Computational modeling of concrete fracture.* doctoral thesis, 1988.

[194] A. Anthoine, G. Magonette, and G. Magenes. Shear-compression testing and analysis of brick masonry walls. In Geraldduma, editor, *10th European Conference on Earthquake Engineering*, pages 1657–1662, 1994.

[195] G. Magenes and G. M. Calvi. In-plane seismic response of brick masonry walls. *Earthquake Engineering & Structural Dynamics*, 26(11):1091–1112, 1997.

[196] L. Binda, C. Tiraboschi, G. Mirabella Roberti, G. Baronio, and G. Cardani. Measuring masonry material properties: detailed results from an extensive experimental research, part i: Tests on masonry components. *Rep*, 5, 1996.

[197] G. Magenes and G. M. Calvi. Cyclic behaviour of brick masonry walls. In *10th World Conference on Earthquake Engineering*, pages 3517–3522, 1992.

[198] M. Jirasek and M. Bauer. Numerical aspects of the crack band approach. *Computers and Structures*, 110-111:60–78, 2012.

[199] F. J. Vecchio and M. P. Collins. The modified compression-field theory for reinforced concrete elements subjected to shear. *ACI J.*, 83(2):219–231, 1986.

[200] G. P. A. G. v. Zijl. *Computational modelling of masonry creep and shrinkage.* Thesis, 2000.

[201] T. Raijmakers and A. Vermeltfoort. Deformation controlled tests in masonry shear walls. Report B-92-1156, TNO-Bouw, 1992.

[202] P. Lourenço. *Computational strategies for masonry structures.* Doctoral thesis, 1996.

[203] L. Pelà. *Continuum damage model for nonlinear analysis of masonry structures.* Phd thesis, 2009.

[204] G. Milani. Simple homogenization model for the non-linear analysis of in-plane loaded masonry walls. *Computers & Structures*, 89(17):1586–1601, 2011.

[205] P. Lourenco and J. Rots. On the use of micro-models for the analysis of masonry shear walls. *Computer methods in structural masonry-2. Swansea*, pages 14–26, 1993.

[206] F. Messali, M. Pari, R. Esposito, J. G. Rots, and D. den Hertog. Blind prediction of a cyclic pushover test on a two-storey masonry assemblage: a comparative study, 2018.

[207] F. Parisse, S. Cattari, R. Marques, P. Lourenço, G. Magenes, K. Beyer, B. Calderoni, G. Camata, E. Cordasco, M. Erberik, C. İçel, M. Karakaya, D. Malomo, C. Manzini, C. Marano, F. Messali, G. Occhipinti, B. Pantò, O. Saygili, and M. Sousamli. Benchmarking the seismic assessment of unreinforced masonry buildings from a blind prediction test. *Structures*, 31:982–1005, 2021.

[208] A. Aşıkoğlu, G. Vasconcelos, P. B. Lourenço, and B. Pantò. Pushover analysis of unreinforced irregular masonry buildings: Lessons from different modeling approaches. *Engineering Structures*, 218:110830, 2020.

[209] F. Cannizzaro, G. Castellazzi, N. Grillanda, B. Pantò, and M. Petracca. Modelling the nonlinear static response of a 2-storey urm benchmark case study: comparison among different modelling strategies using two-and three-dimensional elements. *Bulletin of Earthquake Engineering*, 20(4):2085–2114, 2022.

[210] S. Jafari, J. G. Rots, and R. Esposito. A correlation study to support material characterisation of typical dutch masonry structures. *Journal of Building Engineering*, 45:103450, 2022.

[211] F. Graziotti, U. Tomassetti, S. Kallioras, A. Penna, and G. Magenes. Shaking table test on a full scale urm cavity wall building. *Bulletin of earthquake engineering*, 15(12):5329–5364, 2017.

[212] F. Graziotti, U. Tomassetti, A. Rossi, B. Marchesi, S. Kallioras, M. Mandirola, A. Fragomeli, E. Mellia, S. Peloso, F. Cuppari, G. Guerrini, A. Penna, and G. Magenes. Shaking table tests on a full-scale clay-brick masonry house representative of the groningen building stock and related characterization tests. Report EUC128/2016U, EUCENTRE, 2016.

[213] U. Tomassetti, A. A. Correia, F. Graziotti, A. I. Marques, M. Mandirola, and P. X. Candeias. Collapse shaking table test on a urm cavity wall structure representative of a dutch terraced house. Report, EUCENTRE, 2017.

Curriculum Vitæ

1990/11/28	Date of birth in Heraklion, Crete, Greece
2008-2014	Diploma in Civil Engineering, Faculty of Civil Engineering, University of Thessaly, Volos, Greece, Specialization: Structural Engineering
2014-2016	Master of Science in Structural Engineering, Faculty of Civil Engineering & Geosciences, TU Delft, Delft, the Netherlands, Specialization: Concrete structures
2017-2018	Researcher, Faculty of Civil Engineering & Geosciences, TU Delft, Delft, the Netherlands
2018-2024	PhD in Computational Mechanics, Faculty of Civil Engineering & Geosciences, TU Delft, Delft, the Netherlands, Thesis: Orthotropic Continuum Constitutive Model For Masonry Structures and Comparative Studies Promotors: Prof. dr. ir. Jan G. Rots & dr. Francesco Messali
2022-	Seismic engineer, BAM A&E, Bunnik, the Netherlands

List of Publications

Journal articles

1. Paris, V., Damiani, N., Sousamli, M., Ehrenbach, I., Lorello, M., Nettis, A., Montanino, A. and Meriggi, P., 2022. Traditional tools and modern technologies for the analysis of mansory structures: the case of the Church of Saint Andrea in Anagni. STRUCTURAL, 241(art. n. 12), pp.1-14.

2. Sousamli, M., Messali, F. and Rots, J.G., 2022. A total-strain based orthotropic continuum model for the cyclic nonlinear behavior of unreinforced brick masonry structures. International Journal for Numerical Methods in Engineering, 123(8), pp.1813-1840.

3. Xie, Z., Sousamli, M., Messali, F. and Rots, J.G., 2021. A sub-stepping iterative constitutive model for cyclic cracking-crushing-shearing in masonry interface elements. Computers & Structures, 257, p.106654.

4. Parisse, F., Cattari, S., Marques, R., Lourenço, P. B., Magenes, G., Beyer, K., ... & Sousamli, M. (2021, June). Benchmarking the seismic assessment of unreinforced masonry buildings from a blind prediction test. In Structures (Vol. 31, pp. 982-1005). Elsevier.

5. Longo, M., Sousamli, M., Korswagen, P.A., van Staalduinen, P. and Rots, J.G., 2021. Substructure-based 'three-tiered'finite element approach to soil-masonry-wall interaction for light seismic motion. Engineering Structures, 245, p.112847.

Conference papers/talks

1. Mirra, M., Sousamli, M., Longo, M. and Ravenshorst, G., 2021. Analytical and numerical modelling of the in-plane response of timber diaphragms retrofitted with plywood panels. In 8 th International Conference on Computational Methods in Structura l Dynamics and Earthquake Engineering, COMPDYN.

2. Sousamli, M., Messali, F. and Rots, J.G., 2020. Constitutive model for the nonlinear cyclic behavior of brick masonry structures. In Brick and Block Masonry-From Historical to Sustainable Masonry (pp. 694-701). CRC Press.

3. *Sousamli, M., Messali, F. and Rots, J.G.,*: Constitutive Model for the Non-Linear Cyclic Behaviour of Masonry Structures. Congress on Numerical Methods in Engineering, University of Minho, Portugal (2019)

4. Schutte, W., Sousamli, M., Blom, C.B.M. and Attahiri, M., 2018. UHPC Pedestrian bridges and measured human induced vibrations. In High Tech Concrete: Where Technology and Engineering Meet: Proceedings of the 2017 fib Symposium, held in Maastricht, The Netherlands, June 12-14, 2017 (pp. 1522-1529). Springer International Publishing.

Acknowledgments

Back in September my partner and I bought our first house. While I was packing my belongings, I found a letter I wrote back in 2018. The letter, addressed to my future self, was part of a graduate school course I followed at the very beginning of my PhD. In this letter, each one of us had to evaluate ourselves, our actions and feelings regarding our research, and advise our future selves on how to overcome challenges that might arise. A part of the letter was devoted to our network and its importance and the people we want to acknowledge, and I remember distinctively our instructor asking us "imagine it's your defense date, who do you see around you in the room?" Even though, at the time, I questioned the usefulness of such an assignment, my "future self" appreciated finding it and reading it 5.5 years later, and was very glad to realize that even more people were added to "my list of acknowledgments" over the last years. This chapter is for them.

First and foremost, I would like to express my gratitude to my promotor *Prof. Jan Rots* for giving me the opportunity to work as a researcher in TU Delft after graduating from my master, and for trusting my capabilities enough to offer me a PhD position. His knowledge on the topic of computational mechanics and masonry structures, as well as his though-provoking questions and constructive feedback during our meetings, helped me improve the quality of my research. I am deeply grateful to my co-promotor *Dr. Francesco Messali* for the countless hours he spent discussing and evaluating all the variations I did in my code during our weekly meetings and for his always constructive and polite feedback. In the challenging times of Covid-19, I could not have asked for a more supportive supervisor, being understanding but at the same time helping me to keep on track. I also really appreciate the patience they both showed during the last one year and a half, when I started working in a company and writing the last part of my thesis was no longer my top priority. I would also like to extend my gratitude to my doctoral committee comprising *Prof. Daniela Addessi*, *Prof. Gabriele Milani*, *Prof. Max Hendriks*, *Prof. Bert Sluys* and *Prof. Luca Pelà* for agreeing to take part in my defence process, taking time to read my work and providing me with valuable feedback.

Prof. Panos Tsopelas, my passionate professor of structural dynamics during my undergraduate studies in Greece, and my supervisor during my diploma thesis, was the one that made me love structural dynamics, and the first to advice me to do a PhD. I wish to every undergraduate student to come across professors and mentors like him. Moreover, I will be forever grateful to my master thesis supervisor *Dr. Kees Blom* for providing me with the most fun and interesting master thesis topic I could have wished for. Both my friends and I still recall with excitement jumping on footbridges and measuring their response. His child-like enthusiasm about anything he would work on inspired me and reignited my interest and passion for research, at a time that I was questioning my own capabilities. He, and *Prof. Dick Hordijk* were the ones that introduced me to the structural mechanics group, and for that I will be always grateful.

For the last one year and a half I am working in BAM A&E, my first industry job after 5 years in academia, and I couldn't have hoped for a smoother transition to a new environment. I would like to thank my colleagues *Mark Spanenburg, Jelmer Feenstra, Jack English, Joe White, Robin van Esch, Nan Lin, Miguel Catanho, Jake Mayston, Holly Wright, Rick de Goeij, Reiner Simarmata, Casper van der Krift, Marica Wit, Graham Browne, Alistair Boys* and my office bestie *Maria Politi*, for making my first industry job so enjoyable and setting my expectation bar high. Special thanks to my boss *Mischa Falger* for giving me the opportunity to work with them, and for being a truly supportive and understanding boss that takes the time to get to know his team better.

One of the advantages of doing a PhD in TU Delft is that I got to meet and interact daily with some exceptional colleagues. From those I would like to give special mention to the colleagues of the structural mechanics group with whom I shared many lunch and coffee breaks, beers at PSOR after our seminars, dinners around Delft and many discussions over our desks; these are: *Dr. Manimaran Pari, Dr. Samira Jafari, Dr. Langzi Chang, Dr. Rita Esposito, Dr. Tasos Drougas, Dr. Anjali Mehrotra, Dr. Edwin Meulman, Michele Longo, Dr. Michele Mirra, Lucia Licciardello, Marina Damiola, Dr. Onur Arslan, Paul Korswagen, Maria Belen Gaggero, Alfonso Prosperi, Niels Kostense* and *Giorgos Stamoulis.* More specifically, I consider myself lucky to have shared the office with *Samira* and *Lucia*, two of the kindest and sweetest women and friends I have met. On the same note, I am glad to have met and worked with *Dr. Rita Esposito*, whose dynamic and outgoing nature inspired me. The three of them made up for the overall lack of female researchers on the sixth floor. The beautiful trips to Crete, Groningen, and Italy with *Michele, Edwin, Marina* and *Paul* will be memories that I will cherish forever, and I wish for more trips like these to come. I also want to say a big thank you to *Langzi* for all the music, books, movies and photos we shared, as well as for all the long walks and philosophical and silly discussions we had. He was a tremendous source of support throughout the pandemic and a precious friend, and still is.

TU Delft is also where I met some of my best friends during my master. My "structural engineering friends" *Aivaras Aukselis, Tudor Brata, Sunny Taorem, Evangelos Goulas, Erdem Gokcek* and *Arsha Shiri*, thank you for all the laughs over the years, and for the most enjoyable annual Christmas dinners and Secret Santas since 2015. I am especially thankful to *Arsha* for all the memes, all the series and movies recommendations, and all the funny and deep discussions over food we've had over the years. To my "lindyhop friends" *Clara Moreno, Jorge Machin, Dani Pino* and *Karan Gupta*, thank you for the awesome memories during our master, for all the dances, the crazy jumping on bridges, the dinners and the parties. I miss you all and hope to have a big reunion soon. In Delft I also got to meet *Marina Damiola, Elisa Paletti, Luca Negovanovic, Manuel Ribeiro* and *Sara Pereira*, with whom I shared many joyful dinners and parties. To my "Greek family" outside of Greece *Natalia Aloupi, Stavros Panagoulias, Giorgos Katsaounis, Eftichia Zoidi, Stefanos Athanasiadis, Pavlos Chatzoudis*, thank you for helping me miss home less when I'm with you. And to my wonderful girls *Georgia Skroubelou* and *Angeliki Kouka* whom I met in Volos back in 2008, moved together to the Netherlands and are still here, as well as to my dears *Lida Barou* and *Chrysanthi Anastasiou*, thank you so much for being in my life. I wouldn't be the same person if I hadn't met you and shared a big part of my life with you. And, finally, to my three favorite housemates over the years, *Ana Olasolo Alonso, Ezgi Yuksel* and *Apostolos Bougioukos*, thank you for being the closest thing to family while studying in Delft, and for

not being only housemates but also great, caring and wise friends.

Travelling to my support group back in Greece, I would like to firstly thank my high school friends *Dimitris Stivachtis, Manolis Savvidakis, Alexis Tzanakis* and *Maria Menegaki* for growing up next to me and still making me feel like a high-school student whenever I meet them. To my group of friends from Plaka, some of whom I know since I can remember myself, thank you for all the beautiful memories, all the swims, all the philosophical conversations and all the games we played in the middle of August's nights, summer after summer. Specifically, *Zacharias Markakis, Effie Mitsi, Aliki Koutoura* and *Nikitas Aggeletos* will always have a special place in my heart.

Some of the strongest friendships I formed over the years were during my university years in Greece. That's where I met *Despoina Chioktouridi, Despoina Spilioti, Dimitris Sourlas, Dimitris Pleouras, Thanasis Patsiouras, Christina Deligianni, Lefkie Siozou* and *Giorgina Ntasenou*, whom I can still call great friends after all these years, even though more than 2600km separate us. It is sad to miss some of the great milestones of your best friends due to the distance separating you, but the feeling of meeting each other after a long time and feeling that not a day has passed, and knowing you can depend on them for whatever you need no matter the distance is irreplaceable. That's what you are to me *Giorgina, Christina* and *Lefkie*. It was during my university years in Volos that I also met my italian teacher *Theodora Laskou*, my *mama d'oro*, who acted like a teacher, life coach, psychologist, friend and mom whenever I needed it during my years there. I am truly thankful to have met her and have her in my life and I wish I will have as a full, fulfilling, wise and animal-filled life as her.

I wouldn't be where I am today, nor who I am today, had it not been for my loving family. Since I was a kid they always believed in me and motivated me to be better, and tried to raise me to be a kind person. I grew up feeling loved and supported, had a beautiful childhood playing with my brother and cousins on the streets of my neighborhood, and having big and noisy feasts with my extended family to celebrate not only holidays, but any major achievements of each one of us. Thank you to all of you, especially my grandparents, my aunts *Eleni, Vicky* and *Mary*, my cousins *Giorgos, Vaggelio* and *Magda* and my two uncles *Antonis*. My mom and dad both started their PhDs in their forties while having full-time jobs and two kids going through adolescence. I don't know if growing up and seeing them study in the evenings and weekends influenced my decision to do a PhD... Probably; but when I was a teen I couldn't really grasp it. Now, especially after spending one year and a half working full time while finishing a PhD in parallel, and knowing how challenging it is, I have nothing but the utmost respect for them for doing this for years while raising my brother and me. I love you both a lot, and I will forever appreciate everything you did for me. To my brother, *Fotis*, thank you for being the nicest brother in the world and for always letting me take advantage of your kindness, and thanks also to *Francesca*, his better half, for finding a friend and a sister with the warmest of hearts in her.

At last, to my partner and life companion, *Cesar*, whom I met on my second day in the Netherlands, more than nine years ago, and has been with me on this journey ever since, thank you. Thank you for loving me; thank you for supporting my decisions, even when you don't agree with them; thank you for believing in me, even when I don't believe in myself; thank you for trying to understand me, even when I don't understand myself, thank you for pushing me and making me a better person. And mostly, thank you for

being you, for being the greatest travel companion, the greatest cat-dad to Butter, and the greatest walking encyclopedia to always answer all my questions regarding history and politics. I love you!

Marianthi
Rotterdam, December 2023